CARDIFF UNIVERSITY

SCHOOL OF ENGINEERING

The Impact of Turbulence and Turbine Operating Condition on the Wakes of Tidal Turbines

Timothy Ebdon
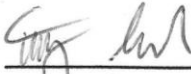
2019

APPENDIX 1 - STATEMENTS AND DECLARATIONS TO BE SIGNED BY THE CANDIDATE AND INCLUDED IN THE THESIS

STATEMENT 1

This thesis is being submitted in partial fulfilment of the requirements for the degree of ...PhD
(*insert PhD, MD, MPhil, etc., as appropriate*)
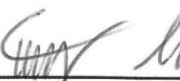
Signed _____

Date _10 / 8 / 19_____

STATEMENT 2

This work has not been submitted in substance for any other degree or award at this or any other university or place of learning, nor is it being submitted concurrently for any other degree or award (outside of any formal collaboration agreement between the University and a partner organisation)

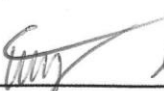Signed _____

Date _10 / 8 / 19_____

STATEMENT 3

I hereby give consent for my thesis, if accepted, to be available in the University's Open Access repository (or, where approved, to be available in the University's library and for inter-library loan), and for the title and summary to be made available to outside organisations, subject to the expiry of a University-approved bar on access if applicable.

Signed _____

Date _10 / 8 / 19_____

DECLARATION

This thesis is the result of my own independent work, except where otherwise stated, and the views expressed are my own. Other sources are acknowledged by explicit references. The thesis has not been edited by a third party beyond what is permitted by Cardiff University's Use of Third Party Editors by Research Degree Students Procedure.

Signed _____

Date _10 / 8 / 19_____

WORD COUNT _57 890_____

(Excluding summary, acknowledgements, declarations, contents pages, appendices, tables, diagrams and figures, references, bibliography, footnotes and endnotes)

Acknowledgements

This thesis is dedicated to Johanna, for whom no amount of thanks would be enough.

Abstract

This thesis examines the impact that turbulence and turbine operating condition have on the wake of a horizontal axis tidal turbine, and the implications of this impact for array design. This is done via the use of computer simulations using a scale-resolving hybrid turbulence model known as detached eddy simulation, which combines a Reynolds-averaged Navier-Stokes model in the near-wall region with large eddy simulation-like behaviour in other regions. This allows turbulent fluctuations to be resolved in the wake region whilst reducing the computational expense when compared to a pure large eddy simulation model. These computer simulations were supported by extensive flume measurements at three tip-speed ratios and three different turbulence conditions, which were used for both validation of the computational model, as well as data in their own right.

It was shown that turbulence intensity has a significant impact on the wake; increasing wake recovery, reducing wake swirl and increasing the width of the downstream region impacted by the wake, whilst simultaneously reducing the magnitude of this impact. In addition, high turbulence intensities appear to have some impact on the mean performance characteristics of the turbine and cause large increases in the magnitude of the fluctuations of these performance characteristics. These increases in fluctuations become larger still as the turbulence length scale increases. Turbulence length scale was not found to have a significant impact on the wake, however, an impact could not be ruled out.

The turbine operating condition was also found to have a profound impact on the resulting wakes. In the near wake, centreline velocity recovery was found to increase with increasing turbine thrust due to flow being diverted towards the turbine nacelle. For a volumetric averaged wake, greater power extraction was found to cause the greatest near-wake deficit. Wake swirl was found to be at a maximum at the point of peak turbine torque, whilst wake width was found to increase with increasing tip-speed ratio (and therefore turbine thrust).

It was found that the detached eddy simulation turbulence model produced good agreement with the experimental results across a wide variety of turbulence conditions. This is expected to be of interest to array designers wishing to optimise array configurations due to its ability to accurately predict both wakes and turbine performance, including transient effects.

Contents

List of Figures

vii

ix

List of Tables

Nomenclature

$$
\begin{aligned}
A &= \text{turbine swept area / m}^2 \\
C_P &= \text{power coefficient} \\
C_T &= \text{thrust coefficient} \\
C_\theta &= \text{torque coefficient} \\
D &= \text{rotor diameter / m} \\
D_\omega &= \text{Cross-diffusion term of } \omega \\
F_{DES} &= \text{DES turbulent kinetic energy dissipation multiplier} \\
F_T &= \text{Thrust force / N} \\
G_\phi &= \text{axial flux of angular momentum} \\
G_k, G_\omega &= \text{Production term of } k \text{ or } \omega \\
G_x &= \text{axial flux of axial momentum / m}^{-1} \\
g &= \text{gravitational acceleration / m s}^{-2} \\
\mathscr{I} &= \text{integral scale / s} \\
k &= \text{turbulence kinetic energy / J} \\
L_t &= \text{turbulence length scale / m} \\
l &= \text{characteristic length / m} \\
\dot{m} &= \text{mass flow rate / kg s}^{-1} \\
p &= \text{pressure / Pa} \\
\overline{p} &= \text{time-averaged pressure / Pa} \\
r &= \text{radial direction vector} \\
R &= \text{turbine radius / m} \\
Re &= \text{Reynolds number} \\
s &= \text{standard deviation of a sample set} \\
s_p &= \text{RMS fluctuations due to precision error} \\
s_t &= \text{RMS fluctuations due to turbulence} \\
S &= \text{swirl number} \\
S_k, S_\omega &= \text{Source term of } k \text{ or } \omega \\
t &= \text{time / s} \\
T &= \text{time over which a result has be averaged / s} \\
\overline{u} &= \text{time-averaged velocity / m s}^{-1} \\
\mathbf{u} &= \text{three dimensional velocity vector / m s}^{-1} \\
u_i &= \text{instantaneous velocity in } i \text{ direction / m s}^{-1} \\
u' &= \text{velocity fluctuation / m s}^{-1} \\
U &= \text{average velocity / m s}^{-1} \\
U &= \text{confidence interval} \\
v &= \text{characteristic velocity} \\
v &= \text{free stream velocity / m s}^{-1} \\
w &= \text{tangential velocity / m s}^{-1} \\
x_i &= \text{direction vector in } i \text{ direction} \\
x_i &= i^{\text{th}} \text{ variable} \\
\overline{X} &= \text{mean of a sample set} \\
\hat{\mathbf{x}} &= \text{unit vector in the } x \text{ direction} \\
Y_k, Y_\omega &= \text{Dissipation term of } k \text{ or } \omega \\
\hat{\mathbf{y}} &= \text{unit vector in the } y \text{ direction} \\
\hat{\mathbf{z}} &= \text{unit vector in the } z \text{ direction}
\end{aligned}
$$

Greek Symbols

Δx_i	=	error in i^{th} variable
δ_{ij}	=	Kronecker delta
η	=	Kolmogorov length scale
ε	=	turbulence kinetic energy dissipation rate / $\mathrm{J\,s^{-1}}$
λ	=	tip speed ratio
μ	=	dynamic viscosity / $\mathrm{Pa\,s}$
μ	=	population mean
μ_b	=	bias error
μ_p	=	precision error
μ_t	=	eddy viscosity / $\mathrm{Pa\,s}$
μ_{tot}	=	combined standard uncertainty
ν	=	kinematic viscosity / $\mathrm{m^2\,s^{-1}}$
ω	=	rotational velocity / $\mathrm{rad\,s^{-1}}$
ω	=	turbulence frequency / Hz
ϕ	=	a generic scalar
$\rho(\tau)$	=	autocorrelation coefficient
ρ	=	density / $\mathrm{kg\,m^{-3}}$
σ	=	population standard deviation
σ_p	=	standard deviation due to precision error
σ_t	=	standard deviation due to turbulent fluctuations
τ	=	time lag / s
τ	=	turbine torque / $\mathrm{N\,m}$

Acronyms

ADV	Acoustic Doppler Velocimeter
AoA	Angle of Attack
BEMT	Blade Element Momentum Theory
CFD	Computational Fluid Dynamics
CMERG	Cardiff Marine Energy Research Group
DDES	Delayed Detached Eddy Simulation
DES	Detached Eddy Simulation
DNS	Direct Numerical Simulation
DOE	Design Of Experiments
HATT	Horizontal Axis Tidal Turbine
HAWT	Horizontal Axis Wind Turbine
HPC	High Performance Computing
IFREMER	Institut français de recherche pour l'exploitation de la mer
IPCC	Intergovernmental Panel on Climate Change
LDA	Laser Doppler Anemometer/Anemometry
LES	Large Eddy Simulation
MRF	Moving Reference Frame
NTU	Non-dimensional Time Unit
PIV	Particle Image Velocimetry
RANS	Reynolds-Averaged Navier-Stokes
ROMS	Regional Ocean Modelling System
RPM	Revolutions Per Minute
RSM	Reynolds Stress Model
SAS	Scale Adaptive Simulation
SBO	Surrogate-Based Optimisation
SGS	Sub-Grid Scale
TI	Turbulence Intensity
TSR	Tip Speed Ratio
UDF	User Defined Function

Chapter 1

Introduction

Excavations of a tidal powered horizontal grain mill on the foreshore of Strangford Lough in Northern Ireland show that humans have been aware of the energy available in tidal flow and utilising this since at least the 7th century CE[1]. The use of the tides to produce useful energy has developed through the centuries, with the first commercial usage of tides to produce electricity on a significant scale appearing in 1967 with the Le Rance tidal barrage power station in Northern France[2]. This has been followed by other tidal barrage facilities in Canada, Russia, China and Korea, amongst others. Tidal stream turbines offer the ability to use tidal energy for the production of electricity but at a lower cost and with less environmental impact than barrage schemes[2]. In order to fully optimise the layout of arrays of tidal turbines (tidal farms), as well as to identify the potential environmental impacts from a turbine or an array of turbines, the wakes produced downstream of tidal turbines need to be accurately determined and understood. The aim of this thesis is to examine the use of a scale-resolving turbulence model in conjunction with extensive flume-testing in order to analyse whether this modelling approach offers advantages over previous modelling methods in reproducing the behaviour of the turbine wakes.

1.1 Climate change and the need for renewable energy

The 5th report from the Intergovernmental Panel on Climate Change (IPCC), released in 2014, found that there was unequivocal evidence from multiple, independent datasets that the global climate has been warming between 1880 and 2012[3]. The effects of this have included: an increase in precipitation in the Northern hemisphere, changes to the salinity of the world's oceans, an increase

in the acidity of the oceans, a decrease of sea ice in the Arctic, and a sea level rise which has been greater than that found in the previous two millenia.

The report also found evidence that the current atmospheric concentrations of greenhouse gases such as CO_2, NO_x and CH_4 are higher than they have been for the last 800 000 years, and that the anthropogenic emissions of these gases is extremely likely to have been the main driver of global warming since the mid 20th century. Key figures from the IPCC report have been reproduced in Figure 1.1.

Climate change is expected to have many and varied effects on both human and natural systems. These could involve the extinction of threatened species that undergo loss of habitat and cannot migrate, to the movement of wildlife (e.g. fish from areas of high ocean temperature or increased salinity), as well as more frequent extreme weather conditions, particularly more extreme hot weather events, extreme precipitation events and the impact that rising sea levels could have on coastal communities. The report concludes that even with a complete cessation of anthropogenic emissions of greenhouse gases some of these effects may continue for decades or centuries into the future, and that a continuation of anthropogenic emissions will probably lead to an increase in the strength of these effects, with a possibility that above certain 'threshold' values, these effects could undergo a step-change in intensity, or become irreversible[3].

A reduction in anthropogenic emissions is therefore essential if the extent of climate change is to be minimised. The cause for increases in carbon emissions by humans (as can be seen in Figure 1.1c) is mostly due to a rising global population and economic growth leading to increasing energy demand per person. Many industries require large amounts of energy, which to date has been mostly produced by the burning of fossil fuels such as coal, oil and natural gas, either in order to produce heat, or to produce electricity. This has been a major cause of global carbon emissions, and a reduction in the dependence on the burning of fossil fuels for energy must be achieved in order to reduce these emissions.

In addition to this, fossil fuels require millions of years to form, and are being consumed at a rate much greater than the the rate at which they are being replenished. Countries such as the UK have been exploiting fossil fuel reserves of coal, oil and gas since the industrial revolution, and the limited extent of supplies means that there is an increase in the reliance on imported fossil fuels. Geo-political factors can threaten supply of these imported fossil fuels, and thus energy diversification is desirable in order to ensure security of supply.

Both a desire to reduce carbon emissions as well as a desire to ensure the security of energy supply can be aided by a switch to renewable sources of energy. Renewable energy sources are naturally replenished at approximately the same
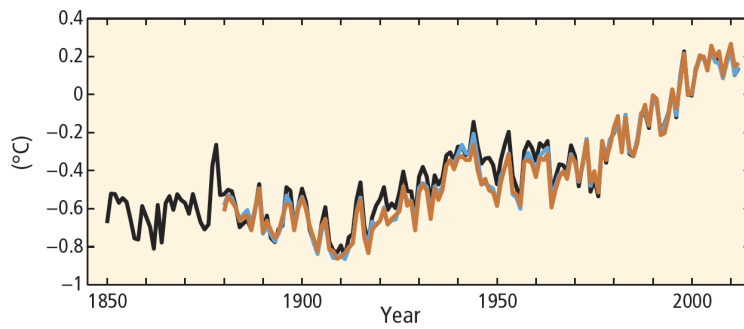
(a) Globally averaged land and sea temperature anomaly relative to the average for the period 1986–2005. The different lines represent different datasets.
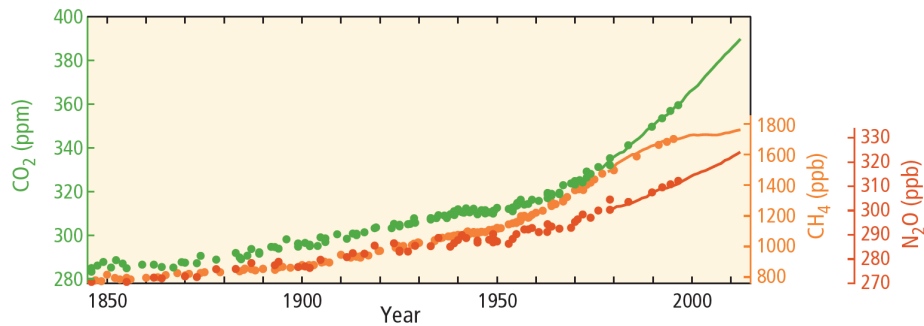
(b) Globally averaged atmospheric greenhouse gas concentration.
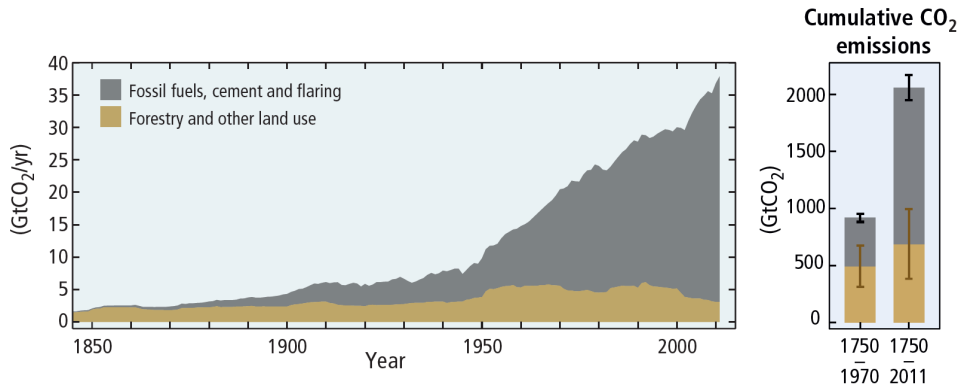
(c) Global anthropogenic CO_2 emissions.

Figure 1.1: Key figures from the 5th IPCC report, showing the trend in rising temperatures, greenhouse gas concentration, and anthropogenic emissions[3]

rate at which they are used, and, as they do not rely on the burning of fossil fuels, do not contribute to anthropogenic emissions of greenhouse gasses. Common forms of renewable energy include wind, solar, wave and tidal. Of these, wind and solar energy are the most mature technologies, with a combined installed

3

capacity of 276 GW in the European Union in 2017, representing nearly 30% of all electricity produced in the region[4]. Marine renewable energy such as tidal and wave energy show great promise due to the huge amounts of energy contained within the movements of the world's seas and oceans. The exploitation of this great resource is the motivation behind this thesis.

1.2   Marine renewable energy

Marine renewable energy comes in three main forms: tidal range which use the gravitational potential energy due to a difference in water height, tidal stream which use the kinetic energy of tidal flows, and wave energy. In addition to this, offshore wind energy production is sometimes also classified as marine renewable energy due to its location, however, this does not use the kinetic energy contained in seas to produce energy.

The tidal energy resource around the UK can be divided into two distinct resource types, tidal **range** and tidal **stream** resources. It has been estimated that upwards of 10% of the electrical requirements of the UK could be produced from tidal energy, with approximately half of this coming from stream and half from range resources[5]. The geographical distribution of tidal range and stream resource around the UK can be seen in Figures 1.2a and 1.2b respectively. From these diagrams it can be seen that in general there is little overlap of areas which could be utilised for tidal range and tidal stream schemes, meaning that the two technologies are unlikely to come into conflict. Even in areas where there is an overlap, such as in the Severn Estuary, it is not anticipated that the two technologies will come into conflict, mainly due to the different depths of water required for the two types of scheme.

Of all the forms of marine renewable energy, tidal energy, whether 'range' or 'stream' currently appears to be showing the most potential. Whilst all forms of marine renewable energy are intermittent to some extent, the amount of wave energy available at any given time is mostly dependent on the prevailing weather conditions. As the weather is inherently variable and unpredictable, so is the wave resource. The amount of power available from tidal resources is also intermittent due to tidal cycles; however, in contrast to other sources of renewable energy such as wave, wind, and solar energy, this intermittency is highly predictable.

A comparison of the differences between tidal range and stream schemes shows that the different technologies are subject to different challenges and opportunities. Tidal range schemes predominantly consist of 'proven' technologies; the turbines required are similar to those currently used in large scale hydro-electric schemes, and the civil engineering challenges of building large

(a) UK tidal **range** resource   **(b)** UK tidal **stream** resource
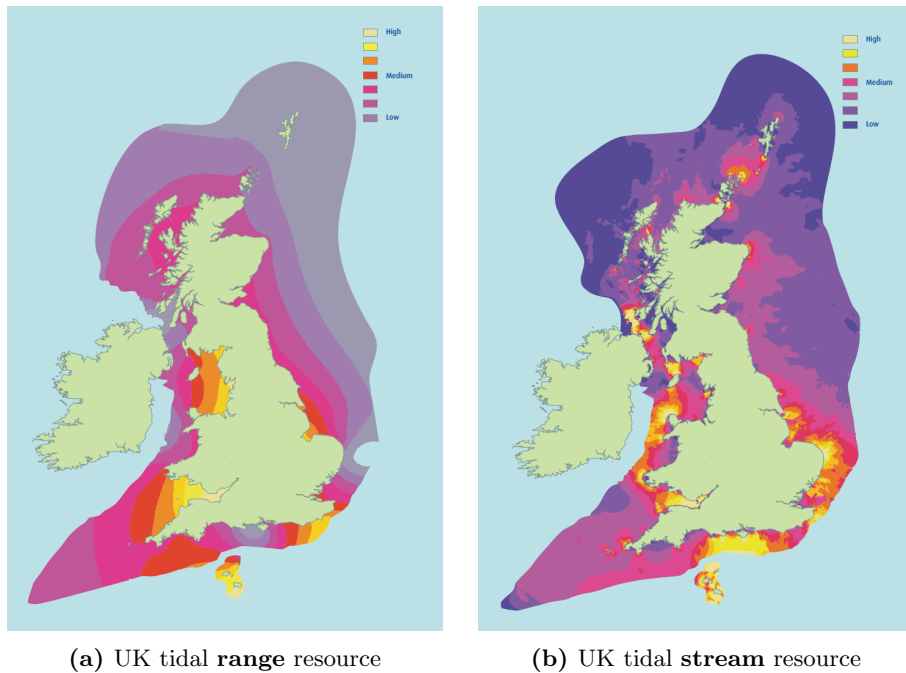
Figure 1.2: United Kingdom tidal range and stream resource, reproduced from [5]

barrages and coastal defences are also well understood[2]. In contrast to this, tidal stream turbines currently face the challenge of adapting technologies used in wind turbines to the much harsher submarine environment, and information regarding the effects of normal operation for a full size turbine over many years is not yet available. In addition to this, technology must be developed to secure power transmission to shore, where it can be imported to the electricity grid. A tidal barrage is inherently connected to land, and therefore does not suffer from this difficulty, and proposed tidal lagoons, if not themselves connected to the land, would only require a single connection to be made, and power conversion equipment could be housed above the surface, on the lagoon wall itself. On the other hand, tidal barrage schemes are huge undertakings in terms of materials, time and therefore capital requirements. It is expected that such schemes could be expected to have working lifetimes of over 100 years, and long return-on-investment times, which could make private funding of such schemes difficult[5]. Individual tidal stream turbines would have much smaller capital investment requirements, and arrays could be built to suit the available capital. In addition to this, whilst both stream and range schemes are expected to have an overall environmental benefit with regards to a reduction in carbon emissions, the size and nature of a barrage means that it could have large effects on the

local marine environment, with consequences for habitats and biodiversity, fish and other aquatic wildlife, as well as complications for maritime navigation if the area upstream of a barrage needs to be accessed by ship. These impacts, whilst often significant, are not necessarily detrimental; for example, at the site of the La Rance barrage, the local flora and fauna suffered "almost total destruction" in the three years of the barrier's construction, but subsequently recovered to show greater levels of bio-diversity than equivalent, adjacent sites[6]. Tidal stream turbines can be placed so as not to conflict with maritime navigation routes, and are expected to have much less of an impact on the environment, although the UK Sustainable Development Commission described the lack of data available regarding this as "a real issue"[5]. The improved modelling of wakes will play a major part in allowing accurate environmental assessments to be made.

1.2.1   Tidal stream turbines

Tidal stream turbines provide a method of low carbon, renewable energy production. Most renewable energy sources (wind, solar, wave) are inherently dependent on the weather, and therefore have a certain degree of intermittency (i.e. whether or not the wind is blowing, or the sun is shining). Whist individual tidal stream turbines do provide intermittent power because they do not produce electricity at slack water, this intermittent behaviour is highly predictable. Intermittency comes in two forms – daily intermittency due to the diurnal tides around the UK, but also a monthly intermittency due to the cycle of spring/neap cycles. Calculations show that careful siting of tidal turbines around the UK coastline could take advantage of the time delay between tidal flows to provide a constant, uninterrupted electricity supply of 45 MW using an installed capacity of around 200 MW, essentially removing the problem of daily intermittency[7]. This was achieved by utilising 6 potential sites dispersed around the UK coastline, in the area of the Menai Straights, and estuary locations at the Severn, Mersey, Clyde, Tyne and Humber rivers. The approximately monthly spring/neap tide cycles are harder to mitigate against, as they are a global phenomenon, and therefore occur at the same time, regardless of geographical location. A report by the sustainable development commission has suggested that the predictable variability of power output due to the spring/neap cycle can be mitigated against at "very low cost"[5].

1.2.2   Modelling of turbines

As with many industries reliant on the exploitation of fluid flows, the tidal stream turbine industry has used a combination of numerical modelling and

scale testing in order to reduce the financial risks involved in installing full-scale turbines at tidal sites. Much modelling of tidal turbines has been conducted to examine a diverse range of factors from blade design to flow-misalignment to ambient turbulence and their impacts on turbine performance. Largely due to the computational costs associated with large, detailed models of turbines, the majority of this work has concentrated on the performance of individual, isolated turbines. In order to most effectively exploit the tidal stream resource, which is found in areas of limited geographical extent, tidal turbines are expected to be deployed in arrays, and the close proximity of turbines to one-another in these arrays has the potential to lead to interactions between them. In contrast to the wind, the tidal resource is highly predictable in both speed, direction and temporal variations. Therefore, there is more potential for optimisation in the array layout of tidal stream turbines, by minimising detrimental interactions and maximising positive interactions between the turbines.

In order to achieve this end, it is crucial to improve the current understanding of the physical processes occurring in the wake of tidal stream turbines; what factors influence the size and shape of the wake, and what is the nature of the turbulent flow in the wake region. Knowledge of this will inform array layout, allowing the right compromises to be made in order to maximise energy extraction whilst reducing turbine loading and capital costs, and minimising any potential impacts that turbine arrays might have on the wider environment. This can be achieved by building confidence in a numerical model of turbine wakes through validation against flume experiments and/or full-scale models and prototypes. These models can subsequently be used to explore a wider range of conditions experienced by the turbines to increase our understanding of the interaction of wakes and turbines, leading to optimised array designs. To date, most modelling of tidal turbine wakes has been conducted using Reynolds-Averaged Navier-Stokes (RANS) turbulence models, however, these have been shown to over-predict the extent of the wake when compared to experimental measurements[8], [9], demonstrating the need for a different approach. For this reason, this thesis investigates the use of a Delayed Detached Eddy Simulation (DDES) turbulence model for modelling the turbulent mixing processes in the wake region.

1.3   Thesis aims and objectives

The aim of this thesis is two fold. Firstly, it is to assess the capabilities of the scale-resolving DDES turbulence model as a tool for the modelling of tidal stream turbine wakes. Subsequently, after identifying from the research literature turbulence intensity, length scale and turbine operating condition as factors

which have been suggested to affect the size, shape and character of the wake, the model was applied in conjunction with flume testing to establish how these factors may affect wake development downstream of a tidal stream turbine.

This was achieved via the following objectives:

- The creation of a Computational Fluid Dynamics (CFD) model for a single turbine using a DDES turbulence models.

- The execution of a testing campaign to examine the wakes in a flume tank as a means of obtaining data on wakes and to validate the numerical model.

- The use of the DDES turbulence model to assess the impact of ambient turbulence intensity, turbulence length scale and turbine operating condition on the size, shape and character of the wake.

1.4 Thesis layout

Chapter 1 introduces the thesis, the importance of renewable energy sources, and tidal energy. It also contains the thesis aims and objectives, as well as the thesis layout.

Chapter 2 contains a literature review describing the tidal resource and previous work which looks at tidal turbines and their simulation. This explains the importance of and need for wake modelling, reviews the current level of understanding in the research community of tidal turbine wakes, and places the DDES turbulence model within the context of previous work.

Chapter 3 provides a detailed look at the mathematics of turbulence and the turbulence modelling used in this work.

Chapter 4 sets out some of the techniques used to analyse turbine performance and wakes, as well as methods used to quantify the uncertainties in flume measurements.

Chapter 5 details the CFD model used.

Chapter 6 describes the flume testing campaign used for validation of the CFD model.

Chapter 7 presents the results of this work; the validation of the CFD model, and the effect of turbulence and turbine operating condition on the wake.

Chapter 8 provides the thesis conclusions and recommends further work for the future.

Appendix A contains the User Defined Function (UDF) written in the C programming language in order to retrieve force and torque information from the CFD models.

Chapter 2

Literature Review

This review is intended to give the reader an introduction to the field of tidal energy and tidal energy research. Climate change and the need for low-carbon energy resources has been discussed in the introduction, so this literature review will start by examining some of the advantages and disadvantages offered by tidal energy and the different approaches to extracting energy from tidal waters including device types. Following this, a more focussed examination is made of research into the performance and loadings on axial flow turbines. This leads onto a discussion of the current research into modelling and experimental measurement of wakes of isolated turbines, small groups of turbines and larger arrays. Finally, the integration of tidal turbine arrays into ocean-scale models is examined, along with the potential wider environmental impacts of large-scale turbine arrays.

2.1   Tidal energy

Tidal currents in the seas and oceans occur due to the gravitational interaction of the moon, the sun and these large bodies of water. The tidal movements of the seas and oceans give rise to two phenomena which can be exploited for the production of renewable energy. These are tidal currents – the movement of water from one place to another, and tidal range – periodic changes in water depth due to the accumulation of water in a particular region. The rotation of the earth on its axis and the orbital motion of the moon make this interaction periodic in nature. As the period of rotation of the earth is approximately 24 hours, and the orbital period of the moon 29.5 days, the tidal cycle contains frequency components with periods of approximately 1 day and 1 month. The behaviour of tides is an active field of study in itself, and predictions of tidal heights and currents strengths is complicated by the presence of land masses and

bathymetry, particularly when resonance effects are created due to the geometry of an estuary or presence of a continental shelf[10].

Notwithstanding these complications, the fact that the relative positions and orientation of the sun, moon and earth are highly predictable means that tidal currents and tidal heights have the theoretical potential to also be highly predictable[10]. In reality, once an area of particularly high activity has been identified by computer models, it is likely that measurements will be made using Acoustic Doppler Current Profiler (ADCP) equipment (for tidal stream sites) or depth measurement buoys (for tidal range sites), to confirm that the site is suitable for a tidal energy scheme.

2.1.1 Resource estimation

Mapping the currents on the surface of the world's seas and oceans has been carried out since man first started going to sea. Measurements of tidal heights, times and currents have been crucial for safe navigation and for the production of maritime charts. Modern day maritime charts use a combination of buoy measurements and computational simulations in order to predict the surface currents relevant to sailors. When taken together, this information, whilst very important, is only of limited use in the assessment of tidal energy resource, due to data from nautical charts being concentrated on tidal heights and velocities at the surface.

Estimates have put the amount of power dissipated globally on continental shelves at approximately 2.5 TW[11]. As noted by Bahaj, approximately 0.25 TW of this is dissipated around the UK, and if only 10% of this could be utilised, then that would equate to approximately 220 TW h per annum - approximately half of the UK's energy needs[12]. Whilst this resource is generally diffuse, it is concentrated at specific sites, around headlands or in natural channels such as tidal races around the channel islands, the Pentland Firth in Scotland, and along the west coast of the UK, from the Severn to the Hebredies[13].

In addition to this, whilst the tidal resource is predictable and reliable, it is, by its nature, intermittent. Studies have been conducted to examine the possibility of using tidal arrays at different locations to reduce the inherent intermittency of tidal power. A study by Hardisty[7] showed that it could be possible to use the phase shift of the tides at 6 different UK locations to produce 45 MW of base-load electricity supply from 200 MW of installed turbine capacity. The study was based on analytical predictions of tidal flow rates, using the mean spring tidal velocity from Admiralty Tidal Diamond data. These data give the flow on the surface of the water at specific locations, so the locations used may not be the most suitable or have the strongest currents, but the work

does show the potential of tidal stream energy to supply consistent power to the UK grid, given the use of appropriately phase-shifted sites. Whilst this study is promising in terms of reducing the intermittency of tidal flows during a given day, monthly variations in the strength of tides (spring and neap tides) are globally synchronised, which would mean there would still be significant variability over the course of a month[10].

Restrictions on the siting of tidal stream turbines

By no means can all of the dissipated tidal energy can be utilised. Placement of devices for extracting energy from tidal currents is restricted by a variety of factors, both physical and economic, and more precise estimates of the useable tidal energy resource depend strongly on what assumptions are made. Determining where tidal turbines may be placed is not simply a matter of determining where flow speeds are largest. There are many other factors which determine the precise siting of tidal turbines[13].

Local flow conditions Flow conditions at a tidal site can be heavily influenced by local bathymetry[14], and a regional-scale model may not have the resolution to predict the flow conditions at a precise position within a region of generally elevated flow speed.

Sea-bed conditions Tidal turbines must have some way of fixing their position in the sea. There is a wide variety of proposed methods for doing this, from piles, to anchor cables, to hanging turbines from floating or submerged pontoons. What all of these methods have in common is that, to a greater or lesser extent, they must be fixed to the sea bed. Different sea bed conditions may preclude certain types of mooring, or rule out the possibility of mooring altogether.

Shipping lanes Tidal turbines in shallow water have the potential to conflict with maritime traffic, and therefore need to be sited outside of established shipping lanes, or at sufficient depth so as not to obstruct shipping, even with the effect of tides and waves.

Position in water column The depth dependence of tidal flow velocities due to the drag of the sea-bed can be approximately described by a $\frac{1}{7}^{\text{th}}$ power law[15]. This means that the flow-velocity increases and the shear across the turbine decreases the closer the turbine is placed to the water surface. However, the turbine cannot be placed too close to the surface for reasons of cavitation[16], the need to keep the turbine fully submerged even during extreme weather conditions, and the avoidance of obstruction of maritime traffic.

Proximity to land Ideally, turbines should be placed in easy-to-access waters close to both a port from which maintenance can be undertaken, and infrastructure which allow the turbine to be connected to the electrical grid. The further away turbines are from such locations, the more costs increase, making some sites uneconomical.

2.2 Tidal range

There are two very different approaches to producing electricity from tidal energy: using the tidal range, and using tidal currents. Tidal range schemes consist of an impoundment, in the form of either a tidal barrage or lagoon, which can store a body of water separately from the open sea. Water is selectively allowed to enter or is released in order to create a head difference between the water within the impoundment and the open sea. Once a large enough head has been achieved, water is then released from one side of the barrier to the other through turbines installed in sluiceways, allowing the production of electricity.

As with other forms of tidal energy, tidal range schemes have the advantage of being very predictable, due to the predictable nature of the tides. They also have the advantage of only requiring mature, well understood technology; both with respect to the types of turbines which are required, as well as the engineering of the tidal impoundment or barrier wall itself. Maintenance of turbines can also be assured as the passages in which the turbines are located can be engineered to allow access to the turbine for maintenance and repair.

On the other hand, tidal range schemes are typically very large civil engineering projects, requiring large amounts of up-front investment. The La Rance tidal scheme in northern France takes advantage of the shape of the local coastline to use a 710 m barrage and 24 turbines to give a rated capacity of 240 MW, and has been operating since 1966[17]. In areas with a large tidal range, but with less favourable coastal geometry, larger impoundments are required. In the UK, the area with the largest tidal range resource is the Severn Estuary, in which various tidal range schemes have been proposed. During the decade leading up to the time of writing, the scheme under most active consideration was the Swansea Bay tidal lagoon, to take advantage of the 10.5 m tidal range in Swansea Bay. The scheme proposes the building of a 9 km horseshoe shaped embankment to enclose an area of 11.5 km^2 for a rated power of 320 MW, and a levelised cost of energy estimated to be approximately £150 /MW h[18]. Clearly, building a 9 km embankment in an area of active tides is a large civil engineering undertaking; for comparison, the 1.1 km Cardiff bay barrage, completed in 1999, cost £220M[8].

A more ambitious scheme to create a barrage across the Severn Estuary

from Cardiff to Weston-Super-Mare would require the building a 16.1 km long barrage, but would, in a similar way to the La Rance tidal scheme, utilise the local geography to create a large impoundment area when compared to the length of artificial embankment required[5]. This means that the cost per MW h is estimated to be lower than for schemes such as the Swansea tidal lagoon, and with a generating capacity of 8.6 GW, it could provide 4.4% of the UK electricity needs (2006 data)[5]. However, this type of barrage comes with added complications when compared to a tidal lagoon. Firstly, a barrage in this location would block shipping traffic from the ports of Cardiff, Newport and Avonmouth. This problem has been alleviated at La Rance by a ship-lock built into the barrage itself and this could be implemented in a Severn barrage, however, it should be noted that there are no major commercial ports upstream of the La Rance barrage; the large commercial port of St-Malo is located downstream. In addition to difficulties regarding shipping, a barrage across the Severn estuary would also have a large effect on the both tidal heights and times upstream of it. Studies have suggested that areas of wetland which are periodically flooded by the tides could move or disappear, endangering these particularly sensitive habitats[5].

Overhanging all of these schemes is the necessity of raising the initial capital to fund the scheme. Given the maturity of the technology used and the expected increase in energy demand, it seems that these schemes should provide a relatively secure return for investors. However, the amortisation time is high, and this has led to the reluctance of both government and commercial creditors to invest, culminating in 2018 with a decision by the UK government not to invest in the Swansea lagoon[19]. Tidal stream technologies are the focus of this thesis, and as such tidal range schemes will not be discussed any further.

2.3 Tidal stream

Tidal stream devices are placed in areas of high tidal flow, and convert the kinetic energy in the flow into electrical energy. Most devices either in operation or subject to active research can be placed into one of three categories: axial-flow turbines, cross-flow turbines or oscillating devices.

2.3.1 Device types

Axial-flow turbines

Axial-flow turbines have their axis of rotation aligned horizontally, in line with the direction of flow. For this reason, they are often referred to as horizontal axis tidal turbines (HATTs). Much of the technology for this class of turbines

has been taken directly from the wind energy industry, with this informing areas such as blade and generator design, as well as giving some insight into the flow physics occurring in the vicinity of the turbine rotor itself. Significant differences between wind and tidal turbines remain however. Tidal turbine rotor diameters are smaller than for wind turbines, as the higher fluid density means that structural forces on a tidal turbine of equivalent size would be much greater. The thrust per unit area on a body in a fluid is proportional to the density of the fluid, and the square of the fluid velocity[20]. A wind turbine operating in a high winds of 40 $\mathrm{m\,s^{-1}}$ in air with a density of 1 $\mathrm{kg\,m^{-3}}$, will experience only $^1/_6{}^{\mathrm{th}}$ the thrust per unit area of a turbine operating in a high velocity tidal flow of 3.1 $\mathrm{m\,s^{-1}}$ in water with a density of 1000 $\mathrm{kg\,m^{-3}}$. Correspondingly, for the thrust forces to be similar, the area of the marine current turbine must be $^1/_6{}^{\mathrm{th}}$ that of the wind turbine, with a radius $^1/_{\sqrt{6}}$ the size.

In addition to this, the tidal stream sites with best access will be closer to shore and in shallower water (typically depths of less than 40 m), but turbines placed in these depths must be limited in diameter so as not to be so close to the surface that they become a danger to shipping at low tides with storm swells, and not so close to the sea bed that they experience unacceptable cyclic loading due to velocity shear. As well as this, flow effects such as cavitation must be accounted for in the design of a tidal stream turbine[16], but do not exist with wind turbines. Finally, the underwater marine environment itself creates difficulties; devices must be well sealed against the ingress of salt water and resistant to bio-fouling, which could change the flow around the turbine itself.

As this thesis concentrates on axial-flow turbines and their wakes, some of the different concepts in the area will be explored in more detail. Different manufacturers have been and are exploring different concepts based around axial flow turbines, in order to try to address some of the major challenges of tidal turbine technology. These challenges include maintenance, installation, reliability and turbine performance. Attempts to find the best compromise between these factors has led to some notably different design concepts and strategies.

Atlantic Resources AR1500 This three-bladed turbine concept is probably the most reminiscent of the commonest form of wind-turbine technology. There are multiple manufacturers currently developing turbines of this style; as an example, the Atlantic Resources AR1500 turbine will be described, an image of which is shown in Figure 2.1. The three bladed turbines are connected via a gearbox to a generator contained in a nacelle. The entire turbine yaws so that the rotor faces the oncoming flow, and the

carbon-fibre blades can be collectively pitched to shed power, maintaining rated power output beyond the rated flow velocity. Atlantic Resources claim a 25-year design life, with three planned services during that time. The turbine has a 16 m diameter rotor, which is designed to give a rated power of 1.5 MW at a flow velocity of 3.0 m s^{-1}[21].

Four turbines of similar design have been installed at the European Marine Energy Centre in Orkney, with two of these supplying 700 MW h to the grid in August 2017; a world record for monthly production at the time[22].

Figure 2.1: Installation of Atlantic Resources AR1500 turbine at EMEC in Orkney[23].

It should be noted that there are multiple groups working on turbines of a similar design, this one has just been used as an example. It is also the most similar full-scale turbine to that which has been modelled in this thesis.

SeaGen The SeaGen concept combines two turbines and a monopile support structure in a single unit. It has been operating in Strangford Lough, Northern Ireland, and connected to the grid from 2008, with a rated power of 1.2 MW[27]. It was decommissioned and removed in 2017[28]. The twin turbines are of a two-bladed design and rotate in opposite directions. The turbines do not yaw, rather, the blades pitch when the current direction

(a) The SeaGen turbine[24].
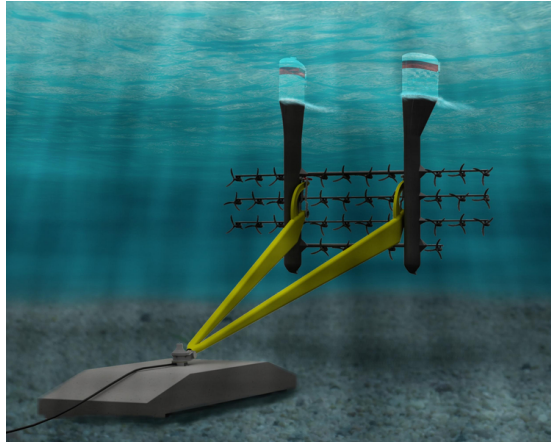
(b) A proposed array of Instream turbines from Schottel Hydro[25].

(c) The 16 m diameter OpenHydro device[26].

Figure 2.2: Examples of axial flow tidal turbine devices.

reverses, causing the turbines to rotate in the opposite direction. This removes the need to add a yawing mechanism to the turbines, but does increase the complexity of the design of the blade pitching mechanism. Numerical studies have indicated that the influence of a stanchion and support structure on turbine performance is much greater if the support structure is upstream of the turbine, rather than downstream of it. The decrease in power of a turbine due to the presence of the nacelle and stanchion has been demonstrated to be as much as twice as great for a configuration where the rotor was placed downstream of the stanchion, compared to the case where it was upstream of the stanchion[29]. This decrease in power output for half of the tidal cycle must be weighed against the increased cost and complexity of a yawing device when making a design decision about the economics of a particular turbine.

One of the major advantages of the SeaGen system is its integration of the monopile and two turbines. The turbines are secured to a moveable 'batwing' structure, either side of the monopile, which protrudes from the water's surface. The wing can be moved up the monopile, bringing the turbines and their blades out of the water for ease of maintenance. This removes the need for specialist heavy-lift vessels, or to have divers operate in strongly tidal regions[27]. The protruding monopile does however preclude the possibility of this system being used in or near shipping lanes, as the structure would present a hazard to navigation. An image of the SeaGen turbines, raised out of the water, can be seen in Figure 2.2a.

'Instream' turbines, Schottel Hydro GmbH The Koblenz based company Schottel Hydro GmbH produces a tidal turbine concept based on the idea of using a larger number of small, modular turbines, rather than the larger turbines of its competitors. Schottel's turbines have diameters of 3–5 m, with a rated power of 70–54 kW at flow speeds of 3.8–2.6 m s^{-1}[30]. The turbines use passive adaptive blades (which flex under high thrusts in order to shed power)[31], and therefore do not require a pitch mechanism, reducing complexity and costs. Using multiple, smaller turbines increases the level of redundancy in an array, which could increase the reliability. Similarly, the smaller diameter means that it is possible to site the turbines in shallower water, which would not be accessible to larger devices. Much of the development work at Schottel has been done in partnership with Tidal Stream Ltd., which develop mooring devices to support multiple turbines and facilitate maintenance. An image of an array of Instream turbines can be seen in Figure 2.2b.

OpenHydro OpenHydro developed an open-centred axial flow turbine, contained within a circular duct, which houses a direct drive permanent magnet generator, as well as serving to increase the flow rate through the turbine itself. The turbine is mounted on a sub-sea base and is placed directly on the unprepared seabed. The commercial OpenHydro design is 16 m in diameter and rated at 2 MW[32]. OpenHydro have focussed on simplicity in their design, in an attempt to increase reliability. The use of a direct drive generator means that no gearbox is required, and the company states that neither seals nor lubricants are required. In addition, the inclusion of an opening at the centre of the turbine is intended to reduce the potential for harm to marine wildlife in the close vicinity of the turbine. In July 2018, a week after achieving the grid connection of a turbine in Canada, it was announced that OpenHydro had been put into administration, with reported debts of approximately € 280M[33]. An image of the OpenHydro turbine is shown in Figure 2.2c.

Cross-flow turbines

Cross-flow turbines are characterised by having their axis of rotation perpendicular to the direction of flow. If this axis is aligned vertically, then they are known as vertical axis tidal turbines (VATTs). With the rotation axis aligned vertically, these turbines can take advantage of flow from any compass direction. This means that installations of VATTs do not need to be able to re-align their devices or change the pitch of the blades when the flow direction changes[34]. Cross-flow turbines can be made with helical or straight blades. Straight blades are essentially an extrusion of a 2D hydrofoil profile, the simplicity of which reduces manufacturing costs[35]. Rotational velocities of cross-flow turbines are generally lower than with axial-flow turbines[35], which reduces the chances of injury to marine wildlife in the event of a collision, however this lower rotational velocity requires a more complex gearbox in order to match the rotational velocity of the turbine to the required rotational velocity of the generator. In addition to this, cross-flow turbines are generally less efficient than axial flow turbines[34], experience more torque ripple, and their low starting torques mean that external starting mechanisms may be required[35]. Cross-flow turbines are not the main focus of this thesis and are therefore not further discussed.

Oscillating devices

Oscillating devices can be either based on a foil or flexible membrane design. The foil devices consist of a wing with a hydrofoil profile as a lifting device.

This wing is connected to an arm which is fixed to a pile with a hinge. Water flowing over the wing causes it and the connecting arm to be moved upwards; a change of angle-of-attack moves the wing and arm downwards, and in this way the kinetic energy in the tidal flow can be turned into electricity. The flexible membrane devices consist of a membrane, bent into a curve by a tensioned cable, which creates a bi-stable configuration. This is aligned with the flow such that the membrane flexes up and down in turn, from one of the stable configurations to the other. Hydraulic dampers can be placed along the length of the device to enable power take off, or the downstream end of the device can be connected to an arm in order to produce useful energy. Flexible membranes have the advantage that they have few moving parts, and are relatively simple to manufacture, however, fine tuning is required with the dampers to give an optimised mechanical response to the flow, and care must be taken in the selection of the membrane material so that it is not susceptible to fatigue. At the time of writing, the French company EEL Energy were actively looking for investment of € 3–7M in order to take their tested prototype, shown in Figure 2.3, to full production. They anticipate a 15 m × 15 m undulating membrane device will produce 1 MW at 2.5 m s^{-1}[36].

Figure 2.3: The EEL undulating membrane concept[36].

Both lifting foil and flexible membrane devices need to be turned to align with the flow direction, assuming they have been configured to move up and down in the water column. It would be possible to configure these to move from

20

side to side in the water column, in which case they could be made to pivot on their mooring stanchion, however the flow dynamics would be complicated by any shear in the water column.

Other types of device

Other devices are available for the harvesting of tidal energy which do not fit neatly into any of the categories named above. An example of one of these technologies, which has recently received approval from the Welsh government for deployment near Anglesey, is the 'Deep Green' device from Swedish company Minesto. Deep Green uses a relatively small (1.5 m diameter) turbine attached to a 12 m wing, which is tethered to the sea bed and acts like a kite. The swooping motion of the kite causes the turbine to experience a higher velocity (Minesto claim up to $10\times$) than the tidal current itself[37], and since the kinetic energy available in the flow is related to the cube of the velocity, a ten-fold increase in velocity through the turbine this would lead to a thousand-fold increase in available energy. This gives a rated power of 0.5 MW in flows of 2.4 m s^{-1} [37], which compares very favourably to the 54 kW rated power of Schottel's 5 m turbine in the same flow velocity[30]. The low size and weight of the device when compared to its rated power suggests lower production costs when compared to its competitors, however, the kite design has additional complications. Power generated at the turbine must be transferred to the seabed, 'flying' such a kite can be expected to require complex control algorithms to allow it to 'fly' in ebb and flood flows, as well as to 'land' at slack water, and 'take-off' when tidal flow resumes. In addition to this, there are possible complications due to interactions with marine wildlife.
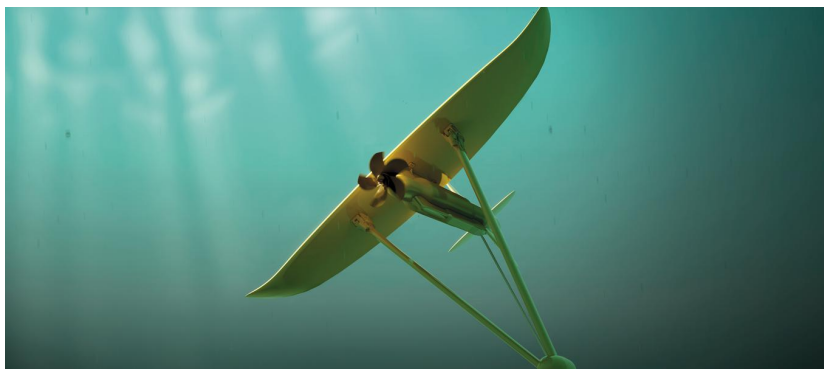
Figure 2.4: The Minesto Deep Green winged-turbine device[37]

2.3.2 Installation and maintenance

When compared to other forms of renewable energy such as wind and solar energy, tidal energy has the advantage of being very predictable. Tidal flows can be predicted long into the future, and are essentially unaffected by changes in weather. These reliable, predictable flows do however lead to complications for the installation and maintenance of tidal devices. Whilst a wind turbine may be sited in an area of higher average wind speeds, the daily or seasonal variation in the weather means that installation and maintenance can be carried out in periods of low wind speeds. By contrast, a tidal energy site may only have periods of a few tens of minutes spaced six hours apart where divers or machinery can be safely deployed in the water, severely complicating maintenance. Different turbine developers have taken different approaches to mitigating these difficulties. These can broadly be separated into two groups: attempting to reduce the need for servicing and maintenance through turbine design or redundancy, and producing turbines which can be quickly brought to the surface.

OpenHydro's open-centre turbine design attempts to reduce maintenance requirements and increase reliability by removing the need for seals, lubricants and gearboxes; gearboxes being the most common source for turbine faults in the wind industry[38]. Schottel Hydro's 'Instream' turbines are smaller, and when deployed in an array reduce the vulnerability of the energy production in the event of the failure of a single turbine. A 1.5 MW deployment would require ca. 25 Instream turbines, when compared to a single AR1500 device. Problems with individual turbines would therefore be, to some extent, mitigated by the larger number of turbines in an array, and the failure of a small number of turbines would not cause a complete failure of the 1.5 MW deployment, and not necessarily require immediate repair. The smaller size and weight of the individual Instream turbines (ca. 1 t dry weight[30]) also means that removal of an individual turbine would not require the heavy lift equipment necessary for an AR1500 with a dry weight of approximately 150 t[21].

Both the AR1500 and SeaGen devices have been designed to be quickly brought to the surface, albeit using very different approaches. The AR1500 connects to its mounting base using a gravity stab system with wet-mate connectors. Once the lower structure has been installed on the seabed, the turbine can be lowered into position without the use of divers or Remote Operating Vehicles (ROVs) as the male part (located on the turbine) connects with the female part (located on the support tower). The weight of the turbine holds it in place[21]. The simplicity of connection means that the turbine can be quickly lowered from or brought to the surface, allowing maintenance to be carried out either on ship or on dry land. In contrast to this, the SeaGen device requires

no heavy-lift ship to bring the turbines to the surface. The surface-penetrating monopile on which the SeaGen devices are mounted allows the turbines to be raised out of the water, allowing maintenance and servicing to be carried out above surface.

2.4   Turbine research

The most important performance characteristics of axial flow turbines (power, thrust and torque), can be described by non-dimensionalised coefficients, C_P, C_T and C_θ respectively[39]. These coefficients relate the power produced by a turbine to the kinetic energy of the fluid passing through it, the thrust force on the turbine to the thrust on a disc of the same area and the torque of the turbine to the maximum theoretical torque. Further explanation and definition of these coefficients can be found in Chapter 4. These coefficients allow straightforward comparison of the performance of turbines of differing diameters in different flow conditions. It has been shown that these coefficients are functions of the non-dimensional Reynolds number, Re, and the tip-speed ratio, λ, which is the ratio of the blade tip-speed to the free stream velocity[15]. The functional relationship of C_P, C_T and C_θ to Re has been shown to be such that, above a particular threshold, each of these coefficients become independent of Re, and therefore effectively become dependent only on tip-speed ratio[8],[15]. The point at which this Reynolds number independence occurs varies from turbine to turbine, but a characterisation of the performance characteristics above this point can then be applied to turbines from model- to full-scale.

Most of the initial research into HATTs concentrated on predictions of turbine performance and loading. Clearly understanding this aspect of turbine design is important if tidal turbines are to become economically viable. Some of the findings from the wind industry (some of which themselves derive from the development of ship propellers) have been transferred directly, such at the Lanchester-Betz limit for the maximum available power from a turbine. This limit (commonly called just the 'Betz Limit'), derives from the fact that turbines produce energy by extracting kinetic energy from a moving fluid. Given that the mass of fluid will not change, this extraction of energy must lead to a reduction in flow velocity behind the turbine. If *all* of the kinetic energy in the fluid were to be extracted, then the flow would come to a standstill on passing through the rotor disc. In this situation, no energy could be extracted, as the stagnation behind the turbine prevents any flow passing through it. On the other hand, the less the fluid is slowed down by the turbine, the less energy is extracted. Momentum theory can be used to examine how the amount of energy extracted by the turbine is related to the change in fluid velocity from

upstream to downstream of the turbine. It can be shown that the ratio of extracted energy to kinetic energy of the stream tube passing through the turbine disc has a maximum of $^{16}\!/_{27}$, or 0.593[39]. This is known as the 'Betz limit' and is not due to any deficiency of turbine design, but solely due to the need for striking a balance between reducing the fluid velocity (and therefore extracting as much energy as possible), whilst not causing the flow to stagnate behind the turbine. It should be noted that the Betz limit applies to axial flow turbines in a free-flowing fluid (i.e. without any blockage effects). If the turbine is placed in a duct (such as with the OpenHydro design), then the acceleration of fluid through the duct can cause the turbine to have a power coefficient higher than suggested by the Betz limit if only the turbine diameter and far-field freestream velocity are used to calculate the available kinetic energy. Similarly, numerical studies of turbines in high local blockage conditions (simulating a closely spaced turbine fence), indicated that a high local blockage can cause the C_P of these turbines to exceed the Betz limit[40]. The boundary conditions used for the model in this study by Schluntz and Willden impose a constant mass flow, and therefore in a real tidal channel where the mass flow is variable and head-driven it can be expected that the increased blockage of the turbines will lead to a reduced flow rate, and therefore the increase in C_P may not be so great in practise. In addition to this, if the blockage is too high, then the flow will be diverted outside and around the duct, rather than through the turbine disc. Nonetheless, the authors note that whilst the C_P of all modelled turbines increased with increasing blockage, designing turbines for the expected blockage brings particular benefits.

2.4.1   Numerical modelling techniques

Numerical modelling of tidal turbines is subject to the compromises involved in computer modelling, namely, a trade-off between solution accuracy, level of solution detail and computational expense. Because of this, a variety of techniques have been employed, each choosing a different point on the spectrum at which to make the compromise. Much of the choice of which method to use depends on what information the user requires, and where the individual user can afford to make compromises. In order of increasing detail (and consequently computational expense), the most common methods are Blade Element Momentum Theory, coupled Blade Element Momentum Theory (BEMT) and Computational Fluid Dynamics (CFD), and Blade Resolving Computational Fluid Dynamics[41]. Within each of these categories there are subdivisions

which themselves can make a great deal of difference to computing time – for example the difference between two-equation turbulence models and Large Eddy Simulation (LES) (discussed below).

Blade Element Momentum Theory

Blade Element Momentum Theory is a numerical method for rapidly computing blade loading and turbine power by combining blade element theory and momentum theory[39]. Momentum theory considers a horizontal axis turbine as an actuator disc, extracting kinetic energy from a moving fluid. Following laws of momentum and mass conservation, expressions are formed for the axial and tangential induction factors. In its most basic form, the method involves discretising the blade in the spannwise direction to create a series of typically 10–20 blade chord sections[42]. The radial location of these chord sections, the blade twist, the flow velocity and the rotational velocity are then used to calculate the incident resultant velocity for the sections. A lookup table or 2D computational method such as the panel method in XFOIL, is then used to calculate the hydrodynamic forces (lift and drag) on each of the chord sections. From the lift and drag forces on the chord sections, the total torque and thrust on the turbine can be calculated. The combination of these two theories leads to an iterative routine for the calculation of turbine torque and thrust. A more complete description of BEMT and its application to wind turbines can be found in [39].

BEMT has the advantage that it can be very quick, particularly if lookup tables are used for foil section data. It does however have a significant number of drawbacks, some of which can be partially overcome through the use of correction functions, or by improving the method used for the 2D hydrodynamic calculation. For example, the basic BEMT model is an integration over a series of discrete 2D foil sections. This fails to take into account 3D effects, such as spannwise flow along the blade. Myers and Bahaj[43] conducted experimental work in a recirculating flume which produced power outputs greatly in excess of that which was predicted using a BEMT model. This "overpower" when compared to the BEMT predictions increased as a larger proportion of the blade operated at a higher Angle of Attack (AoA) than the stall angle. The authors hypothesised that this was due to the failure of the BEMT model (which is based on 2D hydrofoil data) to take into account the stall-delay effect caused by spannwise flow along the blades. Such an under-prediction of power output by a BEMT model could lead to negative effects for turbine power production, for example, causing power production to be prematurely curtailed due to generator overloading, or worse, causing damage to the turbine drive train. Similar

results were found by Porter et al.[44]. They considered a BEMT model which combined the results of a commercial 2D CFD solver for the radial sections with a BEMT model. This was intended to extend the capabilities of the BEMT code to allow it to conduct calculations with unsteady flows. The 2D CFD–BEMT model showed closer agreement to 3D CFD results than that achieved with a BEMT model using results calculated from XFOIL, with lower computational requirements than 3D CFD. These differences in computational expense were found to be marginal for steady-state calculations, but extended to orders of magnitude reduction in computational time for the calculation of turbine power and torque for unsteady flow situations.

Blade element theory presumes that the blade chord is small compared to the circumference of rotation at that radial position, in order that the streamlines can be considered to be moving in a straight line from leading edge to trailing edge. In addition to this, momentum theory assumes that the bladed rotor can be approximated to a porous disc (high solidity). Other 3D effects occur due to the effect of the rotor hub and blade tips. The pressure difference between the suction and pressure sides of the blade inevitably leads to the inducement of a flow around the blade tips, forming a tip vortex. This is a 3D effect which is not taken into account if purely 2D data for lift and drag profiles is used. In order to produce more accurate results, it is necessary to include correction factors and functions for such effects as tip vortices, such as those discussed in the work of Moriarty and Hansen[45] and Burton et al.[39].

Whilst BEMT calculations can take into account the effect of a profiled flow by adding a depth-dependency to the flow velocity, it is more difficult to take into account turbulent features with length scales similar to the diameter of the turbine itself, or the effects of highly turbulent flow conditions. The work reported by Porter et al.[44] was intended as a response to this. In addition to this, BEMT produces estimates for turbine performance characteristics, but does not produce estimates of the length and character of the turbine wake, beyond allowing calculation of the turbine's axial induction factor, a, via the relationship $C_P = 4a(1-a)^2$[39], or some combination of axial and tangential induction factors, combined with various corrections for blade induced turbulence[42]. Despite these shortcomings, BEMT remains an important tool for designers of both wind and tidal turbines, allowing initial design studies to be carried out quickly with minimal computational expense.

Computational Fluid Dynamics

An alternative approach to modelling turbines is to use Computational Fluid Dynamics (CFD) modelling. This method starts with the production of a 3D

model of a turbine within a sea domain, which is then discretised into a grid or mesh. Within the elements of this mesh, the Navier-Stokes equations which govern fluid flow are solved, often using a finite volume method. This allows the calculation of flow variables at the surfaces of the turbine, as well as in the fluid further away from the turbine[46]. This method is far more computationally intensive than the BEMT method, but it also simulates much more of the flow physics, and provides the user with much more detailed data about the behaviour of the turbine and the flow around it. Whilst CFD modelling is by no means free of assumptions, it does require fewer correction factors such as those discussed by Turnock et al.[42] to account for blade induced turbulence in BEMT models. A crucial aspect of CFD modelling is the way in which turbulence in the flow is accounted for, as turbulence plays a crucial role in factors such as flow attachment and momentum mixing. For the purposes of this review, turbulence modelling in CFD studies will be grouped into two categories; those which use a time-averaged approach (known as Reynold-Averaged Navier-Stokes (or RANS) models), and those which use spatial averaging to resolve turbulent fluctuations (known as Large Eddy Simulation (or LES)). Further details of the mathematics of these types of modelling can be found in Chapter 3.

2.4.2 Performance and loading of isolated turbines

Much of the initial research into tidal turbines was spurred by a group working at the University of Southampton. In 2003, Bahaj and Myers[13] identified the potential for tidal stream turbines to produce low-carbon energy in the UK, but stated "virtually no work has been done to determine the characteristics of turbines running in water for kinetic energy conversion". The authors did recognise that much research has been carried out in the related fields of wind turbines and ship propellers, but noted that neither of these two areas completely overlap with the field of tidal stream turbines, which has its own particular challenges. These were identified as: the difficulties of operating in a saline environment, cavitation, maintenance difficulties, biofouling, and the potential of impacts with submerged objects (both natural and man-made). In the decade and a half since the publication of this work, much research has been carried out on both the issues identified by Bahaj and Myers, as well as in many other areas relating to the performance and operation of tidal turbines.

Identification of fundamental blade parameters: blade sections, pitch angles and tip-speed ratios

Perhaps unsurprisingly, early research concentrated on understanding the viability and performance of axial-flow tidal turbines. Investigations into the lift, drag

and cavitation characteristics of 2D hydrofoil profiles in a cavitation tank were made, in order to identify those suitable for tidal turbines[47]. These were then further explored using a BEMT model, to understand the behaviour of these 2D sections when incorporated into a rotating turbine[16], and further improved upon by Batten et al.[48], to incorporate the effects of a profiled flow on the turbine. This study examined the effects of the profiled flow on the turbine performance and blade loading, finding that the fluctuations in blade loading due to the profiled flow were "not insignificant". It also identified cavitation as a design parameter, but suggested that it could be mitigated through careful selection of blade section, angles and tip speeds[48]. This was confirmed in an experimental study which explored appropriate tip-speed ratios and pitch angles for axial-flow tidal turbines, and suggested that cavitation should be avoidable for full-scale devices[49]. The authors also identified turbine-flow misalignment as an important area for future research.

BEMT models for turbine performance

BEMT models such as that used by Batten et al.[16] have been constantly improved upon in an attempt to provide more accurate predictions of turbine performance and loading. Some have even gone so far as to try to create a coupled BEM-CFD model either to try and resolve the flow-field around the turbine in order to look at wakes[50][51], or to improve the predictions of the model (particularly when considering dynamic loading) by using velocity and angle of attack predictions from a BEMT model as inputs to a 2D CFD model for calculating lift and drag parameters of each hydrofoil section[44]. BEMT models are primarily of use for initial blade design, and provide a computationally inexpensive method for predicting performance characteristics. They can also be used to understand the general behaviour of turbines, for example, a recognition that biofouling on blades (increasing roughness), can change the stall angle of blades and is likely to cause the most problems for turbines operating at high tip-speed ratios, due to the increased drag[48].

The loads experienced by tidal turbines and their blades is also of critical importance for turbine designers – both in terms of the magnitude of the maximum loads, as well as the size and distribution of the fluctuations in loading. BEM can provide some initial insight into loads experienced by a turbine, but this is limited to a first order estimate due to the lower fidelity of these models, and lack of inclusion of all of the flow physics. In practise, much of the work of designing commercial turbines is done using BEM alone, with safety factors built-in to the design to account for the lack of fidelity in the computer models. Whilst this may currently be seen by industry as the most cost-effective ap-

proach, it does not provide the insight into the flow-physics provided by CFD. In order to model the forces on the turbine more accurately, CFD must be used. CFD modelling techniques resolve the turbine and the fluid around it to give a fuller representation of the physics of the problem. Generally, CFD studies either use Reynolds-Averaged Navier-Stokes turbulence models (which use a time averaging procedure and a model for the Reynolds stresses), or Large Eddy Simulation (LES) techniques (which apply spatial filtering to the Navier-Stokes equations, directly resolving large-scale turbulence, and only modelling small scale turbulence). Both of these techniques and their associated mathematics are discussed in detail in Chapter 3. As CFD requires the solution of the Navier-Stokes equations in thousands (or more usually millions or tens of millions) of cells, they are more computationally expensive than BEM models.

Impact of flow misalignment on isolated turbines

Misalignment was identified early on by Bahaj et al.[49] as an issue which needed to be addressed by tidal turbine manufacturers. Measurements in tidal channels have demonstrated that ebb and flood tidal currents are not always exactly opposite in direction[14]. This can be due to local bathymetry, or the presence of headlands, tidal channels or larger features. Devices such as the SeaGen device pitch their turbine blades through 180°, but do not change the orientation of the turbine axis, and therefore the impact of flow misalignment on the turbine needs to be assessed. RANS-based CFD simulations of misaligned turbines demonstrate that the decrease in power output can be as much as 7% for a misalignment of ±10°, which is much more than the 1.5% reduction which would be expected if only the change in projected turbine area is taken into account[52]. The power output reduced to 23% less than the aligned case for a misalignment of ±20°, agreeing with the trends found in previous experimental studies[53]. In addition to this, the study found increases in shaft bending moments of approximately 10× despite the reduction in thrust, due to the side forces introduced by the misalignment. Both of these factors will be need to accounted for by the developers of turbines when making a design decision about whether to add a finely adjustable yaw mechanism, a ±180° yaw mechanism, or to pitch the blades about 180°, but make no change to the orientation of the turbine axis. It should be noted however, that this last approach also has consequences for power output of the turbine, even if ebb and flood flows are exactly opposite in direction, with a CFD study showing that placing the turbine rotor downstream of the nacelle and support structure rather than upstream is associated with a decrease in turbine performance[29].

Impact of turbine solidity and shear flows on isolated turbines

RANS-based CFD modelling has been used to show that increasing the numbers of blades on a given turbine will increase the maximum torque and power available from a turbine, with both of these being achieved at a lower tip-speed ratio[54]. The same techniques have also been used for examining the effects of sheared flows on turbines[8]. Due to seabed friction, tidal flows display a velocity shear. If a turbine takes up a significant portion of the water column, then the difference in velocity between the upper and lower portions of the turbine swept area complicate calculations of non-dimensionalised coefficients such as C_P, C_T and C_θ, which require a velocity to be used in their calculation. It was found that non-dimensionalisation, which was found to be appropriate for plug flows could also be applied to these sheared flows, as long as the volumetrically averaged flow across the turbine swept area was used[15].

Sources of load fluctuations on tidal turbines

Fluctuations in loads on turbines can be caused by a variety of factors, some of which are due to the non-uniform spatial distribution of the mean velocity across the region of the turbine rotor; as the turbine rotates blades periodically pass into regions of higher and lower flow velocities, causing cyclic fluctuations in the forces on the blades. Such fluctuations can be caused by a profiled or sheared flow[48][8], as well as by interactions between blades and a supporting structure as they pass each other. These effects are present even in flows with no turbulence or other temporal variations. Another source of fluctuations on the turbine comes from flows which exhibit temporal variations, either in the form of turbulence or due to surface waves. In general, load fluctuations due to flow fluctuations from waves or turbulence can be expected to have some common characteristics, as at least part of their frequency characteristics are not driven by turbine rotational frequency, however, fluctuations due to turbulence can be expected to be more random than those from waves.

Load fluctuations due to waves

Waves were identified early on as being important for the calculation of fluctuating loads on tidal turbines[48]. The effects have been explored both experimentally in tow-tanks[55] and flumes[56], as well as with CFD modelling[57]. Measurements of both towed turbines and turbines in flume tanks show that waves have a negligible effect on the values of *mean* performance characteristics such as C_P, but there is a significant impact on the magnitude of the fluctuations when compared to a baseline case without waves. In the case of the flume experiment, the standard deviation of the power coefficient was found to

be up to six times greater with waves than without, at the point of maximum C_P. It was also shown that the form of the distribution of the fluctuations in C_P was also strongly influenced by the particular wave form used[56]. Luznik et al. concluded that, as both the impact of surface waves and probability of cavitation increase as the turbine approaches the water surface, but that the energy density is highest in this region (due to greater flow speeds), turbine developers will inevitably be faced with a compromise[55]. The RANS based CFD modelling method employed by Tatum et al.[57] produced similar results to those found in the experimental studies, albeit with the suggestion of an approximately 5% increase in mean C_T and approximately 5% decrease in mean C_P. The numerical model used combined CFD simulations of the fluid with a mechanical simulation of the structure (known as Fluid Structure Interaction, or FSI), which allowed the authors to conclude that the inclusion of waves leads to a more complex loading spectrum. Reproducing waves in CFD presents a particular challenge due the requirement to accurately resolve the free-surface and the water/air boundary.

Load fluctuations due to turbulence: experimental testing

Whilst the ability of waves to cause velocity fluctuations in the water column decreases with depth (Tatum et al. suggested that the effect of waves on the turbine can be ignored if the turbine is more than 0.5 wavelengths below the surface[57]), velocity fluctuations due to turbulence are present throughout the water column. In the end, both waves and turbulence create velocity fluctuations, with the difference between them being due to the spectra and spatial coherence of the fluctuations. The larger-scale and spatially coherent fluctuations caused by waves can be reproduced in RANS-based CFD modelling, but the range of length and time scales involved in the accurate modelling of turbulence means that LES becomes the only currently available option if a full description of the spectra of fluctuations is required. As the computational requirements of LES modelling are so much larger than for RANS-based CFD, this kind of modelling has only become available to the research community relatively recently, with physical modelling of turbines in flumes being previously used as the main source of data. That turbulence in a channel flow can have an effect on the forces experienced by a turbine was suggested by a study using solid and porous discs as momentum sinks to represent turbines[58]. These were placed in a recirculating flume in which three different grids were used to create turbulence of varying intensities and length scales, and the drag force on the discs measured. In this study, an increase in turbulence intensity increased the drag coefficient of the discs. This effect was seen up to a turbulence intensity

of 13%, beyond which the drag coefficient remained unchanged. However, the study also showed the importance of the spatial coherence of the turbulence, with a minimum drag coefficient being observed when the integral length scale of the turbulence was half the diameter of the disc. Whilst solid and porous discs cannot be considered to be exactly equivalent to an axial flow tidal turbine, differences in drag coefficient of 20% due to the prevailing turbulence conditions indicate that turbulence intensity and length scale could have an influence on the thrust force on a tidal turbine. A more detailed study, measuring forces and blade loadings on a 0.8 m turbine was made in a recirculating flume in Boulogne-sur-Mer in France[59]. A similar methodology was employed for turbulence to that used by Blackmore et al.[58], but with two grids used instead of three. The authors found that increasing turbulence intensity caused a reduction in both mean C_P and mean C_T of up to 10% in the most extreme cases, as well as a reduction in blade bending moments, but with a corresponding increase in the size of their fluctuations. This agrees with a reduction of mean C_P and C_T with increasing turbulence intensity found by Mycek et al.[60], which also considered the impact of different turbulence intensities on turbines in a flume. Increasing the turbulence length scale also caused an increase in the fluctuations in C_P, C_T and blade bending moments, but increased the mean values of all of these, suggesting a complex interaction between turbulence and the turbine[59]. This could suggest that the turbulence of larger length scales behaves more like the fluctuations caused by the effect of surface waves, perhaps due to the higher level of spatial coherence common between these types of fluctuations.

Load fluctuations due to turbulence: LES modelling

More recent studies using LES modelling have been applied to both model-scale[61] and full-scale turbines[62]. Both of these studies compared the LES models using near-zero inlet turbulence and turbulence of approximately 10%, and validated the models against either flume data[61] or data from a full-scale turbine[62]. In addition to this, Ahmed et al. also compared their results to those obtained using a RANS model[62]. Both studies observed similar effects due to increasing turbulence in the LES models; in both cases there was little or no change to mean C_P and C_T, but a large increase in the size of the fluctuations. The comparison between the RANS model, and the zero-turbulence LES model produced very similar results for means and fluctuations of C_P and C_T, which indicates that for these conditions, a RANS model is sufficient for performance predictions[62]. When turbulence was introduced at the inlet, the mean C_P increased slightly, bringing it closer to the C_P recorded by the full-scale turbine; a similar slight increase in C_P when using an LES model was also found by Afgan

et al.[63]. The magnitude of the fluctuations and spectra of the blade bending moments were also well reproduced by the turbulent LES simulation, although the matching was affected by the limited number of rotations simulated due to the computational cost of LES. Ahmed et al.[62] conclude "LES is capable of realistic simulation of all fluctuating loads for a single device"; but concede that the model presented lacks enough resolution in the wake region for reliable wake predictions, whilst Afgan et al.[63] conclude that LES "provides greater insight into the flow-physics and unsteady loading" than RANS, noting that LES captures flow behaviour such as the interaction of blade-tip vortices with the stanchion which are not seen in RANS modelling.

Clearly, scale-resolving turbulence models such as LES produce much better representations of the turbulent loading on a turbine than RANS based models, as the cost of greater computational expense.

Field testing of tidal turbines

Due to the expense of developing and deploying full scale devices, much of this has been conducted by private companies rather than academic institutions, and therefore there is little detailed information about these tests in the public domain. An exception to this is a four month study of a 50 kW, 4 m diameter Schottel Instream turbine, deployed in Strangford Lough[31]. The turbine was reported to have an efficiency of 34% in a flow of 2.05 m s^{-1} (the turbine's rated velocity is 2.75 m s^{-1}). This reported efficiency is difficult to compare with C_P values reported from experimental turbines and numerical models, as it is the electrical efficiency, after losses due to gearbox, generator etc., whereas conventionally the power used for calculations of C_P is the product of the torque and the rotational velocity (i.e. before any turbine losses). Nonetheless, this work still provides a rare example of information from the operation of a commercial turbine.

2.5 Wake research

The wakes of HATTs have been an active area of research for over a decade at the time of writing. Prior to this, most HATT research concentrated on the performance of individual turbines. The wind industry has been researching the topic for significantly longer, but whilst there are many parallels between wind turbines and tidal turbines, some significant differences remain. One of the major differences is the potential for array optimisation; a consequence of the predictability of tidal flows. Whilst resources such as the *Bayerischer Windatlas*[64] exist to predict average wind resource in a given area, the unpredictable

nature of wind means that its direction and strength can change entirely from one day to the next. This means that whilst an array of wind turbines can be arranged to best take advantage of wind from the prevailing wind direction, a compromise must be made for when the wind comes from a different direction. This variable nature of the wind resource means that, in general, the layout of the arrays is largely based on a minimum spacing between turbines, in order to allow an acceptable level of wake recovery regardless of which direction the wind comes from.

Tidal flows are generally bi-directional with approximately 180° between ebb and flood flows. Tidal flows are predictable and periodic, which means there is much more scope for optimising the layout of tidal turbine arrays. This extends not only to a minimum distance between turbines in the main flow direction, but also allows more complex interactions to be considered, such as cross-stream spacing to take advantage of blockage effects, or alternating rotation directions to take advantages of swirl in the wake, either by enhancing wake recovery, and allowing the rotational velocity of a downstream turbine to account for the rotational component of the fluid.

2.5.1 Wakes of isolated turbines

Empirical and analytical wake models: wind turbines

One approach which has been pursued since the wide scale introduction of wind turbines (and subsequently as the field of tidal turbines has developed) is to attempt to find an analytical or empirical method for the prediction of the wake. The attraction of this approach is that a prediction of the effects of the wake without the need to resolve the flow-field around the turbine would potentially provide a quick method to predict the effects of a turbine on its surrounding environment. Early work in this area was conducted by Lissamann[65], who attempted to develop a "functional and dimensionally correct" analytical model of turbine wakes, based on known profiles of jets and plumes. Whilst no attempt was made to take into account the complex physical interactions in the wake (presumably due to the limitations of computational power at the time), Lissamann does include two turbulence terms – one for the ambient turbulence and one for the turbulence generated by the rotor itself, which are considered important to the development of the wake. These terms are tuned to the limiting cases of a plume and jet flow, and the model applied to wind farms to investigate farm power output for different configurations and wind directions, with agreement to real wind farms found to be reasonable considering uncertainties due to the instability of meteorological conditions and the limited physics contained within the model. Jensen[66] developed an analytical model based

on mass conservation considerations to produce a 'top-hat' lateral profile of velocity deficit downstream of a wind turbine. The theoretical basis of this was adapted by Frandsen et al.[67] to include both momentum and mass conservation, and the resulting model applied to arrays of offshore wind turbines. The 'top-hat' profile, which underestimates velocity deficit at the centre of the wake, and overestimates it at the wake edges, was replaced by Bastankhah and Porté-Agel[68] with a Gaussian profile. This was shown to produce a better match to downstream velocity profiles behind a wind turbine, when compared to LES and experimental data.

Empirical and analytical wake models: tidal turbines

Building on this work with wind turbine wakes, Lam and Chen[69] combined axial momentum theory across an actuator disc with flume measurements from Maganga et al.[53] to develop analytical equations for the prediction of the axial velocity deficit and its lateral distribution downstream of a tidal turbine. The equations for the wake prediction are based on work for ship propellers. These equations were then improved upon to take into account the effects of the turbine hub in order to predict the region of "double-dip" wake deficit seen in the near-wake region[70] in flows with low ambient turbulence intensity. The improved equations were compared to wake measurements made by Pinon et al.[71] in high ambient turbulence conditions, and showed good agreement for the far wake. This model, however, relies on using empirical data from the centreline velocity deficit of each turbine in order to calibrate it.

The disadvantage of these empirical and analytical models lies in the fact that they are attempting to reproduce a wake using a relatively small number of input variables. Real wakes are dependent on many different factors and the complex physical interaction between these factors, and therefore, whilst these empirical and analytical models can produce wake predictions very quickly, their accuracy and ability to provide detailed information about the wake will necessarily be limited due to the simplicity of the underlying model. The accuracy can only be expected to suffer further as turbines are grouped together into arrays, and further complexities are added to the incoming flow such as vertical velocity shear profiles and ocean bathymetry.

CFD wake models: wind turbines

In order to overcome some of the disadvantages of the purely analytical/empirical models, some studies started introducing actuator discs (using both RANS and LES based CFD techniques) into the flow to simulate a turbine by acting as a momentum sink. In their simplest form, these models do not provide any

swirl or time-dependent rotational effects such as interactions between blades and stanchion, nor do they reproduce blade tip vortices. These studies in the area of wind turbine wakes have examined such effects as anisotropy of the turbulence in the wake[72], the impact of terrain on wind turbine wakes[73], the impact of atmospheric turbulence on the wake[74] as well as using the disc to produce more realistic turbulence for a full-geometry simulation of a downstream turbine[75]. Attempts at adapting the actuator disc model to overcome some of its limitations have been made, such as introducing extra terms into the calculation of the turbulence kinetic energy dissipation rate in order to represent the transfer of this energy from large scales to small. This had the effect of producing a better match to experimental data in the near-wake region, but still does not model such effects as vortex shedding from blade tips[76]. RANS modelling of wakes using actuator disc models has sometimes struggled with close matching of experimental data, particularly when terrain or complex geometry is involved[73], but may be of use in reducing computational time by using it to produce more realistic inlet conditions for simulations involving multiple turbines[75]. Other research has been carried out using full rotor geometry and RANS modelling to examine the wake. As an example, this has been shown to produce a good match for the near wake, whilst underestimating the rate of recovery in the far wake[77]. This model used the technique of a Moving Reference Frame (MRF) to simulate turbine rotation, which, whilst appropriate for simulating the flow in the immediate vicinity of the turbine rotor, such a 'frozen rotor' will diverge from the actual flow physics in the wake region, making results here difficult to interpret, as confirmed by Liu et al.[78]. In order to gain a better understanding of the flow-physics in the wake region, either experimental measurements using techniques such as the Particle Image Velocimetry (PIV) used by Whale et al.[79] must be employed, or, as identified by Gómez-Elvira et al.[72] and Vermeer et al.[80] LES or hybrid LES-RANS techniques.

Due to the computational expense necessitated by LES, early work was carried out using actuator discs[81], which was then improved upon by adding a rotational element to the actuator disc to take account of the swirl in the flow induced by a turbine[74]. This was then employed to look at the impact of atmospheric turbulence and wind shear on the wake. It was found that whilst both have an impact, that of turbulence intensity is greater, leading to faster wake recovery, and the point of maximum wake deficit and maximum turbulence intensity in the wake moving closer to the disc. These results were confirmed for tidal turbines by Blackmore et al.[82], who in addition noted that an increase in turbulence length scale further moved the position of maximum velocity deficit towards the disc and increased the rate of wake recovery. The use of actuator discs however, still does not account for the effect of tip-vortices which require

either the full-rotor geometry to be modelled, or the use of actuator lines. Actuator lines are less computationally demanding than full-rotor modelling, and have been used to examine the effects of the LES Sub-grid Scale (SGS) model on the overall results from LES simulations of wind turbines[83]. This study found the impact of the SGS model to be small, with the wake and helical tip vortices from a turbine being well reproduced, however the actuator line approach was less successful in reproducing the forces on the turbine. Full geometry LES modelling has been validated against large wind-tunnel experiments[84] (albeit only against C_P and blade pressure coefficients), in which the authors describe the matching of the LES simulations to the experiment to be "much better" than that for 2-equation RANS models. A detailed examination of the wake was made, revealing similar results to those found by Sarlak et al.[83] regarding the breakdown of helical vortices in the wake region. Other full geometry LES studies have concentrated on only the near wake[85], ignoring turbine performance, but still found interesting behaviour such as the meandering nature of the wake meaning that the time-averaged wake appears much wider than its instantaneous counterpart. Such detailed examination of wake behaviour with time can only be achieved using PIV (which is impractical on large scales) or this kind of CFD modelling which resolves the fluctuations in the flow.

Wake studies: tidal turbines

As with the wakes of wind turbines, tidal turbine wakes can be investigated using a variety of numerical and experimental methods. In their purest form, BEMT models only investigate the effect of a flow on a turbine, which means that they provide no information about the flow around or downstream of the turbine. Numerical models used for the investigation of turbine wakes vary from coupled BEM-CFD models, full-rotor CFD models using RANS turbulence models, to LES simulations using either simplified geometries (discs or line actuators) or full geometry. The choice of model used depends on what information is being sought, the detail required and the computational facilities available. High-fidelity information about vortex structure in the near wake of a single turbine could, for example, require LES modelling techniques and high-performance computing facilities, whereas initial research into array configurations may provide acceptable accuracy when run in a few hours on a desktop computer[41].

The flow measurement techniques necessary to measure 3D flow structures behind turbines are a mature technology, and for the purposes of a tidal turbine wake researcher, have not changed in the last couple of decades. In contrast, computing technology has advanced apace, meaning that, in recent years, re-

searchers have been able to use techniques which would have be prohibitively computationally intensive for earlier researchers. It is then perhaps no surprise that one of the earliest studies of the wake of a tidal turbine was conducted in a flume experiment in 2010 by Maganga et al.[53]. The flume used allowed the turbulence intensity to be varied, and it was found that an increase in turbulence intensity had a significant effect on reducing the length of the wake.

CFD wake models: actuator discs

Early numerical studies sought to reduce computational expense through the use of porous discs to simplify the geometry of a turbine, whilst still producing a wake. Models have been presented by Harrison et al.[86], Malki et al.[50] and Bai et al.[87], amongst others, which all combine an actuator disc approach with RANS-based CFD modelling for the flow field around and downstream of the disc. Harrison et al.[86] compared their model to experiments measuring the wake behind porous actuator discs, finding that the numerical model predicted a wake with less turbulence intensity in the near-disc region, and slower overall wake recovery than in experiments; the authors identify the need to correctly model inlet turbulence for accurate wake results. Malki et al.[50] and Bai et al.[87] use experimental data for C_P and C_T to validate their models, but do not provide validation data for the wake size and shape. The steady-state formulation of both of these models also means that transient effects in the near wake will not be captured. All three of these models have then been used to investigate interactions within small groups of turbines, which will be discussed in more detail later. An attempt to improve on the actuator disc model was made by Bai et al.[88], by employing an actuator line instead of full blade geometry. The agreement of this model to experimental C_P and C_T data from a tow-tank and cavitation tunnel was similar to that of the actuator disc model. The wakes produced by these two models showed more of a difference, with the actuator line model producing a closer match to a fully blade-resolved RANS CFD model. A comparison to experimental wake data was only made to the wake behind a porous disc, with moderate agreement. Attempts to make the actuator disc model more closely match a physical turbine have been made by Nishino and Willden[89], who modified an actuator disc model to take into account the turbulence produced by the turbine blades, in order to more accurately reproduce the mean flow in the near wake. This model was then applied to discs in channels of different blockage and aspect ratios to explore the effects that these may have on the performance and wake of a turbine. The authors concluded that, whilst an increasing blockage did increase both the power extracted by the disc as well as the thrust on the disc, these effects were independent of channel aspect ratio.

However, it was found that an increase in channel aspect ratio causes the wake velocity profile to spread-out, whereas in a channel with a square cross section, the wake remains cylindrical in shape for a greater distance downstream. This has implications for the spread of turbine wakes within closely packed arrays of turbines.

CFD wake models: full-rotor modelling using RANS

A more computationally expensive method of modelling, albeit one which has the potential to provide more information about the flow field near the turbine as well as turbine performance and loading is provided by CFD models which resolve the complete rotor geometry. To date, the majority of this modelling has been done using RANS-based turbulence models, to avoid the expense of LES. These models are specific to the geometry of the particular turbine being modelled, and studies have been made to examine a range of different turbine configurations and flow effects. The dependence of the wake on blade pitch and turbine C_T has been looked at using this modelling approach[8]. This study found that increasing the pitch angle of the blades reduced the wake deficit in the near-wake region, although by $17D$ downstream the difference became insignificant. Increasing the C_T of the turbine led to a greater initial velocity deficit, but to greater recovery from approximately $10D$ downstream. This study was primarily concerned with an evaluation of the effects of velocity shear on the turbine, and found that the profiled flow both caused the wake vortex to be less stable, and caused the wake overall to curve upwards. However, it should be noted that a Moving Reference Frame (MRF) was used for this work, which rotates the flow in a defined region rather than rotating the turbine. This provides some mathematical advantages and accurately replicates the flow in the immediate vicinity of the turbine, however, rotating the fluid rather than the turbine blades could lead to non-physical effects in the wake region, giving inferior performance to sliding mesh schemes[78].

The amount of swirl in a wake (where the flow exhibits both an axial and rotational component) and its effect on wake recovery has also been investigated using RANS-based CFD models. It was found that the levels of swirl in the wake followed the curve for C_θ, and that the distribution of tangential velocities in the wake region suggest the wake has the form of a Rankine vortex, albeit with low levels of swirl for 2 and 3-bladed turbine designs. This suggests that the tangential and axial velocities are not coupled, and that therefore the swirl cannot be used to predict wake development[54]. Swirl increased with the number of blades however, and the authors postulated that coupling might occur

with four or more blades, for a different turbine design, or a different mean flow velocity.

The effect of flow misalignment on wake recovery has also been explored using full-rotor RANS models, and it was found that, in addition to a reduction in the power produced by, and the thrust forces acting on a turbine, the wake length was also slightly reduced, and with a misalignment angle of $\pm 10°$, the wake recovered to 90% of the upstream velocity at $7D$ downstream, whereas for the aligned case this only happened after $10D$[29]. The structure of the near wake has also been explored using a RANS-based full-rotor CFD model, and validated against PIV measurements[90]. The numerical model produced good agreement with the PIV measurements, showing good agreement of the wake velocity profiles in the very near wake region both qualitatively and quantitatively. The modelled wake and measured wake did start to diverge towards the end of the modelled domain (5 diameters downstream of the rotor plane), possibly because, as the wake develops, the recovery processes are dominated by mixing between the wake and the free stream[65], and this is less likely to be captured by the particular type of RANS model used (a k-ω SST turbulence model) which relies on an assumption of isotropic turbulence.

CFD wake models: LES for tidal turbines

CFD studies which can be expected to produce the most accurate reproduction of flow features in the wake, as well as the turbulent mixing processes between the wake and the free stream will use LES turbulence modelling techniques. Porous discs have been used by Blackmore et al. who investigated the effects of turbulence intensity and length scale on the wake of the disc[82]. Numerical simulations have the advantage that turbulence intensity and length scale can be varied independently of each other; something which is very difficult to do in flumes with, for example, grid-generated turbulence. This study agreed with others in showing that a higher ambient turbulence intensity tended to increase the rate of recovery in the wake region, and moves the location of maximum velocity deficit closer to the disc. It has been suggested that not only the intensity of turbulence, but also the character of turbulence is important[53], and to this end Blackmore et al.[82] investigated the impact of turbulence length scale on the wake. An increase in turbulence length scale was found to increase the rate of wake recovery as well as increasing wake width, and whilst this investigation was based on porous discs, it can be expected that similar effects may be seen on the wakes of turbines. The near-wake of a fully blade-resolved LES model was studied in a research paper primarily concerned with performance and loading on a turbine[63]. Whilst the focus of this paper was not on wake

behaviour, it was still noted that an increase in turbulence intensity led to an increase in the rate of wake recovery[63]. In addition to this, rotational movement in the wake was observed with strong helical wrapping of tip vortices, and a tendency of the wake to meander; thought by the authors to be due to the interaction of the tip vortices and the stanchion. Similar tip vortex patterns, wake meandering and an increase in wake recovery rate with an increase in ambient turbulence intensity were found by Ouro et al.[61], which used LES with an immersed boundary method in order to reduce computational effort due to cell refinement in boundary layer regions. The geometry used in this study did not contain a stanchion, suggesting that the meandering of the inner vortex core might be due to the effects of asymmetrical flume boundaries, rather than stanchion interaction. This is supported by an LES study using actuator lines (without stanchions) to model an array of turbines[91]. This study also showed asymmetry in the wakes, presumably due to the flow shear induced by the presence of a rough sea bed and a zero-shear domain boundary at the water's surface[91]. A recent study by Ahmadi[92] using LES and actuator lines also found that increased upstream turbulence led to faster wake recovery, and moved the point of maximum turbulence intensity in the wake closer to the turbine, in a similar wake to that found by Blackmore et al. for porous discs[82]. This study also indicated that an increase in turbulence intensity causes the width of the wake to increase, and identified turbulence length scale as an additional factor with the potential to influence wake behaviour, which would be worthy of further research. Other LES-based models have been proposed such as the "vortex method" used by Pinon et al.[71] which advects particles carrying vorticity. This model allows the modelling of a turbine without the need to resolve the boundary layer around the blades, although as the authors concede, this also means that effects due to flow separation at the blades cannot be modelled. After tuning, the model was shown to be capable of producing a good match to wake measurements made in a flume. The model used in the study does not however allow accurate turbulence characteristics to be introduced at the domain inlet, and it remains to be determined whether the tuning for a particular turbine geometry is applicable more generally.

Flume-based wake studies

Measurements have been made in the wakes of actuator discs[93], as well in some cases behind individual turbines[53], [60], [94]. The work of Maganga et al.[53] showed that an increase in turbulence intensity causes faster wake recovery, was confirmed by Mycek et al.[60], who concluded that, whilst an increase in ambient turbulence intensity only had a limited effect on the mean C_P and C_T,

the wake was "deeply influenced" by the upstream turbulence, and that the "wake shape, length and strength largely depend on the upstream turbulence conditions". A study with single turbines has also considered the effects of wide, shallow channels, to try and match possible geometric conditions in ocean channels, which found only small levels of asymmetry in the wake expansion[95]. Investigations into the turbulence produced in the near wake (between 1.5 and 7 diameters downstream of rotor) were made by Tedds et al.[96] who noted that the rotation of the turbine blades induced significant anisotropy into the turbulence, and suggested therefore that numerical models which rely on the assumption of isotropic turbulence (e.g. 2-equation RANS models) may struggle to accurately reproduce the flow in this region. It was also noted that the rate of decay of turbulence kinetic energy in the wake region was "significantly different to that observed downstream of grids, meshes or perforated disks, suggesting that previous modelling approaches, which neglected swirl effects and modelled the turbine by absorption discs, may significantly over predict the TKE decay rate of HATT wakes."[96]. This would suggest that the *quantitative* results of porous discs may not be directly applicable to tidal turbines, however, *qualitative* effects such as those noted by Blackmore et al.[82] could well still be applicable. A similar, high fidelity set of measurements using an Acoustic Doppler Velocimeter (ADV) in the wake of a turbine was published recently by Chen et al.[97], who measured to 20 diameters downstream of the rotor. This low ambient turbulence study with a relatively high blockage ratio of 16% by turbine swept area found that the centreline velocity recovered to 90% of the free stream velocity approximately 11 diameters downstream of the rotor. As seen in a previous LES study[63], it was found that the stanchion had a significant influence over the wake in its immediate vicinity, but this was limited to the near-wake region. Morandi et al.[94] conducted a flume study where measurements were made immediately behind the turbine rotor. These measurements were phase-locked with the turbine's rotational frequency in order to identify how wake features relate to the position of blades. The study demonstrated the complexity of the near-wake structure, and also indicated that some features of the near-wake such as the strength of the tangential velocity component, are dependent on the turbine operating condition (tip-speed ratio).

2.5.2 Interactions within small groups of turbines

If tidal turbines are going to provide a significant contribution to energy production, then it is expected that they will be deployed in arrays. Placing turbines in close proximity to one another leads to the possibility of interactions between these turbines, potentially both positive as well as negative. Understanding
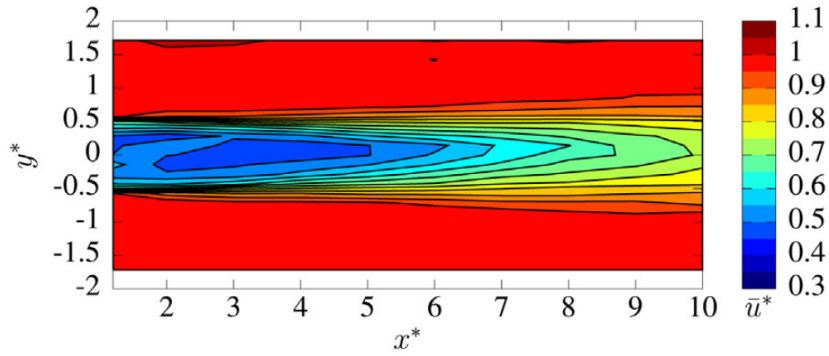
(a) Normalised axial velocity behind a turbine in an ambient turbulence intensity of 3%. Axial and cross-stream dimensions are normalised against turbine diameter.
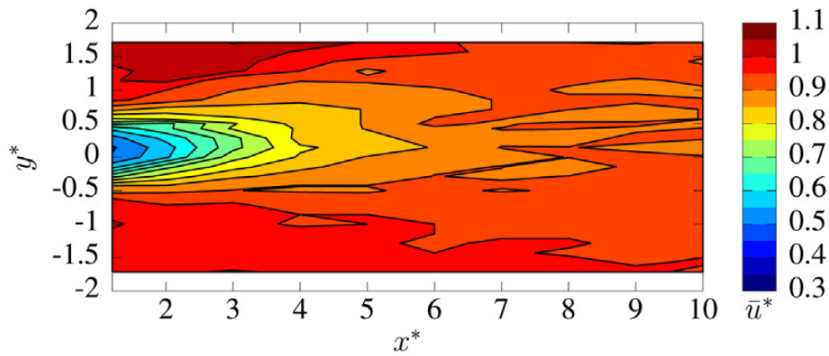
(b) Normalised axial velocity behind a turbine in an ambient turbulence intensity of 15%. Axial and cross-stream dimensions are normalised against turbine diameter.

Figure 2.5: A comparison of axial velocities in turbine wakes, from Mycek et al.[60]. This study is one of the first to carry out direct comparisons of turbine wakes under different turbulence conditions in a flume.

these interactions will be of critical importance to array designers wishing to extract the maximum power from a given area of seabed, whilst at the same time balancing the economic requirements of reducing loading (particularly fluctuating loads) on turbines, minimising capital costs such as turbine manufacture and grid connection as well as maintenance and deployment costs. To this end, many studies have been carried out in order to gain a greater understanding of the effects of factors such as blockage, channel aspect ratio array spacing and the rotational directions of turbines.

Lateral spacing and blockage effects: numerical studies

The issue of blockage is one which separates the tidal industry from the wind industry. Wind turbines operate in the lower portion of a very tall fluid column, whereas tidal turbines are expected to operate in regions where their diameter takes up a significant portion of the overall depth of the fluid column. Whilst a turbine very close to the surface could have an impact on local water depth[98], in practise it is not thought likely that turbines would be placed so close to the water surface due to the hazard presented to shipping, the increased likelihood of cavitation or to their vulnerability to high loading in the event of large waves. Nonetheless, the limited water depths reduces the space available for fluid to divert around a turbine in the vertical direction, and with many turbines placed in a "fence" in a tidal channel, the possibility for fluid to divert laterally around the turbines is also reduced. As with studies on the wakes of single turbines, much of the initial research into blockage effects used actuator discs, either experimentally or using BEM-CFD models[89],[40]. These models typically used reflective boundary conditions to simulate infinitely long fences of turbines whilst only needing to perform calculations around a single turbine. Whilst both of these studies confirm the importance of blockage in the context of tidal turbines, it was also shown that greater performance advantages could be by obtained by adjusting turbine design to the specific blockage conditions anticipated[40]. Using full-rotor RANS-based CFD, the effects of position of the turbine in the water column have also been investigated[99]. This indicated that placing the turbine close to a boundary (either a free surface or the seabed), led to the wake being skewed to one side due to interactions between the rotating wake and the boundary[99], an effect also seen with LES simulations using rotating actuator lines to model turbines[91]. In addition to this, a RANS-based CFD study by Zhang et al.[9] found that the rate of wake recovery was decreased as a turbine was placed closer to the sea bed, which the authors suggest is due to a reduction in mixing between the wake and free stream region.

Studies into blockage effects lead naturally on to the study of the effect of longitudinal spacing on turbine performance and wake. Turnock et al.[42] used a coupled BEM-CFD model to examine the effects of turbine separation both laterally and longitudinally, applying their model to an idealised 1 km^2 area of sea bed. Of the lateral spacings used, the authors found that a spacing of 2 turbine diameters provided the highest power output from a row of turbines, due to localised blockage effects, and suggested that a staggered array (i.e. not having downstream turbines directly inline with upstream turbines) could provide benefits. This lateral spacing has been supported by other numerical models using a BEM-CFD method[87],[100], as well as with full-rotor RANS-based CFD[101]. These three studies found that lateral spacings of 2.5D[87], 2D[100] and 2D[101], gave the highest C_P for turbines in this row. This full-rotor CFD study[101] also found that a second row of turbines should be placed at least 5D downstream of the first row and offset or staggered to give the best overall performance. These studies considered the effects of arrays in which all the turbines were operating at the same condition, however, it is also possible to vary the operating condition of individual turbines within an array, leading to a considerable enlargement of the variable space. It is possible to define a "resistance coefficient", which can be varied to alter the thrust on individual discs in an actuator disc model. Hunter et al.[102] investigated the tuning of tidal array configurations using this parameter, finding that overall array power output was optimised using a uniform value of resistance coefficient across all turbines, which resulted in a non-uniform distribution of C_P and C_T across the turbines in the array. Whilst this study used actuator discs, the implication is that the operating condition of the turbine also has an effect on the wake and the interactions between turbines in an array – important information for array developers which will be further explored in this thesis.

Lateral spacing: flume studies

Few studies to date have experimentally examined the impact of the lateral spacing of turbines on their interactions. This is in part due to the cost of producing multiple turbines, and the lack of facilities large enough to accommodate multiple turbines side-by-side. The University of Manchester's wide flume is one such facility, and a study has been carried out there examining the effects of lateral and longitudinal spacing on the wakes of tidal turbines[103]. The study found that for lateral spacing greater than 3D, the wakes of the individual turbines are unchanged from the case of an isolated turbine, but for spacing of 2D or less, the wakes from the individual turbine merge to form one single wake

by $4D$ downstream of the plane of the rotors. If turbines are to be placed this closely together in arrays, then this result would suggest that it may be possible to model the far-wake region of the combined wake of a row of turbines using a simplified model, without resolving the complete geometry of each individual wake. In addition to this, the study found that waves had only a limited impact on the far wake of the groups of turbines. Another study, this time using PIV measurement techniques, demonstrated the complex nature of turbine interactions within an array[104]. This found that a reduction in lateral spacing between turbines could increase the array centreline wake recovery as flow was diverted between two turbines towards the centreline; however, if the spacing was reduced too far then this effect is reversed, resulting in a detrimental impact on downstream turbines on the array centreline. This study also highlighted the need for the tip-speed ratios of turbines within an array to be tuned to the local flow velocity, and demonstrated that the impact of changes to array spacing was more significant for conditions of low upstream turbulence. Field tests of multiple turbines pushed by a barge in a lake have also been conducted to examine the interactions between turbines and the dependence on turbine spacing, albeit not by directly measuring the wakes themselves, but rather by measuring the change in C_P due to the presence of a second turbine[105]. The study examined both lateral spacing and longitudinal spacing of two identical turbines, finding that lateral spacings of $2D$ produced a performance increase of up to 6%, in agreement with studies discussed above. Due to the restrictions on the size of the barge, a maximum longitudinal spacing of $6D$ could be measured, which revealed a 59% reduction in performance, However, when the downstream turbine was offset by $1.5D$ or $3D$ from the centreline of the upstream turbine, no negative effects were observed, giving an idea of the effective width of the wake at this point.

Longitudinal spacing of turbines

Many studies have examined the rate of wake recovery behind the turbine, both numerically and experimentally ([8], [54], [53], [106]). Examining the length of the wakes in this way naturally feeds in to considerations of longitudinal spacing of turbines within arrays. It is clear that, as downstream distance increases, the wake will recover, and therefore the greater the longitudinal spacing between turbines, the faster the flow experienced by a downstream turbine will be. These greater flow speeds mean that more energy is available for a downstream turbine to extract. Array designers will have to make a decision as to where to place downstream turbines based on maximising the longitudinal distance between rows of turbines, whilst still maximising the power produced per unit area of

seabed. Understanding exactly how much power is available to downstream turbines as well as any increases in load fluctuations will be crucial for optimising tidal array economics.

Turbulence and wake recovery

It has been shown that an increase in ambient turbulence causes faster wake recovery[53],[63],[82],[61], and an experimental study using porous discs[93] in the wake of one another has confirmed this to be the case. This means that the wake length of a downstream turbine will be dependent on the distance it is placed from an upstream turbine, as this distance impacts the turbulence experienced by the downstream turbine. However, it was established early on that not only the strength of the turbulence, but also its character is important[53], and this was confirmed by Mycek et al.[106]. This study measured the performance of single turbines in ambient turbulence intensities of 3% and 15%, and compared these to the performance of turbines in the wakes of an upstream turbine. The downstream turbines were positioned in such a way that the turbulence intensity at the rotor was 3% or 15%, but this time generated due to the wake of the upstream turbine. Comparisons of performance of the turbines showed differences despite the same levels of turbulence intensity, suggesting it is also the nature of the turbine wake which is important. These results lead to the conclusion that for arrays consisting of multiple rows of turbines, sea conditions with higher turbulence intensities will lead to greater possible array densities, and therefore the possibility of extracting more energy from a given area of seabed.

Wake anisotropy and swirl effects

The anisotropy in the wake induced by the rotational effects of the turbine ([96], [107], [91]) has also been investigated in the context of arrays[101], [91]. Both O'Doherty et al.[101] using full-rotor RANS-CFD, and Churchfield et al.[91] using actuator line LES, investigated the impact on array performance of rotating neighbouring turbines in alternating directions. For turbines in the same row, rotating them alternately clockwise and anti-clockwise was found to increase the C_P of these turbines, with the effect becoming more marked as lateral inter-turbine distance was decreased[101]. This is thought to be due to a reduction in velocity shear between the turbines resulting in a reduction on drag at the blade tips and therefore an increase in performance. An additional effect was seen on the wakes of the turbines, with the region of increased turbulence intensity being confined to a smaller volume, which the authors propose could be utilised in the placing of downstream turbines[101]. In contrast, the LES

actuator line study by Churchfield et al.[91] found little performance gain by employing counter-rotation in laterally spaced turbines; however, for turbines placed $4D$ directly downstream of the upstream row, a performance increase of about 3% was found when these were made to rotate in the opposite direction to their upstream counterparts. A flume study by Morandi et al. showed that the wake immediately behind the turbine blades has a significant rotational component to it, and the authors suggested that this might be exploited by producing turbines with two contra-rotating set of blades[94]. This would not be without difficulties however, as the additional rotational component to the flow over the downstream set of blades would mean that care would need to be taken when designing the twist of this set of blades, in order that the local angle of attack remains optimised.

2.6 Array research at channel and ocean scale

At a larger scale, research has been carried out into the layout of tidal arrays and their interaction with the sea on a channel, estuary, or ocean scale. Some of the work has focussed on trying to optimise array layout for power output[108], [109], [110], [111], [112], whilst others have focussed on assessing the possible impacts of tidal arrays on the wider environment[113], [114], [115], [116], [117], [118].

Macro design of arrays

Vennell et al.[110] performed a macro-scale analysis on the economics of large arrays of tidal turbines, using the Pentland Firth and an idealised small channel as an example. A rectilinear arrangement of turbines was assumed, and a simple 1D model applied in order to assess the effects of adding more turbines to a row, as well as adding more rows into a channel. The complicated economics due to the feedback between the tidal flow and the turbines were highlighted; it was found that, up to a certain point, the addition of more turbines to an array not only increased the total output of the array, but also increased the power output of each turbine. Adding more turbines than this led to an increase in array output, but decreased the output from the individual turbines (i.e. diminishing returns). Beyond this point, it was found that adding more turbines actually reduced the overall array output (due to excessive blockage of flow through the channel); clearly an undesirable result. It was also highlighted that the economics of array layout is further complicated by the fact that increasing channel blockage both tends to increase the power output from the turbines, but also increases the thrust loading on individual turbines. Greater structural loads

increase the costs of the individual turbines, therefore the effects of diminishing returns could be, to some extent, offset by using less expensive, less sturdy turbines[110].

Placement of turbines within a fixed-width channel

Models used for sea and ocean modelling have been adapted to allow the incorporation of tidal turbines. One straightforward method of doing this is to simulate the momentum loss due to the presence of turbines by increasing the value of bottom friction at the points where the turbines are located. Such a method has been employed to examine the effect of 4 different layouts of 15 turbines within an idealised channel, using an adaptive mesh model[108]. This method involved no bathymetry or turbulence modelling in the flow, and modelled the turbines in 5 rows of 3 turbines. As with any model where a large number of turbines are involved, the number of possible degrees of freedom to be investigated becomes very large, so studies tend to focus on looking at the effects of very specific changes. In this case, channel width and lateral spacing was fixed (at $7.5D$ between turbines), but it was found that regardless of whether the array was sited in the centre of the channel or to the side, there was little effect on array power, which indicates that it might be possible to preserve shipping lanes in tidal channels without affecting array output. The study also found, in agreement with many other studies[87], [100], [105], [101], that staggered arrangements of turbines yield much higher power outputs than equivalently spaced turbines in rectilinear arrays. This work was later improved upon through the addition of a 2D LES model which was used to look at water level changes as more rows are added to an array within a tidal channel[111]. This study concluded that for many purposes, the simplifications involved in 1D models still produced sufficiently accurate results when used in ocean-scale models, however, it was noted that such models would be too coarse for analysis of sediment transport within an array.

Array optimisation: adjoint method

Fine-tuning of turbine position within an array has also been carried out using an adjoint approach, and this has been applied to idealised channels and headlands, as well as to a case-study in the inner sound of the Pentland Firth[109]. The adjoint approach typically involves providing flow boundary conditions, as well as constraining the placement of the turbines by limiting the geographical area in which they may be placed, and fixing the number of turbines to be used. Such a geographical limit to the area which can be used not only places necessary limits on the number of degrees of freedom to allow optimisation, but represents

a realistic scenario where licenses are granted for exploitation of limited areas of the sea floor. The turbines are initially distributed evenly within the selected area, the positions of the individual turbines are parametrised, and a 2D simulation with the turbines represented by bottom friction changes is carried out, allowing the power extracted by the array to be calculated. The array power output forms a functional to be maximised by modifying the turbine positioning parameters. The algorithm calculates the gradient of the functional, and adjusts the turbine positions to move closer to the maximum of the functional in an iterative procedure. Whilst the model was applied without bathymetric information, with a fixed inflow velocity rather than head-driven velocity and without a turbulence model, it provides valuable physical intuition into array layouts which can improve power output. As can be seen in Figure 2.6, during an optimisation of 256 turbines in an area with the flow from the north west, the algorithm positioned the turbines in long fences perpendicular to the flow, with a large amount of space between them. As confirmed in studies of interactions between small groups of turbines, the lateral inter-turbine spacings were reduced to a minimum, whilst the longitudinal spacing between the fencings was increased as far as possible. Similarly, the fences themselves consist of two rows of turbines, with second row of turbines slightly offset with respect to the first, taking advantage of the blockage effects between turbines, similar to that seen by O'Doherty et al.[101] and others [87], [100]. Other notable features of the optimised layout are the positioning of turbines along the edges of the array, causing the flow to be funnelled in toward the fences, and the "spurs" on the south western edge of the array are thought to act as short fences in this region, taking advantage of the unobstructed flow in this region, whilst being short enough not to cast a wake across the two largest fences. This method shows promise for optimising tidal arrays, and, with the potential of further improvement in the hydrodynamic model and the ability to include other factors in the functional to be optimised, could be a powerful tool for the future.

Array optimisation: Design of Experiments (DOE) method

A more recent study has combined multiple factors into the optimisation process [112]. Instead of running a whole series of different array layouts, a limited number of array layouts were chosen using a Design of Experiments (DOE) approach and assessed in order to judge the 'success' of the layout based on a set of metrics (power, geometric constraints, cost, environmental impact). These assessments were carried out using 3D RANS-based CFD, modelling the turbines as actuator discs. The different assessment metrics were then formulated into functions of turbine position, which could then be used to optimise the

(a) The sea area between Stroma island and Caithness examined using the adjoint method[109].
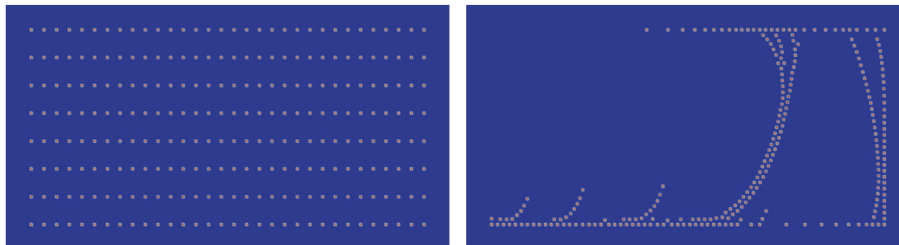
(b) The initial (left) and final (right) positions of a 256 turbine array, optimised using the adjoint method[109].

Figure 2.6: Case study from Funke et al.[109], showing the results of array optimisation in the inner sound of the Pentland Firth using the adjoint method. The flow was modelled in one direction only, and enters the region of the array from approximately the north west (north is towards the top of the page).

turbine layout whilst simultaneously assessing the inherent compromise due to a multitude of factors. The re-casting of the problem as metrics formulated as functions of turbine position allows thousands of permutations to be explored and assessed with minimal computational cost[112].

Incorporating turbine arrays into ocean-scale models

Other studies have assessed the environmental impact of tidal turbine arrays on the hydrodynamics on a regional or ocean scale, which can then be used to assess the impact of turbine arrays on the wider environment. A method of including tidal turbines, represented as actuator discs, into the existing ocean modelling software Regional Ocean Modelling System (ROMS) has been proposed by Roc et al.[119], and later implemented for flow around an idealised headland[114]. It was shown that this model could produce an adequate match to wakes determined experimentally behind actuator discs[120], and went some way to overcoming the difficulties of incorporating turbine-scale simulations into ocean-scale simulations. Nonetheless, limitations exist within the model; firstly, the direction of the turbines is determined by the mesh orientation, which means there is no capability to yaw turbines into tidal flows which are not exactly 180°opposed in ebb and flood directions. The authors suggest that the method could be used to optimise array layout, however, the wakes of turbines have been shown to be different to the wakes of actuator discs[96], and therefore their interactions can also be expected to differ. In addition, some of the simplifications made in the ROMS model (such as turbulence kinetic energy being produced only from velocity shear) could also limit the accuracy of the model within the wake. Nonetheless, such an approach could be useful for assessing larger-scale hydrodynamics due to the presence of an array.

The environmental impact of turbine arrays

Studies looking at the environmental effects of tidal turbines have been conducted for the Bristol Channel[113], Shannon Estuary[115][116], Pentland Firth [117] and Alderney Race[118], amongst others. As the environmental effects of a particular array at a particular site depend on the complex interplay between a great many factors (tidal profile, geography and bathymetry, size of array, sea-bed type), most of these assessments have been conducted as case-studies for specific sites.

1D, 2D and 3D studies have been carried out to study the effects of sediment transport. Tidal asymmetry was found to be an important factor in the impact of an array of turbines on the sediment dynamics in the Bristol Channel, in an early study using a 1D model[113], with sediment transport effects being

more pronounced where the asymmetry is greatest. Effects on sediments could be seen up to 50 km from the position of the array, with sediment changes of approximately 4 m predicted over a 30 year lifetime of a tidal array. With regards to tidal asymmetry, a 2D study of an array in the Alderney Race found that the magnitude of tidal asymmetry was increased due to the presence of the turbines, and that the presence of the array caused differences in sediment transport (albeit small ones) at a range of tens of kilometres[118]. The study examined the impact on sediment with different grain sizes, and suggested an increase in fine sediment up- and downstream of the array, with an increase in coarse sediment in the areas of flow acceleration to the sides of the array. In general, it was found that, due to the complex paths taken by sediment particles in the area, a small change in initial position (or diversion of path) could lead to a large difference in the final point of deposition. Nonetheless, the authors stated that "placing a 290 MW tidal turbine array in an area with great resource ... does not change drastically the hydrodynamics"[118]. A similar result was found in a case study of multiple arrays in the Pentland Firth, using the 3D modelling tool MIKE3[117]. An actuator disc model was used to simulate arrays in four areas of the Firth which have been earmarked for development as tidal stream sites, in order to assess their impact on two areas of mobile sediment. Here the change in bed height due to the turbines over the simulated lunar month was 0.2 m with all four arrays operational, which the authors felt was insignificant compared to the actual bed change in these areas of 5 m. Simulating all four arrays allowed assessment of the linearity of the cumulative effects of each of the arrays. It was found that, for the levels of extraction modelled (totalling approximately 400 MW), the effects of adding each farm accumulate linearly, simplifying assessment of their impacts and interactions.

2D models have been applied to the Shannon estuary, in order to assess the impacts that tidal arrays may have on the tidal cycle itself, including changes to drying heights and times[115][116]. Turbines were modelled as momentum actuator discs, albeit loosely, with multiple turbines per cell. The areas occupied by the tidal arrays was kept constant, with power extraction being varied through varying the spacing (and thus the number of turbines in an array), from $0.5D$ to $5D$ in both the lateral and longitudinal directions. Whilst this turbine spacing may be unrealistic, the work nonetheless provided some interesting insights into what effects power extraction and flow diversion could have. It was found that for power extraction of greater than 20% of the potential power of the tidal zone could have a significant impact on the environment in the estuary, with shifts in the times of high and low tide of up to an hour (in itself, environmentally neutral), and a reduction of tidal range upstream of the array[115]. Whilst this could be seen as a benefit by reducing the risk of flooding

locally, it significantly reduced the area of inter-tidal zones which are flooded and then dry out over the course of the tidal cycle. These zones typically contain environmentally significant ecosystems. The authors also suggested that a reduction in the height of high-water could lead to difficulties with navigation. In a further study, pollutant transport in the estuary was examined, and it was found that the residency time in the estuary could increase by between 12% and 70%, depending on how many turbines were used and the spacing between them. This would indicate that the presence of a turbine array could have significant impacts on the flushing of the estuary region[116].

2.7   Summary of literature review

This review has provided background into the tidal industry, highlighting the need for low-carbon renewable energy resources, and some of the devices currently available in the tidal industry. In addition to this, it has covered past and present research in the area of HATTs, their performance, loadings and wakes, as well as approaches to the optimisation of tidal array layouts and some of the possible impacts these arrays could have on ocean hydrodynamics and the wider environment.

An examination of the research currently available to the research community shows that whilst the fundamentals of turbine performance in steady flows are relatively well understood, there are still many areas to be explored which have great significance for the eventual deployment of the technology on a large scale. Clearly, the interactions of turbines within arrays must be understood if arrays are to be laid out such that they achieve an optimised balance between power extraction, turbine loading, economics and environmental effects. Every potential tidal site is unique, and therefore this balance will be different in each case. In order to be able to predict the behaviour of turbines in all of these conditions, it is important to understand the fundamental behaviour of the turbine and its wake, under different flow and operating conditions. This means understanding the effects of changes in flow and operating condition tend to affect the wake, as well as the development of models which can accurately replicate these effects in specific cases; for a specific turbine geometry, in a specific sea environment, within a specific array layout. Only by gaining this knowledge and modelling ability will it be possible to truly optimise turbines, understand their interactions with each other, and assess their impact on the wider environment.

The literature demonstrates that for turbulent flows, it is only scale-resolving CFD models such as LES which are capable of accurately reproducing the fluctuating loads on the turbine, as well as the wake in its full length. Multiple studies have confirmed that ambient turbulence intensity has an impact on wake recov-

ery, and there is some indication that the length scale of turbulence also has an impact on wake recovery and performance of a downstream turbine, however, this remains to be explored in further detail. Similarly, the turbine operating condition (i.e. where the turbine is operating on the C_P, C_T and C_θ curves) appears to have an impact on the nature of the wake, but the precise nature of this is still to be determined. This thesis will therefore concentrate on these issues; the impact of turbine operating condition, ambient turbulence intensity and length scale on the size and shape of the wake of a HATT. For this research, a hybrid RANS-LES turbulence model will be used in combination with flume measurements, and the numerical model will be assessed in its ability to produce similarly accurate reproductions of turbine loading and wakes, but at reduced computational cost when compared to LES models.

Chapter 3

Theory

3.1 Turbulence

Turbulence is present in most flows of interest to engineers. This is principally a question of scale. The Reynolds number of a flow is given by:

$$Re = \frac{\rho v l}{\mu}$$ (3.1)

with v and l being characteristic velocities and lengths of the fluid and geometry in question[20]. The Reynolds number gives an indication of the flow regime, and is important when comparing experiments carried out at different scales. Two experiments, carried out on scaled geometries but at the same Reynolds number can be expected to experience the same flow regime, and therefore the results can be directly compared. Above a particular Reynolds number, fluid flows become inherently unstable, and turbulence occurs. As the Reynolds number is dependent on fluid velocity and length, larger geometries with higher velocity fluids are more likely to experience a turbulent flow regime. Many, if not most flows of interest to engineers fall within a turbulent flow regime.

Turbulence has a profound and complex influence on the behaviour of fluid flows, and the study of turbulence is a large and vibrant area of academic study. The following introduction to turbulence is intended to provide the reader with an overview of some of the key characteristics and properties of turbulent flows which will be required for an understanding of the modelling and analysis within this thesis. For a comprehensive introduction to turbulence and the related mathematics, the reader is directed to Tennekes and Lumley[121].

3.1.1 Properties and characteristics of turbulent flows

Turbulence is a property of fluid *flows*, not fluids themselves. A fluid completely at rest exhibits no turbulence. A turbulent flow can be defined as one in which the fluid properties (velocity, pressure etc.) fluctuate around a mean value. These fluctuations express themselves as 'eddies'; regions of fluid which exhibit vortical motion in three dimensions. These fluctuations are irregular, and their random nature means that turbulence cannot be described deterministically, but rather, statistically. For a repeated laboratory experiment, this means that it will not be possible to reproduce the individual fluctuations at a particular point in space and time, despite careful control of boundary conditions.

Turbulence exists over a wide range of length and time scales. The largest turbulent eddies in a flow are determined by the geometry of the fluid region, for example, the width of a channel. These eddies have characteristic length and velocity scales of the same order as that of the whole fluid domain, making them effectively inviscid. As they are stretched by interactions with the mean flow, their inviscid nature means that angular momentum is conserved, causing their rotational velocity to increase, and the radius of these rotating bodies to decrease. This leads to the production of smaller eddies. These smaller eddies pass on their energy to eddies which are smaller still, until the eddies become so small that they are largely influenced by viscous forces, rather than inertial forces. At this point, the kinetic energy of these eddies is dissipated into the flow in the form of heat. The source of this energy is the work done by the mean flow on the larger eddies, and which is dissipated by the larger eddies passing their energy to smaller eddies, a process known as the energy cascade[46]. The turbulent energy in the flow is therefore distributed over a wide range of length scales, from the largest length scales associated with the geometry, down to the viscous, dissipative scales. This also means that turbulent flows are associated with increased energy losses due to the dissipation of turbulent kinetic energy.

As large eddies behave in an effectively inviscid manner, with their scales being related to the turbulence producing processes (step height, boundary layer thickness etc.), their behaviour can be expected to be anisotropic – i.e. the fluctuations in each direction are not the same, and heavily dictated by the fluid geometry and boundary conditions. In contrast to this, the fluctuations of the smaller, dissipative eddies are smoothed out by the viscous action of the fluid, making them more isotropic. The small time scales associated with these fluctuations means that their behaviour is influenced by the viscosity of the fluid, and the rate at which they are supplied with energy by the larger scale turbulence. If one assumes that the flow is in equilibrium then the rate at which energy is supplied to these eddies is the same as the rate at which it is

dissipated, leading to the conclusion that these smaller eddies are isotropic, and dependent on the viscosity and rate of energy dissipation, but not on the overall problem geometry. This difference between the properties of large eddies, which are highly problem dependent, and smaller eddies, which show a more universal behaviour, will be important when considering the modelling of turbulence in CFD[46].

The vortical motion of turbulent eddies means that turbulence leads to the mixing of fluid in directions and at rates that would otherwise not occur. This mixing leads to the transfer of, amongst other fluid properties, momentum, heat and contaminant concentration. It is this increased rate of mixing that leads to turbulence having such profound effects on fluid flows. The transfer of momentum, for example in a turbulent boundary layer, can prevent flow detachment over an aerofoil. The transfer of heat can lead to increased efficiency of heat exchangers and promote the mixing of hot and cold air in a room, and the mixing of fluids can be used to improve combustion efficiency[121].

The exchange of fluid momentum from a region of high fluid velocity to low fluid velocity and vice-versa tends to increase the velocity of low-velocity regions, and reduce the velocity of high-velocity regions. This leads to an increase in the shear stresses experienced by the fluid in this region, due to the presence of the turbulence. These additional shear stresses are known as the Reynold stresses, and the modelling of them is critical in CFD.

3.1.2 Mathematical descriptors of turbulence

To properly analyse and compare the nature of the flow in the wake of a tidal turbine, descriptors of the turbulence need to be used. These allow an assessment of the strength of the turbulence, but also how it develops in space and time. Due to the difficulty of ensuring that Laser Doppler Anemometry (LDA) measurements in different directions are synchronised with each other, and the fact that the equipment used allowed a maximum of two directions to be simultaneously measured, unless otherwise stated, the following metrics have been calculated for one direction only.

Mean velocity

The simplest descriptor of the flow is the mean, or time-averaged velocity. This is defined in the following way:

$$\overline{u} = \frac{1}{T} \int_{t_0}^{t_0+T} u(t)\mathrm{d}t \tag{3.2}$$

This is the most common metric used when characterising wakes, is easily obtainable from CFD (regardless of turbulence model used), and from flume measurements with a LDA.

Turbulence intensity

Turbulence intensity (TI) is a metric used to indicate the strength of the fluctuations when compared to the mean flow. For this work, it is defined as the 1-dimensional Root Mean Square (RMS) velocity, divided by the mean velocity in that direction, and expressed as a percentage.

$$\text{TI} = \frac{\sqrt{\overline{u'^2}}}{\overline{u}} \times 100 \tag{3.3}$$

This definition works when the average velocity in the measurement direction is non-zero. However, in cases where $\overline{u} = 0$, the turbulence intensity becomes undefined, and in these cases it may be more appropriate to use the RMS velocities alone to assess the strength of turbulent fluctuations.

Integral length scale

In addition to knowing the strength of the turbulence, a full understanding of the nature of a turbulent flow requires knowledge of the size of eddies in the flow. The integral length scale gives an estimate of the turbulence scales which contain the most energy, and is calculated via the integration of the autocorrelation coefficient. The autocorrelation coefficient, $\rho(\tau)$ indicates the length of time over which a signal (in this case a velocity, $u(t)$) is correlated with itself, and is defined in the following way:

$$\rho(\tau) \equiv \frac{\overline{u(t)u(t+\tau)}}{\overline{u^2}} \tag{3.4}$$

where τ is the amount of time through which the original signal has been lagged. The autocorrelation coefficient is equal to unity at a time lag of $\tau = 0$, as the signal is perfectly correlated with itself. As the time lag increases, the signal becomes less correlated with itself, until eventually the autocorrelation coefficient drops to zero, as the signal no longer demonstrates any correlation with itself. Integrating the autocorrelation coefficient gives a measure of time over which the signal is correlated with itself, the integral scale:

$$\mathscr{I} \equiv \int_0^\infty \rho(\tau)\mathrm{d}\tau \qquad (3.5)$$

This measure of time over which the signal is correlated with itself can then be multiplied by the mean velocity $\overline{u}$, to give an approximate distance over which the signal is correlated with itself. Whilst the integral is defined between limits of 0 and ∞, any practical measurement of velocity is necessarily finite in duration, and therefore in practice, $\rho(\tau)$ is usually integrated to the point where the autocorrelation coefficient reaches zero[121] or a threshold defined by the level of noise in the measurements[59]. It may be noted that it is also possible to calculate an integral length scale by making multiple, simultaneous measurements, shifted in space, rather than applying a time-shift to a single measurement which is fixed in space.

3.2 Turbulence modelling in CFD

The governing equations for fluid flow can be seen as a mathematical expression of the conservation laws of physics (conservation of momentum, conservation of mass, conservation of energy), for a fluid which can be treated as a continuum. They can be derived by considering a finite volume of fluid, applying conservation laws for mass and momentum and accounting for normal forces and stresses on each face of the finite volume. Assuming that the system is in thermodynamic equilibrium, and that the fluid is Newtonian, this yields a closed system of seven equations in seven unknowns, the solution to which is a velocity field. They were independently derived and published in the 19th century by Claude-Louis Navier and Sir George Stokes. The Navier-Stokes equations are a series of equations for momentum, energy and continuity, and are often seen in slightly different formulations, depending on the application for which they are being used. The most important of the Navier-Stokes equations for this work are the instantaneous equations for momentum and continuity in an incompressible fluid. The momentum equation can be written in tensor form as[121]:

$$\frac{\partial u_i}{\partial t} + u_j \frac{\partial u_i}{\partial x_j} = -\frac{1}{\rho}\frac{\partial p}{\partial x_i} + \nu \frac{\partial^2 u_i}{\partial x_j \partial x_j} \qquad (3.6)$$

and the continuity equation can be written as[121]:

$$\frac{\partial u_i}{\partial x_i} = 0 = \mathrm{div}\ \mathbf{u} \qquad (3.7)$$

Tensor notation is indicated by the suffices i, j and k. By convention, i or $j = 1$ corresponds to the x-direction, i or $j = 2$ the y-direction, and i or $j = 3$ the z-direction. Here, ν represents the kinematic viscosity. Variables in bold type face indicate the full vector, in all three directions.

3.2.1 Reynolds-Averaged Navier-Stokes models

Reynolds-Averaged Navier-Stokes (RANS) models have been the mainstay of CFD turbulence models for over 40 years. They range in complexity, and have been successfully applied to a wide variety of different flows.

RANS models recognise that engineers are often concerned with mean (or time-averaged) flows. RANS models are based around the process of Reynolds decomposition, whereby a fluctuating (and therefore time dependent) flow variable, $u(t)$, is decomposed into a mean component, $\overline{u}$, which is independent of time, and a fluctuating component $u'(t)$. This need not only apply to velocities, but to any turbulent flow variables, such as a generic scalar, ϕ[121].

$$u(t) = \overline{u} + u'(t) \qquad \text{and} \qquad \phi(t) = \overline{\phi} + \phi'(t) \tag{3.8}$$

These decomposed variables are then substituted into the instantaneous Navier-Stokes equations for incompressible fluid flow, which yields the following for the continuity (equation 3.9) and momentum (equation 3.10) equations[46]:

$$\frac{\partial \overline{u}_i}{\partial x_i} = 0 = \text{div } \overline{\mathbf{u}} \tag{3.9}$$

$$\frac{\partial \overline{u}_i}{\partial t} + \overline{u}_j \frac{\partial \overline{u}_i}{\partial x_j} = -\frac{1}{\rho}\frac{\partial \overline{p}}{\partial x_i} + \nu \frac{\partial^2 \overline{u}_i}{\partial x_j \partial x_j} + \frac{1}{\rho}\frac{\partial}{\partial x_j}\left(-\rho \overline{u'_i u'_j}\right) \tag{3.10}$$

The Navier-Stokes equations with the decomposed variables are very nearly formally identical to the Navier-Stokes equations with the instantaneous flow variables, but this time re-cast in terms of the time-averaged velocity. The only difference is in the inclusion of the last term, $-\rho\overline{u'_i u'_j}$, which has the form of a stress, and arises from the averaging process. This term is known as the **Reynolds stresses**, and must be modelled in order to close the Navier-Stokes equations. It is the modelling of this term that is done by RANS turbulence models.

There are various models for the modelling of the Reynolds stresses. These range in complexity from one equation models such as the mixing length model, through two equation models such as the k-ε, k-ω and k-ω SST, to the most

complex formulations such as the Reynolds Stress Model (RSM), which require seven transport equations to be solved in order to close the Navier-Stokes equations[46].

Two-equation models such as the k-ε, k-ω and k-ω SST, attempt to model the Reynolds stresses via the Boussinesq approximation. Boussinesq approached the problem of modelling the Reynolds stresses by assuming that they, like the viscous stresses, might be proportional to mean rates of deformation within the flow. The Boussinesq approximation is based on experimental evidence that in isothermal flows of incompressible fluids, turbulence decays, unless there is shear in the flow. It can also be shown that turbulence stresses increase as the rate of deformation increases. Mathematically, the Boussinesq approximation is:

$$\tau_{ij} = -\rho \overline{u_i' u_j'} = \mu_t \left(\frac{\partial \overline{u_i}}{\partial x_j} + \frac{\partial \overline{u_j}}{\partial x_i} \right) - \frac{2}{3} \rho k \delta_{ij} \qquad (3.11)$$

where μ_t is the turbulence (or eddy) viscosity, δ_{ij} is the Kronecker delta (equal to zero unless $i = k$, in which case it is equal to 1) and $k = \frac{1}{2}(\overline{u'^2} + \overline{v'^2} + \overline{w'^2})$[46]. This approximation therefore assumes that turbulence is isotropic. This assumption is a valid one for turbulence on a small length scale, but becomes less appropriate as length scales increase[46]. An alternative approach to modelling the Reynolds stresses via the Boussinesq approximation is taken with the RSM. In this model, transport equations are solved for each of the Reynolds stresses, with scale determining equations for ε or ω, also being required, leading to a total of seven transport equations for closure in 3D.

It is important to note that the process of Reynolds decomposition is a form of time-averaging, and the solution to the Reynolds-averaged Navier-Stokes equations is a time-averaged velocity field. Consequently, CFD simulations using the RANS equations cannot provide information about fluctuations in the flow, as these fluctuations have not been resolved. RANS models, in effect, are an attempt to model the mean flow *given the presence of turbulence*; they do not provide information about the turbulence itself.

The k-ω SST turbulence model

To illustrate the form of a two-equation turbulence model, the k-ω SST turbulence model is detailed here. This is in part by way of an example of a RANS turbulence model, but also because the k-ω SST model is that which is used for the RANS modelling carried out within this thesis. In addition, it has been demonstrated that this turbulence model can produce accurate predictions of turbine performance for the turbine modelled here[8][107].

The k-ω SST model was developed in order to combine the advantages of two previous turbulence models, the k-ε, and the original (or Wilcox) k-ω model. The k-ε model has been used for many years, and has proved to be robust for flows far from boundaries, for example in external aerodynamics applications. It does however, require the use of special treatments known as 'wall functions', in order to accurately take into account the effects of the boundary layer. By contrast, the k-ω model can be integrated to the wall without the need for extra wall treatments, but results are strongly dependent on the assumed values of ω and k in the free stream. The k-ω SST model uses a blending function to combine these two, with the k-ω model being used at boundaries to obviate the requirement for wall functions, and the k-ε model being applied in the free stream, to avoid the sensitivity of the k-ε model to the choice of boundary conditions.

The two turbulence models approach the problem of modelling the Reynolds stresses and closing the RANS equations by considering the dynamics of turbulence – specifically, the transport of turbulence kinetic energy, k, and the rate of dissipation of turbulence kinetic energy, ε. In the k-ω model, the turbulence frequency, $\omega = \varepsilon/k$ is used, and a length scale $l = \sqrt{k}/\omega$ is defined. This gives an eddy viscosity of:

$$\mu_t = \rho k/\omega \tag{3.12}$$

Following the formulation used by ANSYS[122], the transport equation for k is:

$$\frac{\partial}{\partial t}(\rho k) + \frac{\partial}{\partial x_i}(\rho k \overline{u_i}) = \frac{\partial}{\partial x_j}\left[\left(\mu + \frac{\mu_t}{\sigma_k}\right)\frac{\partial k}{\partial x_j}\right] + G_k - Y_k + S_k \tag{3.13}$$

where G_k represents the production of turbulence kinetic energy, S_k represents a source term, and $Y_k = \rho\beta^* k\omega$ represents the rate of dissipation of k, where $\beta^* = 0.09$ is a model constant.

The transport equation for ω is:

$$\frac{\partial}{\partial t}(\rho\omega) + \frac{\partial}{\partial x_j}(\rho\omega\overline{u_j}) = \frac{\partial}{\partial x_j}\left[\left(\mu + \frac{\mu_t}{\sigma_\omega}\right)\frac{\partial\omega}{\partial x_j}\right] + G_\omega - Y_\omega + D_\omega + S_\omega \tag{3.14}$$

where G_ω, S_ω and Y_ω are production, source and dissipation terms respectively, and D_ω is the cross-diffusion term, which arises from the $\varepsilon = k\omega$ transformation of the diffusion term in the ε-equation in the k-ε model[46]. The cross diffusion term is defined as:

$$D_\omega = 2(1 - F_1)\rho\frac{1}{\omega\sigma_{\omega,2}}\frac{\partial k}{\partial x_j}\frac{\partial\omega}{\partial x_j} \tag{3.15}$$

where $\sigma_{\omega,2} = 1.168$ is a model constant. F_1 is a blending function[122] chosen such that, at the wall, the model runs purely as a k-ω model, in the free stream runs purely as a k-ε model, with a smooth transition occurring approximately halfway between the wall and the edge of the boundary layer[46].

3.2.2 Large Eddy Simulation

An alternative approach to Reynolds-averaging is known as Large Eddy Simulation (LES)[46]. Instead of using the process of Reynolds decomposition, LES first filters the Navier-Stokes equations, either in physical or wavenumber space. Typically, this takes the following form:

$$\overline{\phi}(\mathbf{x}, t) \equiv \iiint_{-\infty}^{\infty} G(\mathbf{x}, \mathbf{x}', \Delta)\phi(\mathbf{x}', t)\, \mathrm{d}x_1'\, \mathrm{d}x_2'\, \mathrm{d}x_3' \qquad (3.16)$$

where:

$$
\begin{array}{rcl}
\overline{\phi}(\mathbf{x}, t) & = & \text{filtered function} \\
\phi(\mathbf{x}', t) & = & \text{original (unfiltered) function} \\
G(\mathbf{x}, \mathbf{x}', \Delta) & = & \text{filter function} \\
\Delta & = & \text{filter cutoff width}
\end{array}
$$

In a finite volume formulation, the cell width makes a convenient filter cutoff width, Δ, for a top-hat filter. However, Gaussian filters and spectral cutoffs may also be used[46]. The filter passes large-scale turbulence features which are then directly resolved, but filters out turbulent features smaller than the filter width. These are then treated with a Sub-Grid Scale (SGS) model. The SGS model may be thought of as analogous to a RANS model, and takes into account both the effects of the SGS turbulence on the resolved flow, as well as interactions between the SGS fluctuations themselves[46]. LES therefore treats large and small scale turbulent features differently, recognising that large and small eddies have different physical properties. Larger eddies tend to be less isotropic, subject to vortex stretching, and more dominated by inertial forces, whereas small eddies tend to be more isotropic and dominated by viscous forces[121].

As LES models directly resolve large scale turbulence, they provide a better representation of the effects of these than RANS models, particularly two-equation RANS models which rely on the Boussinesq approximation, and its assumption of turbulence isotropy. They also, in contrast to RANS equations, resolve the *fluctuations themselves* rather than just their *effect on the mean flow*. This means that data from LES simulations allows the user to carry out statistical analysis on the fluctuations, in a similar manner to that possible with

experiments in a flume or wind tunnel. The disadvantage of LES models is the greatly increased computational expense when compared to RANS models[46].

One of the reasons for this is that LES mesh densities generally need to be higher than for RANS models, particularly in near-wall regions where the boundary layer must be resolved. In addition to this, some of the techniques commonly used for minimising the number of cells in meshes for RANS models (such as elongating the cells in the direction of the expected flow) are not applicable in LES models due to the implementation of the filtering algorithm. As the filtering algorithm is typically based on cell size, and turbulence inherently 3-dimensional in nature, all turbulent fluctuations that are less than the largest cell dimension will be treated with the SGS model. If not only small scale turbulence, but also medium scales are being treated with the SGS model, then the reason for using LES will be to some extent negated. LES models also need to be run for more timesteps than RANS models, as the results are inherently transient in nature, and sufficient sampling of flow variables must be carried out in order to achieve convergence of flow statistics.

It is for this reason that to date, little LES modelling of turbine wakes has been carried out using the full turbine geometry. Studies have been carried out using LES by simplifying the turbine geometry through the use of actuator discs[82], or actuator lines[123], [92], or by reducing domain sizes such that the far wakes are not modelled[85]. It is for this reason that hybrid scale-resolving models, such as the Detached Eddy Simulation (DES) method used in this work, were developed.

3.2.3 Detached Eddy Simulation

Detached Eddy Simulation is a turbulence model which has been developed in an attempt to combine the computational efficiency of RANS turbulence models with the ability of LES models to model turbulent fluctuations, rather than just the effect of turbulence on the mean flow[124].

At first glance, it may seem that the approaches of RANS and LES modelling are incompatible with one another, due to RANS models employing time averaging, whereas LES employs spacial filtering (or averaging). The DES model however recognises that once averaging has been carried out, then all information about *how* that averaging took place is lost. After averaging, both LES and RANS effectively become turbulence viscosity models, albeit with a different method employed for the calculation of the turbulence viscosity[122]. The DES model used in this work employs a k-ω SST turbulence model in areas close to walls, where the lower mesh requirements of a RANS model are desired, and switches to LES-like behaviour far from walls in the wake region. To

switch from one mode to the other, the model modifies the turbulence viscosity calculated in the k-ω SST model via the turbulence kinetic energy dissipation term. The extent to which it is modified (if at all) from the standard k-ω SST model depends on the ratio of the local turbulence length to the local cell size. Where local grid size is large and turbulence length scale small, the turbulence kinetic energy dissipation term from the standard k-ω SST turbulence model remains unmodified, and the model runs in pure 'RANS mode'. If, however, the turbulence length scale is large and the local grid size is small, then the turbulence kinetic energy dissipation term is modified via a multiplier, F_{DES}, effectively changing the way in which the turbulence viscosity is calculated, and switching to 'LES mode'.

$$Y_k = \rho\beta^* k\omega \quad \text{becomes} \quad Y_k = \rho\beta^* k\omega F_{DES} \tag{3.17}$$

$$\text{where} \quad F_{DES} = max\left(\frac{L_t}{C_{des}\Delta_{\max}}, 1\right) \tag{3.18}$$

The turbulence length scale, L_t defined as[122]:

$$L_t = \frac{\sqrt{k}}{\beta^*\omega}$$

and the calibration constant is $C_{des} = 0.61$. The variable β^* is defined as in equation 3.13.

In some cases with refined grids, the switch from RANS to DES can take place within the boundary layer, leading to premature flow separation[124], a phenomenon known as Grid-Induced Separation (GIS). In order to prevent this, shielding functions are provided in ANSYS Fluent in order to "protect" the boundary layer[122], ensuring that a RANS solution is applied and preventing the DES limiter from activating too soon. One of these schemes is known as "Delayed Detached Eddy Simulation" (DDES), is recommended by ANSYS[125], and is the scheme used for this work.

It should be emphasised that whilst the principles behind LES and RANS are different (that of spatial averaging as opposed to time averaging), both models are eddy viscosity models. The final equations are formally identical to each other, regardless of which approach is taken — it is only the value of the computed eddy viscosity which is different. In conventional RANS models, time averaging is carried out to obtain the RANS equations, and a model is chosen for accounting for the Reynolds stresses which takes no account of the size of local turbulent features. In LES models, a spatial filter is applied to get to the resulting LES equations, meaning that the size of local flow-features

and local cell size are taken into consideration when calculating a value for the eddy viscosity. The DES model, when running in "RANS mode" is an unchanged version of the k-ω SST model, which is a conventional RANS model and makes no consideration of local turbulent length scales when calculating eddy viscosity. However, where the DES criteria is triggered (equation 3.18 not equal to 1), the value of Y_k (and hence the eddy viscosity) becomes dependent on considerations of the relationship between local turbulence length scale and local cell size. As the resulting equations of RANS and LES models are formally identical, differing only in the method used to calculate eddy viscosity (with LES using spatial considerations of local cell size and flow features), the calculation of eddy viscosity by DES using similar considerations to that of LES can be seen as analogous to running an LES turbulence model.

As noted by Ferziger in [46], there are situations in which LES may only require around twice the computational resources required by RSM. RSM, with its seven transport equations is employed when anisotropy of turbulence means that it is no longer appropriate to use the Boussinesq approximation. Since the wake behind a HATT has been shown to be highly anisotropic[96], the extra information that can be obtained by using DDES instead of an RSM model (i.e. the information relating to mean flow and the statistics of the resolved fluctuations) would justify the use of DDES over RSM, and could justify its use over RANS models generally.

3.2.4   Direct Numerical Simulation

The instantaneous Navier-Stokes equations are sufficient for a complete description of fluid flow, as long as the domain of interest has been discretised into control volumes smaller than the smallest turbulent length scales, and a time-step smaller than the smallest turbulent time scales is used. In this case, the flow becomes essentially invariant within each control volume for the duration of a time step, and can be accurately represented by a single value for each flow variable. This technique is known as Direct Numerical Simulation (DNS), and is an extremely powerful technique for analysing fluid flows and associated phenomena, particularly those for which experimental measurements are currently impossible[46]. However, for the control volumes to be sufficiently small, they need to be smaller than the length of the smallest fluctuations in the flow, which can typically be of the order of 0.1 to 0.01 mm [46]. Unfortunately, discretisation of a fluid domain into control volumes this small requires a huge amount of control volumes to be created for a domain of the size required for the ac-
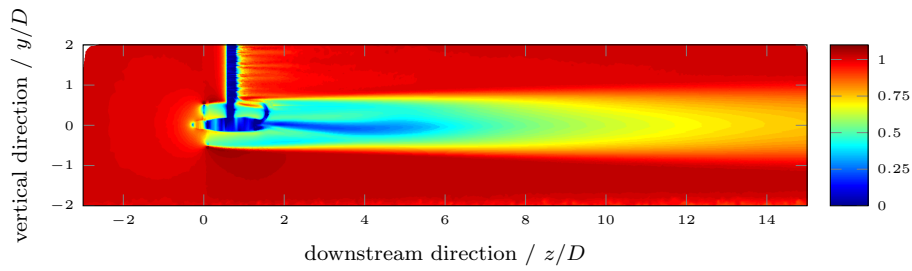
(a) Normalised axial velocity, RANS (k-ω SST) turbulence model.
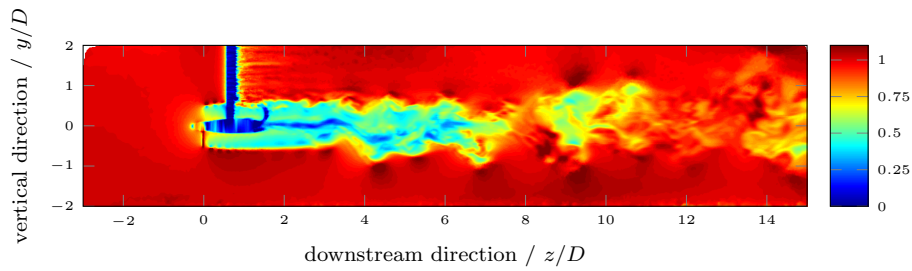
(b) Instantaneous normalised axial velocity, DES turbulence model.
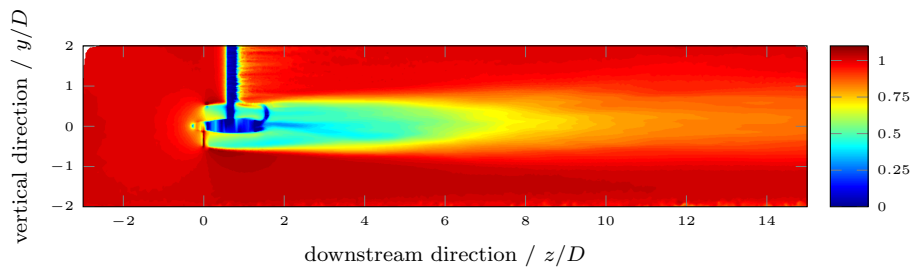
(c) Time-averaged normalised axial velocity, DES turbulence model.

Figure 3.1: A comparison of axial velocity, produced by different turbulence models. It is clear from a comparison of 3.1a and 3.1b that the DES model resolves turbulent features which are not available in RANS models. Nonetheless, it is still possible to obtain time-averaged velocity values (as in 3.1c), which are qualitative similar to the results of the RANS model, should these be of interest to the user.

curate representation of a tidal stream turbine[1], and models containing such a large number of control volumes cannot be simulated using current computing capabilities.

3.3 Swirl

Swirling flows are those in which tangential (rotational) momentum is transferred in an axial direction. They have been studied for many years due to their significance in combustion devices as swirling flows can have positive effects on both flame stability and mixing[126]. Swirling flows are also of interest in aircraft design due to the vortices created at wing tips. In this case, the aim is to reduce the swirl as far as possible. Swirling flows have been shown to have an effect on jet growth, entrainment and decay[127], and could have similar effects on tidal turbine wakes due to the similarities between jets and wakes. In addition to this, the level of swirl in a wake can be considered to be an important characteristic of the wake, and has implications for the layout of tidal turbine arrays as it can potentially limit the spread of the turbulent region behind a turbine[101]. Accurate representation of flow rotation in the wake region is important as it has the potential to alter the angle of attack of the blades on downstream turbines, and could conceivably be utilised to improve energy extraction if downstream turbines were to rotate in the opposite direction to their upstream counterparts, or if contra-rotating turbines are used[94]. In addition to this, an understanding the nature of rotation in the wake provides an insight into mixing and wake recovery processes. It has also been shown that the swirl characteristics of the flow downstream of a HATT are affected by the solidity of the turbine[54], with an increase in solidity corresponding to an increase in the amount of swirl found in the wake.

3.3.1 Swirl number

A non-dimensionalised measure of the swirl, the swirl number, S, can be defined in order to indicate the strength of the swirl in a jet. The swirl number is based on the ratio of the axial flux of angular momentum to the axial flux of axial momentum across a given area, which is then divided by a characteristic length in order to produce a non-dimensionalised measure of the swirl. These equations are detailed by Lilley[127] for jets, and have also been applied to tidal turbine

---

[1]For the 0.5 m turbine modelled in this work in a 2 m $\times$ 4 m $\times$ 9 m flume, if this domain is discretised into control volumes of 0.1 mm^3, then a total of ca. 10^{14} control volumes will be required, compared to the ca. 10^7 used for the DES study detailed here. Add to this the extremely small timesteps which are required, and it is easy to see how quickly such a system becomes uneconomical.

wakes[107]. Swirl number, S, is defined as:

$$S = \frac{G_\phi}{G_x r} \tag{3.19}$$

where $r = R$, the turbine radius, by convention (although the radius of the wake could also be used). G_ϕ is the axial flux of angular momentum, given by:

$$G_\phi = \int_0^R (wr)\rho u 2\pi r \, \mathrm{d}r \tag{3.20}$$

where w is the tangential velocity, and u is the axial velocity. G_x is the axial flux of linear momentum, consisting of both a momentum and a pressure term, and given by:

$$G_x = \int_0^R u\rho u 2\pi r \, \mathrm{d}r + \int_0^R p 2\pi r \, \mathrm{d}r \tag{3.21}$$

To exactly follow this definition of swirl number, profiles of both velocity and static pressure would need to be measured. However, this is not always possible due to experimental conditions and the complexity of swirling flows. Beér and Chigier[128] showed that it is possible to obtain satisfactory values for swirl using only geometric considerations and velocity profiles, by assuming static pressure to be constant over R. This "geometric swirl number" can then be used to compare the swirl imparted to a flow for geometrically similar systems, without requiring profiles of static pressure to be obtained[129]. It is this "geometric swirl number" which will be used in this thesis. If the static pressure can be assumed to be constant over R, then equation 3.21 simplifies to:

$$G_x = \int_0^R u\rho u 2\pi r \, \mathrm{d}r \tag{3.22}$$

Whilst the swirl number provides a convenient and simple metric for the comparison of swirling flows, the full behaviour of these flows is complicated. An integrated value such as the swirl number involves a loss of detail regarding the distribution of the swirl velocity, and in some cases it has been shown to be inadequate for the description of the subsequent development of the flow[130].

Chapter 4

Turbine and Wake Analysis Methods

4.1 Turbine performance

It has been shown that the performance of tidal turbines operating under certain conditions may be described by a series of non-dimensionalised performance metrics for power, thrust and torque[15]. When using these non-dimensional coefficients for turbines operating above a particular Reynolds number (equation 3.1), the turbine performance curves collapse onto themselves such that the performance becomes a function only of the tip-speed ratio, λ:

$$\lambda = \frac{\omega R}{v} \tag{4.1}$$

where ω is the rotational velocity, R is the turbine radius, and v is the free stream velocity. For the calculation of the tip-speed ratio (equation 4.1), as well as the following performance metrics (equations 4.2–4.4), a value of velocity is required. The velocity most often used for these calculations is the time-averaged free stream velocity. However, turbines in a marine environment may be subject to highly sheared flows, due to the bottom friction of the sea bed. Depending on the profile of the flow, the velocity experienced by these turbines may vary greatly across the turbine face. For these cases, it has been shown that is more appropriate to use the volumetric average of velocity across the face of the turbine[15]. The turbines modelled in this work are not subject to a highly sheared environment, and therefore the time-averaged free stream velocity at the centreline has been used.

4.1.1 Power coefficient

The power coefficient, C_P, relates the total power produced by the rotor to the total kinetic energy available in the fluid which passes through its swept area. The rotor power (i.e. the power before any mechanical or electrical losses within the turbine) can be expressed as the torque of the blades, τ, multiplied by the rotational velocity, ω. The rate of change of kinetic energy of the fluid passing through the turbine can be calculated using $\frac{1}{2}\dot{m}v^2$, where $\dot{m} = \rho A v$, and A represents the swept area of the turbine. Combining these gives the equation for the non-dimensionalised power coefficient[15]:

$$C_P = \frac{\tau\omega}{0.5\rho A v^3} \tag{4.2}$$

4.1.2 Thrust coefficient

In a similar way to the power coefficient, the thrust on the turbine can be expressed using a non-dimensionalised coefficient, known as the thrust coefficient, C_T. This relates the thrust on the turbine, F_T, to the equivalent thrust on an object of the same frontal area, with a drag coefficient equal to unity.

$$C_T = \frac{F_T}{0.5\rho A v^2} \tag{4.3}$$

4.1.3 Torque coefficient

The torque coefficient, C_θ, relates the torque produced by the rotor to the maximum theoretical torque.

$$C_\theta = \frac{\tau}{0.5\rho A v^2 r} \tag{4.4}$$

4.2 Wake analysis metrics

All objects within a fluid flow produce a wake. The length, width and characteristics of the wake are dependent on the shape of the object, and the nature of the flow and the fluid itself. The wake induced by the presence of the object is a region of slower moving fluid with increased turbulence when compared to the free stream. Mixing takes place between the higher velocity free stream and the lower velocity wake, and the associated change in momentum causes the wake to gradually return to the same velocity as the free stream. This is known as wake recovery. Just behind the object, the lower velocity wake and higher velocity free stream regions are distinct from one another, separated by a thin, highly sheared layer; flow recirculation is often observed in this near
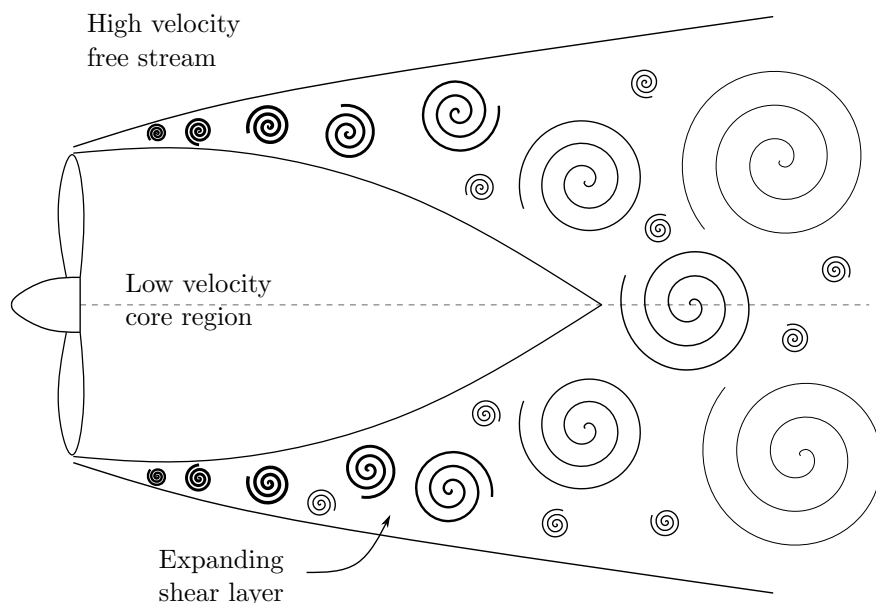
Figure 4.1: A schematic of the wake description found in section 4.2. Flow direction is from left to right. This figure is intended as a schematic representation of the text in section 4.2; in practise the different regions will not be expected to have such clear boundaries between them, nor is the schematic intended to be to scale.

wake region. As the fluid progresses downstream, momentum exchange takes place across the shear layer, leading to wake recovery taking place from the outside towards the centre. At the same time, the shear layer becomes thicker, extending outwards into the free stream and inwards towards the centre of the wake, whilst simultaneously decreasing in strength. The overall area affected by the wake becomes wider, but the strength of the wake itself (the velocity deficit) decreases. At some point downstream of the object, the shear layer reaches the centreline of the wake. Beyond this point, the flow is still affected by the presence of the object upstream, exhibiting increased turbulence and a remaining velocity deficit, but the bounds of the wake become less defined. Eventually, very far downstream of the object, viscous effects will damp down and dissipate any remaining turbulence and the wake will continue to recover, until it is indistinguishable from the upstream flow. This description is shown schematically in Figure 4.1.

This qualitative description of a wake will be recognised by flow physicists, but in order to compare wakes, quantitative metrics must be developed. Clearly, an area of reduced flow velocity and increased turbulence has the potential to impact downstream turbines; reduced flow velocity will reduce the energy available to downstream turbines, and increased turbulence could lead to fluctuations

73

in the loads experienced by downstream turbines. In addition, changes to the behaviour of the fluid around and downstream of the turbine could impact the local environment with the potential to change sediment transport dynamics or water turbidity. Whilst the importance of being able to quantify both the strength of the wake as well as the size of the region it affects is clear, developing quantitative metrics by which to do this is more difficult. This is because of the highly turbulent nature of the wake, meaning that the width and length can fluctuate with time.

4.2.1 Wake length

In general, wake recovery occurs at a higher rate in the near wake, where the difference between the velocities of the wake and the free stream is greatest, and the exchange of momentum is most effective. As the wake and free stream become more similar to each other, the effect of momentum mixing reduces, and the rate of recovery decreases. In other words, the velocity in the wake region recovers asymptotically to the free stream velocity. For practical measurements of wake length, it is necessary to take a velocity threshold where it can be said that the wake has 'recovered'. The choice of this velocity threshold is essentially arbitrary, but for the purposes of this work, a value of 90% wake recovery (10% deficit) will be used, unless otherwise stated.

Centreline velocity recovery

Probably the simplest method of quantifying the length of the wake is by analysing the recovery of the time-averaged axial velocity along the turbine centreline. This has the advantage of being easily extracted from CFD modelling, or measured experimentally in a flume or in the field. However, it only provides information about the centreline axial velocity, and does not contain any information about the distribution of velocity in the wake region – information of critical importance to turbine developers. In addition to this, wake recovery occurs from the outside towards the centreline, meaning that centreline measurements can potentially under-estimate the level of wake recovery. Using this information alone could lead to a turbine developer using an unnecessarily large downstream spacing for the layout of a turbine array, reducing the amount of energy which can be extracted from a site of limited geographical extent.

Volumetric averaged velocity

In order to account for the distribution of flow velocity behind the turbine, the volumetrically averaged velocity has also been used. This is an area-weighted

estimate of the time-averaged axial velocity through the swept area of the turbine. This was recorded at regular intervals downstream from the turbine, and has been shown to give a better estimate of the energy available to a downstream turbine[8]. This is trivial to extract from CFD data; the time-averaged velocity is integrated over the swept area of the turbine at different downstream stations. However, due to the time required to make measurements in a flume, these were only taken on a horizontal plane. In order to obtain an estimate of the volumetric flow over the swept area of the turbine, a shell (or disc) integration was performed on the measured velocity profiles, following the procedure used by Mycek et al.[60] and reproduced in Figure 4.2. The same procedure must then be carried out on the CFD data in order to provide results for comparison. If this is not done, then there is the potential for the wake of the stanchion to significantly influence the integration of the mean velocity over the turbine swept area in the CFD, which would not be accounted for purely by taking a shell integration from the horizontal plane in the flume data.
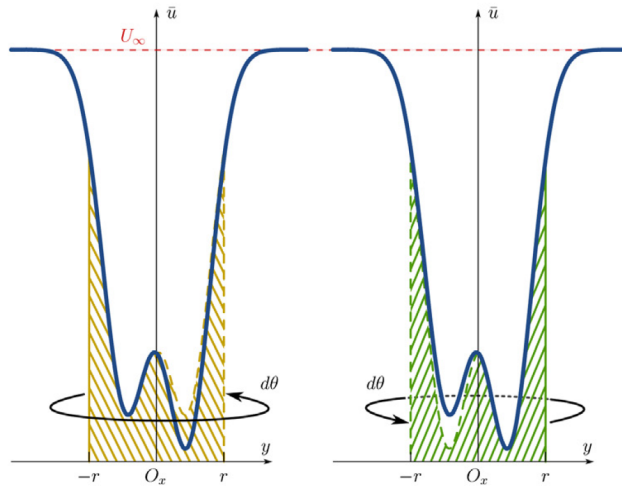
Figure 4.2: The shell (or disc) integration method used by Mycek at al.[60]. On the left (in yellow), the integration is carried out on the left half of the wake; on the right (in green), the integration is performed on the right half of the wake. The results from the two halves are combined to give a pseudo axisymmetric result. Figure reproduced from Mycek et al.[60].
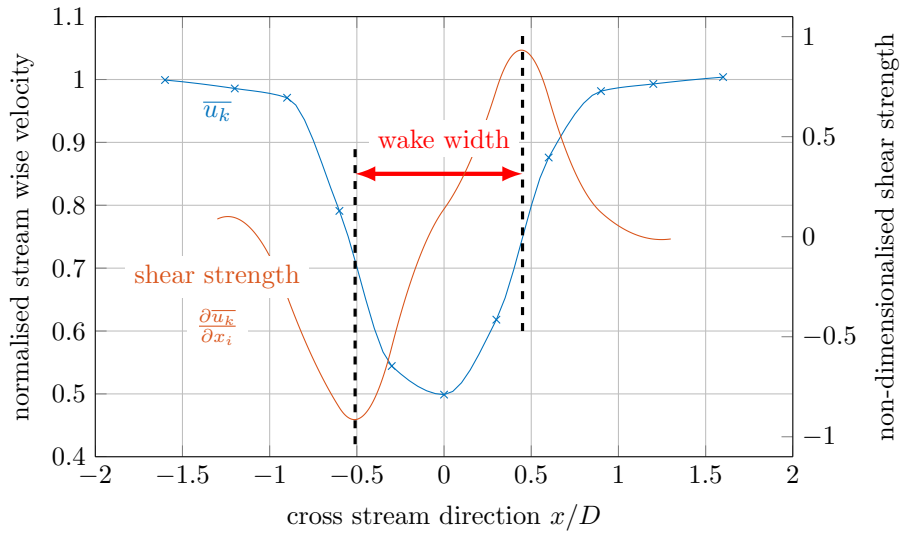
4.2.2 Wake width

Initially, a turbine wake is approximately as wide at the turbine rotor itself. As it develops downstream however, mixing takes place between the high-velocity free stream, and the lower velocity wake region, causing a layer of sheared

flow. Initially this shear is high and the the shear layer thin, but as the wake develops, the thickness of this shear layer increases, and the velocity gradient (shear) decreases. This simultaneous change in both thickness and strength of the shear layer makes it difficult to define a single, definitive, definition of the wake; this difficulty is only compounded by recalling that studies suggest that the turbine wake meanders in time[63],[61]. Therefore, three different methods have been proposed and used in the analysis of turbine wakes in this thesis; a width metric based on the point of maximum-shear, a width metric based on a fixed velocity threshold, and a width metric based on a full-width half-minimum method. All three methods have been designed to be implemented for measurements of time-averaged axial velocity in a rake parallel to the plane of the turbine rotor.

Wake width based on the point of maximum-shear

One method of defining the position of the edges of the wake is by using the point of maximum-shear. In this case, the point of maximum-shear is defined as the position with the greatest rate of change in the time-averaged axial velocity in the cross-stream direction $max\left(\frac{\partial \overline{u_k}}{\partial x_i}\right)$. The width of the wake is taken to be the distance between the points at which this shear is a maximum. The application of this method to a velocity wake profile can be seen in Figure 4.3.

Figure 4.3: Wake width calculation using the maximum-shear method.

Wake width based on a fixed velocity threshold

For array designers, a more useful definition of wake width may be the width of the region with a velocity deficit above a certain threshold. This threshold may be set arbitrarily, and for this work has been chosen to be 90% wake recovery (10% velocity deficit) of the time-averaged axial velocity when compared to the free stream velocity. As the wake recovers from the outside inwards due to the mixing of momentum from the free stream, it is expected that the wake width (following this definition) will decrease as it develops downstream of the turbine. Once all of the wake has recovered to more than 90%, the calculated wake width will become zero. The application of this method to a velocity wake profile can be seen in Figure 4.4, and has been recently used in a CFD study by Ahmadi[92].
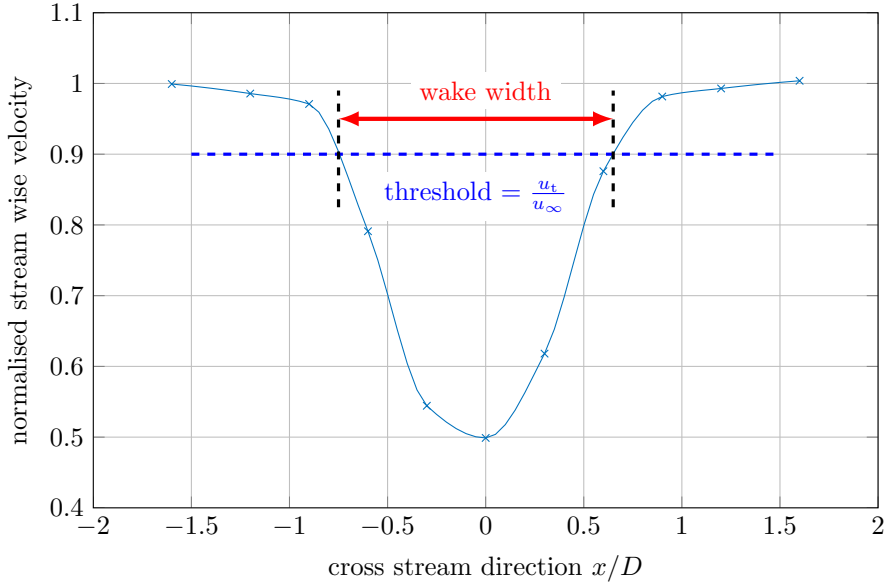
Figure 4.4: Wake widths calculation using the fixed velocity threshold method.

Wake width based on the full-width half-minimum of the velocity deficit

A third approach, which recognises that the width of the region affected by the wake increases even as the velocity deficit decreases, is taken by a width measurement metric based on the idea of a full-width half-minimum. The full-width half-maximum in a concept often used in statistics and signal processing to analyse the width of a peak. This method uses a velocity threshold, but the threshold at a particular downstream position is chosen as half of the maximum

velocity deficit at that downstream position in the wake. Once half of the maximum velocity deficit has been calculated, the width is calculated as the cross stream extent of the wake which has a velocity deficit equal to this value. The application of this method to a wake velocity profile can be seen in Figure 4.5.
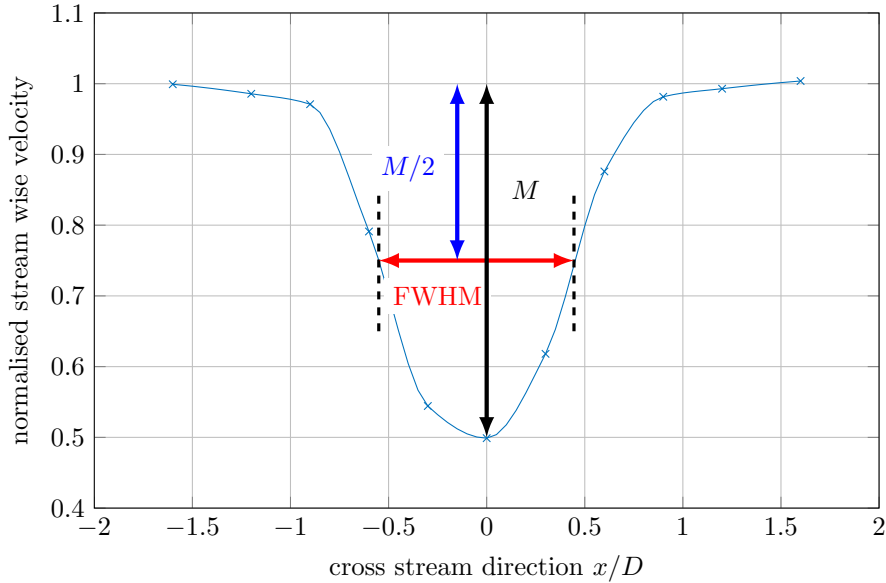
Figure 4.5: This figure shows how wake widths can be calculated using the Full-Width Half-Minimum (FWHM) method.

4.2.3   Swirl

As discussed in Section 3.3, the calculation of the swirl number is dependent on the calculation of the flux of rotational momentum, and the flux of axial momentum. In order to calculate these, both the rotational and axial components of the flow must be known. As with the volumetric averaged velocity, for the CFD results, calculation of the fluxes of axial and rotational momentum at different downstream positions is trivial as they can be easily extracted from a series of planes defined so as to cover the swept area of the turbine. These are then applied to equation 3.19, in order to calculate the swirl number. For flume results, vertical and axial velocities were measured on the horizontal plane containing the turbine axis. These two directions correspond to the tangential and axial velocities respectively. These were then applied to equations 3.20, 3.22 and then 3.19 in order to calculate the swirl number. In order to do this, shell integrations were performed in a similar way to that used for the calculation of volumetric averaged velocity from the flume data. As these measurements

are only taken on the horizontal plane, any effects due to the influence of the stanchion are minimal, however, any effects due to shear in the flow will also not be identifiable. In order to ensure parity between the CFD and experimental results, the same shell-integration procedure was also applied to the CFD data.

4.3 Uncertainty analysis

Ideally, measurements made when conducting an experiment will be both accurate and precise. The accuracy of measurements describes how well the measurements reflect the true value of a measured quantity. Precision on the other hand is related to the repeatability of a particular measurement; it indicates how closely grouped a series of measurements will be to each other, and represents the random scatter inherent when measuring particular physical properties. Quantification of the uncertainty of measurements is crucial in order to evaluate the significance of reported findings. Errors associated with measurements can be divided into two categories: precision error and bias error. Precision error is related to the repeatability of a particular measurement, whereas bias (or offset) error, gives an indication of the accuracy of a measurement. This type of error is inherent to the measurement equipment itself, and is often provided in data from manufacturers. This is also the type of error associated with reference uncertainty for standard quantities such as density, ρ, or g, the gravitational acceleration. In general, a measurement can be considered to contain both precision error μ_p and bias error μ_b, which can be combined to give the combined standard uncertainty, μ_{tot}, in the following way:

$$\mu_{\text{tot}} = \sqrt{\mu_p{}^2 + \mu_b{}^2} \qquad (4.5)$$

In many instances, for example the calculation of C_P, multiple variables containing measurement uncertainties will be combined. In order to calculate the uncertainty associated with the propagation of errors within a general function f, of n independent variables, the following must be applied[131],[132]:

$$\mu_f = \sqrt{\left(\frac{\partial f}{\partial x_i}\right)^2 \Delta x_i{}^2 + \left(\frac{\partial f}{\partial x_{ii}}\right)^2 \Delta x_{ii}{}^2 + ... + \left(\frac{\partial f}{\partial x_n}\right)^2 \Delta x_n{}^2} \qquad (4.6)$$

where x_i represents the ith variable, and Δx_i represents the error in the ith variable. In order to convert a combined uncertainty such as that obtained from equations 4.5 or 4.6 into the more commonly applied uncertainty intervals, it must be multiplied by a coverage factor, k. Assuming a Gaussian distribution

of errors, a coverage factor of $k = 1.96$ will give a 95% confidence interval. This implies that, should repeated measurements be made and these intervals created, then it would be expected that 95% of these intervals will contain the true value[133]. It is applied in the following way:

$$U = k\mu \tag{4.7}$$

For the experimental work conducted in this thesis, both precision and bias errors will be present, as both of these are associated with physical measurements. However, for the numerical simulations, no physical measurements were made, and therefore no bias error can be present. Nonetheless, when quoting mean values, it is important to quantify uncertainties associated with the mean values. These were evaluated for the CFD simulations by applying the central limit theorem and standard error of the mean. For the experimental measurements, the bias uncertainty of the equipment used was included.

4.3.1 Central limit theorem

The central limit theorem relates the mean, standard deviation and distribution of a population to the mean, standard deviation and distribution of sample sets of the same population. In cases where it is not possible to analyse a complete data set, central limit theorem allows confidence intervals to be created around the mean gained by taking a sample of data points from the population. Consider a population of unknown mean, μ, unknown standard deviation, σ, and unknown distribution. If a series of sample sets are made of this population and the mean, $\overline{X}$, of each of these sets found, then central limit theorem dictates that these sample means form a normally distributed group, with the following mean and standard deviation[133]:

$$\mu_{\overline{X}} = \mu \qquad \text{and} \qquad \sigma_{\overline{X}} = \frac{\sigma}{\sqrt{n}} \tag{4.8}$$

where $\mu_{\overline{X}}$ is the 'mean of means', $\sigma_{\overline{X}}$ the standard deviation of the means and n the size of the sample set. The more sample sets are taken, the closer the distribution becomes to being Gaussian, and the larger each sample set, the narrower the distribution becomes.

In this thesis, mean velocities are quoted frequently, whether from CFD or from experimental measurements. These mean values are obtained by taking a single sample set from a larger overall population. The goal of applying central limit theory in this case is to gain an understanding of how well the mean of the sample, $\overline{X}$, represents the true mean of the population, μ, and to allow

confidence intervals to be created. At first glance, this does not appear possible, as neither σ nor $\sigma_{\overline{X}}$ are known. However, if the sample size is reasonably large, then the standard deviation of the sample set, s, provides a close approximation to the standard deviation of the entire population, σ. Therefore, the standard deviation of the sample means (known as the standard error) can be approximated by[133]:

$$\sigma_{\overline{X}} \approx \frac{s}{\sqrt{n}} \tag{4.9}$$

As the distribution of the sample means is known to be normal, confidence intervals can then be built around this estimate of standard error using equation 4.7. This allows an evaluation of how representative the sampled mean is as an estimate of the true mean of the complete population, μ.

4.3.2 Uncertainty in turbine performance

Turbine C_P and C_θ were calculated using equations 4.2 and 4.4. The bias uncertainties in the measurement of the relevant variables are shown in Table 4.1. These have been determined either from manufacturers data or from the methods used for instrument calibration[134]. No data were available from the manufacturer for bias uncertainties relating the torque generating current to the motor torque. The standard deviation of each measured quantity was determined for each data set (i.e. the measurement for each tip-speed ratio), with their combined standard uncertainties being calculated using equation 4.5. As it is the *mean* C_P and C_θ which are being sought, it is the magnitude of the fluctuations, rather than their source which is relevant for the calculation of precision uncertainties; therefore the precision uncertainties were calculated via the standard deviations in C_P and C_θ and the application of central limit theory.

Table 4.1: Bias uncertainties in variables required for calculation of turbine performance.

	bias uncertainty
τ / $\mathrm{N\,m}$	n/a
ω / $\mathrm{rad\,s^{-1}}$	0.20
ρ / $\mathrm{kg\,m^{-3}}$	2
r / m	0.005
v / $\mathrm{m\,s^{-1}}$	0.02

Equation 4.6 was applied to equations 4.1, 4.2 and 4.4, to give the following expressions for the bias uncertainties in the values of λ, $\overline{C_P}$ and $\overline{C_\theta}$ due to the propagation of the uncertainties:

$$\mu_\lambda = \left|\frac{\overline{\omega}r}{\overline{v}}\right|\sqrt{\left(\frac{\Delta x_\omega}{\overline{\omega}}\right)^2 + \left(\frac{\Delta x_r}{r}\right)^2 + \left(\frac{\Delta x_v}{\overline{v}}\right)^2} \tag{4.10}$$

$$\mu_{C_P} = |\overline{C_P}|\sqrt{\left(\frac{\Delta x_\tau}{\overline{\tau}}\right)^2 + \left(\frac{\Delta x_\omega}{\overline{\omega}}\right)^2 + \left(\frac{\Delta x_\rho}{\rho}\right)^2 + \left(\frac{2\Delta x_r}{r}\right)^2 + \left(\frac{3\Delta x_v}{\overline{v}}\right)^2} \tag{4.11}$$

$$\mu_{C_\theta} = |\overline{C_\theta}|\sqrt{\left(\frac{\Delta x_\tau}{\overline{\tau}}\right)^2 + \left(\frac{\Delta x_\rho}{\rho}\right)^2 + \left(\frac{3\Delta x_r}{r}\right)^2 + \left(\frac{2\Delta x_v}{\overline{v}}\right)^2} \tag{4.12}$$

Bias and precision uncertainties were combined using equation 4.5 and a coverage factor of $k = 1.96$ applied to give confidence intervals of 95% (assuming a Gaussian distribution), which were included on plots of $\overline{C_P}$ and $\overline{C_\theta}$ as error bars. For the calculation of $\overline{C_P}$ and $\overline{C_\theta}$ from the CFD simulations, the same method was applied, but without any bias errors as no physical measurements are made in the CFD.

4.3.3 Uncertainty in flow measurements

Within this thesis, values for time-averaged velocity, $\overline{u}$, 1D turbulence intensity and integral length scale, L_t, obtained from LDA measurements in the IFRE-MER flume are quoted. Each of these are calculated from the data file provided by the LDA, containing pairs of values of instantaneous velocity and the time at which that velocity was measured. Each of these individual measurements of instantaneous velocity is subject to a range of uncertainties from a variety of sources, some of which are bias uncertainties and some of which are precision uncertainties. The effect that each type of uncertainty will have on $\overline{u}$, turbulence intensity and L_t is dependent on what type of uncertainty it is. A summary of the different uncertainties which affect the instantaneous velocity measurements can be found in Table 4.2. The 'rotational alignment' uncertainty derives from the fact that the crossed beams of the LDA must be aligned with the global coordinate system of the tank. Should the beams measuring axial velocity be misaligned with the axial direction in the tank, then this will cause the LDA to record a velocity lower than the true velocity. Alignment was achieved by projecting the LDA beams towards the underwater observation window in the flume, and aligning the vertical pair of laser beams with a known vertical reference from the flume's PIV traverse system. Using this technique, the misalignment uncertainty is judged to be $\leq \pm 0.5°$, the cosine of which must be multiplied by the true magnitude of the velocity to give the uncertainty. For

this purpose, it is assumed that the true velocity vector is aligned in the axial direction, so for both calculations in the axial and vertical directions, the mean axial velocity, $\overline{u_z}$, is used.

Table 4.2: Summary of uncertainties associated with LDA velocity measurements

Uncertainty source	Uncertainty size	Uncertainty type
manufacturer's calibration	0.001 m s^{-1}	offset/bias
rotational alignment	$0.1\% \ \overline{u_z}$	offset/bias
measurement standard deviation	0.1%	precision

When calculating uncertainties in mean velocity, turbulence intensity and L_t, it is important to consider the effect each type of uncertainty has on the calculated value. This is further complicated by the fact that it is not a constant velocity which is being measured, but rather, one which would be expected to fluctuate, even if the measuring equipment was perfectly precise and accurate. Where possible, uncertainties due to precision error should be separated from uncertainties due to the fluctuations in velocity being measured.

When calculating the uncertainty in the mean velocities, the bias uncertainties will cause an offset in the mean velocity calculated. The precision uncertainties can be quantified by using the standard deviation of the sampled velocities, s, and applying central limit theorem as discussed in section 4.3.1. This will combine precision uncertainties in the measuring equipment as well as the uncertainties due to the velocity fluctuations.

For a value of mean velocity, $\overline{u}$, calculated from n samples of velocity with a sample set standard deviation of s, the uncertainties were calculated as follows:

Firstly, the bias error was calculated using the calibration uncertainty and the uncertainty caused by rotational misalignment:

$$\mu_b = \overline{u_z} \times 0.001 + 0.001 \text{ m s}^{-1} \tag{4.13}$$

Then the precision uncertainties were calculated using central limit theorem:

$$\mu_p = \frac{s}{\sqrt{n}} \tag{4.14}$$

These were then combined using equation 4.5 and a coverage factor of $k = 1.96$ applied as per equation 4.7 to yield a 95% confidence interval. Mean velocities

are therefore quoted as:

$$\text{mean velocity} = \overline{u} \pm 1.96\sqrt{[(\overline{u_z} \times 0.001) + (0.001)]^2 + \left(\frac{s}{\sqrt{n}}\right)^2} \qquad (4.15)$$

Equation 3.3 shows that the calculation of 1D turbulence intensity relies itself on the calculation of two other quantities: the mean velocity and the RMS of the velocity fluctuations. If the uncertainties in these can be quantified, then they can be combined to give the combined uncertainty. Uncertainties in the calculation of mean velocity have been detailed above, which leaves only the calculation of the uncertainty in the RMS fluctuations of the flow. As both the instantaneous velocities and the mean velocity are subject to the same bias errors, these cancel each other out, leaving only the precision error in the measurements[1]. The fluctuations in the measured velocities have two sources: the precision error in the measuring instrument, and the fluctuations in the true velocity. As these two sources are expected to be independent of each other, they can be added together using the law of cosines. If σ_t is the standard deviation due to turbulent fluctuations, and σ_p the standard deviation due to the precision error in the instrument, then the combined standard deviation is:

$$\sigma = \sqrt{\sigma_t^2 + \sigma_p^2} \qquad (4.16)$$

Given that the number of samples in the set is very large (in all cases, the number of samples is greater than 10 000), the standard deviation of the sample, s, can be considered a good estimate of the true standard deviation, σ. Therefore, the RMS velocity fluctuations due to turbulent fluctuations can be estimated to be:

$$\sqrt{s^2 - s_p^2} = s_t \qquad (4.17)$$

In this way, both bias and precision uncertainties have been eliminated from the calculation of the RMS velocity fluctuations. These can then be divided by the mean velocity, $\overline{u}$ (which has already had its uncertainty established) in order to produce an estimate of the uncertainty for the 1D turbulence intensity.

Calculation of the turbulence length scale, L_t involves the integration of the autocorrelation coefficient of the fluctuations to give the integral time. This is then multiplied by the mean velocity to produce a length scale. As the

---

[1]The bias error due to rotational misalignment will, strictly speaking, show a slight dependence on instantaneous velocity (with error increasing at higher velocities). However, in a 1D measurement such as that made here, neither the overall magnitude nor the direction of the instantaneous velocity can be determined. Therefore, in common with the other velocity calculations in this thesis, the mean axial velocity has been used, and the bias errors in the mean and instantaneous velocities cancel each other out.

84

autocorrelation coefficient is normalised, the magnitude of the fluctuations is not important, but rather, their distribution in time. As with turbulence intensity, because the calculations are related to the fluctuations from the mean, bias or offset uncertainty is not relevant; only precision uncertainty is important. The manufacturers of the LDA give a value for the precision uncertainty, but no indication of how these uncertainties are distributed in time. This means it is not possible to isolate the impact of precision uncertainty on L_t from that due to fluctuations in the velocity caused by turbulence. Nonetheless, the fluctuations caused by turbulence intensity are in all cases at least one order of magnitude greater than those due to precision uncertainty, and in most cases more than two orders of magnitude greater. It was therefore considered that these uncertainties will have no discernible impact on the calculation of the integral time scale. It could be argued that precision errors in the time base of the LDA may have an effect in the integral time scale calculated, however, the data file records incident time with a precision error of $\pm 5 \times 10^{-7}$ s. Comparing this to the average sample interval of 5×10^{-3} s, these precision errors are considered to be negligible.

Calculations of wake widths are based on methods, rather than formulae, which means that an estimation of the impact of errors in velocity and position is difficult to quantify. Monte-Carlo methods could be used to apply fluctuations to each velocity and position measurement, but the expense of this was deemed unjustifiable. Instead, the uncertainty in relative positions between two points measured using the horizontal traverse (± 1 mm) was applied to the widths to give an approximation of the uncertainty.

Calculation of volumetric averaged velocity involves the integration of measured velocities across the swept area of the turbine. These integrations are performed numerically on the measured wake profiles, rather than analytically, which makes a calculation of the uncertainties involved difficult, and as the integration process is a form of averaging, the impact of precision uncertainties will tend to decrease when compared to the impact on single measurement. Nonetheless, bias or offset uncertainties will still be present, so these were retained as the uncertainties for volumetric averaged velocities.

Calculation of swirl has similarities to the calculation of volumetrically averaged velocities, but involves the numerical integration of both the axial and tangential velocities. Monte-Carlo methods could be applied in both of these cases to assess the impact of the uncertainties, but this is beyond the scope of this work.

Uncertainties in CFD flow results

In the CFD simulations, no physical measurements are made so there can be no error due to bias of measuring instruments. However, as mean velocities quoted in this thesis are calculated by averaging a sequence of instantaneous velocities, there will be uncertainty in the calculated mean due to the sample size and the level of fluctuations in the flow. As the sample size increases, and as the level of fluctuations decreases, so the calculated velocity becomes a closer match to the mean velocity which would be calculated if a sample of infinite length could be taken. An estimate of this match is given by the central limit theorem. For all the results quoted in Chapter 7, 10 000 samples were used in order to calculate the mean velocity. As an example, applying the central limit theorem to a mean velocity calculated from 10 000 samples with a relatively high turbulence intensity of 30%, equation 4.9 gives the standard error to be 0.3% of the mean. Applying a coverage factor of $k = 1.96$ to produce a 95% confidence interval gives error bars of $\pm 0.6\%$ of the mean value recorded. These are smaller than the width of lines used on the charts, and therefore, for clarity, have been omitted. Calculations of turbulence intensity from the CFD are not subject to any bias or precision errors, only the uncertainty in the value of the mean. Given how small these uncertainties are, these have also been omitted from charts of turbulence intensity. All other displayed quantities have been treated in the same way as for quantities measured physically in the flume, neglecting any bias or precision uncertainties.

Chapter 5

CFD Methodology

A CFD model was created in ANSYS Fluent for a 3-bladed 10 m diameter, horizontal axis turbine, based on a turbine used before in research in the Cardiff Marine Energy Research Group (CMERG)[8], [107]. This particular blade geometry has also been used in a scale-model turbine, and was used again within this work for the purposes of validation. Initially, a 10 m diameter turbine geometry was used, with a nacelle and monopile stanchion connecting it to the seabed. This configuration was chosen as it allowed the DES model to be developed from RANS models which had already been well characterised, allowing an assessment to be made of the changes due to the use of the new turbulence model. A study was then conducted to ensure independence of the solution from the mesh used for spatial discretisation. As it became clear that the available computational resources would not allow parallel studies of both a 10 m turbine for assessment of full-scale wakes, and the 0.5 m diameter turbine for model validation, all further CFD study was carried out for the model-scale geometry, as this provides the most direct comparison to flume data. Turbine blade geometry was scaled to match the 0.5 m turbine, the nacelle was adapted to be identical to that of the model turbine, and the CFD mesh was also scaled, in order to model the new geometry. In addition to this, the timestep size was reduced, allowing the Courant-Friedrichs-Levy (CFL) number (equation 5.1) to remain within an appropriate bound for this turbulence model[125].

Simulations were then run to analyse the wake for nine different flow conditions comprising of three values of turbulence intensity and three values of turbulence length scales. For each flow condition, three different values of tip-speed ratio were used, corresponding to that found previously for maximum C_P and C_θ as well as one corresponding to a high value of C_T. This gave a total of 27 runs for the CFD study into the impact of turbulence intensity and length scale on the wake. Two further cases were run with different turbulence

intensities and length scales, corresponding to the conditions measured in two specific flume experiments, for the purposes of model validation.

Additionally, the turbine was simulated at a range of seven tip-speed ratios in a low-turbulence regime, in order to assess the impact of turbine operating condition (i.e. where it is operating on the C_P, C_T and C_θ curves) on the wakes. The tip-speed ratio corresponding to maximum C_P was recreated experimentally in a flume, for the purposes of validation.

This battery of numerical simulations allowed an assessment to be made of the dependence of turbine wakes on tip-speed ratio, on turbulence intensity and on turbulence length scale. Numerical simulations allow turbulence intensity and length scale to be varied independently of each other, but this is not possible in flume experiments. Due to the difficulty of reproducing exact turbulence conditions in the flume, a more limited number of experimental cases was used for validation. The turbulence conditions chosen for the experiments were designed to cover as wide a range of turbulence intensities and length scales as possible, and three different tip-speed ratios were also tested in order to try and validate the dependence of the wakes on the turbine operating condition. This should provide confidence in the numerical method over a range of turbulence and turbine operating conditions, allowing conclusions to be drawn from simulations which were not directly reproduced in the flume.

5.1 ANSYS Fluent

The work contained within this thesis was conducted using the commercial CFD code ANSYS Fluent. Fluent uses a finite volume method for solving the continuity and momentum equations for fluid flow. Fluent 15.0 was used for the initial setup and mesh independence study on a Hewlett Packard Z840 workstation, with flume-scale simulations being carried out using Fluent 18.0 on Cardiff University's HPC facilities.

5.2 Simulating turbine rotation

ANSYS Fluent gives two methods for simulating rotational movement of a body within the fluid, a Moving Reference Frame (MRF) and a sliding mesh scheme. The MRF scheme allows the construction of a subdomain around the moving body (in this case, the turbine blades and hub), within which a rotational component is added to the Navier Stokes equations of the flow in this subdomain, commensurate with the radial position of the point with respect to the axis of rotation. As the turbine itself is not rotating, there is no requirement for relative

motion of two mesh regions, meaning that the mesh of the main and subdomains can conform to each other, reducing numerical dissipation. The addition of the rotational component to the flow within the MRF produces relative flow over the turbine blades which is equivalent to that which would be produced from a moving turbine in a non-rotating flow, and as such, this model is computationally efficient for problems where the only interest is in the turbine performance data (for example, that used by Mason-Jones[8]). The downstream flow from an MRF scheme is however not the same as that produced by a moving turbine in a non-rotational flow. Since all of the flow within the MRF (which is necessarily larger than the turbine itself) is given a rotational component, even areas outside the region of direct influence by the turbine will be caused to rotate. The implications of this can be understood by imagining the scenario with a empty MRF (i.e. no turbine present). In this case, the fluid in the MRF acquires a rotational component without any structure being present to impart this. The MRF itself will produce a swirling wake, even when there is no turbine present. An additional complication comes if a realistic turbine is being modelled, where the presence of a nacelle and stanchion introduce rotational asymmetry into the model. In this situation, a 'frozen' turbine will have a fixed spatial relationship between the blades and the stanchion. This could mean modelling a situation where a blade constantly diverts the flow onto or around the stanchion for the whole length of the simulation, a situation which in reality is only a transient phenomenon. This can, to some extent, be alleviated by averaging the turbine performance over multiple simulations with the turbine rotated slightly between each run, however this still does not provide physically accurate results for the wake region[78].

The other scheme for simulating the rotation of a turbine within ANSYS Fluent is the sliding mesh scheme (as used, for example, by Morris[107]). This involves the creation of two separate domains, with two independent meshes. For the turbine, a cylindrical domain is created within the main domain, encompassing the rotating parts of the turbine. This cylinder is then physically rotated with each timestep, in accordance with the pre-determined rotational velocity. The mesh of the rotating domain and the main domain are not necessarily conformal, and the two meshes slide past each other at the mesh boundaries. In this scheme, no rotational component is added to the Navier-Stokes equations as fluid enters the rotating domain, the flow is transposed onto the correct cell within the rotating domain. At the next timestep, the mesh is rotated, but the flow data is transposed onto the cell which now appears at this point in space. In this way, the flow is given a rotational component due to its interaction with the turbine blades, not by virtue of the fact that it enters the rotating mesh zone. This scheme also allows for flow interactions between the turbine

blades and stanchion, and allows these cyclic interactions and the resultant wake to be evaluated. The disadvantage of the sliding mesh scheme is that it is more numerically dissipative than the MRF scheme, as the mesh boundaries are non-conformal (meaning that the position of the nodes on the boundary of one domain to not conform to the position of the nodes on the boundary of the neighbouring domain), however, given its ability to more accurately produce a wake, and to allow temporal effects such as blade/stanchion interactions to be modelled, the sliding mesh scheme has been chosen for this work.

5.3   Simulating transient flow effects

All numerical simulations presented here were based on a transient formulation. Following initialisation, an unsteady RANS run was made using a k-ω SST turbulence model, and run for the time taken for a particle to pass completely through the domain, defined as a Non-dimensional Time Unit (NTU)[83]. This was used to initialise the flow-field before switching to a DES turbulence model, as recommended by ANSYS[125]. Following the switch to the DES turbulence model, the simulation was run for at least one more NTU, in order for the flow-field to reach a statistically steady state before sampling for time averaging was begun.

Time step sizes were chosen in order that the CFL number in the wake region was less than one, i.e.:

$$\text{CFL} = \frac{\overline{U}\Delta t}{\Delta x} < 1 \qquad (5.1)$$

Where $\overline{U}$ is the local average velocity, Δt is timestep size and Δx is the local grid size. ANSYS note that this is not an absolute limit, and this criterion should be applied in the main scale-resolved region and that it is expected that this limit will be exceeded in other areas[125].

Whilst temporal accuracy in the wake region is as required by ANSYS, a 4.5° change in rotor position between timesteps results in a change of tip position of approximately one chord length. This means that, at that the blade tips, the CFL criteria is not upheld. This could potentially impact on both the accuracy and stability of the models. Stability was not found to be a problem, but inaccuracies in flow modelling at the blade tips could lead to inaccuracies in the prediction of turbine performance as well as affecting how tip vortices are replicated. Nonetheless, as these tip vortices propagate downstream, their velocity is characterised by that of the free-stream, rather than the speed of the blade tips, meaning that the CFL criteria is once more upheld. In addition, inaccuracies due to temporal discretisation will decrease as we move from the

tip to the hub, and at 70% chord (where the largest pressure drop is). Analysis of the impact of time-step size in a manner analogous to that for mesh independence would be of value, however, given the time constraints and the fact that the focus of this study was the mid to far wake, this was not carried out. A reduction in time step size would be most beneficial for improving the near-wake accuracy, in the proximity of the blade tips.

The 10 m diameter turbine was run with timestep size of 0.05 s, which gave a typical angular resolution of 6.5° per timestep. This is the same timestep size previously used successfully when studying this turbine with the k-ω SST turbulence model, which is the basis for the DES model used here[8],[107].

In order to maintain a similar CFL number to that used in the 10 m diameter model, the flume model used a timestep size of 0.005 s, which gave a typical angular resolution of 4.5° per timestep. Time averaging in these models was carried out over 10 000 timesteps following the initial k-ω SST and DES runs, allowing time-averaging to take place over 50 s of flow-time. This gave good convergence for mean velocities, and adequate convergence for 1D turbulence intensities measured in the wake region. The sample rate of 200 Hz was approximately the same as that obtained in the flume measurements, allowing direct comparison of the two for the purposes of validation (see section 6.3).

Fifty iterations were used per timestep, typically requiring 250 s on 32 cores on the HPC facility. Convergence monitoring was carried out with x-, y- and z-velocity residuals typically achieving convergence to 10^{-7} (10^{-6} in the case of z-velocity), and 10^{-6} in the case of k and ω. Convergence of the continuity residual was typically 2×10^{-3}, thought to be due to the highly turbulent nature of the flow and the non-conformal mesh boundary between the rotating domain and static reference domain. These are broadly in line with that recommended by ANSYS[125]. In addition to the monitoring of residuals, one point monitoring velocity upstream, and four points monitoring velocity downstream were output at each iteration. All of these were shown to have stabilised within the 50 iterations used, even within the most turbulent regions of the wake.

5.4   CFD geometry: flume model

The turbine geometry used for flume-scale numerical modelling is 3-bladed, 0.5 m diameter design. The blade geometry is based on a Wortmann FX 63-137 profile, with a twist of approximately 30° from root to tip. The blade geometry is the same as that used in [8], [107] and [29]. The turbine nacelle has a total length of 763 mm, with a maximum diameter of 160 mm. A hydraulic hose from the downstream face of the nacelle housed the cabling for motor power and instrumentation. This was also reproduced in the CFD model. The nacelle was

suspended from approximately its centre by a 71 mm diameter stanchion which protruded out of the water. A visual comparison between the CFD geometry and the physical model in the flume can be seen in Figure 5.1.

(a) The turbine modelled in this work.

(b) The physical turbine model in the flume.
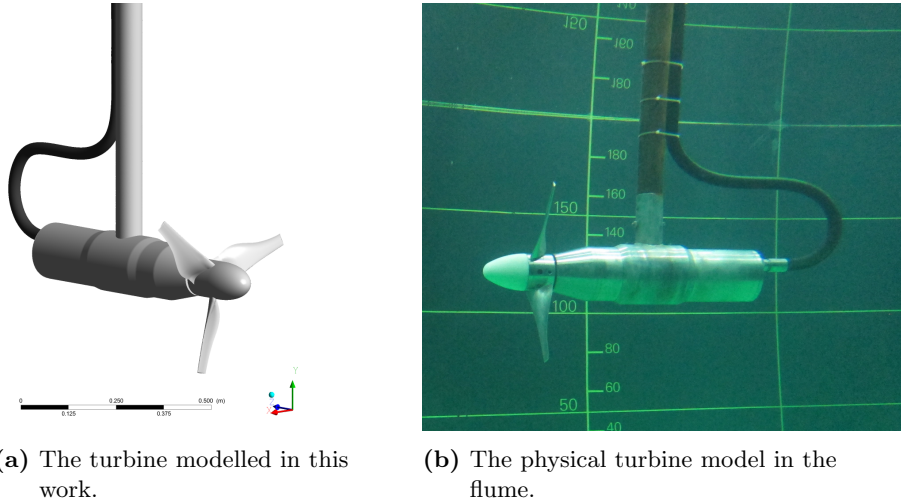
Figure 5.1: A comparison of the CFD (left) and physical models (right) of the turbine.

The turbine was suspended in the centre of the cross-sectional area of a flume, with a width of 4 m and depth of 2 m, giving a blockage ratio by turbine swept area of approximately 2.5%. The CFD domain extended 1.5 m upstream of the rotor, and 7.5 m downstream, representing a modelled domain of from $z/D = -3$ to $z/D = 15$. The upstream domain boundary was set as a constant velocity inlet with specified turbulent conditions, including the addition of synthetic turbulent perturbations (discussed further in section 5.5). The downstream domain boundary was a constant pressure boundary with a gauge pressure of 0 Pa. A zero-shear condition was applied to the upper domain boundary rather than representing a free surface, in common with other low-blockage numerical simulations. All other boundaries (both flume walls and turbine) were treated as stationary no-slip walls, using the default roughness coefficient of 0.5.

In order to provide more control over the mesh, the CFD domain was divided into different regions. Directly surrounding the turbine rotor itself was a cylindrical, rotating sub-domain, with a mesh which was non-conformal with respect to the reference domain. This was used to achieve the mesh movement required in order to simulate rotation. The turbine nacelle, hose and stanchion were meshed in a single, unstructured region in order to ease mesh creation in this region of complex geometry. A further, cylindrical, region was created which joined this and extended to the domain outlet. This region, coaxial with the turbine and with a diameter of 0.75 m, allowed a swept, structured mesh to

92
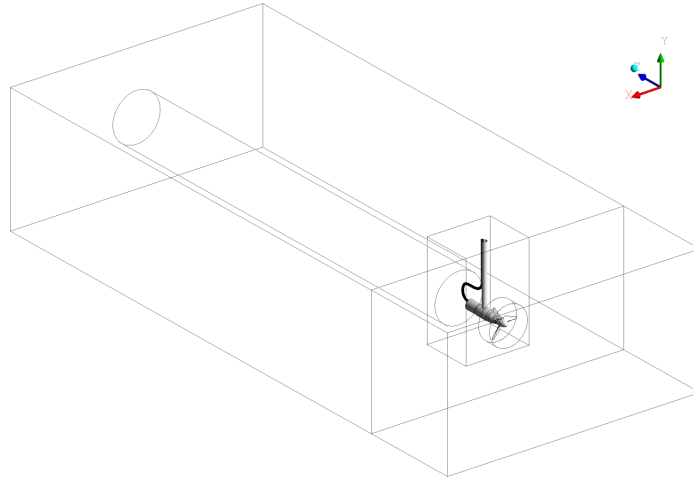
Figure 5.2: Diagram of the flume-scale CFD domain showing the different regions into which it was subdivided for the purposes of mesh refinement.

be created which could be refined in the wake region. A representation of the different mesh regions can be seen in Figure 5.2.

5.5 Inlet boundary conditions

Fluent provides the user with limited control over the turbulence at the upstream domain boundary. Inlet turbulence was specified via turbulence intensity and a length scale, described by ANSYS as representing the length scale of the turbulence features containing the most energy; similar to the definition of the integral length scale[59]. For LES or DES simulations, the user is able to select the production of turbulent perturbations at the inlet, and for this, a vortex method was used which is based on a Biot-Savart rule[122]. The user must specify the number of seed-vortices at the boundary face, and for these simulations 1 000 vortices was selected, in keeping with the ANSYS recommendation of this value being approximately $^1/_4$ of the number of cell faces at the inlet[122].[1]

Inlet boundary conditions for scale-resolving simulations are an area of active research. As ANSYS Fluent is commercial CFD software, the user does not

---

[1]When migrating the model to the HPC facilities in Cardiff, it was found that there was a slight discrepancy between the wakes predicted using Fluent 15.0 and Fluent 18.0. Further investigation showed that this was due to differences in the inlet turbulence. Communication with ANSYS revealed that the definition of turbulence length scale had been changed by a factor of $C_\mu{}^{3/4} = 0.164$, and therefore length scales set in Fluent 15.0 needed to be multiplied by $^1/_{0.164}$ in order to produce the same results in Fluent 18.0. Using this factor to adjust the inlet length scales brought the results back into agreement with each other.

have complete control over the way turbulence is created at the inlet. Research in this area has been carried out to compare different methods for producing turbulence[135], or methods for producing grid generated turbulence for LES simulations[136]. Others have simulated turbulence by running precursor simulations in order to allow the build up of turbulent features in a channel, which were then applied to an array of turbines[91].

Given the limited ability of a user of Fluent to alter the process by which turbulence is produced at the inlet, it was decided that the best way to confirm the turbulence in the flow upstream of the turbine was to conduct identical 1D analysis to that which was carried out on the flume measurements to determine turbulence intensity (equation 3.3) and integral length scale (the integral time scale from equation 3.5, multiplied by the mean velocity). For the purposes of model validation, this gives the best idea of how comparable the inlet conditions are. Other synthetic turbulence generation methods or precursor simulations may be preferable in order to more closely match the spectrum of turbulent fluctuations in 3 dimensions, however, due to the complexity of implementation or prohibitive additional computational expense, these were not used in this study.

5.6 Solver settings

In addition to the above geometry and boundary conditions, the following solver settings were used:

General solver settings The 3D, double precision, pressure based transient solver was used with an absolute velocity formulation.

Viscous Model The Detached Eddy Simulation viscous model was used, with the k-ω SST underlying RANS model. Instead of a specific shielding function, the "Delayed Detached Eddy Simulation" (DDES) option was used to ensure the boundary layers were treated with the RANS model, and that the transition to 'LES mode' did not occur too soon[125].

Materials Liquid water from the Fluent database was used for the fluid, with a density of $998.2 \, \mathrm{kg \, m^{-3}}$ and constant dynamic viscosity of $0.001003 \, \mathrm{kg/ms}$.

Cell Zone Conditions The motion of the cell zone containing the turbine rotor was defined by a rotational velocity (in $\mathrm{rad \, s^{-1}}$), about the z axis, with a rotation-axis origin of (0,0,0)

Solution Methods The SIMPLEC pressure-velocity coupling scheme was used, as suggested by ANSYS[125] for use with the DES turbulence model. As

required by Fluent, the transient formulation is Bounded Second Order Implicit.

Monitors Monitors of area-weighted averaged instantaneous z-velocity were used with one point upstream, and four points downstream of the turbine. These were printed to the output file/command line at each iteration for monitoring solution convergence. In addition, a further 175 area-weighted average instantaneous z-velocity were defined, and output to monitor files at the end of each timestep for detailed analysis of the 1-dimensional turbulence characteristics such as integral length scale and turbulence intensity. As these monitor points closely resemble the data recorded in the physical flume, this allowed direct comparison of results for the purposes of validation.

Solution Initialization 'Hybrid Initialization' was used for the initialisation of the original transient k-ω SST model. This was then used as the starting point for the DES based simulation.

Calculation Activities A complete case and data file was saved every 50 timesteps for the purposes of providing a point from which a re-start could be made in the event of a hardware or software crash, as well as for saving all flow data to allow analysis of the development of flow properties over time. A combined case and data file pair comprise approximately 10 GB of data, and thus saving a case and data file after every timestep was prohibitive.

All other, unnamed settings were kept in their default configurations.

5.7 User Defined Functions

ANSYS Fluent allows the user to enhance its capability by writing their own functions which can be dynamically loaded. These User Defined Functions (UDFs) can take a variety of forms, and can be implemented in order to adapt the mathematical model of the flow physics, change boundary conditions or to enhance post-processing capabilities[137]. For each timestep, a case and data file represent approximately 10 GB of hard-drive space, so for simulations which may require 10 000 timesteps, the total memory requirement would be approximately 100 TB per run. The work contained within this thesis would therefore have memory requirements of the order of 1 PB. In order to keep the memory requirements within a manageable limit, the maximum rate at which the complete flow information (case and data file) was saved was every 50th timestep. However, in order to retain a complete picture of the fluctuations in turbine

performance and loading, a UDF was written to calculate the torque and forces in all three axes at the end of each timestep. These were calculated both for the turbine itself (blades and hub), as well as for a single blade to allow later calculation of in-plane bending, out-of-plane bending and pitching moments on the blade. This was written to a text file at each time step, for later analysis, with the most important of these data also printed to the screen.

The UDF (shown in appendix A) was based on one used by Mason-Jones[8], but with significant adaptations for use with the particular turbine geometry and computational setup used within this work. The UDF of Mason-Jones was designed for a steady state model using an MRF. This meant that the UDF was designed to be run in "on demand" mode, i.e. run when the user calls the function. The CFD model used in this work was a transient model as is required for use with the DES turbulence model, and turbine rotation is implemented using a sliding mesh scheme. The UDF had to therefore accept manual inputs of rotational speed, and to execute at the end of every timestep, writing the most important data to a text file, rather than only when called by the user.

In addition, the way in which the torque around each of the Cartesian axes was calculated in order to correctly observe the sign convention. This is required if a resultant bending moment and direction is to be calculated at a later point.

The previous version of the UDF was designed to be loaded into ANSYS Fluent running on a single processor. Due to the computational expense of the DES turbulence model, all of the runs in this work have used parallel computing to speed up the process. This required the UDF to be re-written to take into account the computational structure of parallel computing with ANSYS Fluent.

When running in parallel mode, Fluent automatically divided up the mesh into sections, which are evaluated separately and in parallel on different 'compute nodes', given numbers from 0 to n. In addition to this, another processor is used as the 'host', which is used to communicate commands from Fluent Cortex to compute node-0, which in turn passes the instructions on to the other compute nodes. The results of computations carried out on the compute nodes are in turn passed back to the host via compute node-0[137]. As the mesh is divided up automatically between the compute nodes, an individual node could be tasked with processing some, all, or none of the cells and faces relevant to the turbine blades. These calculations must be synchronised and global sums found before printing the results to the screen, or writing the results to a file. In addition to this, tasks such as printing to screen or writing files should only be undertaken once for each timestep, rather than once for each node. To implement this, and to create a UDF which can be used for both serial and parallel calculations, compiler directives were used. These direct the compiler to compile different parts of the UDF for use specifically on compute nodes, the host

node, or when computing in serial mode.

To ensure that output commands are only executed once per timestep, these tasks have been delegated to the host. However, as no mesh data is available to the host, global sums must first be calculated using the `PRF_GRSUM1()` command, which stores this global sum on all compute nodes (including node-0). These sums are then passed to the host using the `node_to_host_real_n()` command. Synchronisation between the different compute nodes is ensured using the `PRF_GSYNC()` command.

Finally, the output of the UDF has been adapted such that the output is not only printed to the screen, but also written to a text file located in the working directory. The variables timestep, flow time, turbine x-moment, turbine y-moment, turbine z-moment and turbine thrust, as well as the moments about the x, y and z axes for blade 1 are written in tab de-limited format to a new line at each timestep, for ease of post-processing.

5.8 Mesh independence study

In keeping with CFD good practise a mesh independence study was carried out. CFD simulations tend to improve in accuracy as mesh densities increase, particularly in areas of complex flow. However, the time required to achieve a flow solution also increases with increasing mesh density. The aim of a mesh independence study is to examine to what extent the flow simulation results are dependent on the mesh – in essence, to carry out a cost-benefit analysis on the mesh, and to show that the results achieved are not unduly affected by the quality of the mesh used.

In general, if an identical case (geometry, boundary and initial conditions) is run with an increasingly hi-fidelity mesh, then the solution obtained will become more and more accurate, with an associated increase in the computational requirements. This increase in accuracy is in general non-linear, leading to diminishing returns in terms of increases in accuracy for increased computational costs. The user must decide at what point the mesh density is high enough that inaccuracies in the results when compared to experimental data are due to the underlying mathematics of the model, rather than the mesh, whilst minimising computational costs as far as possible.

5.8.1 CFD geometry: ocean scale model

Early modelling and the mesh independence study were carried out using an ocean-scale model of the turbine. Appropriate mesh densities were identified from this, and then applied to the flume-scale model. The geometry of the

flume model can be found in section 5.4.

The ocean-scale model was based on that used in previous work in CMERG [8], [107], [29], which informed the selection of the geometry. A domain was created, representing an idealised region of sea floor containing a single turbine of 10 m rotor diameter, including a nacelle and monopile structure connecting the turbine to the seabed. The domain had dimensions of 90 m $\times$ 45 m $\times$ 280 m in the cross-stream, vertical and streamwise directions. The centre of the turbine rotor was located in the centre of the domain width, 30 m from the upstrem inlet, and 11 m from the sea floor. Because of the focus of this work is on turbine wakes, much effort was put into optimising the mesh in order to provide the most accurate results for the wake. To this end, the mesh was divided into 4 separate regions in order to improve mesh control and allow different areas to be refined independently of each other. The rotor was meshed within a cylindrical subdomain 12 m in diameter (as used previously [8], [107], [29]) in order to implement a sliding mesh scheme to simulate turbine rotation. Downstream of this, the turbine nacelle and stanchion were meshed in a single region to allow refinement in the near-wake. Downstream of this a 15 m diameter cylindrical domain was created coaxial to the turbine which stretched to the domain outlet. This cylinder allowed a structured swept mesh to be used for more efficient flow calculations, as well as allowing more control over mesh refinement within this domain. Outside of this subdomain, the rest of the fluid was meshed using an unstructured mesh. The conformal boundary between the structured mesh of the cylindrical subdomain and the unstructured mesh of the rest of the fluid domain leads to a higher mesh density along this boundary, causing an increase in mesh density in the critical region of the wake shear layer. The subdomains can be seen in Figure 5.3.

The sea-bed and turbine surfaces in the ocean model had no-slip conditions imposed upon them; external domain walls and upper face were given a zero-shear condition. For the purposes of the mesh independence study, the inlet velocity was set to a constant velocity of 3.086 m s^{-1} (equivalent to 6 kt), turbulence intensity of 3%, length scale of 5 m using the vortex method of introducing turbulent perturbations with 1 000 seed vortices. The domain outlet was a constant pressure outlet with a gauge pressure of 0 Pa. The turbine rotational velocity was 2.25 rad s^{-1}, corresponding to a tip-speed ratio of $\lambda = 3.65$, which has previously been shown to correspond to the point of maximum C_P for this turbine[8], [107].

The simulation was run for 1 000 timesteps with a timestep size of 0.1 s using a k-ω SST turbulence model, to initialise the DES simulations. At this point, the turbulence model was changed to the DES turbulence model, and the simulation run for a further 4 000 timesteps of 0.05 s, representing a flow time
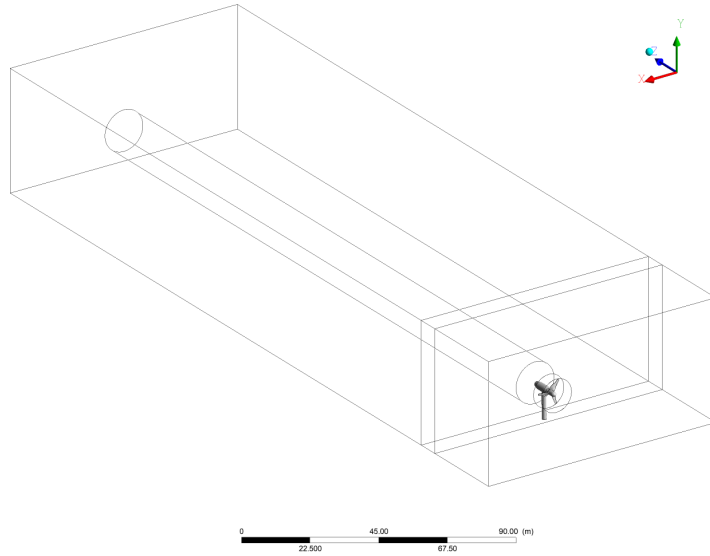
Figure 5.3: Diagram of the ocean-scale CFD domain showing the different regions into which it was subdivided for the purposes of mesh refinement.

of 200 s. Time averaging was conducted over the last 1 000 timesteps, in order that any transient effects may have passed out of the domain.

All other model setup parameters were identical to the flume-scale CFD model described in Section 5.6.

5.8.2 Rotor region

The turbine geometry used in this study has been the subject of many previous numerical and experimental studies within CMERG[107][8]. The mesh used in the sliding mesh region of the rotor was based on the mesh sizings used and shown to be independent for a k-ω SST turbulence model[8]. These findings were further confirmed by flume tank tests. As the DES turbulence model applies a k-ω SST turbulence model in the region around the turbine, it was appropriate to apply this mesh in this case as well.

5.8.3 Near-turbine region

For the region around the turbine nacelle, an unstructured mesh was created, in order to fit this complicated geometry. This region of the mesh was directly downstream of the rotating sliding mesh of the turbine, and so it was expected that this would have an influence on the near-wake of the turbine. In order to determine what impact this region has, four different mesh densities were

created. The downstream extent of the domain was truncated at $z/D = 15$, as it was anticipated that all effects on the wake would have presented themselves by this point, and reducing the domain length from $z/D = 25$ reduced the required computational time. A summary of the meshes used for the near-turbine region, and the associated computational time required can be seen in Table 5.1.

Table 5.1: Mesh sizes for near-turbine region. The time per timestep quoted allows relative comparisons to be made of the computational requirements for different mesh sizes.

	Elements (near-wake region)	Time per timestep /s	Relative time
Coarse	1.24×10^6	≈ 678	t
Medium-coarse	2.06×10^6	≈ 720	$1.06t$
Medium-fine	4.55×10^6	≈ 864	$1.27t$
Fine	9.48×10^6	≈ 1125	$1.66t$

The main area of interest for this work is the wake, and therefore the wake recovery will be used as the main indicator of mesh independence. Due to practical constraints, this is often measured in flume or tow-tank experiments at points axially downstream of the turbine. However, as CFD provides results for the whole flow-field, it is also informative to examine a volumetric averaged flow across the swept area of the turbine (as discussed in Chapter 4), providing a measure of the amount of energy available to a downstream turbine. This analysis was carried out on the mean axial velocity field at the end of the run where time sampling for averaging was carried out. The results for normalised mean centreline velocity for the different meshes are shown in Figure 5.4, and the results for the velocity averaged over the swept area of the turbine are shown in Figure 5.5. These results indicate that mesh refinement in this area has very little impact on either the centreline or swept area averaged velocities, despite a nearly 10-fold increase in the number of cells in this region.

In order to gain more insight into how the model is functioning in this region, further analysis was conducted on the value of $1/F_{DES}$. Plotting the value of $1/F_{DES}$ gives an insight into whether the DES turbulence model is operating in 'RANS mode' or 'LES mode'. Equations 3.17 and 3.18 show how the model uses F_{DES} to alter the turbulence kinetic energy dissipation term, Y_k, and therefore to switch from RANS-like behaviour to LES-like behaviour. Where the model is operating in 'RANS mode', $F_{DES} = 1 = 1/F_{DES}$. Where the model is modifying Y_k in order to replicate LES-like behaviour, $F_{DES} > 1$, and therefore $1/F_{DES} < 1$. A plot of $1/F_{DES}$ therefore highlights the regions in which RANS and LES like behaviour is being reproduced; where $1/F_{DES} = 1$, the model
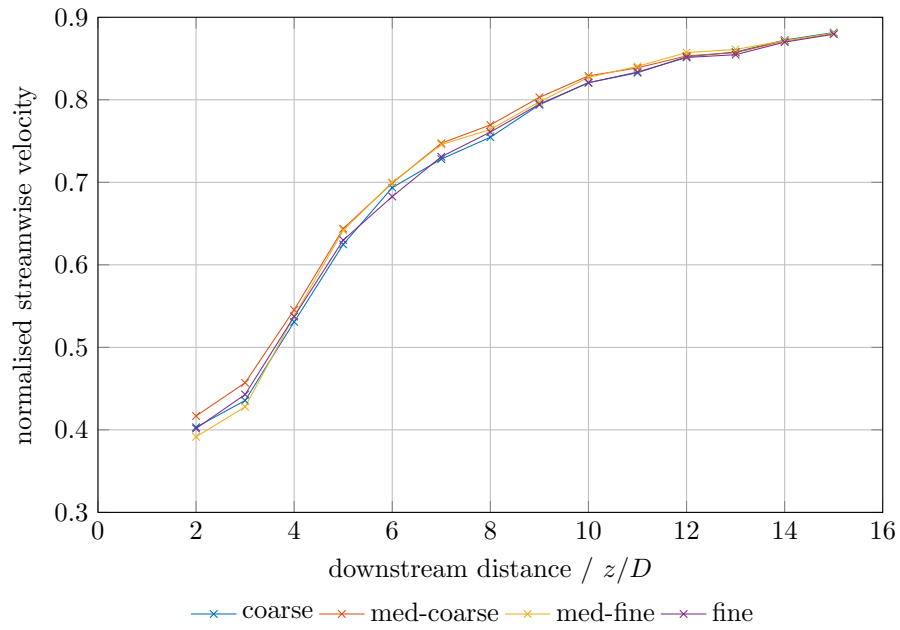
Figure 5.4: Normalised centreline velocities for near-turbine region mesh independence study
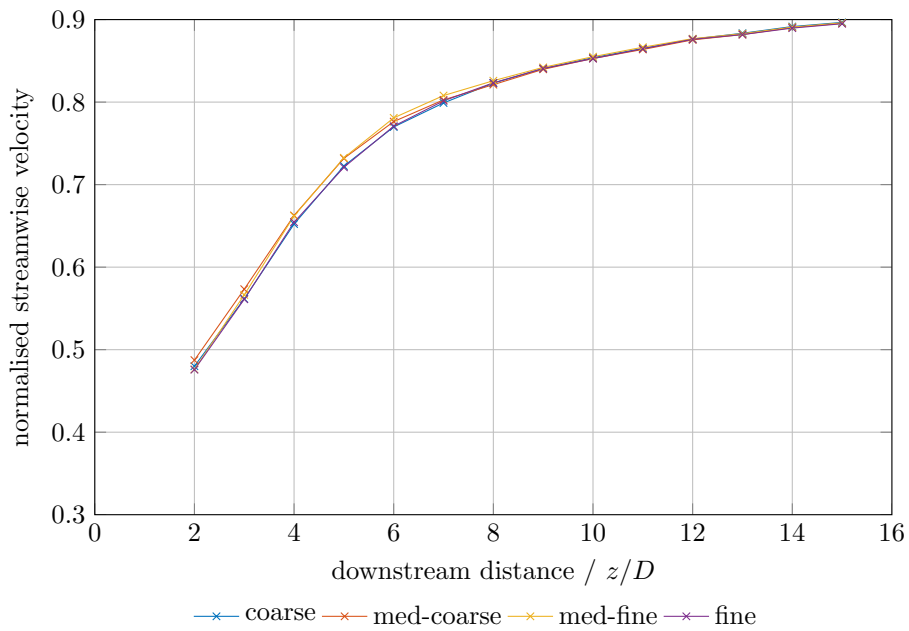
Figure 5.5: Normalised streamwise velocities, averaged over turbine swept area for near-turbine region mesh independence study
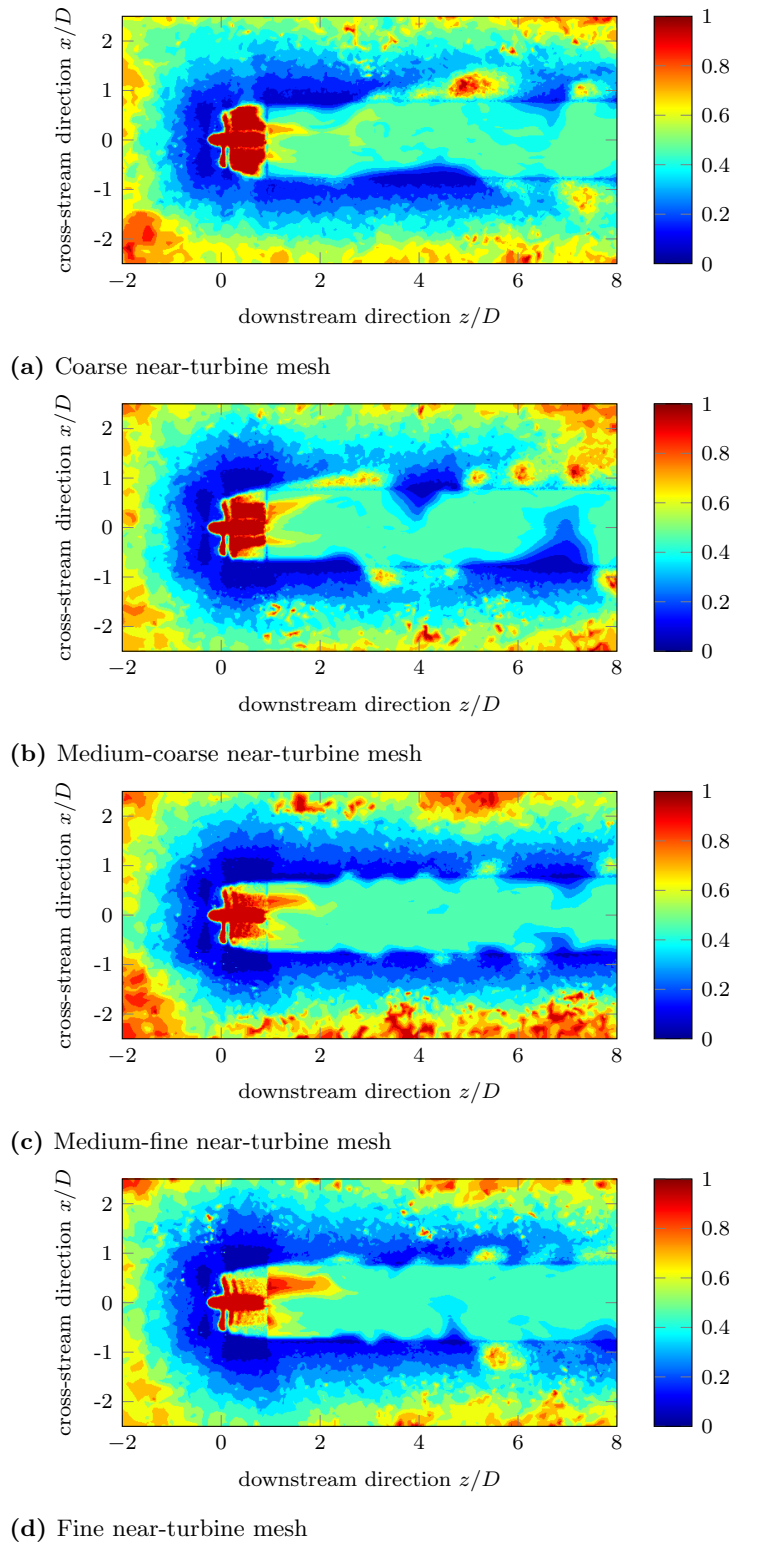
is running in unmodified 'RANS mode', and where $1/F_{DES} \neq 1$, the model is running in 'LES mode'.

Plots of $1/F_{DES}$ on a horizontal plane through the turbine axis can be seen in Figure 5.6. These plots are produced using the value of F_{DES} at the final timestep in each run; they are therefore not time-averaged values, and some of the differences are therefore due to individual turbulent features at that moment. Due to the way MATLAB interpolates the values, the turbine is shown in red (i.e. $1/F_{DES} = 1$); this simply indicates that the boundary layer around the turbine itself is operating in 'RANS mode', as expected. Examination of Figures 5.6a to 5.6d indicates that turbulence in the region downstream of the turbine blades, but inboard of the blade tips has a small length scale, as the turbulence model runs in RANS mode in this region in all but the finest mesh. However, as Figures 5.4 and 5.5 show, this has a negligible effect on the overall length of the wake, suggesting that the mixing processes in the wake region are not heavily affected by whether this small-scale turbulence is resolved or not. Given the increase in the computational time required as the cell count increases in this area, the 'medium-coarse' mesh was selected for further modelling. It is possible that the finer mesh could provide greater accuracy and detail of the turbulence in the very near wake (within $z/D = 2$ of the turbine rotor), but as this is not the focus of this study, the additional computational expense was deemed unjustifiable.

5.8.4   Wake region

The region of swept, structured mesh in the area of the wake region, was re-meshed to three different mesh densities, in order to examine the impact of this on wake recovery and wake width. Due to the large common surface between the cylindrical wake region and the surrounding region, an increase in the density of cells in the cylindrical wake region also leads to a significant increase in the cells in the adjoining region, and therefore both the number of elements created in the cylindrical wake region, as well as the corresponding total number of elements are quoted in Table 5.2. It can be seen that the mesh density in the region under investigation approximately doubles between the coarse and fine meshes.

As with the near-turbine region, wake recovery has been used as the main criteria in assessing the effect that mesh density has on the flow solution. Figure 5.7 gives the results for the normalised centreline axial velocity, and Figure 5.8 gives the same information over the swept area of the turbine. In contrast to the results for the near-turbine region, the mesh density in the wake region appears to have an impact on the calculated flow, with the coarse mesh showing sig-

(a) Coarse near-turbine mesh

(b) Medium-coarse near-turbine mesh

(c) Medium-fine near-turbine mesh


(d) Fine near-turbine mesh

Figure 5.6: Comparison of $1/F_{DES}$ for different near-turbine meshes

nificantly faster wake recovery than then others (ca. 10% faster than the 'fine' mesh at a downstream distance of $z/D = 10$). The 'medium' and 'fine' meshes show much better agreement with each other, with typical differences of 2—3% in wake recovery. This behaviour is typical of a mesh dependence study, where, after a certain degree of refinement, further mesh refinement has little effect on the flow solution achieved, and serves only to increase the computational cost.

As the difference in calculated results between the 'medium' and 'fine' meshes is small, but the refinement represents an increase in computational time of approximately 1/3, the 'medium' mesh was chosen for further work within this study.

Table 5.2: Mesh sizes for cylindrical wake region. The time per timestep quoted allows relative comparisons to be made of the computational requirements for different mesh sizes.

	Elements (wake region)	Elements (total)	Time per timestep /s	Relative time
Coarse	2.24×10^6	8.90×10^6	≈ 576	t
Medium	3.85×10^6	12.15×10^6	≈ 772	$1.34t$
Fine	4.80×10^6	13.47×10^6	≈ 1035	$1.79t$
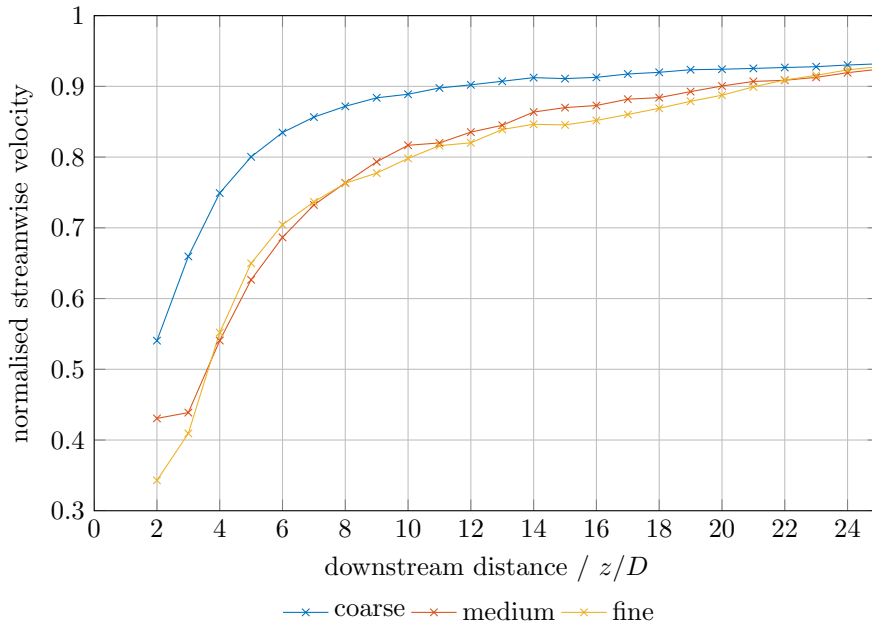
Figure 5.7: Normalised centreline velocities for wake cylinder region mesh independence study

5.8.5 Flume Walls

For validation purposes, testing was carried out in the recirculating flume at the Institut Français de Recherche pour l'Exploitation de la Mer (IFREMER) in Boulogne-sur-Mer (see Chapter 6 for full description). In order to assess the ability of the DES model to reproduce the wake measured in the flume, the CFD model was adapted to model the precise geometry of the turbine as well as the working section of the flume. The precise geometry used is detailed in section 5.4. The model was produced by scaling the mesh used for the 10 m diameter turbine models. Due to the change in turbine blade Re, there is an improvement in the value of y^+ on the blade, with the vast majority of the blade giving $30 \leq y^+ \leq 50$ (well within recommended limits[125]). This indicates that the laminar and sub-laminar regions will not be resolved using this grid, as the first cell is approximately in the log-law region[46]. Reynolds numbers based on chord length at 70% blade span ranged from approximately 90 000 for low free stream velocity, low TSR experimental runs, to approximately 210 000 for the higher free stream velocity, high TSR runs. Typical values of Reynolds number were approximately 120 000. This indicates that the hydrofoil is operating approximately in the region where laminar-turbulent transition may be expected to occur (although the exact point of transition is heavily dependent
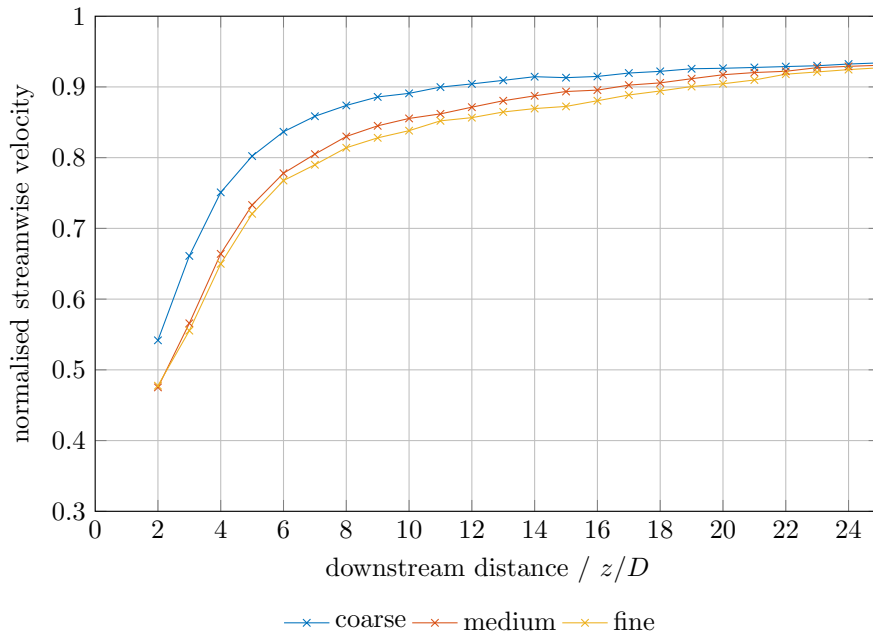
Figure 5.8: Normalised streamwise velocities, averaged over turbine swept area for wake cylinder region mesh independence study

on the precise geometry of the hydrofoil itself). A value of y^+ of 30–50 for the k-ω SST model assumes that the boundary layer has entirely undergone turbulent transition; nonetheless, this does not appear to severely affect the accuracy of the predictions of the turbine performance when compared to experiments under low-turbulence conditions[8], [15], [29], [107]. This previous work shows that the performance of this turbine, when operating under these conditions, is dependent on tip-speed ratio only and is independent of Reynold number. It is thought that this indicates that the point at which the transition from laminar to turbulent behaviour has already occurred for this particular hydrofoil geometry. . In addition, the highly turbulent ambient flow used in these experiments can be expected to provide additional energy to the boundary layer, promoting the attached boundary layer behaviour and lack of separation bubble expected of fully turbulent boundary layers at higher Reynolds numbers. Given these considerations and the fact that this study focusses on turbine wakes, the additional computational expense of further reducing the values of y^+ on the turbine blades was not deemed to be justified.

Another difference between the ocean-scale and flume-scale models is that the flume has walls on which a no-slip boundary condition must be implemented. Whilst the flow behaviour at the flume walls themselves is not of interest to this study, these boundaries must be adequately resolved in order to ensure that they do not have an impact on the wake of the turbine. In order to establish the effect of wall cell resolution on the wake and performance of the turbine in the CFD models, further CFD runs were carried out.

Three different degrees of mesh refinement were investigated, which shall be referred to as 'coarse', 'medium' and 'fine'. The only regions of the mesh which were affected by this refinement were the walls of the flume; the area of rotating mesh around the turbine, the meshing of the nacelle and stanchion, and the meshing of the wake region were unaffected. As a specified shear of zero was used for the top of the domain, a refinement of the mesh at this boundary was not investigated. For this flume model, an inlet velocity of $1.5\,\mathrm{m\,s^{-1}}$, turbulence intensity of 1.75%, and turbulence length scale of 0.5 m were used, Following the setup with a k-ω SST model then switching to the DES turbulence model and running for one NTU to allow the model to settle, time-averaging was carried out for a period of 28 s. The effect of increasing the mesh refinement at the flume walls was then examined via three different metrics; the rate of wake recovery, the width of the wake, and the performance characteristics of the turbine.

**Impact of flume wall resolution on wake recovery**

The most commonly used measurement of a wake is the rate of wake recovery. To this end, the results for mean axial velocity have been compared for three different mesh densities. The result for 28 s of time averaging is presented for both the mean axial velocity along the axis of the turbine (Figure 5.9), as well as for the volumetric average velocity across the entire rotor swept area (Figure 5.10). Both these figures show a slightly faster rate of wake recovery for the finest wall resolution, with the larger discrepancy demonstrated in the results for the velocities taken along the centreline of the turbine. This can be explained by the process of area averaging used to produce Figure 5.10 smoothing out spatial fluctuations. The effect of this is underlined in Figures 5.11 and 5.12, which show the effect of increasing sample time on the mean values reported. These two figures only show the effect of increasing sample time on the mean velocities for the fine mesh, but they are indicative of the effect for all three meshes. Both show that the sampling time of 28 s is sufficient for adequate convergence of the mean velocities in the wake region, although the results for the swept area show slightly faster convergence, as expected, due to the additional spacial averaging which takes place in this case. Given the level of convergence demonstrated in Figures 5.11 and 5.12, the differences between the meshes was deemed to be negligible.
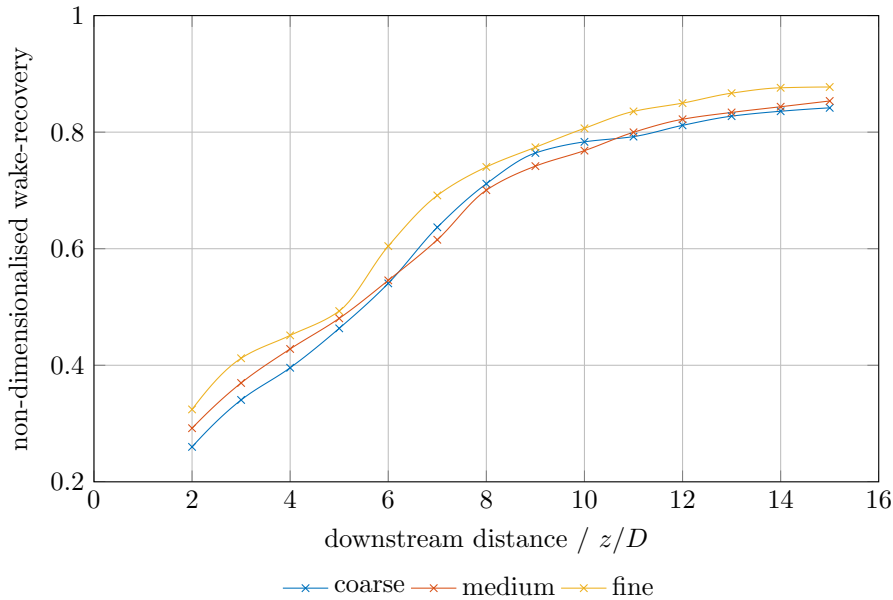
Figure 5.9: Normalised mean axial centreline velocities for three different wall cell resolutions. A smooth interpolation has been used between data points.
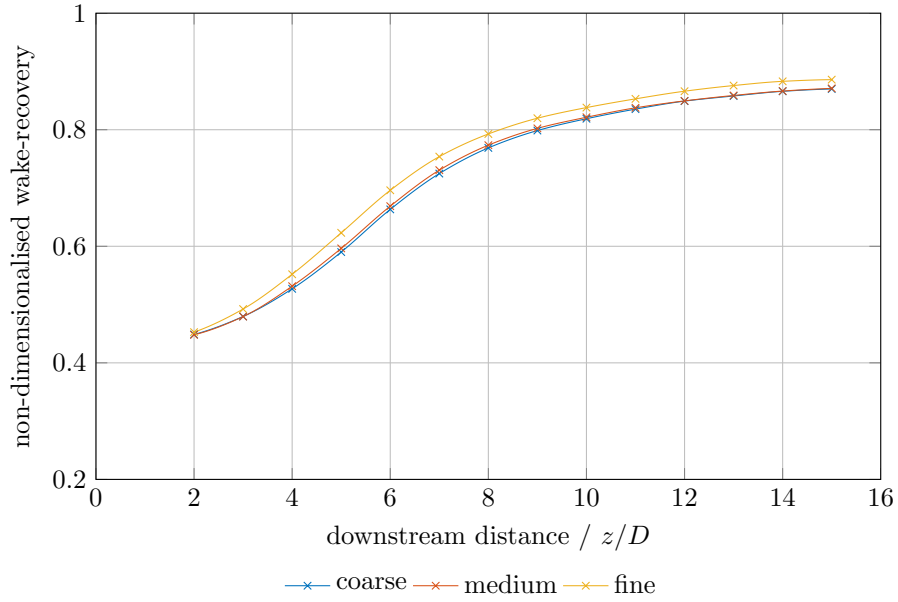
Figure 5.10: Normalised mean axial velocities, averaged over the swept area of the turbine, for three three different wall cell resolutions. A smooth interpolation has been used between data points.
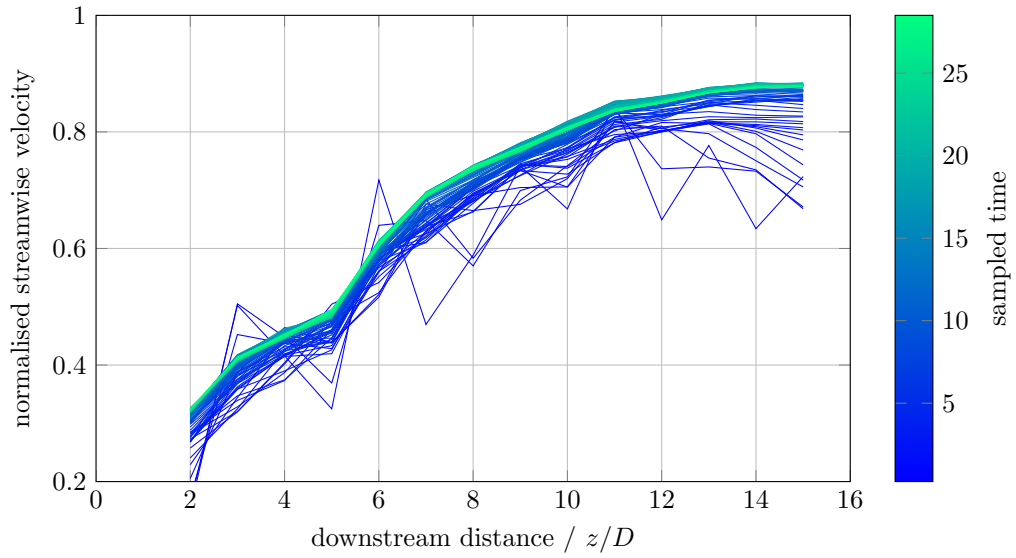
Figure 5.11: Normalised mean axial centreline velocities (fine mesh), showing the effect of increasing sampling time on the mean
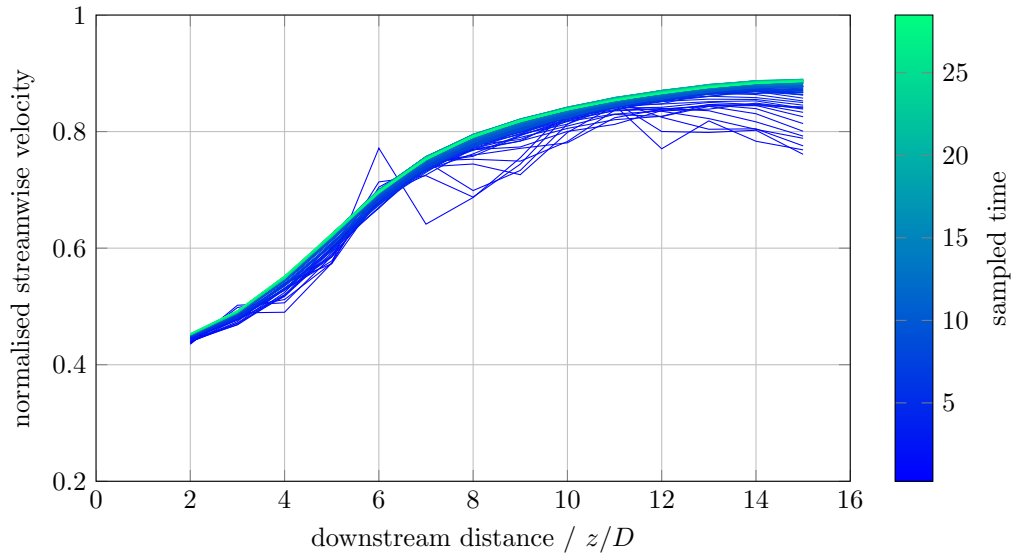
Figure 5.12: Normalised mean axial velocities (fine mesh), averaged over the swept area of the turbine to show the effect of increasing sampling time on the mean

Impact of flume wall resolution on wake width

It could be expected that poor resolution of the flume wall boundary layer could affect the width of the wakes in the downstream region, therefore this was also investigated. Mean axial flow velocities on the two-dimensional horizontal plane containing the turbine axis were analysed to produce comparison metrics for the width of the wake. Figure 5.13 shows wake widths obtained using the three meshes using the fixed-threshold width metric, outlined in Chapter 4, and Figure 4.4. The threshold used was set at 90% of the freestream velocity. This simple wake metric can be expected to show wake width decreasing as downstream distance from turbine increases, due to a decrease in the area of the wake less than 90% recovered. Figure 5.13 shows that the flume wall resolution has a small effect on the width of the wake when calculated using this metric, with the coarse boundary mesh generally resulting in a slightly narrower wake and the fine mesh resulting in a slightly wider wake. All three show very similar trends. To add some context to the differences, the convergence of the wake width using this metric with increasing sample time is shown in Figure 5.14. This shows that whilst this width metric demonstrates adequate convergence within this sample time, the level of convergence is not great enough to render the differences between the coarse, medium and fine mesh densities (Figure 5.13) significant.

The "full-width half-minimum" method for calculating wake widths (de-
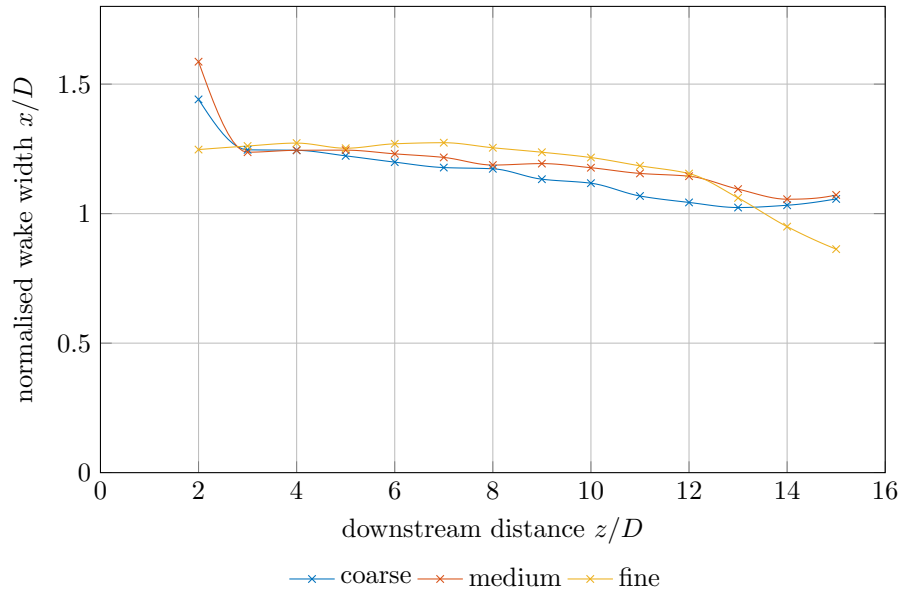
Figure 5.13: Wake width calculations, based on the width of the wake at a threshold value of a normalised streamwise velocity of 0.9, for three different wall cell resolutions. A smooth interpolation has been used between data points.
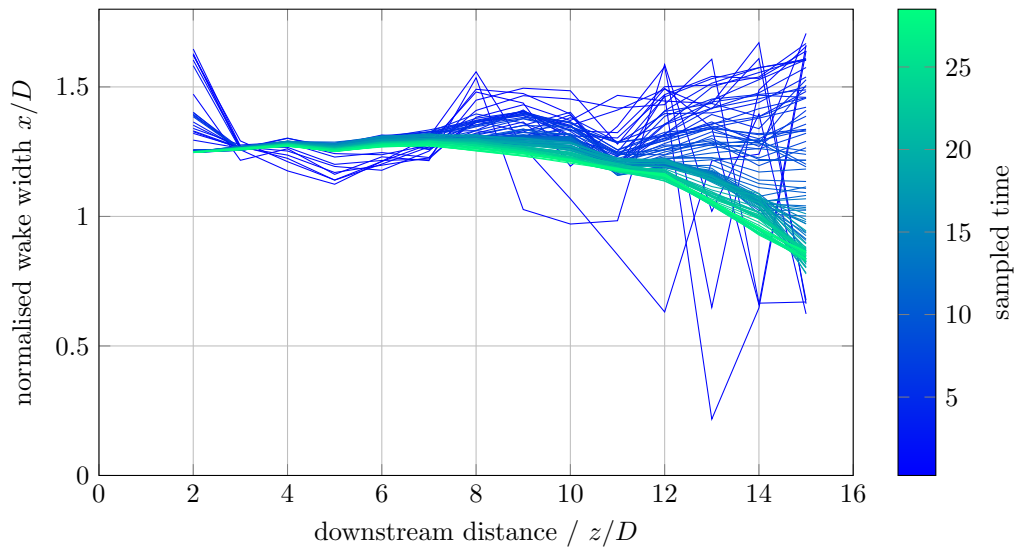
Figure 5.14: Wake width based on normalised velocity of 0.9 (fine mesh) to show the effect of increasing sampling time on the mean

scribed in Chapter 4), was also applied to these three cases. Results for wake width based on the full-width half-minimum approach can be seen in Figure 5.15. This shows an initial narrow wake, probably caused by a high wake deficit in the near wake ($z/D = 2$), which increases, then decreases until ca. $z/D \approx 6$ before steadily increasing. This behaviour is demonstrated regardless of which flume wall mesh density is used, with reasonable agreement between all three meshes. The agreement decreases slightly in the far wake ($z/D \geq 10$), but this can be to some extent explained by the fact that the wake by this point is significantly weaker and less clearly defined. The increase in wake width indicates that the tails of the wake profiles are getting longer, and the peak velocity deficit reducing in magnitude. This means that small differences in peak deficit can have a larger effect on the calculation of the width, and therefore agreement can be expected to reduce in this far wake area. Convergence of the wake width using this method but increasing sample time is shown in Figure 5.16. As with the fixed-threshold method, this in general shows adequate convergence, but the convergence is least good in the area where the wake is becoming weaker and less well defined, which is also where there is least agreement between the curves produced from the three meshes.

A third metric was also used for the comparison of wake widths, this time based on the point at which maximum velocity shear occurs. This attempts
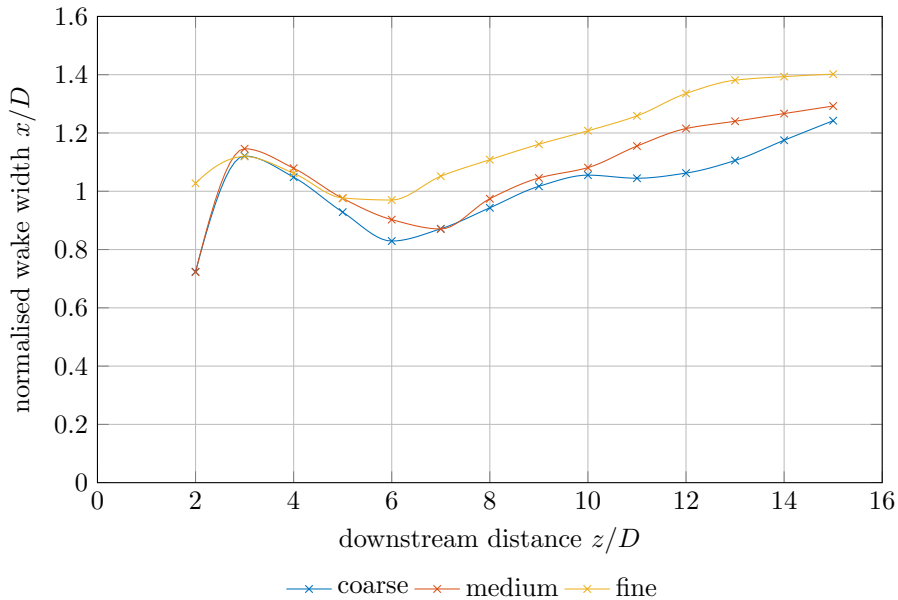
Figure 5.15: Wake width calculations, based on the Full Width at Half Minimum, for three different wall cell resolutions. A smooth interpolation has been used between data points.

to define a point within the shear layer between the wake and the free stream, which can then be used to calculate a wake width. Results for this metric are shown in Figure 5.17. This demonstrates very good agreement between all three meshes until $z/D = 5$ downstream, and between the medium and fine meshes until $z/D = 6$ downstream. Beyond this point, agreement in the general trend remains reasonable between the medium and the fine mesh, but the coarse mesh shows a narrower wake. As with the other two width metrics, the convergence with increasing sample time was plotted in Figure 5.18. This demonstrates that convergence is good until approximately $z/D = 5$, from which point it deteriorates, becoming poor. The strength of the shear in this near-wake region is higher, making the definition of the edge of the wake much clearer. As the strength of maximum shear decreases with increasing downstream distance, the wake edge becomes less clearly defined, which is one reason for the poorer convergence in this region. In addition, the shape of the wake profiles is important, with this wake measurement metric demonstrating convergence difficulties when applied to wake profiles which are approximately v-shaped. In these cases, there is a large cross stream extent with a very similar shear, and therefore any slight change in mean axial velocity can drastically affect the position of point of maximum shear, leading to convergence difficulties. The other two metrics are less sensitive to the shape of the wake profile, and therefore produce faster convergence. Given this convergence difficulty in the far wake region, the differences between the medium and fine wall meshes are not felt to be significant. The sensitivity of the maximum shear metric to wake profile shape is discussed in detail in section 7.5.3.

For all three width measurement metrics used, the three mesh resolutions produce curves showing the same general trends in wake width development with downstream distance. The fine wall resolution generally produces slightly wider wakes and the coarse wall resolution produces slightly narrower wakes, however, given the levels of convergence demonstrated for these metrics, the differences are small. In all cases, the differences between the widths produced by each mesh are smallest in the regions of best convergence.

The aim of this work was to examine whether changes in turbulence intensity, length scale or turbine operating condition impact the width of the wake. To this end, the absolute width of the wake is less important; what is more important is that the model can indicate whether one of these factors causes a wake to become wider or narrower. Given that the overall trends appear unaffected, the difference between the widths are small, and the difficulty in precisely defining the width of a wake, there appears to be little difference in the impact that each mesh has on the wake width, and particularly between the medium and fine meshes.
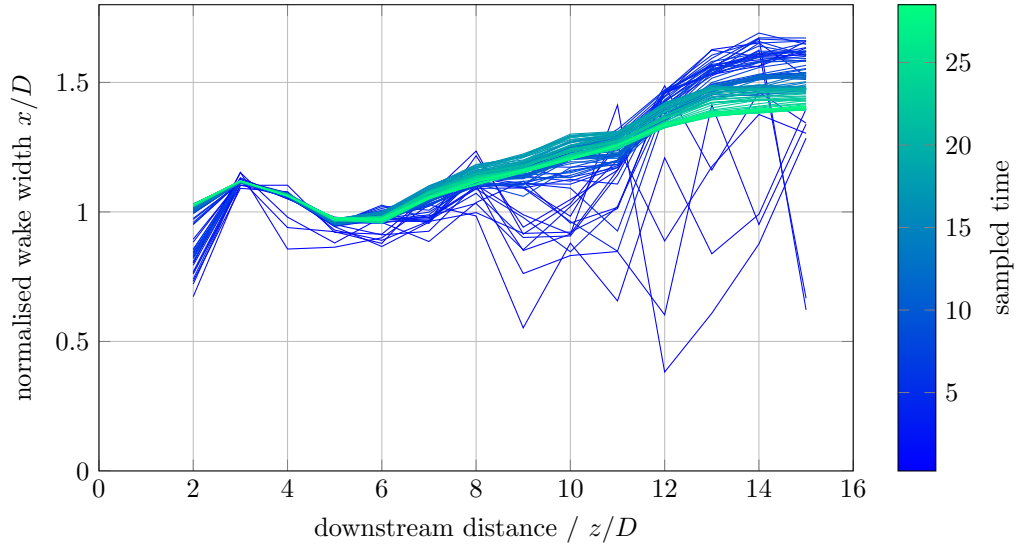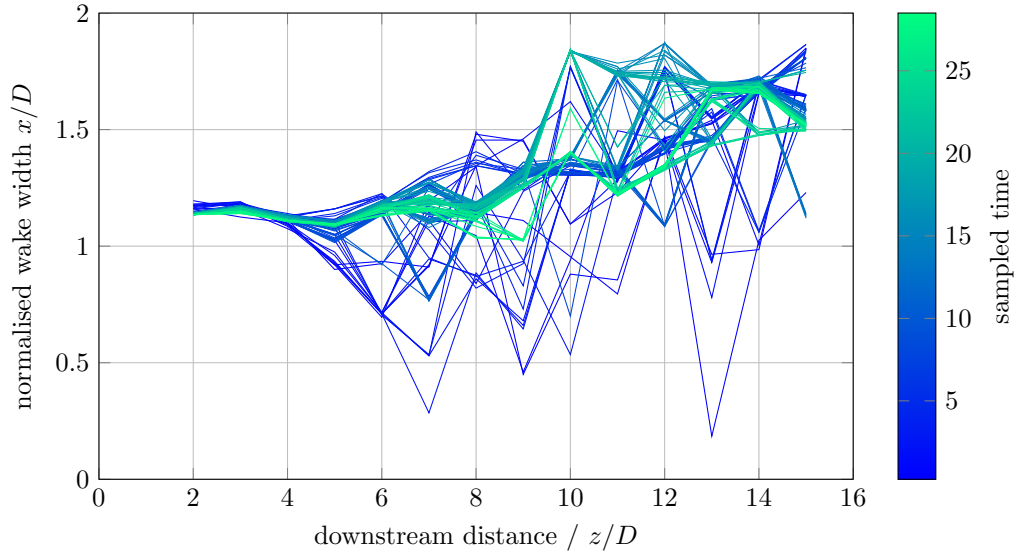
Figure 5.16: Wake width based on Full Width at Half Minimum (fine mesh) to show the effect of increasing sampling time on the mean.
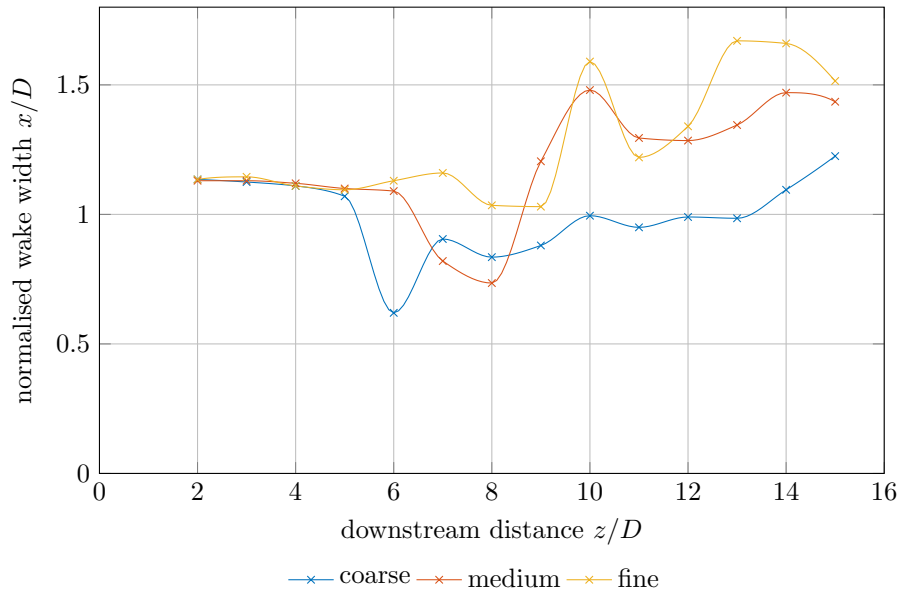
Figure 5.17: Wake width calculations, based on the point of maximum shear, for three different wall cell resolutions. A smooth interpolation has been used between data points.

Figure 5.18: Wake width based on point of maximum shear (fine mesh) to show the effect of increasing sampling time on the mean.

Impact of flume wall resolution on turbine performance characteristics

Whilst not the main focus of this study, the performance characteristics of the turbine in each of the three models were recorded and analysed to determine whether the cell resolution at the flume walls has an effect on these metrics. Changes in C_P, C_T or C_θ might indicate that the flume boundary layer is varying greatly, manifesting itself as blockage-like effects on the turbine. The mean values of C_P, C_T and C_θ can be seen in Table 5.3. These results show that there was effectively no difference in the mean values, with the largest discrepancies apparent in the value for C_P, which shows a difference of $< 0.25\%$. Such small differences are unsurprising for a low-blockage model such as this, where the swept area of the turbine is $< 2.5\%$ of the cross sectional area of the flume. The performance differences found were so small as to be considered negligible.

Table 5.3: Impact of flume wall resolution on turbine performance

	$\overline{C_P}$	$\overline{C_T}$	$\overline{C_\theta}$
Coarse	0.440	0.862	0.1206
Medium	0.440	0.862	0.1206
Fine	0.441	0.863	0.1208

114

Summary of flume wall resolution study

Three different wall resolutions have been studied for their impact on wake recovery, wake width and turbine performance. Differences in turbine performance between the three mesh densities were found to be virtually zero, and differences in wake recovery were found to be very small. There appears to be some impact on the absolute width of the wakes measured using three different metrics, although when put in context with the convergence of these metrics with sample time, and the fact that wake width is to be used an indicator of the trends of impact of turbulence intensity, length scale and operating condition on the wake, these differences can be considered small. For this study, therefore, the 'medium' wall resolution was chosen for CFD studies of the turbine in the flume.

5.8.6 CFD mesh summary

Table 5.4: Summary of mesh used for CFD study. The mesh for the turbine region is equivalent to that used in [8] and [107].

Region	Equivalent mesh density	Number of cells
turbine rotor	as per previous studies	1.55×10^6
turbine nacelle region	medium-coarse	2.96×10^6
wake region	medium	2.39×10^6
outer region	medium wall resolution	4.48×10^6
Total		$\mathbf{11.38 \times 10^6}$

Table 5.4 summarises the meshes used for each region in the flume CFD model. Densities used are equivalent to those investigated in the mesh independence study for the 10 m diameter turbine.

In addition to a mesh independence study, simulations using an 'empty box' (i.e. the flume geometry without the presence of the turbine) would also have been of value. Such a study would have allowed the impact of the mesh on the development of turbulence to be assessed without the presence of the turbine, and could have potentially given further insights into the performance of the DES turbulence model in this application. However, due to time constraints, this was not possible in the work for this thesis, and only the direct impact of the mesh on the turbine was assessed.

Summary of sizings used for mesh control

The following summary is designed to assist a reader wishing to reproduce the mesh themselves. The sizings are those used in ANSYS meshing for the final,

flume-scale model used in this thesis. Reference to Figure 5.2 may be helpful for the identification of the different mesh regions.

Upstream region This is the region from the flume inlet to the turbine.

- Flume inlet face: Face sizing of 1×10^{-2} m, behaviour: hard.
- Upstream region: Body sizing of 5×10^{-2} m, behaviour: soft.
- Flume walls and floor: Face sizing of 0.1 m, behaviour: hard.
- Flume surface: Face sizing of 0.3 m, behaviour: hard.
- Interface to turbine region: Face sizing of 1.25×10^{-2} m, behaviour: soft.

Turbine region The mesh sizings for this region containing the turbine rotor were chosen to match those used in previous studies using a k-ω SST turbulence model for this turbine.

- Interface to upstream region: Face sizing of 1.25×10^{-2} m, behaviour: soft.
- Interface to downstream region: Face sizing of 5×10^{-3} m, behaviour: soft.
- Outer $^1/_3$ of blades: Face sizing of 1×10^{-3} m, behaviour: soft.
- Mid $^1/_3$ of blades: Face sizing of 2.5×10^{-3} m, behaviour: soft.
- Inner $^1/_3$ of blades: Face sizing of 4×10^{-3} m, behaviour: soft.
- Turbine hub: Face sizing of 4×10^{-3} m, behaviour: soft.
- Turbine shaft: Face sizing of 4×10^{-3} m, behaviour: soft.
- Turbine body: Face sizing of 4×10^{-3} m, behaviour: soft.

Turbine surround This region enclosed the large majority of the turbine body, as well as the hose and stanchion.

- Interface to turbine region: Face sizing of 5×10^{-3} m, behaviour: soft.
- Interface to wake region: Face sizing of 1×10^{-2} m, behaviour: soft.
- Turbine body, stanchion and hose: Face sizing of 4×10^{-3} m, behaviour: soft.
- Turbine surround region: Body sizing of 2×10^{-2} m, behaviour: soft.

Wake region This is the cylindrical region from approximately the back of the turbine to the flume outlet.

- Upstream face: Face sizing of 1×10^{-2} m, behaviour: soft.

- Downstream face: Edge sizing of 5×10^{-3} m, behaviour: soft.

- Sweep method with the following settings: A free face mesh type of Quad/Tri, 400 divisions along length with a sweep bias of 2, with smaller cells upstream.

Surrounding flume region This region is the remainder of the simulated volume, and encloses the cylindrical region of the wake. At the interface with the wake region, the boundary was conformal, and dictated by the sizings used for meshing the wake region.

- Flume walls and floor: Face sizing of 0.1 m, behaviour: hard.

- Flume surface: Face sizing of 0.3 m, behaviour: hard.

5.9 Migration to High Performance Computing (HPC) facilities

Due to the high computational expense in performing the characterisations and the large number of permutations of turbulence intensity, turbulence length scale, and turbine rotational velocity investigated, the Raven High Performance Computing (HPC) facilities at Cardiff University were used. Tests were carried out on a single case and with comparisons made between the cases for wake recovery and turbine performance. It was found that there was a small difference between the results for these two cases. Upon consulting with ANSYS, it was found that this is due to a difference in the definition of turbulence length scales between the two versions; converting from one to the other required multiplication by a factor of 1/0.164. Once this had been carried out, the differences between the runs with the two cases became negligible. All CFD cases reported in this thesis (other than the mesh independence study) were run using Raven (the Cardiff HPC facility), and are therefore comparable with each other.

5.10 Post-processing

ANSYS allows post processing within Fluent, as well as providing a dedicated post-processing suite, CFD-Post. It can be used for simple displaying of data, and is particularly useful for such common actions as displaying results on surfaces (e.g. turbine blades or other surfaces for display). However, in order to

allow more flexibility in the analysis of data, Fluent was used to export solution data to MATLAB for further processing.

Once the CFD runs were completed, flow data was extracted on the horizontal and vertical planes containing the turbine axis, as well as planes perpendicular to the axis at positions $z/D = 2$, $z/D = 3$, $z/D = 4$, ..., $z/D = 15$. This flow information was then processed using scripts written for MATLAB, which then presented the data either as charts or as 2D maps of the particular flow property, allowing direct comparison with measurements made in the flume.

5.11 Summary of CFD runs

A summary of the CFD runs conducted for this study can be seen in Table 5.5. The values for velocity, turbulence intensity and lengths scale were the target values for each run, the actual values as recorded at a monitor point upstream of the turbine rotor are shown later, in Chapter 7.

Table 5.5: Summary of CFD runs conducted.

velocity	target TI	target L_t	tip-speed ratio	run no.
		0.25 m	2.5	1
			3.65	2
			4.5	3
	5%	0.5 m	2.5	4
			3.65	5
			4.5	6
		1 m	2.5	7
			3.65	8
			4.5	9
		0.25 m	2.5	10
			3.65	11
			4.5	12
$1.1 \mathrm{\,m\,s^{-1}}$	10%	0.5 m	2.5	13
			3.65	14
			4.5	15
		1 m	2.5	16
			3.65	17
			4.5	18
		0.25 m	2.5	19
			3.65	20
			4.5	21
	20%	0.5 m	2.5	22
			3.65	23
			4.5	24
		1 m	2.5	25
			3.65	26
			4.5	27
			2.5	28
$1.02 \mathrm{\,m\,s^{-1}}$	11.7%	0.19 m	3.65	29
			4.5	30
			2.5	31
$1.03 \mathrm{\,m\,s^{-1}}$	17.5%	0.43 m	3.65	32
			4.5	33
			1.5	34
			2.5	35
			3	36
$1.5 \mathrm{\,m\,s^{-1}}$	1.75%	0.5 m	3.65	37
			4	38
			4.5	39
			5.5	40

Chapter 6

Flume testing: Experimental Methodology

6.1 Turbine description

6.1.1 Turbine geometry

The turbine used for this work is a three-bladed, horizontal axis design, with blades based on a Wortmann FX 63-137 section. The diameter of the rotor is 0.5 m, and the blades have a twist of 30° from root to tip. These are attached to a hub of 100 mm diameter via root stubs and grub screws. This rotor geometry has been the subject of much research in CMERG, both computationally and experimentally[107], [8], [52], [56], [57]. The turbine nacelle, constructed from stainless steel, is 763 mm long and has a maximum diameter of 160 mm. The turbine hub is directly connected to a Bosch Rexroth type MST130E-0035 synchronous torque motor which is housed within the nacelle along with a slip ring and associated electronics for control and instrumentation. Electric power and sensor cables are routed out of the downstream face of the nacelle within a hydraulic hose, enabling them to be brought to the surface without compromising the watertight sealing of the turbine itself. The control system to which the turbine is attached allows it to be operated in two different modes; constant rotational velocity, or constant torque. The motor can be used to either drive or brake the turbine, with turbine torque being measured via the electrical current required to either drive or brake the turbine. For all the experiments detailed in this thesis, the constant rotational velocity mode was used, replicating the constant rotational velocity used in the CFD study. The turbine assembly is suspended under water by means of a steel stanchion, 71 mm in diameter. A schematic showing the internal layout of the turbine can be seen in Figure 6.1,

a photograph of the turbine in the flume can be seen in Figure 5.1b and further details of the turbine can be found in Allmark[134].

6.1.2 Sensors, data recording and instrumentation

The turbine was initially designed for physical testing to measure loads on, and power output of a turbine, with a specific focus on condition monitoring[134], but it has also been used for work investigating the impact of misalignment[29], and surface waves. It has been designed to allow the use of 2, 3 or 4 blades, with one of the blades being instrumented with strain gauges to measure the bending moments on the blade root. In addition, strain gauges on the stanchion are designed to measure the thrust force on the turbine. Unfortunately, due to persistent problems with these sensors, the only data that it was possible to obtain for this turbine was that of torque, obtained via the torque generating current. This was calibrated before the turbine was positioned in the flume, allowing the torque generating current to be directly converted into the mechanical torque on the turbine rotor[134]. This method therefore automatically accounts for electrical losses, as well as those due to friction in bearings or seals.

Data acquisition (as well as turbine control) was carried out using a National Instruments PXIe-8135 embedded controller and PC. Acquisition was limited by buffer size; consequently a higher sample rate leads to a shorter length of time over which data can be acquired. A sample rate of 200 Hz was used, which allowed 41 s of data to be sampled. This gives a sample rate identical to that from the CFD simulations, with data being sampled over a similar amount of time to the 50 s simulated numerically.

6.1.3 Uncertainty analysis

Uncertainty analysis was conducted for the turbine performance characteristics of C_P and C_θ (thrust data was not available from the experiments). These were calculated via equations 4.2 and 4.4 respectively. The techniques and equations described in section 4.3 were applied to the measured variables, which had their uncertainties defined by Allmark[134], which provides a detailed uncertainty analysis used in the commissioning of the turbine. When collecting the data for the power curves presented in this thesis, upstream velocity was not simultaneously measured, but rather, the flume pump set-point used in the wake measurements was used. Therefore, the reference velocity used for the calculation of C_P, C_T and C_θ is based on a mean velocity, rather than an instantaneous one.

ITEM NO.	PART NUMBER	DESCRIPTION	QTY.
1	Drive Shaft		1
2	1_ASM_6008_2RS1	Bearing	2
3	Motor End Plate		1
4	Front Seal	Fitted with O-rings	1
5	Rotor_Inner		1
6	Stator_Outer		1
7	Slip Ring		1
8	Encoder		1
9	Conical Section	Moisture sensor location	1
10	Nacelle Body		1
11	End Plate	Fitted with O-rings	1
12	Instrumented Hub	Load Measurements	1
13	0.5m Blade	2, 3 and 4 Blade Configs	2
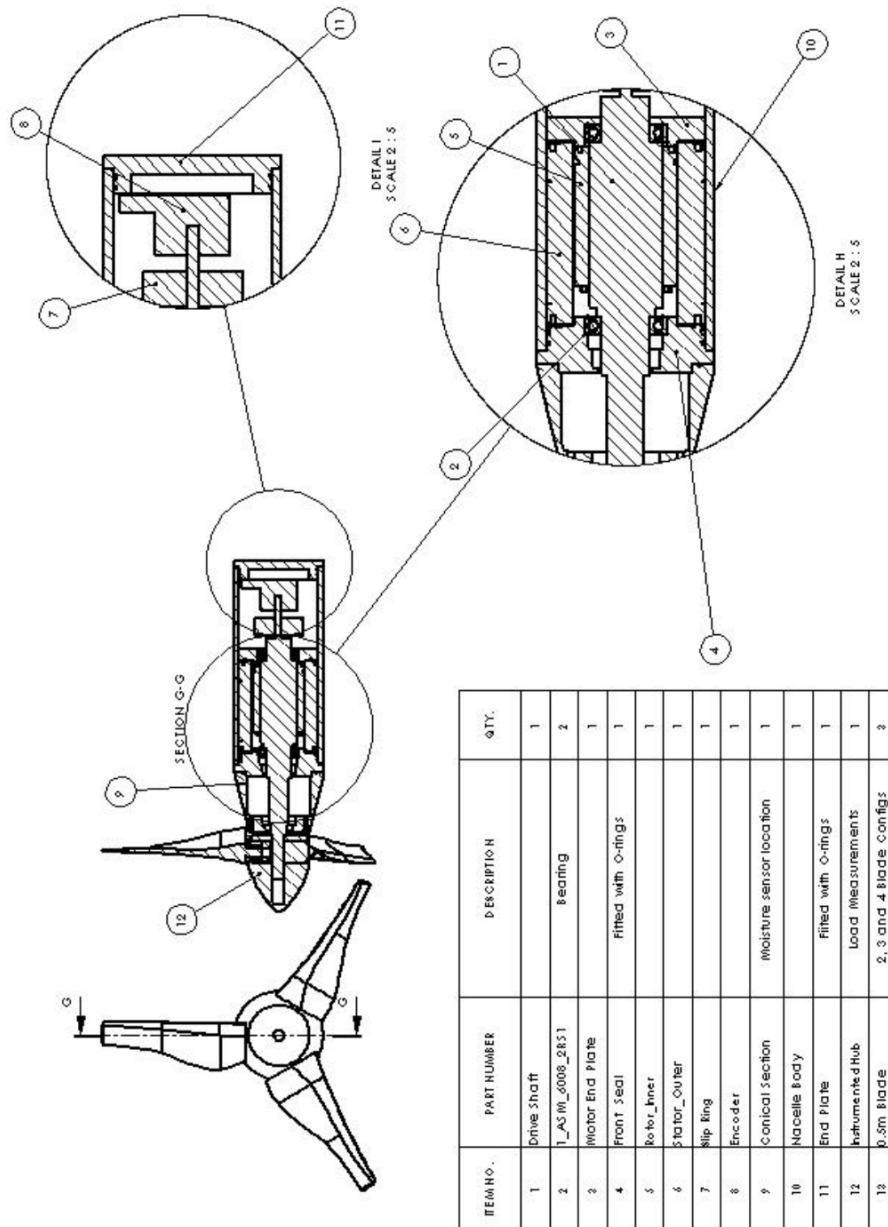
Figure 6.1: A cross-section schematic of the model scale turbine used in the flume testing described herein. Schematic taken from Allmark[134].

122

6.2 Flume description

Testing was carried out in the flume facility of the Institut Français de Recherche pour l'Exploitation de la Mer (IFREMER) in Boulogne-sur-Mer. This recirculating flume has a working section approximately 4 m wide, 2 m deep and with a useable length of approximately 18 m. It is capable of flow speeds of 0.1–2.2 $\mathrm{m\,s^{-1}}$, but for turbine testing was only used to a maximum of 1.5 $\mathrm{m\,s^{-1}}$. A schematic of the flume can be seen in Figure 6.2

6.3 Flow measurement techniques

Flow measurement was made using a two-axis Laser Doppler Anemometer (LDA) system. This technique is a well established, non-invasive technique for measuring fluid velocities. Flow velocity measurements along an axis are made using a laser, split into two beams which are adjusted to be coincidental at a point some distance from the head of the device. In the case of the device used in the flume testing in this thesis, this distance was 0.5 m. Where the two beams coincide, an interference pattern in created, consisting of bands of constructive and destructive interference – effectively light and dark stripes. When seed particles pass through the control volume where the beams cross a 'burst' is produced as they pass through the light and dark regions. The frequency of these flashes, detected by the receiving optics, indicates the speed of the particle. Various refinements can be made to improve the accuracy of the device, for example, one of the split beams is commonly passed through a Bragg cell, which allows the direction of movement of the particle to be determined. The Bragg cell slightly shifts the frequency of one of the beams. This causes the interference fringes to move through the control volume, rather than being fixed in position. A stationary particle will produce a 'burst' with a particular frequency, but a movement in one direction will cause the frequency to increase, whereas movement in the other direction will cause it to decrease. Subtracting the frequency shift from the received signal therefore allows the determination of both the magnitude and direction of the particle's velocity.

A second measurement axis can be added by using a second laser, with its split beams aligned at 90° to the first and with a different colour, in order to allow the receiving optics to discriminate between signals coming from the primary or secondary axis. The beams are angled such that the control volume of the second laser is coincident with the first, so that particles passing through the control volume simultaneously produce a signal for both the primary and secondary measurement axes. This was the method used in the flume testing detailed within this thesis. It is possible to add a third measurement axis with a
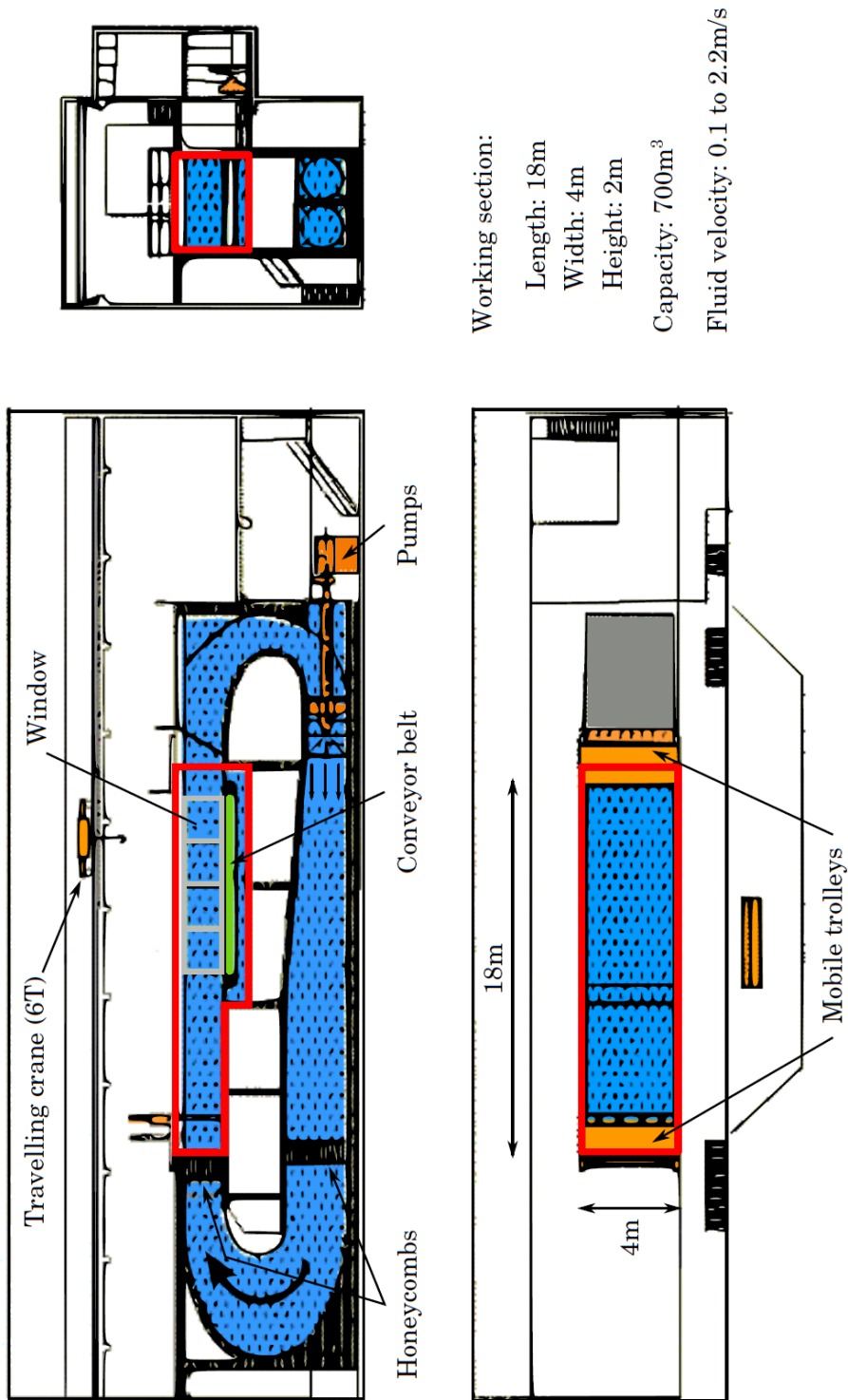
Figure 6.2: A schematic of the IFREMER recirculating flume, from Mycek[60].

Working section:

Length: 18m
Width: 4m
Height: 2m
Capacity: 700m^3
Fluid velocity: 0.1 to 2.2m/s

Pumps

Window

Conveyor belt

Travelling crane (6T)

Honeycombs

18m

4m

Mobile trolleys

third laser, however, this third laser must be perpendicular to the other two, and therefore cannot be contained within the same head unit, and requires careful alignment in order that the three control volumes be coincident. The system in this thesis used the backscattered light in order to allow the transmitting and receiving optics to be both contained within the same head unit.

The LDA system used in this work was a 2D DANTEC FiberFLOW, provided by IFREMER, and calibrated by the manufacturer to $\pm 0.001 \, \mathrm{m\,s^{-1}}$. The control volume through which a particle must pass in order for a measurement to be made is $0.12 \, \mathrm{mm} \times 0.12 \, \mathrm{mm} \times 2.51 \, \mathrm{mm} = 0.04 \, \mathrm{mm^3}$. The device does not have a fixed data rate; it is dependent on a variety of factors such as the level of seeding in the tank etc., however, for the measurements detailed here, the data rate was approximately 150–200 Hz.

The LDA system was attached to a traverse, capable of moving the device in two directions. This traverse was fixed to one of the steel I-beams which span the flume, allowing the measurement procedure to be automated in the cross-stream and vertical directions. The measurement positions and times were pre-programmed, allowing the LDA measurements to be made for one downstream station (in a plane perpendicular to the turbine axis), before the I-beam was moved by hand to the next downstream measurement position. As the absolute position of the LDA was set by clamping the traverse to the I-beam, which itself is positioned via measurements using laser- and tape measures, absolute position errors are considered to be of the order of ± 0.5 cm, however, as the horizontal traverse is automated using a worm drive, *relative* position errors between two points in the cross-stream direction are considered to be approximately ± 1 mm.

The September 2016 test campaign was conducted in conjunction with other tests for which the LDA had been set up to measure in the axial and cross-stream directions. It was this configuration therefore which was used to measure velocities in the wake region on a horizontal plane containing the turbine axis. For the 2018 test campaigns, the head of the LDA was positioned to allow measurement of velocity in the axial and vertical directions. Measurements on a horizontal plane containing the turbine axis then yield axial and tangential velocities, which were subsequently used to examine flow rotation and swirl in the wake.

For each measurement, the DANTEC data acquisition system produced a text file containing details of the velocity measured, and the time at which the velocity was measured. Analysis of the data files was automated in MATLAB, producing values for mean velocity, RMS velocity and integral scale in both measurement directions. Where necessary, re-sampling was carried out in order to obtain a uniform sample rate, with sample period smaller than the smallest recorded by the LDA. This analysed data could then be used to produce maps

and charts of the velocity, as well as being combined to identify swirl in the wake, using the method outlined in section 4.2.

6.4   Flow conditions

Flume testing was conducted in three separate campaigns (September 2016, April 2018 and June 2018) in conjunction with work carried out for other projects. These three campaigns sought to examine the wake under three different types of flow condition; a low turbulence condition (1.75%), obtained using all available flow-smoothing at the tank, and two campaigns which used grids constructed of aluminium frames and marine plywood and placed upstream of the turbine to induce turbulence. The dimensions of the grids followed those used by Blackmore et al.[59], which were used to examine the effects of turbulence on the performance and loading of a tidal turbine. In the study by Blackmore et al., length scales of between 0.18–0.82 m were achieved, corresponding to approximately 0.5–1.5 times the diameter of the turbine rotor studied in this thesis, which was the region of interest. Using grids about which data had already been published allowed an estimation of the turbulence intensity and length scales to be expected before going to the tank. The fine grid was installed by fastening it to a length of metal channel on the base of the flume, and clamped to an I-beam above the surface of the water. The anticipated increase in turbulence intensity and the rate of its decay produced by the coarse grid meant that this was installed as far upstream as possible by using strops to strong points immediately upstream of the honeycombs at the inlet to the working section (honeycombs visible in Figure 6.2). A drawing of the grids, taken from Blackmore et al.[59], can be seen in Figure 6.3. A photograph of the fine grid installed in the flume in April 2018 can be seen in Figure 6.4.

Before installing the turbine in the flume, the flow downstream of the grids was characterised. This was done via a sequence of LDA measurements in the centre of the cross sectional area of the flume. These were carried out for 1000 s each, in order to obtain high confidence in the higher-order statistics. Plots showing how velocity, turbulence intensity and integral length scale develop with distance downstream of the grid are shown in Figures 6.5, 6.6 and 6.7 respectively for the fine grid, and 6.8, 6.9 and 6.10 for the coarse grid. Error bars have been omitted from these figures for clarity, as in all cases 95% confidence intervals were less than 0.5% of the values shown in the figures.

The figures for the fine grid show that the velocity behind the grid increases with downstream distance (most likely due to the near-grid velocity being affected by the position of individual bars, with this effect becoming less influential as downstream distance increases), turbulence intensity decreases with down-

126
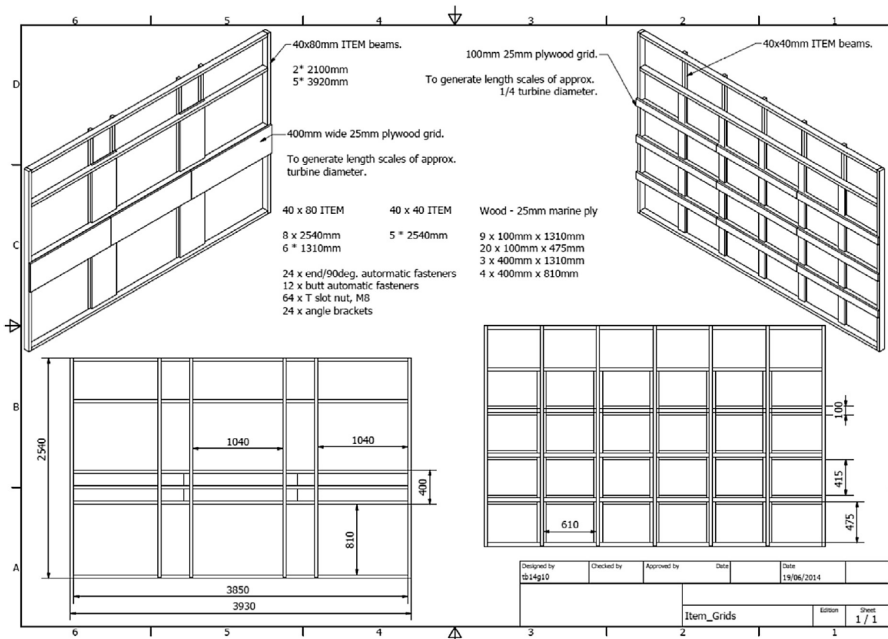
Figure 6.3: Schematic of the grids used to create turbulence. Figure taken from Blackmore et al.[59].
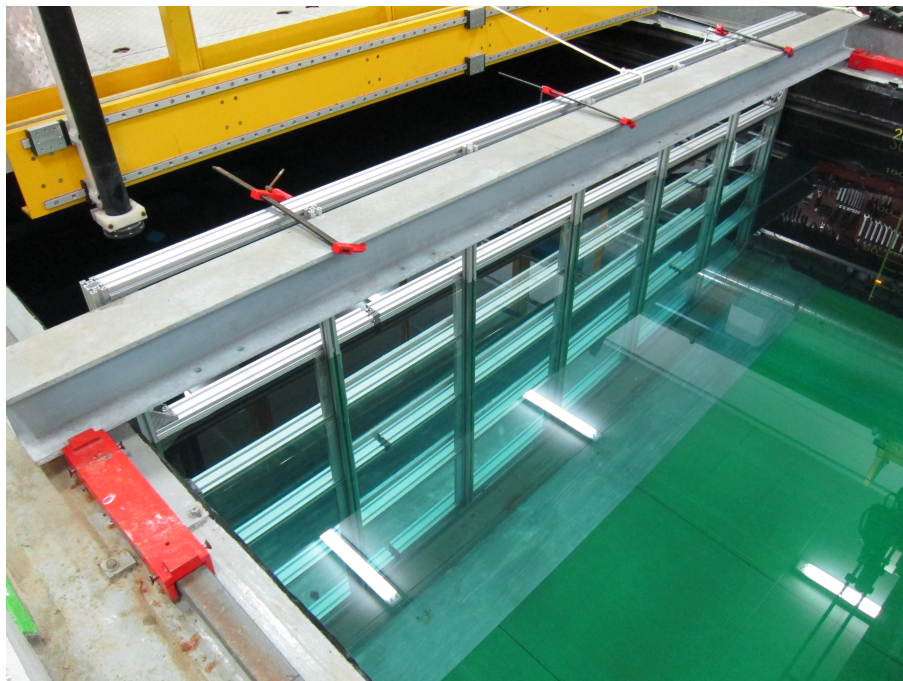
Figure 6.4: The fine grid installed in the IFREMER flume, viewed from downstream, April 2018.
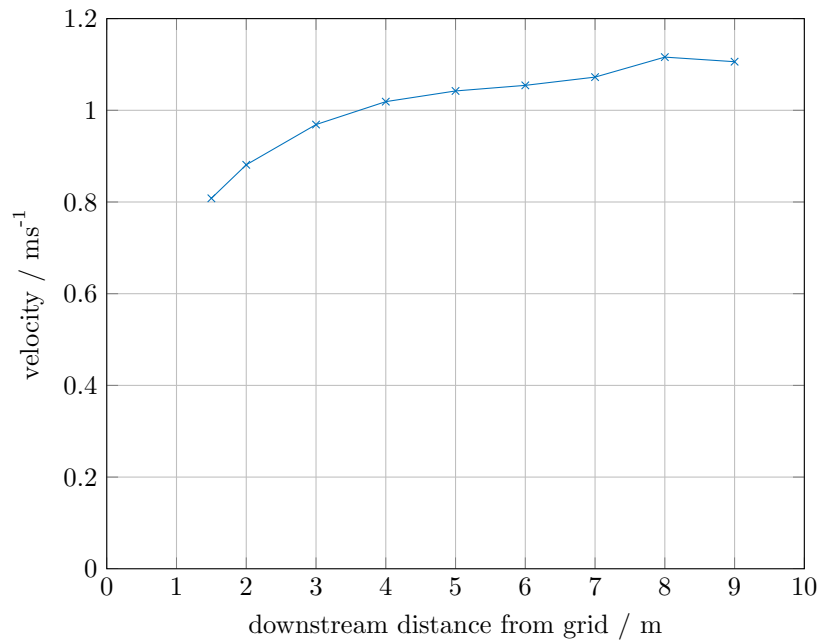
Figure 6.5: Flow velocity behind the fine grid, measured at the centre of the cross-sectional area of the flume.
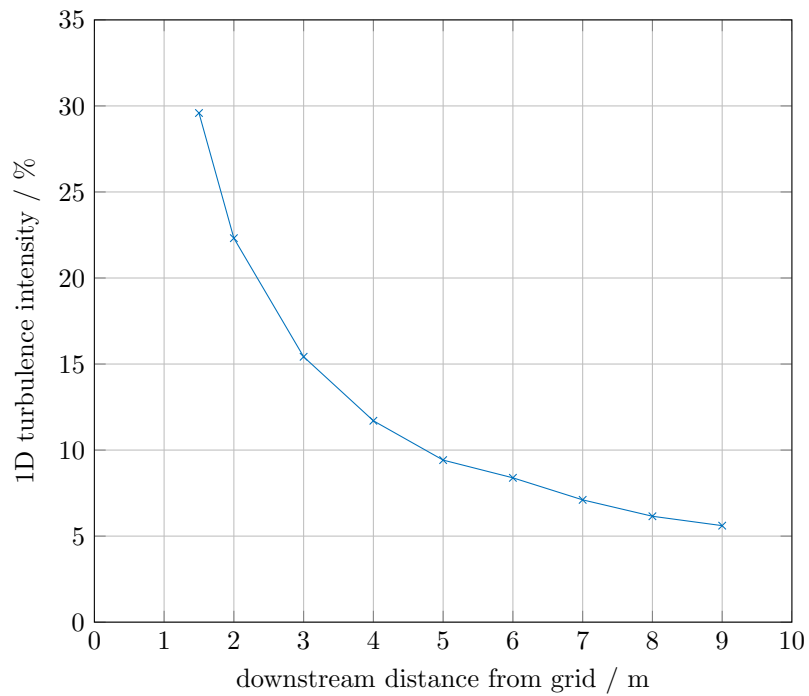
Figure 6.6: 1D turbulence intensity behind the fine grid, measured at the centre of the cross-sectional area of the flume.
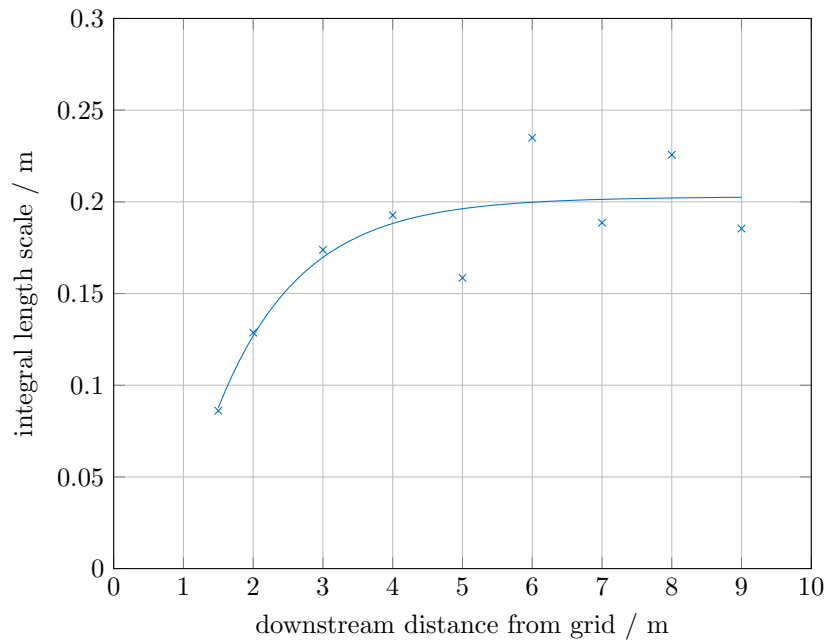
Figure 6.7: Integral length scale behind the fine grid, measured at the centre of the cross-sectional area of the flume.
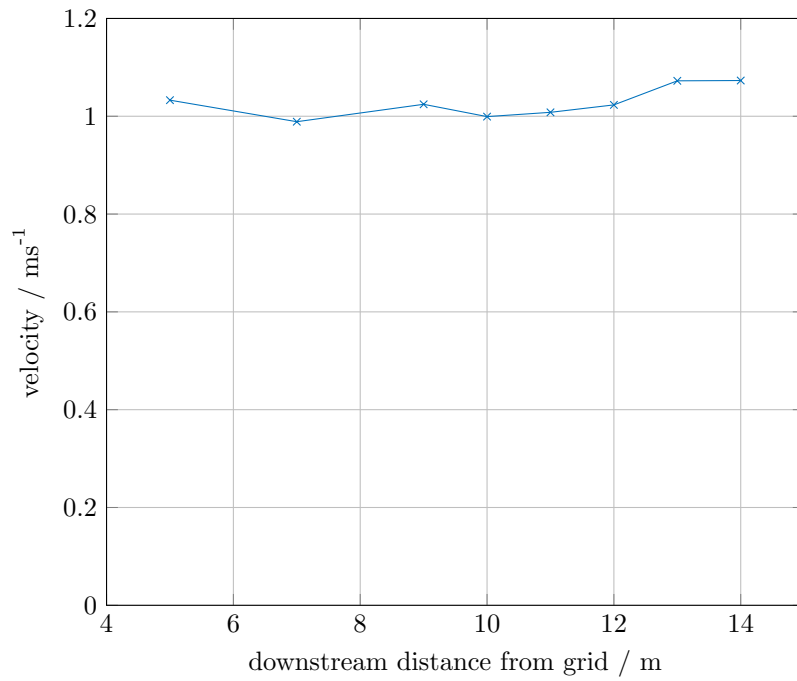
Figure 6.8: Flow velocity behind the coarse grid, measured at the centre of the cross-sectional area of the flume.
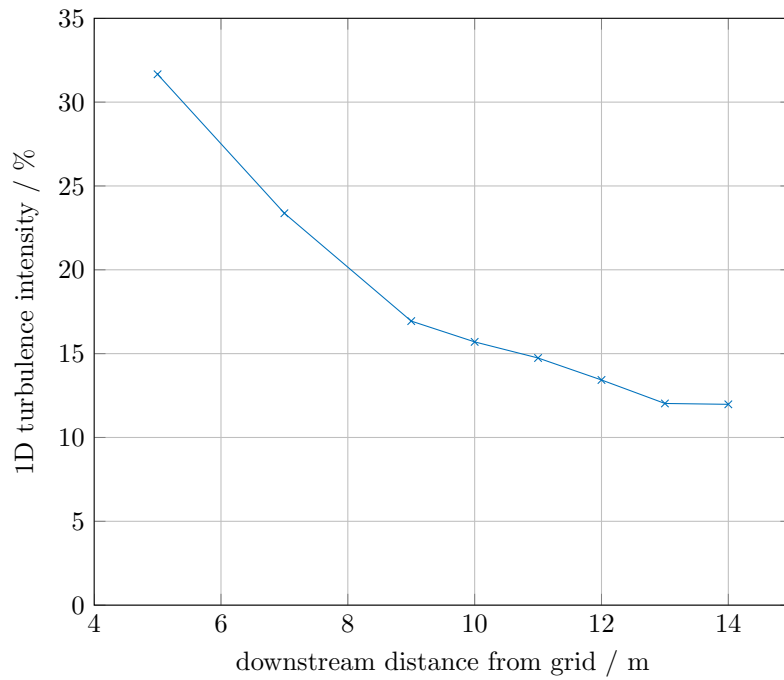
Figure 6.9: 1D turbulence intensity behind the coarse grid, measured at the centre of the cross-sectional area of the flume.
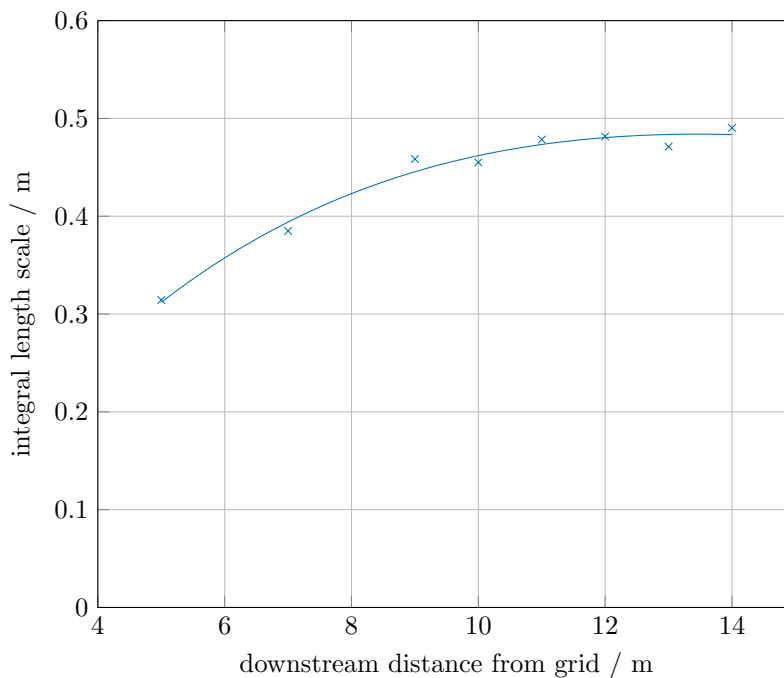
Figure 6.10: Integral length scale behind the coarse grid, measured at the centre of the cross-sectional area of the flume.

Table 6.1: A comparison of the results of the flow uniformity tests across the swept area of the turbine for the fine grid. Position of points used can be seen in figure 6.11.

measurement point	1	2	3	4	5
mean velocity / $\mathrm{m\,s^{-1}}$	1.08	1.02	1.09	1.06	1.04
1D turbulence intensity / %	11.9	11.6	11.6	11.8	12.2
integral length scale / m	0.19	0.21	0.20	0.28	0.21

stream distance, showing the dissipation of turbulence, and integral length scale tends to increase, indicating the dissipation of the shorter length scales with time. Based on the analysis of flow development behind the grid, as well as consideration of the space required to carry out wake measurements, the turbine rotor was placed at a distance of 4 m downstream of the fine grid, which gave a velocity of $v = 1.02 \mathrm{~m\,s^{-1}}$, turbulence intensity of 11.7% and $L_t = 0.19 \mathrm{~m\,s^{-1}}$.

The figures for the coarse grid show similar trends to that of the fine grid, albeit as anticipated with a higher turbulence intensity and greater turbulence length scale. No measurements were made closer than 5 m from the grid, as the turbulence intensity was measured to be over 30% at this point, and higher turbulence intensities were not required. The turbine was placed 9 m downstream of the coarse grid, as this was the greatest distance that it could be placed from the grid, whilst still leaving enough space downstream of the turbine for wake measurements.

Once the centreline measurements had been made and the turbine position chosen, flow uniformity across the swept area of the turbine was assessed by re-measuring at the chosen position on the flume centreline, as well as ±0.25 m in both the horizontal and vertical directions, at the limits of the turbine swept area (shown in Figure 6.11). Each of these measurements was made for 500 s. The results from these measurements can be seen in Table 6.1 for the fine grid, and Table 6.2 for the coarse grid. These show the flow to be reasonably uniform across the swept area of the turbine, with the integral length scale being approximately twice as large behind the coarse grid when compared to the fine grid; approximately of the order of a turbine diameter and a turbine radius respectively.

For the test campaign conducted in the low turbulence conditions without any grid, vertical profiles of axial velocity and turbulence intensity were made across the region where the turbine was present (Figure 6.12). This shows the velocity to vary from 1.50–1.53 $\mathrm{m\,s^{-1}}$ across the diameter of the turbine, and the turbulence intensity to vary from 1.75%–2% across the diameter of the turbine, indicating a low turbulence, highly uniform flow.

A summary of the flow conditions and tip-speed ratios for which wake mea-

Table 6.2: A comparison of the results of the flow uniformity tests across the swept area of the turbine for the coarse grid. Position of points used can be seen in figure 6.11.

measurement point	1	2	3	4	5
mean velocity / $\mathrm{m\,s^{-1}}$	1.04	1.02	0.94	1.04	1.09
1D turbulence intensity / %	16.4	16.6	18.6	16.5	15.2
integral length scale / m	0.44	0.42	0.51	0.44	0.41

surements were made can be seen in Table 6.3. The September 2016 campaign was conducted without any grids upstream of the turbine, and therefore in a low turbulence condition. The April 2018 flow conditions was achieved using the fine grid, and the June 2018 conditions using the coarse grid.

6.4.1 Wake measurement positions

Test campaign, September 2016

The test campaign in September 2016 measured one wake, at a tip-speed ratio of $\lambda = 3.65$. The wake measurement was made on the horizontal plane containing the turbine axis. Measurement points were made at cross-stream positions of $x/D = \pm 1.6, \pm 1.2, \pm 0.9, \pm 0.6, \pm 0.3$ and $x/D = 0$ at downstream positions of $z/D = 4, 5, 6, 7, 9$ and 11. Each measurement was made for 100 s.
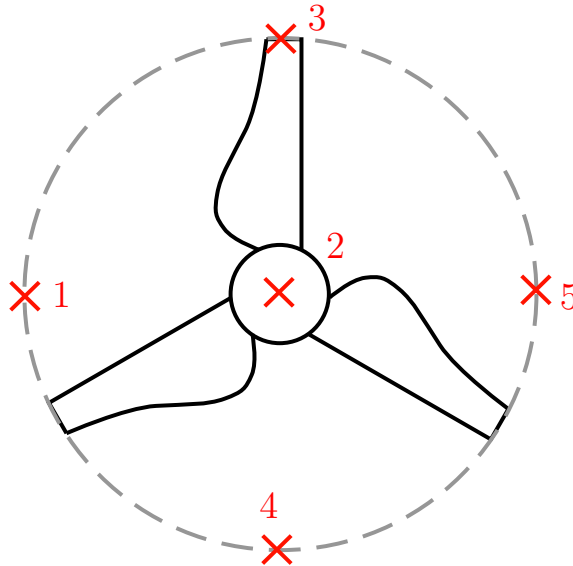
Figure 6.11: Positions used for flow uniformity measurements (as viewed from upstream). Measurements were made in the plane where the turbine would be placed, but without the turbine present.

(a) Mean streamwise velocity

(b) Turbulence intensity profile
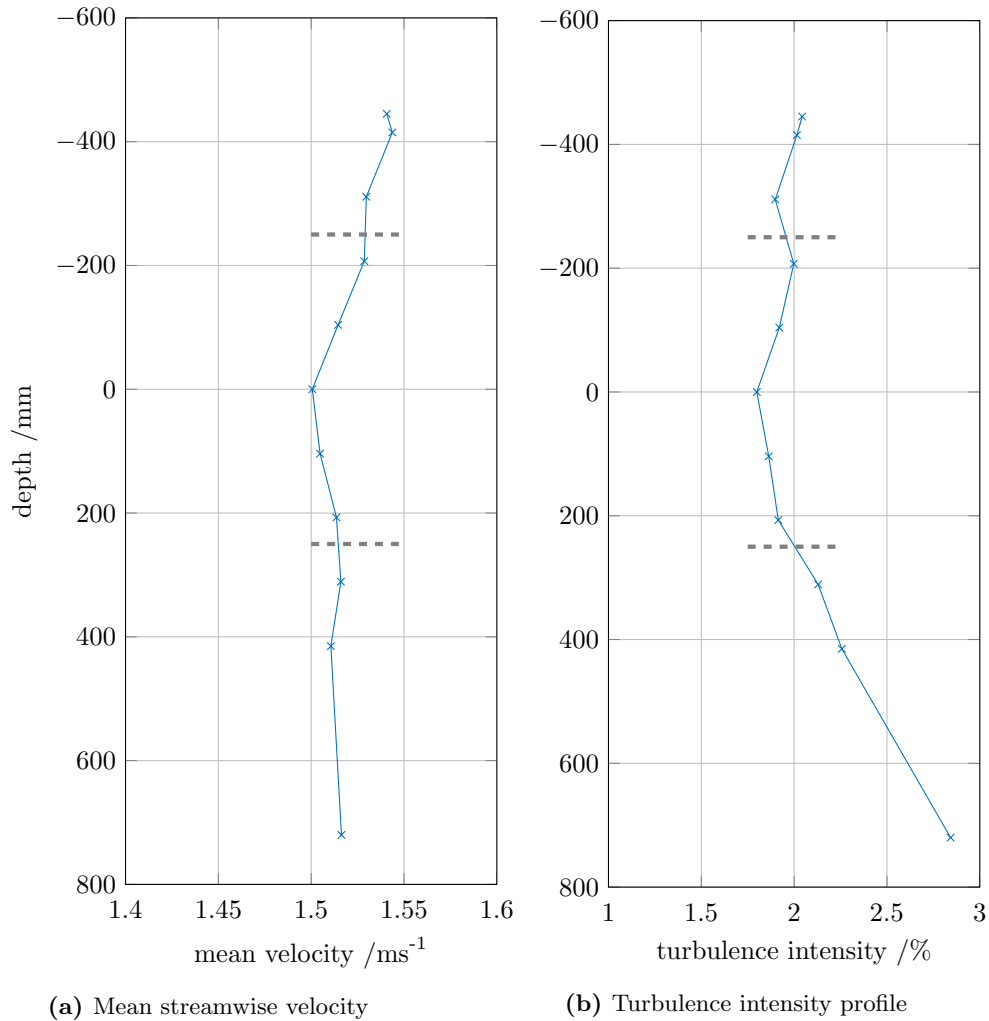
Figure 6.12: Flow profile information, measured at $z/D = 3$ upstream of the turbine plane. Turbine axis is located at a depth of 0 mm, negative values of depth indicate positions closer to the surface of the flume, positive values indicate positions closer to the bottom of the flume. Error bars have been omitted for clarity, as 95% confidence interval bounds are within 0.4% of the reported values in all cases. Grey dashed lines indicate the position of the turbine.

Table 6.3: A comparison of the different flow conditions used in each testing campaign. All quoted metrics are the flow conditions at the turbine rotor position.

Campaign date		September 2016	April 2018	June 2018
grid used		none	fine	coarse
distance from grid / m		n/a	4.0	9.0
velocity / $\mathrm{m\,s^{-1}}$		1.5	1.02	1.03
1D Turbulence intensity / %		1.75	11.7	17.5
integral length scale / m		0.5	0.19	0.43
	2.5		✓	✓
tip-speed ratios tested	3.65	✓	✓	✓
	4.5		✓	✓

Test campaigns 2018

The test campaigns in April and June 2018 measured wakes, at tip-speed ratios of $\lambda = 2.5, 3.65$ and 4.5 and for the flume conditions present at that test (Table 6.3). The wake measurements analysed in this thesis were made on the horizontal plane containing the turbine axis. Measurement points were made at cross-stream positions of $x/D = \pm 2.0, \pm 1.6, \pm 1.2, \pm 0.9, \pm 0.6, \pm 0.4, \pm 0.2$ and $x/D = 0$ at downstream positions of $z/D = 2, 3, 4, 5, 7, 9$ and 12. Measurements were made for 100 s, except at the centreline, where measurements were made for 400 s.
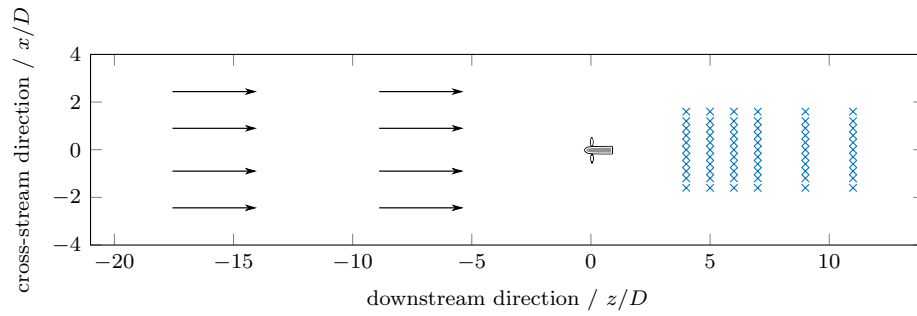
(a) LDA measurement positions, September 2016 campaign (no grid).
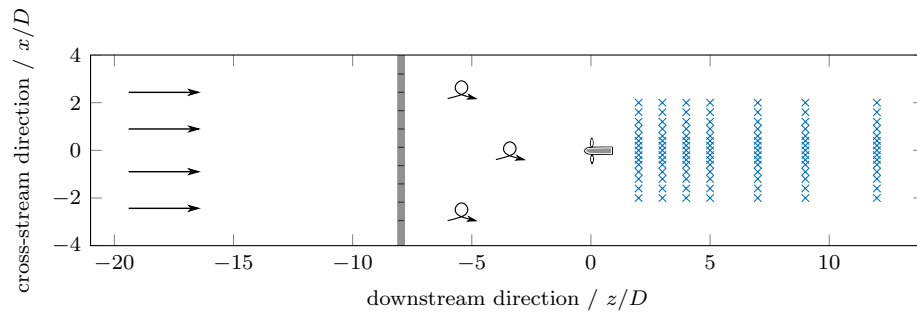
(b) LDA measurement positions, April 2018 campaign (fine grid).
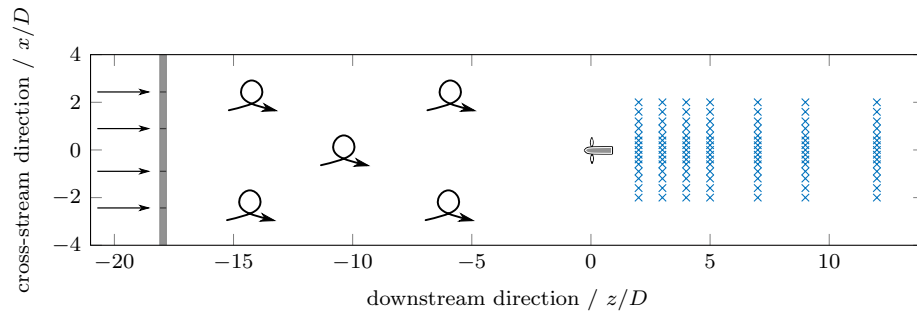
(c) LDA measurement positions, June 2018 campaign (coarse grid).

Figure 6.13: A schematic of LDA measurement positions for the three different flume testing campaigns (viewed from above). Position of grid (where applicable) is shown in grey; wake measurement positions are represented by the blue crosses.

135

Chapter 7

Results

7.1 Flow conditions

The results presented are from both flume measurements and CFD models, allowing the validation of the CFD model. In addition to this, the impact on the wake of turbine operating condition, as well as upstream turbulence intensity and length scale was investigated. The impact of tip-speed ratio on the wake was investigated by analysing CFD results of seven different tip-speed ratios in a low-turbulence flow, approximating that used in the 2016 flume testing campaign. The impact of turbulence intensity and length scale was investigated by conducting 27 CFD runs for three different tip-speed ratios, inlet intensities and length scales. In order to confirm the upstream flow conditions, analysis was carried out on an upstream monitor point to determine the actual turbulence intensity and length scale experienced by the turbine in the CFD models. These showed that despite defining the upstream conditions identically, these did not necessarily lead to identical measured flow conditions. A table showing the target and actual flow conditions for each CFD run is shown in Table 7.1. A run was completed for the $\lambda = 4.5$ case to match the June 2018 conditions (in the table marked as "run 33"), however, the data was subsequently found to be corrupted and has therefore not been used. Despite the differences between the target and actual flow conditions, it was nonetheless possible to find groups of cases which differed from each other only in upstream turbulence intensity or length scale for comparison.

7.2 Representation of uncertainties

Uncertainties were calculated following the procedures described in Chapter 4. Where error bars are displayed on charts, they represent confidence intervals of

Table 7.1: Target conditions vs. actual conditions, CFD. The numbers presented here were obtained by analysing a monitor of instantaneous axial velocity, placed at $z/D = 2$ upstream of the turbine rotor plane, at the centre of the flume.

Target values			Measured values				
			λ	v / m s^{-1}	TI / %	L_t / m	run no.
			2.5	1.10	2.29	0.44	1
		$L_t = 0.25$ m	3.65	1.09	2.56	0.45	2
			4.5	1.10	1.59	0.39	3
			2.5	1.10	4.22	0.83	4
	TI = 5%	$L_t = 0.5$ m	3.65	1.10	4.52	0.83	5
			4.5	1.10	1.86	0.79	6
			2.5	1.10	1.64	1.45	7
		$L_t = 1.0$ m	3.65	1.10	1.66	1.45	8
			4.5	1.10	1.55	1.45	9
			2.5	1.10	6.74	0.45	10
		$L_t = 0.25$ m	3.65	1.08	4.67	0.47	11
			4.5	1.10	4.64	0.45	12
			2.5	1.10	5.32	0.78	13
$v = 1.1$ m s^{-1}	TI = 10%	$L_t = 0.5$ m	3.65	1.10	1.37	0.55	14
			4.5	1.10	3.91	0.82	15
			2.5	1.10	3.71	1.50	16
		$L_t = 1.0$ m	3.65	1.10	3.70	1.49	17
			4.5	1.10	2.36	1.37	18
			2.5	1.11	12.43	0.45	19
		$L_t = 0.25$ m	3.65	1.08	10.45	0.44	20
			4.5	1.09	9.55	0.45	21
			2.5	1.10	8.22	0.82	22
	TI = 20%	$L_t = 0.5$ m	3.65	1.11	15.21	0.85	23
			4.5	1.11	10.55	0.81	24
			2.5	1.09	7.82	1.50	25
		$L_t = 1.0$ m	3.65	1.09	7.76	1.44	26
			4.5	1.10	4.96	1.41	27
$v = 1.02$ m s^{-1} (Apr 2018)	TI = 11.7%	$L_t = 0.19$ m	2.5	1.01	11.38	0.19	28
			3.65	1.00	12.40	0.20	29
			4.5	1.00	12.40	0.20	30
$v = 1.03$ m s^{-1} (Jun 2018)	TI = 17.5%	$L_t = 0.43$ m	2.5	1.00	16.62	0.41	31
			3.65	0.99	14.56	0.41	32
			4.5	–	–	–	33
			1.5	1.50	1.44	0.82	34
			2.5	1.50	1.44	0.82	35
			3	1.50	0.62	0.75	36
$v = 1.5$ m s^{-1} (2016)	TI = 1.75%	$L_t = 0.5$ m	3.65	1.50	0.96	0.81	37
			4	1.50	1.44	0.82	38
			4.5	1.49	1.44	0.82	39
			5.5	1.49	1.37	0.81	40

95%. This indicates that if the measuring procedure was repeated 100 times, then it can be expected that 95 of the values calculated would lie within these bounds. Where error bars are not displayed, they have either not been calculated (in the case of numerically integrated quantities such as L_t or swirl) or the calculated bounds of the 95% confidence intervals were within 1% of the reported value. In these cases, they have been omitted for clarity.

Both CFD and experimental data are presented as curves, with crosses marking the positions where an experimental measurement was taken. If error bars are present, then the crosses may have been omitted, for clarity.

7.3   Turbine performance

7.3.1   Flume results

Plots of $\overline{C_P}$, $\overline{C_T}$ and $\overline{C_\theta}$ for the low turbulence, medium turbulence and high turbulence cases are shown in Figures 7.1, 7.2 and 7.3. Information regarding $\overline{C_T}$ was only available from the low-turbulence campaign in 2016, but not in the subsequent campaigns. The thrust data was measured via strain gauges on the steel stanchion of the turbine. This strain is caused by the thrust on the turbine causing a bending moment about the clamping point (above the waterline), which results from the force on all parts of the turbine and support structure, including nacelle, hose and stanchion. It has therefore been included for indicative purposes, but does not provide data for direct comparison with the CFD results, as these record the force on the turbine blades and hub only. Error bars on $\overline{C_P}$ and $\overline{C_\theta}$ have been calculated using the procedure outlined in Chapter 4, with an assumed uncertainty in the mean velocity of ± 0.02 m s^{-1} as the upstream velocity was controlled by setting the flume pump to the same power setting as was used for a previous known velocity, rather than through simultaneous measurement of the velocity whilst recording data from the turbine.

The curves of $\overline{C_P}$ and $\overline{C_\theta}$ from the flume experiments show agreement between all three turbulence cases (within the experimental uncertainties), demonstrating the same trends and similar magnitudes for all cases. As found in previous experimental work with this turbine, the position of maximum $\overline{C_P}$ was found to occur at a tip-speed ratio of approximately $\lambda = 3.65$, with maximum torque occurring at a tip-speed ratio of $\lambda = 2.5$. Nonetheless, it appears that the medium-turbulence case has, in general, the lowest $\overline{C_P}$, the high-turbulence case the highest $\overline{C_P}$, and the low-turbulence case between these two. This could be an indication of transition effects in the boundary layer of the turbine blades. As discussed in section 5.8.5, the Re at which the blade is operating is around
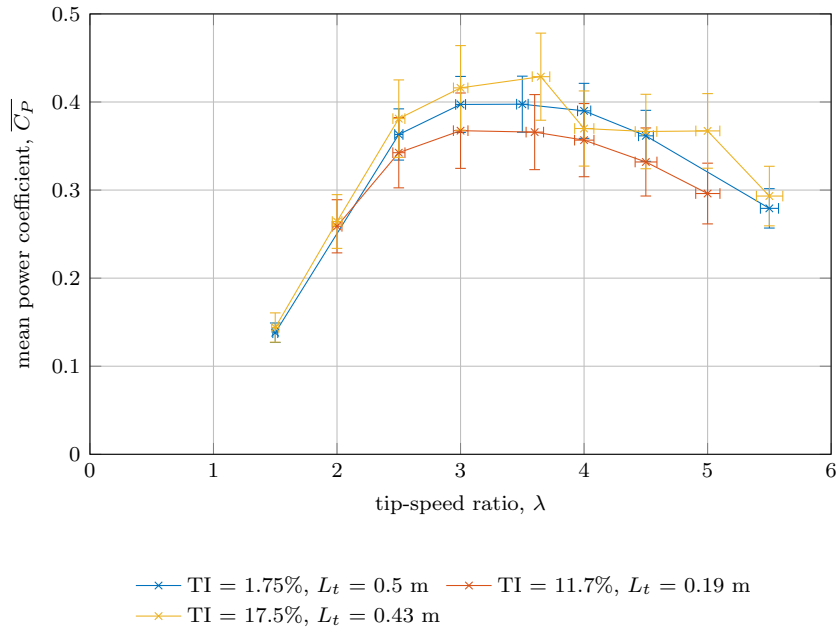
Figure 7.1: $\overline{C_P}$ vs. λ, flume results.
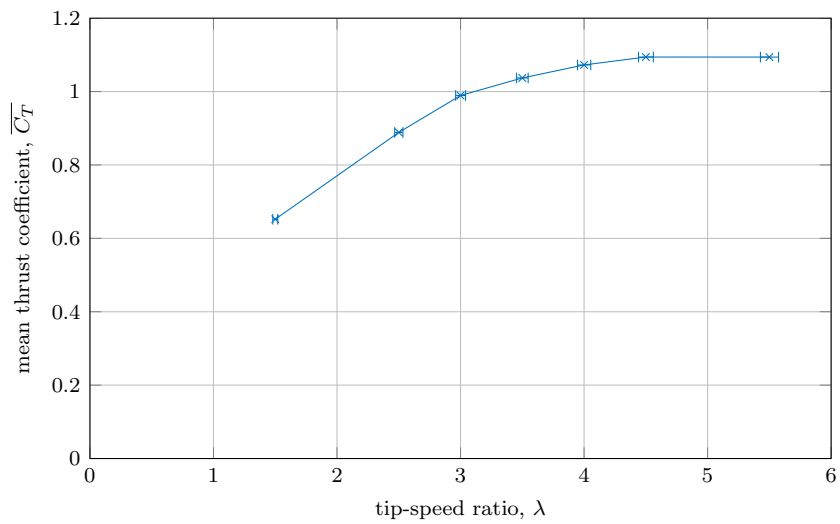
Figure 7.2: $\overline{C_T}$ vs. λ, flume results.
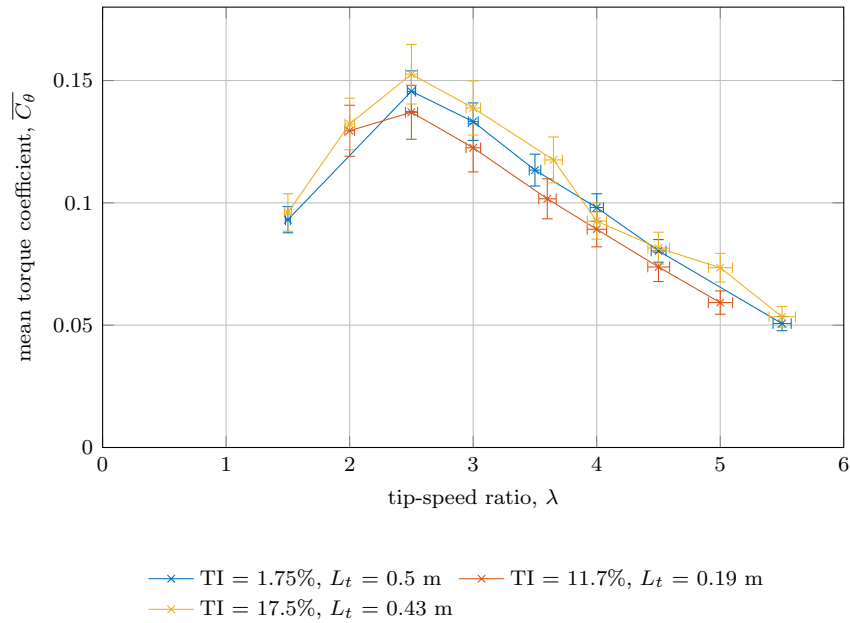
Figure 7.3: $\overline{C_\theta}$ vs. λ, flume results.

the point of transition from laminar to turbulent flow. In general, it might be expected that an increase in turbulence, which will disrupt the flow over the turbine blade, will lead to a decrease in turbine performance, explaining the drop in performance from the low-turbulence case to the medium-turbulence case. However, due to the transitional nature of the boundary layer, it is possible that a separation bubble is being formed in these cases. With the large amount of turbulence in the high-turbulence case, it is unlikely that any separation bubble will survive due to the increase of energy in the boundary layer. If separation does not take place, then it is possible that, the turbine performance will actually increase in the high-turbulence case, reflecting the behaviour seen in Figure 7.1.

Figure 7.2 shows that $\overline{C_T}$ increases steadily from low values of tip-speed ratio, but that this trend starts to flatten-off around $\lambda = 4$. These results confirm that CFD investigations of tip-speed ratios of $\lambda = 2.5, 3.65$ and 4.5 will give insight into high-torque, high-power and high-thrust turbine operating conditions, respectively.

7.3.2   CFD results

The mean and standard deviations of power, thrust and torque coefficients for all the CFD runs are shown in Table 7.2. For the low-turbulence CFD conditions (run numbers 34–40), power, thrust and torque curves are shown against tip-
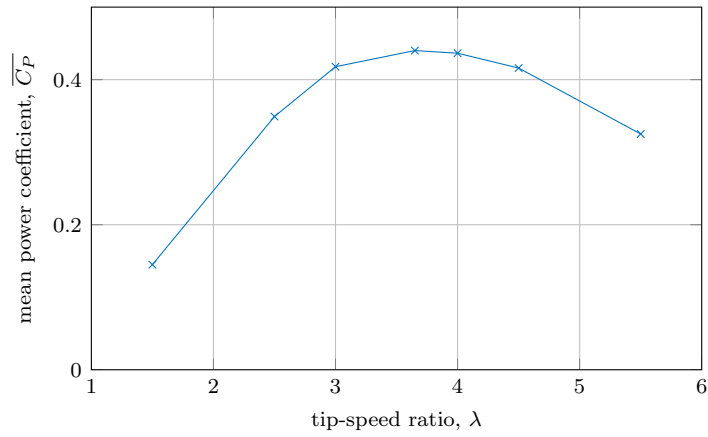
Figure 7.4: $\overline{C_P}$ vs. λ, low ambient turbulence.
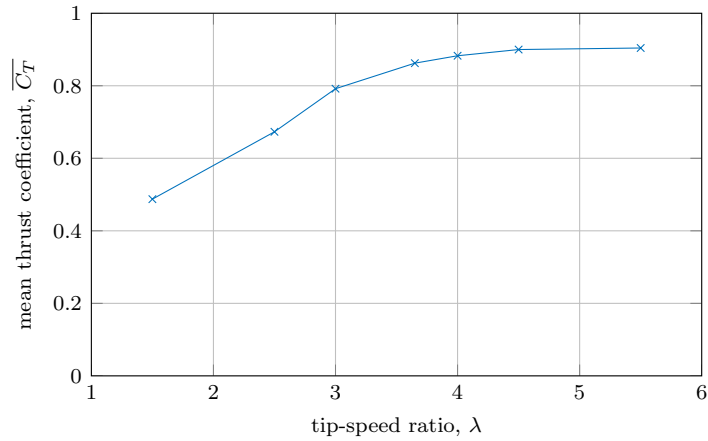
Figure 7.5: $\overline{C_T}$ vs. λ, low ambient turbulence.

speed ratio in Figures 7.4, 7.5 and 7.6 respectively. Such curves are not presented for the other flow conditions, as in these cases only three tip-speed ratios were investigated.

7.3.3   Validation of CFD

Comparisons of CFD results for $\overline{C_P}$ and $\overline{C_\theta}$ were made for all three flume cases, with $\overline{C_T}$ also being compared for the low-turbulence case for which comparison C_T data were available. For the low-turbulence case, these can be seen in Figures 7.7, 7.8 and 7.9, for the flume case using the fine grid in Figures 7.10 and 7.11, and for the flume case using the coarse grid in Figures 7.12 and 7.13.

Figure 7.7 shows that there is good agreement at low values of tip-speed ratio between the flume data and CFD for values of $\overline{C_P}$. The CFD results

Table 7.2: Turbine performance metrics, all CFD runs. The velocity used for the calculations of C_P, C_T and C_θ are the target velocities.

Target flow conditions				mean values			standard deviation, σ			
v / m s^{-1}	TI /%	L_t /m	λ	C_P	C_T	C_θ	C_P	C_T	C_θ	run no.
1.1	5	0.25	2.5	0.35	0.67	0.14	0.0118	0.017	0.0047	1
1.1	5	0.25	3.65	0.43	0.85	0.12	0.0192	0.024	0.0052	2
1.1	5	0.25	4.5	0.41	0.89	0.09	0.0182	0.025	0.0041	3
1.1	5	0.50	2.5	0.35	0.67	0.14	0.0200	0.036	0.0080	4
1.1	5	0.50	3.65	0.44	0.86	0.12	0.0398	0.050	0.0109	5
1.1	5	0.50	4.5	0.42	0.90	0.09	0.0203	0.025	0.0045	6
1.1	5	1.00	2.5	0.35	0.67	0.14	0.0101	0.016	0.0040	7
1.1	5	1.00	3.65	0.43	0.85	0.12	0.0200	0.025	0.0055	8
1.1	5	1.00	4.5	0.41	0.89	0.09	0.0217	0.026	0.0048	9
1.1	10	0.25	2.5	0.35	0.67	0.14	0.0289	0.040	0.0116	10
1.1	10	0.25	3.65	0.41	0.82	0.11	0.0468	0.058	0.0128	11
1.1	10	0.25	4.5	0.44	0.92	0.10	0.0486	0.055	0.0108	12
1.1	10	0.50	2.5	0.34	0.66	0.14	0.0237	0.046	0.0095	13
1.1	10	0.50	3.65	0.44	0.86	0.12	0.0210	0.031	0.0057	14
1.1	10	0.50	4.5	0.44	0.93	0.10	0.0463	0.058	0.0103	15
1.1	10	1.00	2.5	0.34	0.66	0.14	0.0213	0.033	0.0085	16
1.1	10	1.00	3.65	0.43	0.85	0.12	0.0431	0.051	0.0118	17
1.1	10	1.00	4.5	0.44	0.92	0.10	0.0486	0.055	0.0108	18
1.1	20	0.25	2.5	0.36	0.70	0.14	0.0529	0.075	0.0212	19
1.1	20	0.25	3.65	0.43	0.84	0.12	0.0815	0.100	0.0223	20
1.1	20	0.25	4.5	0.43	0.91	0.10	0.1086	0.126	0.0241	21
1.1	20	0.50	2.5	0.33	0.65	0.13	0.0407	0.061	0.0163	22
1.1	20	0.50	3.65	0.50	0.91	0.14	0.1304	0.151	0.0357	23
1.1	20	0.50	4.5	0.44	0.92	0.10	0.1121	0.135	0.0249	24
1.1	20	1.00	2.5	0.33	0.65	0.13	0.0447	0.081	0.0179	25
1.1	20	1.00	3.65	0.42	0.83	0.12	0.0878	0.107	0.0241	26
1.1	20	1.00	4.5	0.40	0.88	0.09	0.0653	0.080	0.0145	27
1.02	11.7	0.19	2.5	0.33	0.66	0.13	0.0365	0.070	0.0146	28
1.02	11.7	0.19	3.65	0.44	0.85	0.12	0.0678	0.090	0.0186	29
1.02	11.7	0.19	4.5	0.42	0.90	0.09	0.0802	0.102	0.0179	30
1.03	17.5	0.43	2.5	0.34	0.68	0.14	0.0728	0.136	0.0292	31
1.03	17.5	0.43	3.65	0.45	0.86	0.12	0.1105	0.144	0.0303	32
1.03	17.5	0.43	4.5	–	–	–	–	–	–	33
1.5	1.75	0.50	1.5	0.14	0.49	0.10	0.0028	0.010	0.0019	34
1.5	1.75	0.50	2.5	0.35	0.67	0.14	0.0074	0.010	0.0030	35
1.5	1.75	0.50	3	0.42	0.79	0.14	0.0062	0.009	0.0021	36
1.5	1.75	0.50	3.65	0.44	0.86	0.12	0.0081	0.010	0.0022	37
1.5	1.75	0.50	4	0.44	0.88	0.11	0.0148	0.017	0.0037	38
1.5	1.75	0.50	4.5	0.42	0.90	0.09	0.0158	0.018	0.0035	39
1.5	1.75	0.50	5.5	0.33	0.90	0.06	0.0164	0.019	0.0030	40
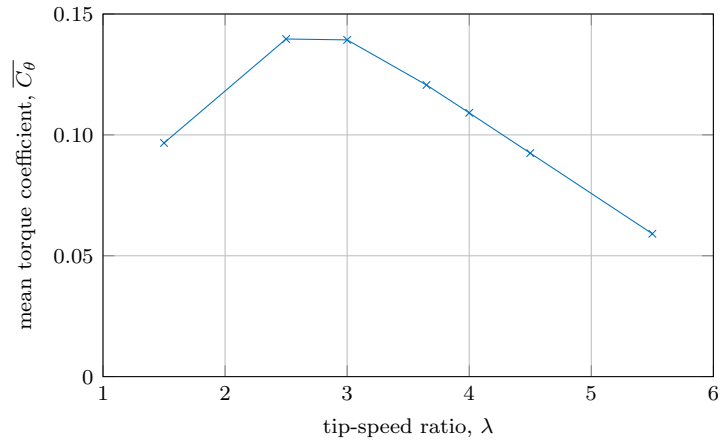
Figure 7.6: $\overline{C_\theta}$ vs. λ, low ambient turbulence.
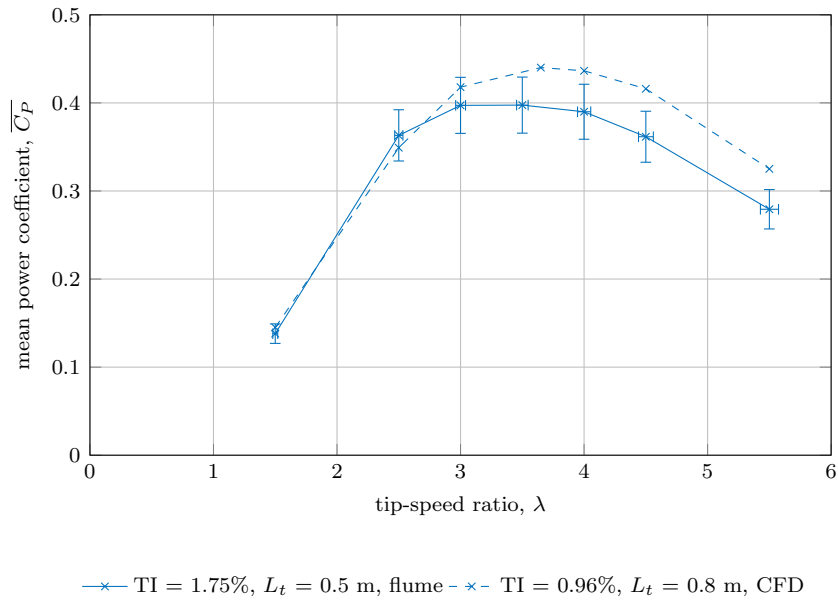
—×— TI = 1.75%, $L_t = 0.5$ m, flume   - -×- - TI = 0.96%, $L_t = 0.8$ m, CFD

Figure 7.7: Validation using low-turbulence flume results, $\overline{C_P}$.
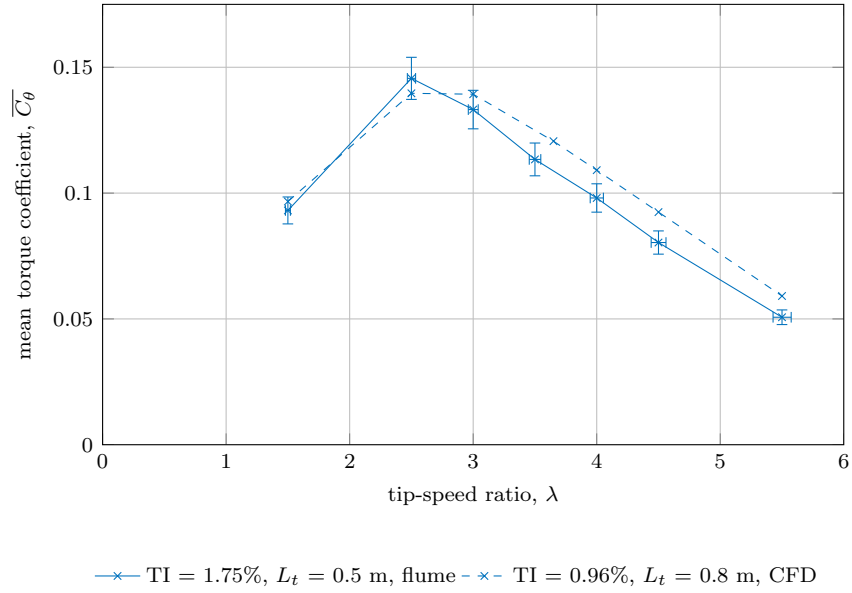
Figure 7.8: Validation using low-turbulence flume results, $\overline{C_\theta}$.
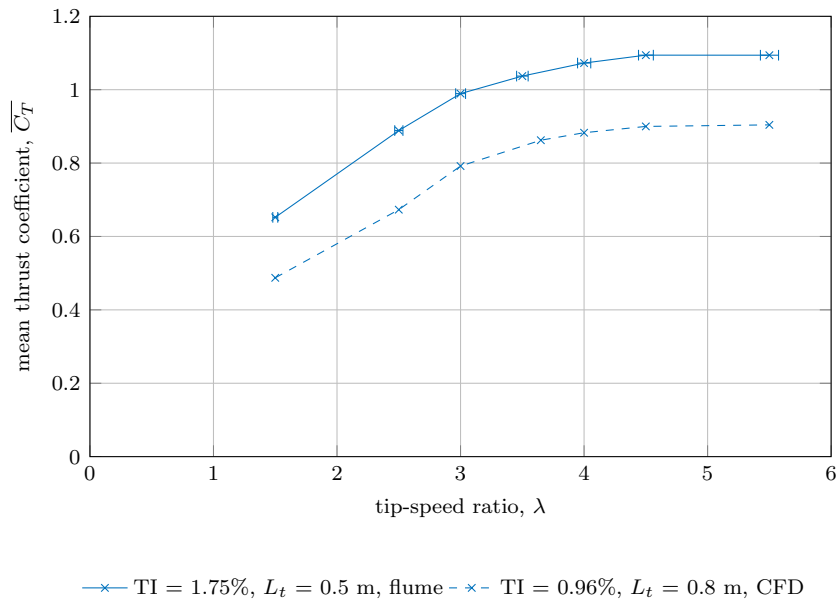
Figure 7.9: Validation using low-turbulence flume results, $\overline{C_T}$.

$$\text{---×--- TI} = 11.7\%, \ L_t = 0.19 \ \text{m, flume} \quad \text{--×-- TI} = 12\%, \ L_t = 0.19 \ \text{m, CFD}$$
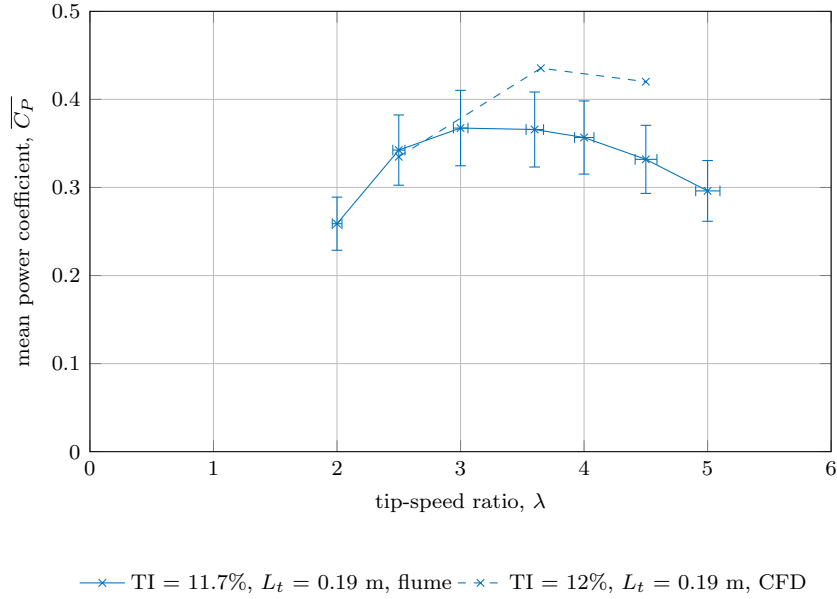
Figure 7.10: Validation using flume results with the fine grid, $\overline{C_P}$.

show a tendency to slightly over-predict $\overline{C_P}$ at higher tip-speed ratios, but overall agreement is good. In a similar way, Figure 7.8 shows that there is good agreement between the CFD and flume results for $\overline{C_\theta}$, with a slight over-prediction once again evident in the higher tip-speed ratios. The reason for this is unclear, but given the v^3 dependence of C_P and v^2 dependence of C_θ, both metrics are very sensitive to slight changes in inflow velocity, so a slight reduction in inflow velocity would lead to a reduction in both $\overline{C_P}$ and $\overline{C_\theta}$ measured in the flume.

Figure 7.9 compares the flume results for $\overline{C_T}$ to the CFD results. Whilst there is a shift between the curves, the shapes are very similar. As discussed above, the C_T calculation for the flume is based on strain gauge measurements on the stanchion, whereas the calculation for the CFD is based on the thrust on the blades and hub only. As both drag on the turbine nacelle and stanchion contribute to the thrust force measured in the flume, these would be expected to increase the calculated value of C_T by a constant amount for all tip-speed ratios. Shifting the curve of $\overline{C_T}$ obtained from the flume down by 0.2 gives an almost exact match between the flume and the CFD; therefore, the CFD data here is considered to be a good match.

Figure 7.10 compares $\overline{C_P}$ data obtained from the flume case using the fine grid, to that from the equivalent conditions in the CFD model. CFD data is available for three points at $\lambda = 2.5, 3.65$ and 4.5. The match here is similar to that from the low-turbulence case, in that a match is within the experimental
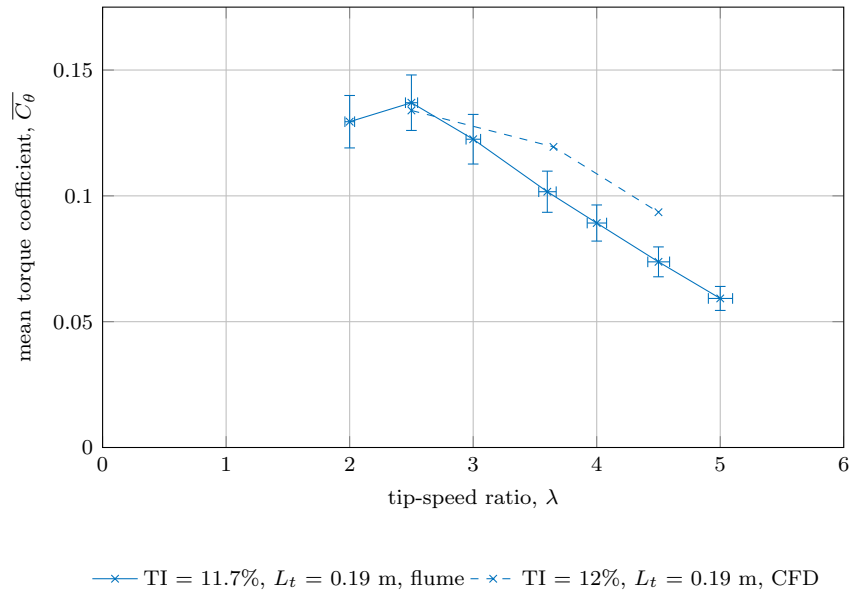
Figure 7.11: Validation using flume results with the fine grid, $\overline{C_\theta}$.

error for tip-speed rations of less than approximately 3.5, with over-prediction of both $\overline{C_P}$ and $\overline{C_\theta}$ beyond this point (see also Figure 7.11). Despite this over-prediction, the CFD data supports the assumption of a peak in $\overline{C_P}$ at $\lambda = 3.65$, and of $\overline{C_\theta}$ at $\lambda = 2.5$.

Figures 7.12 and 7.13 compare flume data to CFD data for $\overline{C_P}$ and $\overline{C_\theta}$ for the high turbulence case, behind the coarse grid. For tip-speed ratios of $\lambda = 2.5$ and 3.65, the CFD predictions lie within the experimental uncertainty from the flume measurements. As stated above (see section 7.1), the data for the $\lambda = 4.5$ case were found to be corrupted, and has therefore not been included in these figures. Whilst these figures only show two points of CFD data, the matching does appear to be better than in the low-turbulence and fine-grid cases. This may be due to the greater level of turbulence intensity preventing a separation bubble forming, and leading to a turbulent boundary layer on the blade in the flume. The CFD turbulence model at the values of y^+ used (see section 5.8.5) assumes a fully turbulent boundary layer, which may explain the better matching in this case.

7.3.4 Impact of turbulence on turbine performance

It is conceivable that both turbulence intensity as well as turbulence length scale could have an impact on turbine performance. Each of the CFD cases 1–27 have their own precise value of turbulence intensity and L_t calculated and recorded in Table 7.1. For each value of tip-speed ratio, nine different turbulence

146
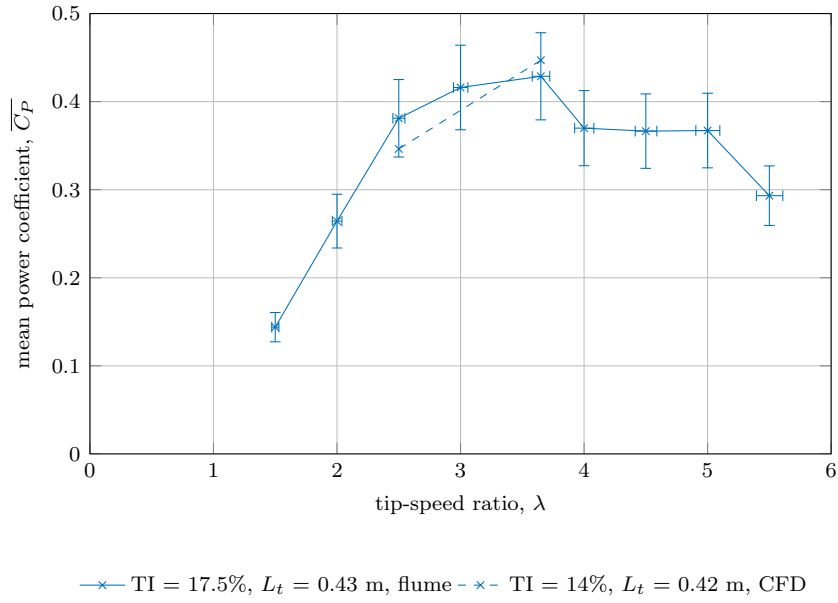
Figure 7.12: Validation using flume results with the coarse grid, $\overline{C_P}$.
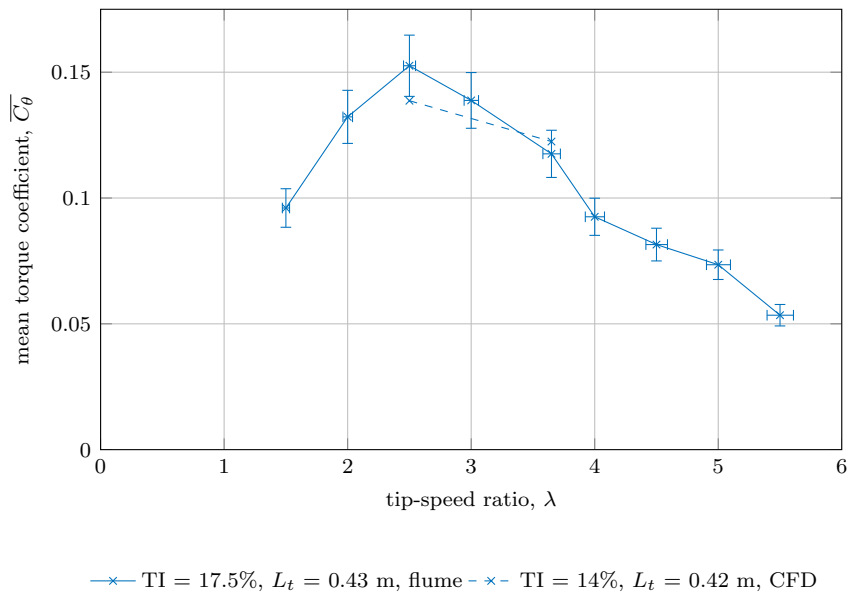
Figure 7.13: Validation using flume results with the coarse grid, $\overline{C_\theta}$.
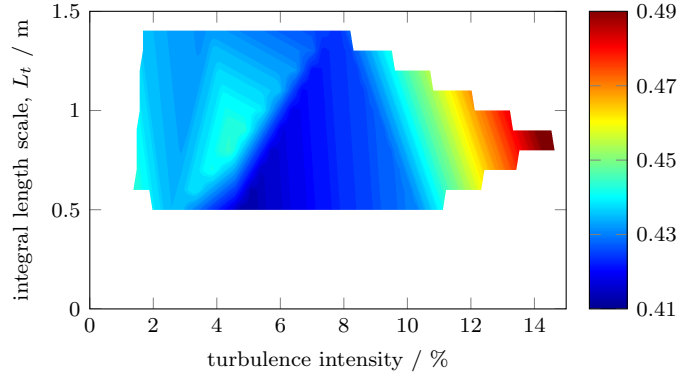
Figure 7.14: Impact of turbulence intensity and length scale on $\overline{C_P}$, $\lambda = 3.65$.

conditions are available. In order to visualise the impact of turbulence intensity and length scale on the turbine performance parameters, Figures 7.14–7.23 plot each performance metric (C_P, C_T and C_θ) against turbulence intensity (on the horizontal axis) and integral length scale (on the vertical axis). Each figure is for a particular tip-speed ratio and their 2D nature allows an assessment of the impact of turbulence intensity and length scale across the complete variable space.

Figures 7.14–7.16, show the impact of turbulence intensity and length scale on $\overline{C_P}$, $\overline{C_T}$ and $\overline{C_\theta}$ for the $\lambda = 3.65$ case. These will be discussed in detail below, but it will be noted that the trends in all cases are the same, regardless of whether it is power, thrust or torque which is being examined. In a similar way, Figures 7.17–7.19 show the impact of turbulence intensity and length scale on σ_{C_P}, σ_{C_T} and σ_{C_θ} (i.e. the fluctuations in power, torque and thrust) for the $\lambda = 3.65$ case. These figures also show the same trends as each other, regardless of which metric is being examined. Therefore, for the $\lambda = 2.5$ and 4.5 cases, only the plots for $\overline{C_P}$ and σ_{C_P} are shown; the trends being the same for the thrust and torque coefficients and their fluctuations.

The impact of turbulence intensity and length scale on mean turbine performance characteristics is presented in Figures 7.20, 7.14 and 7.22 for $\overline{C_P}$ in the $\lambda = 2.5, 3.65$ and 4.5 cases respectively. In addition, Figures 7.15 and 7.16 display the same information for $\overline{C_T}$ and $\overline{C_\theta}$ in the $\lambda = 3.65$ case. It is difficult to establish a clear trend across all tip-speed ratios, other than that a tendency to produce the highest values of performance metrics at the highest turbulence intensities. For all tip-speed ratios, the lowest values of these performance metrics appear to be in the region where turbulence intensity is approximately 6–8%, with lower turbulence intensities producing approximately a 5% increase in performance over the minimum values, and the highest values being seen at the
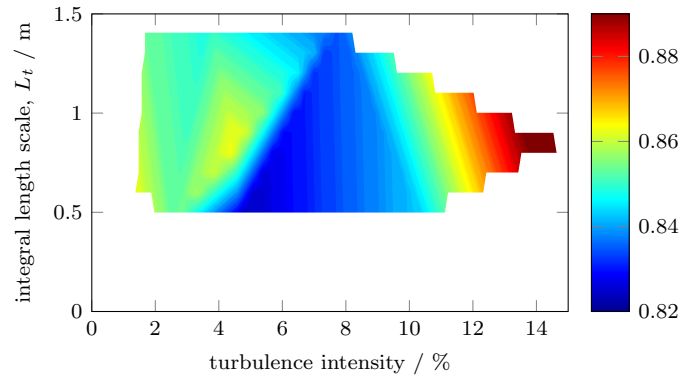
Figure 7.15: Impact of turbulence intensity and length scale on $\overline{C_T}$, $\lambda = 3.65$.
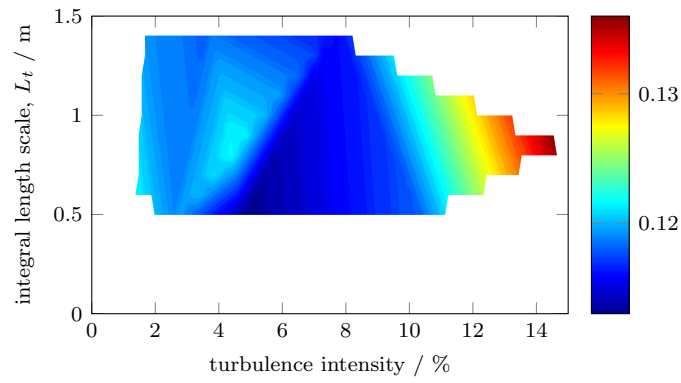
Figure 7.16: Impact of turbulence intensity and length scale on $\overline{C_\theta}$, $\lambda = 3.65$.
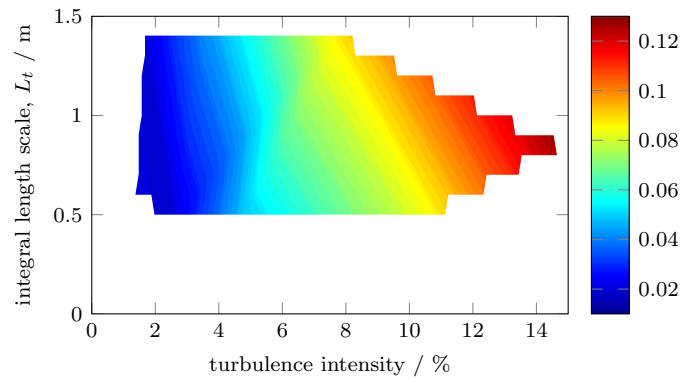
Figure 7.17: Impact of turbulence intensity and length scale on σ_{C_P}, $\lambda = 3.65$.

149
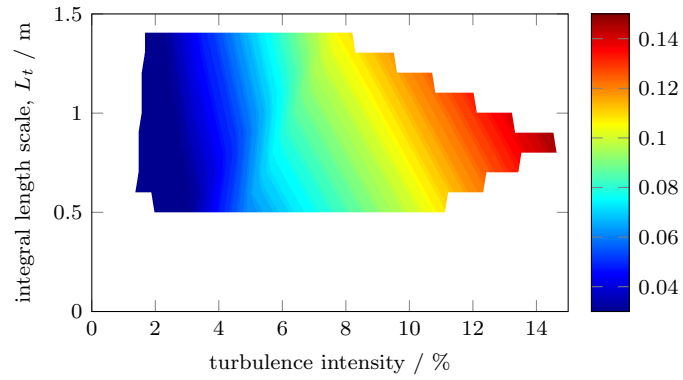
Figure 7.18: Impact of turbulence intensity and length scale on σ_{C_T}, $\lambda = 3.65$.
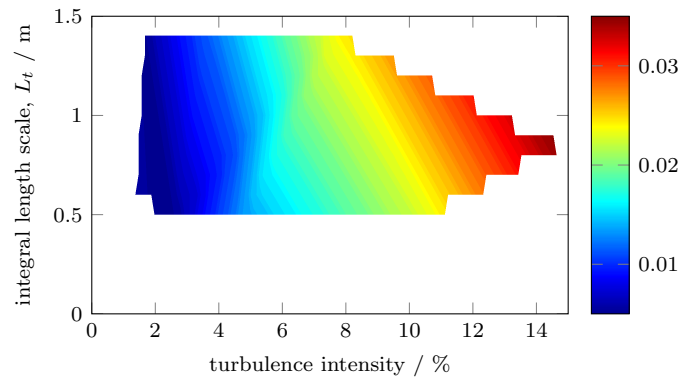
Figure 7.19: Impact of turbulence intensity and length scale on σ_{C_θ}, $\lambda = 3.65$.
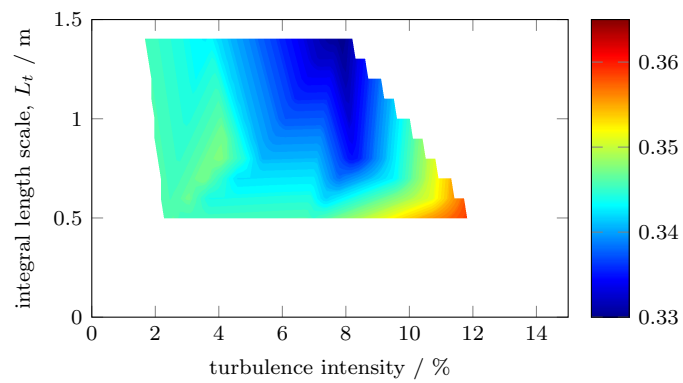
Figure 7.20: Impact of turbulence intensity and length scale on $\overline{C_P}$, $\lambda = 2.5$.
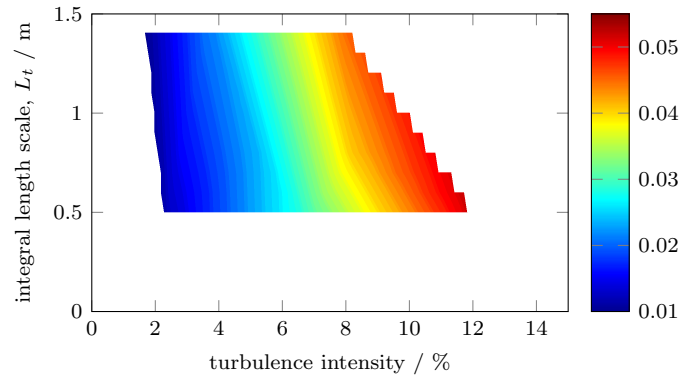
Figure 7.21: Impact of turbulence intensity and length scale on σ_{C_P}, $\lambda = 2.5$.
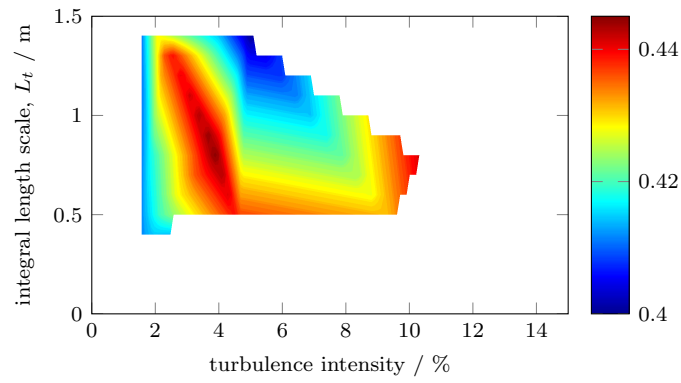
Figure 7.22: Impact of turbulence intensity and length scale on $\overline{C_P}$, $\lambda = 4.5$.
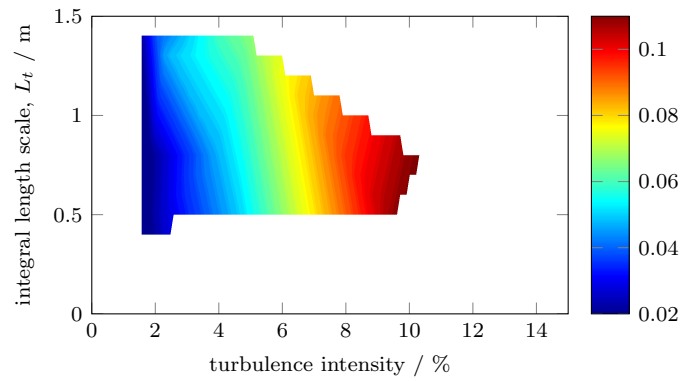
Figure 7.23: Impact of turbulence intensity and length scale on σ_{C_P}, $\lambda = 4.5$.

highest turbulence intensities. It is unclear what might be causing this effect, but it appears to be replicated in the performance of the turbine as measured in the flume experiments (e.g. Figure 7.1) where the highest and lowest turbulence intensities produce the highest performance, and the medium turbulence intensity case producing the lowest performance. This could be due to increasing turbulence intensity generally reducing turbine performance as fluctuations mean that blades are not operating consistently at their design angles of attack, but beyond a certain point the effect of turbulence increasing the amount of energy in the flow begins to outweigh this effect. The fluctuations in the oncoming flow are greater, but due to the v^3 dependence of C_P and v^2 dependence of C_T and C_θ, these performance metrics tend to increase when compared to the results in a low-turbulence flow.

No clear trend, consistent between different tip-speed ratios, can be seen indicating a dependence of mean turbine performance on turbulence length scale.

There is a clear trend showing the impact of turbulence intensity and length scale on the magnitudes of the fluctuations of each of the performance metrics. These can be seen in Figures 7.17–7.19, 7.21 and 7.23. This shows that, for all tip-speed ratios, an increase in turbulence intensity increases the magnitude of the fluctuations (as might be expected). There is also indication of a slight dependence on length scale, with a larger length scale also leading to greater fluctuations in turbine performance, with this dependence becoming more pronounced at higher values of turbulence intensities. This increase in fluctuations with increasing length scale can be explained by considering how turbulence at different length scales interacts with the turbine as a whole. If the turbulence in a flow consists of many small-scale features, limited in spatial extent (regardless of how strong they may be), then it can be expected that a turbine blade or blades may be interacting with many of these features simultaneously. Given the random nature of turbulence it can be expected that these will not be synchronised or coherent with each other, meaning that whilst one feature may contribute to an increase in, for example, C_P, another may simultaneously contribute to a decrease in C_P, leading to little overall change to the value of C_P for the turbine as a whole. In contrast to this, if the spatial extent of each turbulent feature is larger, then the turbine will interact with fewer of these features at any given time. In this case, there will be less of a tendency for the effects of the features to cancel each other out, leading to larger change in the value of C_P, and therefore greater fluctuations.

7.4 Wake recovery

7.4.1 CFD results

Wake recovery will be primarily examined using centreline and volumetric averaged wake recovery curves (as detailed in Chapter 4). However, in order to fully understand some of the effects and impacts (particularly the impact of tip-speed ratio, and the results for wake width), it is useful to present wake profiles for a specific case. Figures 7.24 to 7.30 present wake profiles for cases 34–40 for the low-turbulence CFD conditions.

These profiles show that the shape of the wake profiles is dependent on tip-speed ratio, with low tip-speed ratio, low-thrust cases leading to v-shaped wake profiles, and high tip-speed ratio, high-trust cases leading to wake profiles which approximate to an inverted top-hat shape, with the highest thrust cases leading to profiles with three minima. These will be discussed in detail in section 7.4.5.

7.4.2 Flume results

Results for the low turbulence intensity, fine grid and coarse grid testing campaigns were analysed, with the centreline velocity recovery being presented in Figure 7.31, and volumetric averaged velocity recovery presented in Figure 7.32.
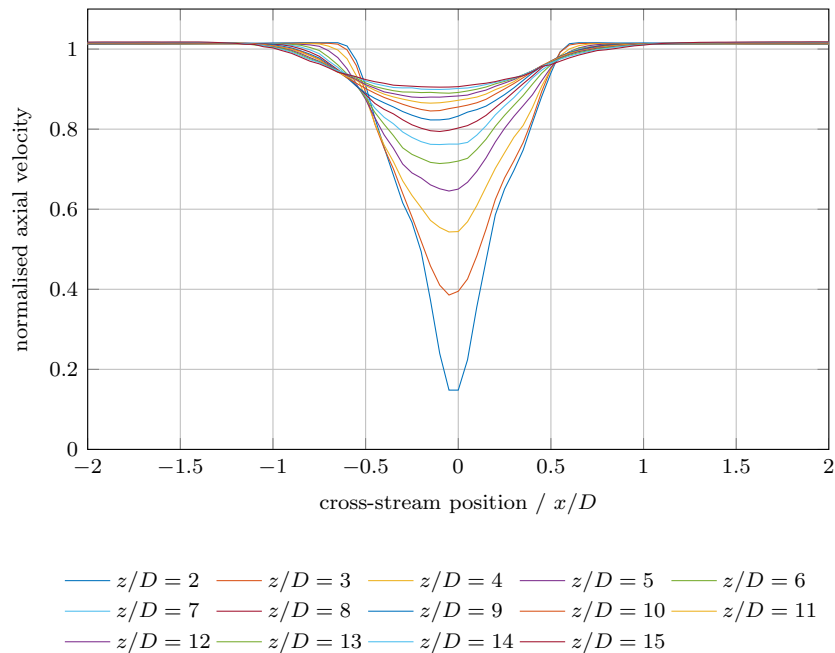
Figure 7.24: CFD wake profiles for the low-turbulence intensity case with a tip-speed ratio of $\lambda = 1.5$.
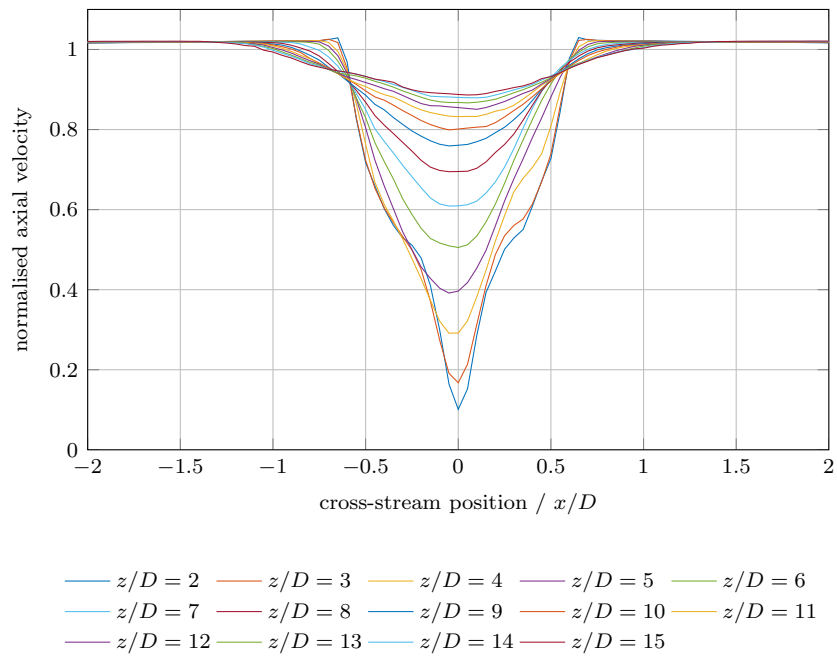
Figure 7.25: CFD wake profiles for the low-turbulence intensity case with a tip-speed ratio of $\lambda = 2.5$.
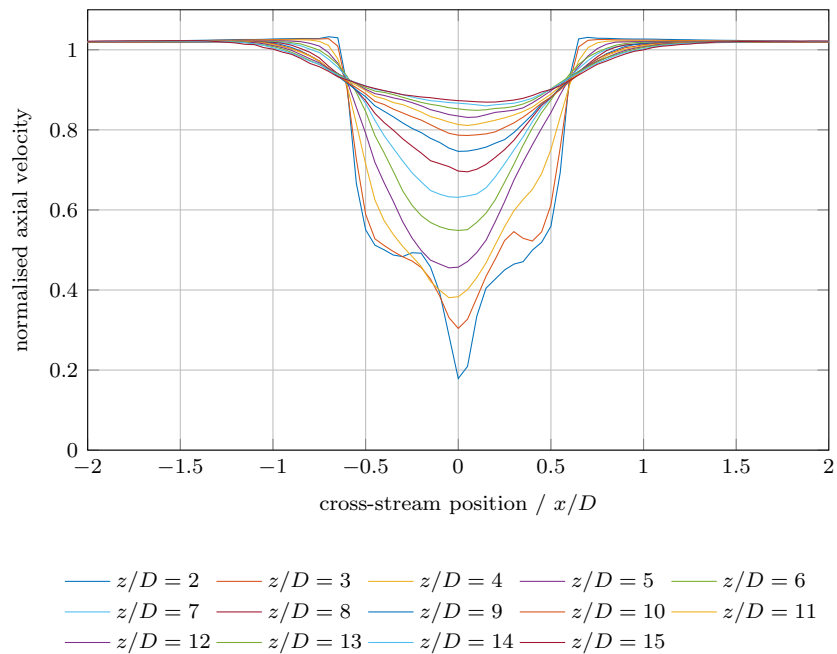
Figure 7.26: CFD wake profiles for the low-turbulence intensity case with a tip-speed ratio of $\lambda = 3.0$.
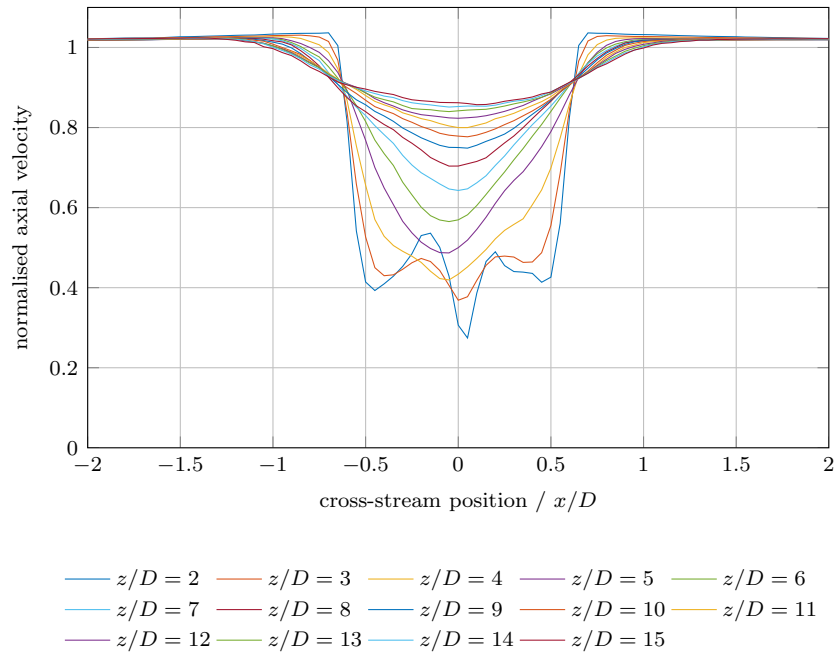
Figure 7.27: CFD wake profiles for the low-turbulence intensity case with a tip-speed ratio of $\lambda = 3.65$.
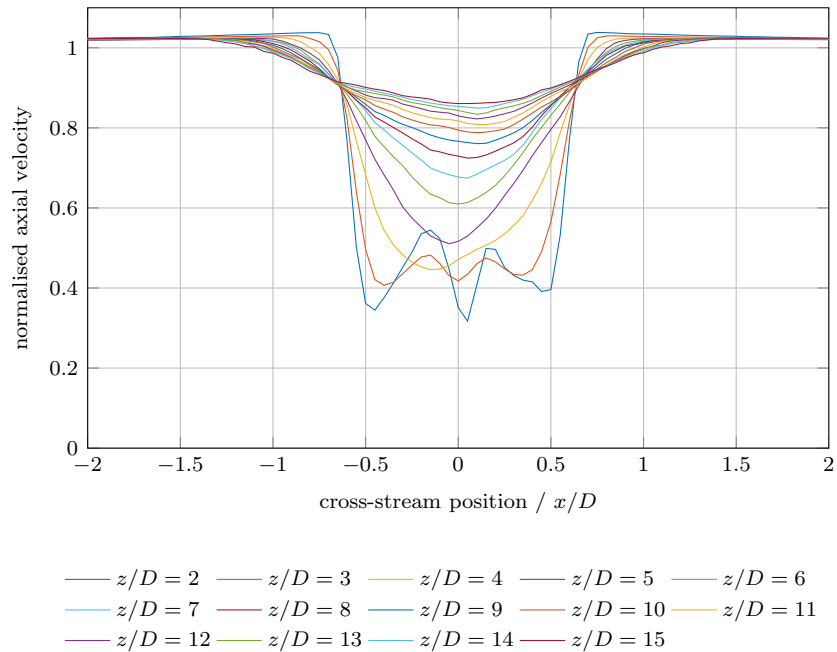
Figure 7.28: CFD wake profiles for the low-turbulence intensity case with a tip-speed ratio of $\lambda = 4.0$.
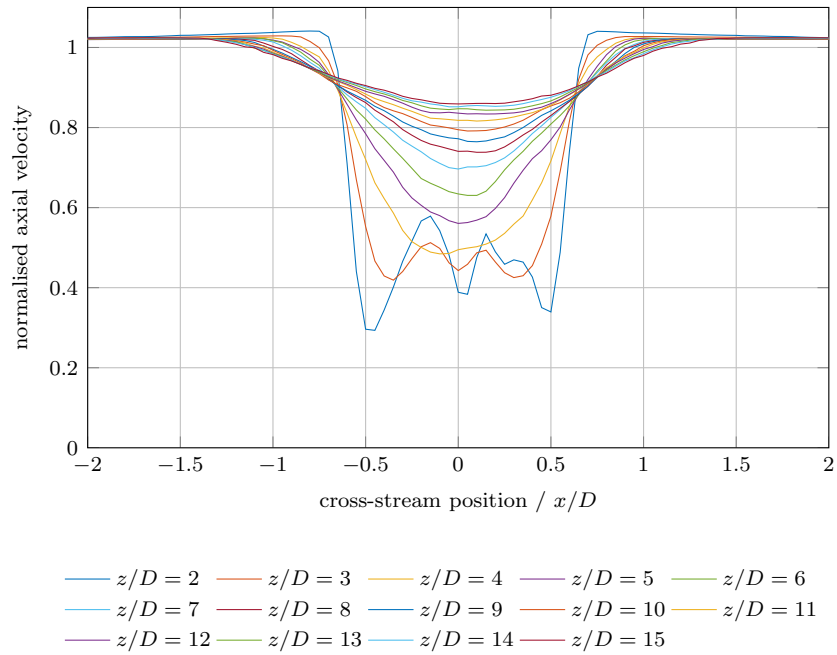
Figure 7.29: CFD wake profiles for the low-turbulence intensity case with a tip-speed ratio of $\lambda = 4.5$.
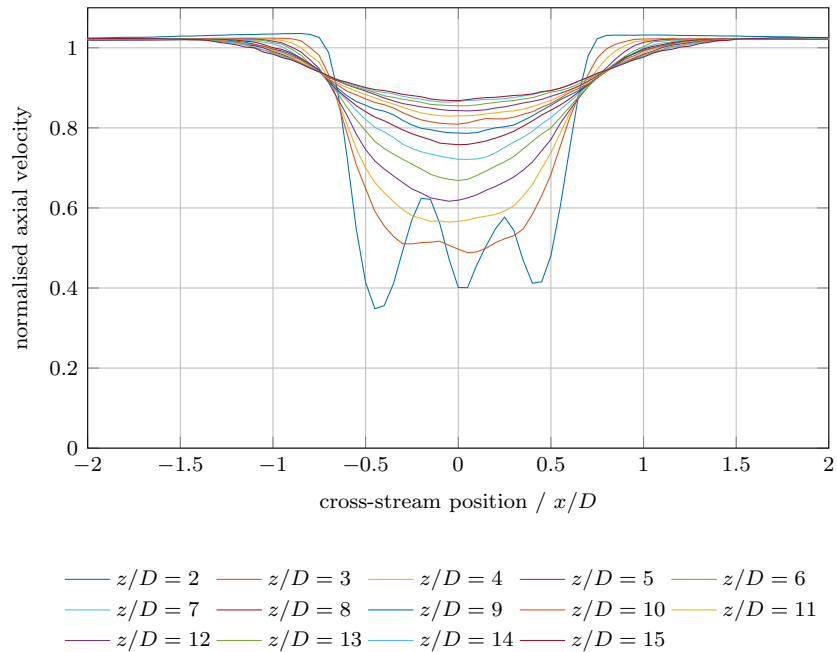
Figure 7.30: CFD wake profiles for the low-turbulence intensity case with a tip-speed ratio of $\lambda = 5.5$.

Both of these figures show a clear trend — that higher turbulence intensity is associated with faster wake recovery. This is expected, and follows trends found in previous experimental work [53],[60]. Further to this, for the two test campaigns using grid-generated turbulence, three tip-speed ratios were used, and a trend is apparent here too; in all cases, the $\lambda = 2.5$ cases shows the fastest overall recovery, with $\lambda = 3.65$ and 4.5 showing similar rates of wake recovery. This would appear to then show a similar trend with tip-speed ratio to that shown by the C_T curve (Figure 7.2) with a larger difference between the thrust at $\lambda = 2.5$ and $\lambda = 3.65$, than between the $\lambda = 3.65$ and $\lambda = 4.5$ cases.

As expected for a wake recovering due to mixing with the free stream, the centreline velocity (Figure 7.31) is consistently lower than the volumetric average velocity (Figure 7.32) until approximately $z/D = 9$ downstream of the turbine, where the normalised velocities becomes similar, regardless of which metric is used. This suggests that by this point the wake region has become homogeneous, and that the mixing layer has reached the centreline.

One area of interest is the near wake ($z/D \leq 4$) centreline recovery for the turbine downstream of the fine grid. In this region, the $\lambda = 2.5$ case is less recovered than the $\lambda = 3.65$ or 4.5 cases, in contrast to the overall trend for the rest of the wake. This suggests that the $\lambda = 2.5$ wake is demonstrating a large amount of inhomogeneity in this near wake region. This could be due to the fact that the blades in the $\lambda = 2.5$ case are producing less thrust, and therefore the influence of the nacelle is greater, leading to a lower velocity core when compared to the rest of the wake region. In addition to this, the $\lambda = 2.5$ case is the case with the greatest rotational motion (swirl — see section 7.6) in the wake, which could be hindering wake mixing in this near-wake region. This trend is not apparent in the highest turbulence intensity case, but this could be due to the greater level of turbulence leading to more mixing, making this effect less apparent. This is supported by CFD results presented below in section 7.4.5.
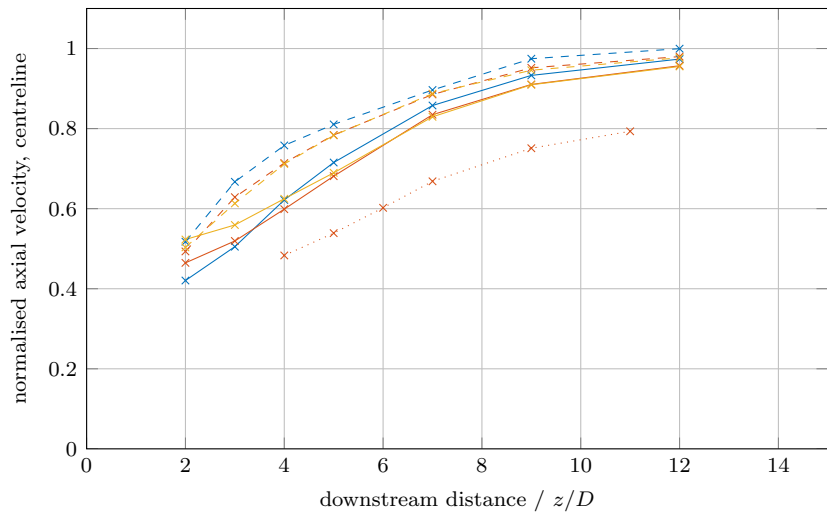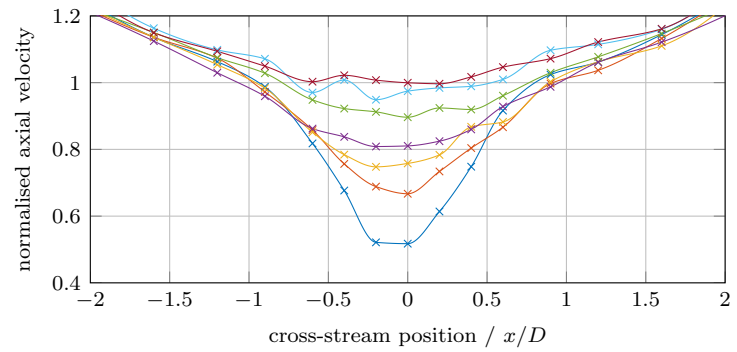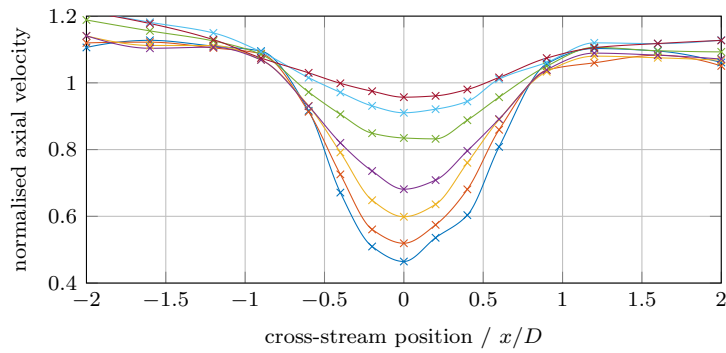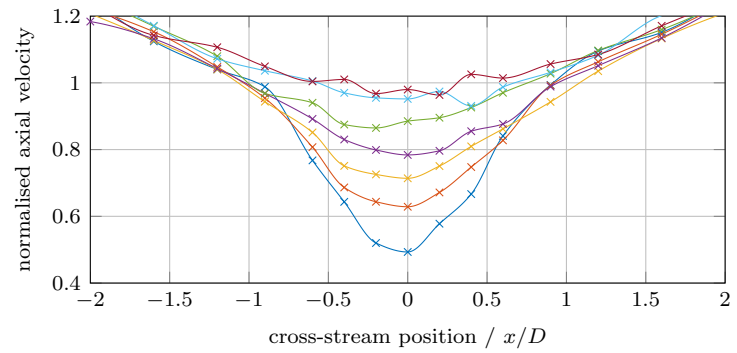
Figure 7.31: Centreline wake recovery: flume results.
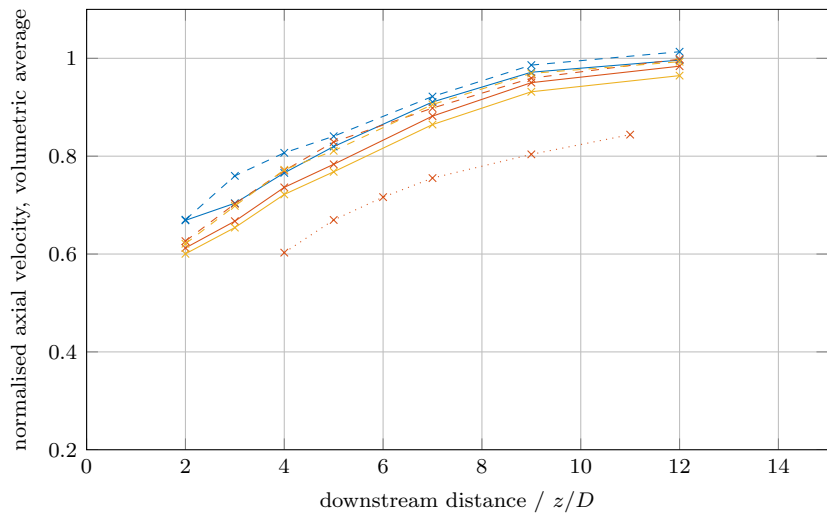
Figure 7.32: Volumetric averaged wake recovery: flume results.
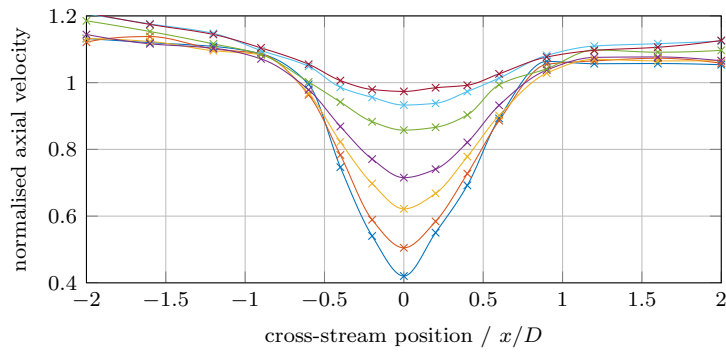
(a) $\lambda = 2.5$, TI = 11.7%, $L_t = 0.19$ m

(b) $\lambda = 2.5$, TI = 17.5%, $L_t = 0.43$ m

(c) $\lambda = 3.65$, TI = 11.7%, $L_t = 0.19$ m

(d) $\lambda = 3.65$, TI = 17.5%, $L_t = 0.43$ m
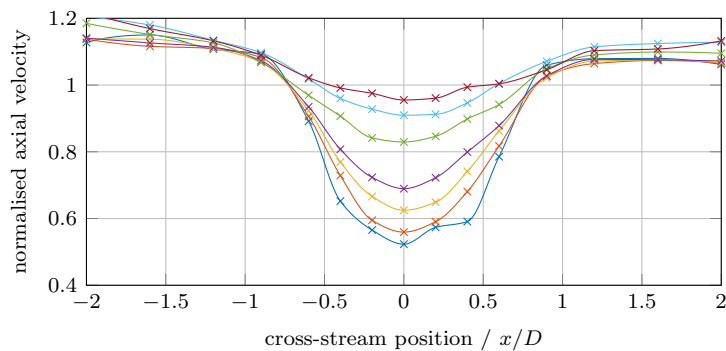
(e) $\lambda = 4.5$, TI = 11.7%, $L_t = 0.19$ m
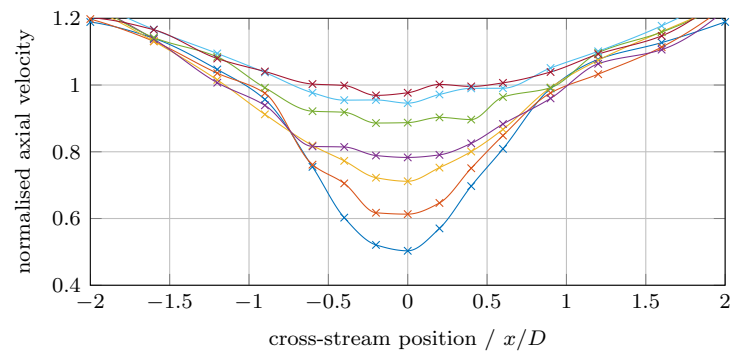
(f) $\lambda = 4.5$, TI = 17.5%, $L_t = 0.43$ m

**Figure 7.33:** Wake profiles for the fine- (subfigures a, c, e) and coarse-grid (subfigures b, d, f) flume cases.

7.4.3 Validation of CFD

Validation of the CFD for prediction of wake recovery is made for the low-turbulence case by comparison of flume results to CFD along the centreline (Figure 7.34) and for volumetric averaged wake recovery (Figure 7.35). These both show good matching in the region for which both CFD and flume data are available, with excellent matching from $z/D = 8$ for the centreline recovery, and from $z/D = 6$ for the volumetric averaged recovery. It can be expected that the volumetric-averaged method will provide slightly better matching, as the combination of area-averaging as well as time-averaging makes this metric less sensitive to slight changes in the velocity distribution within the wake. The small discrepancies between flume and CFD results in the near-wake region can be explained by the fact that the flow field in this region is likely to be more complex and thus more difficult to accurately reproduce in a simulation; additionally, an enhancement of the mesh around the turbine nacelle as discussed in section 5.8.3, could lead to more accurate modelling of this near-wake region, albeit at the cost of additional computational expense. Mixing and recovery in the far wake is likely to be dominated by the outer shear layer of the wake, and therefore less dependent on the mesh directly around the turbine nacelle. This suggests that the DES model has the ability to provide accurate predictions of the recovery of a turbine wake from at least the mid-wake region, in low-ambient turbulence conditions.

The validation plots for wake recovery for the testing campaign behind the fine grid are presented in Figure 7.36 for the centreline wake, and Figure 7.37 for the volumetric averaged wake. As with the low turbulence intensity case, agreement is better in the volumetric averaged wake, again probably due to the combination of both time- and area-averaging. Agreement is generally good, although deteriorates beyond approximately $z/D = 7$, where the CFD under-predicts the recovery by approximately 8%. The difference in recovery rates for the different tip-speed ratios is well reproduced; in the volumetric-averaged recovery a tip-speed ratio of $\lambda = 2.5$ recovers faster than the other two cases, which show similar rates of recovery, with a tendency for the $\lambda = 3.65$ case to recover slightly faster than the $\lambda = 4.5$ case. Along the centreline, this trend of lower tip-speed ratios showing faster recovery is reversed in the near wake region, but this is reflected in both the CFD and the flume results. At a downstream distance of between $z/D = 3$ and $z/D = 5$, the trend in wake recovery with tip-speed ratio reverts to that seen in the volumetric averaged wakes. Whilst the agreement between CFD and flume results behind the fine grid may not be quite as close as in the low-turbulence case, this is to be expected as it is unlikely that the CFD domain inlet will exactly reproduce the precise turbulence
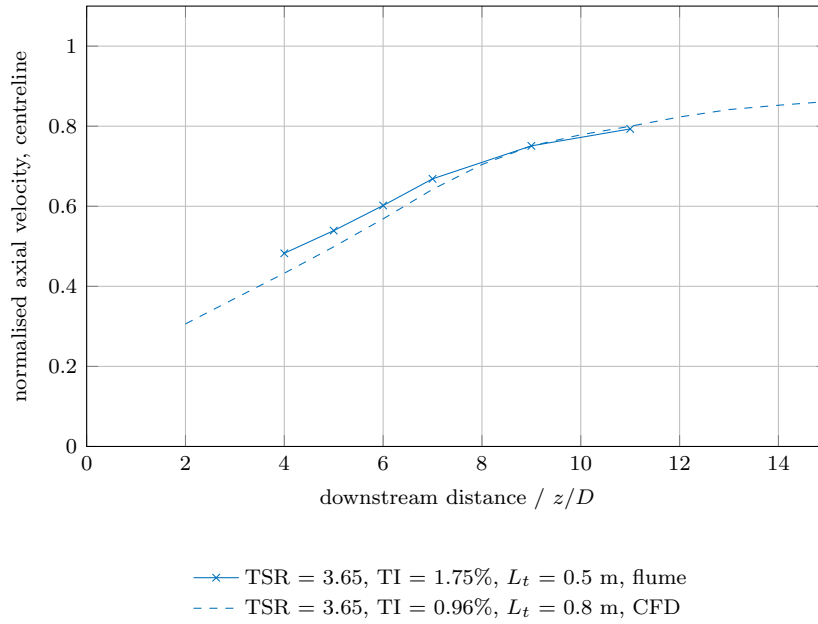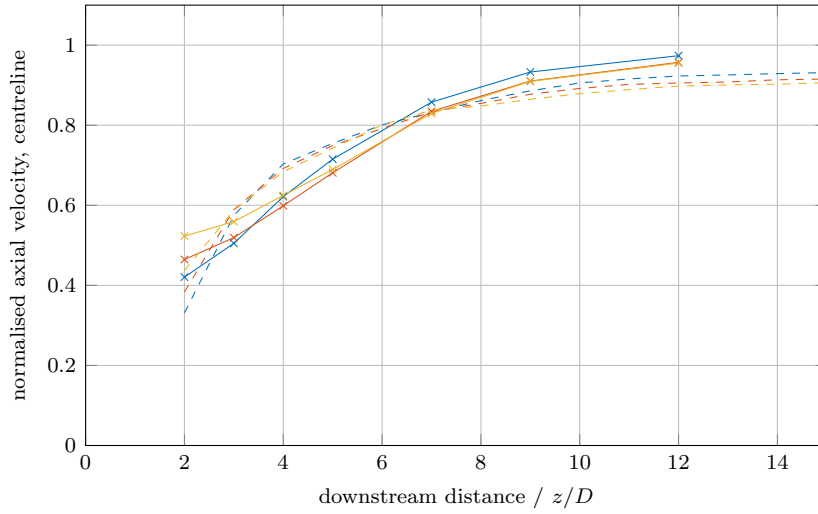
Figure 7.34: Validation of low-turbulence flume campaign: centreline wake recovery.
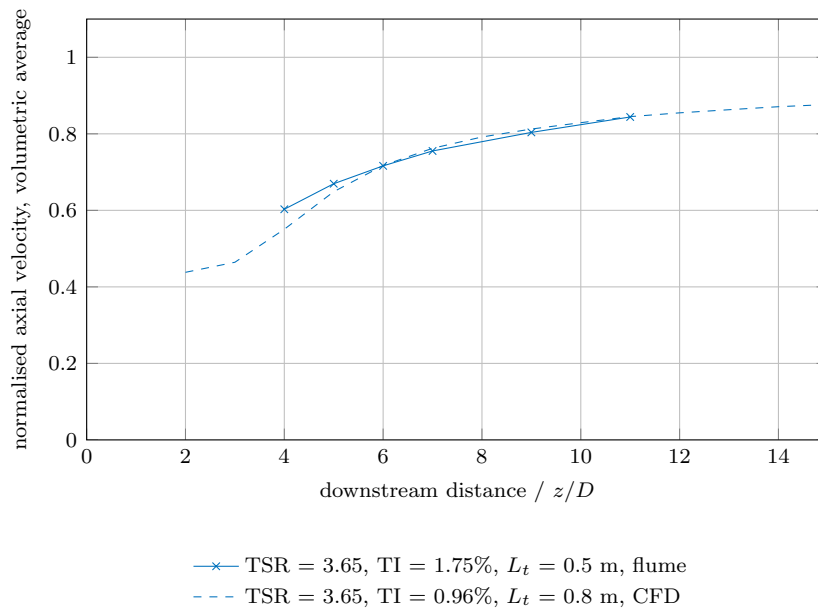
Figure 7.35: Validation of low-turbulence flume campaign: volumetric averaged wake recovery.

Figure 7.36: Validation using flume results with the fine grid: centreline wake recovery.

characteristics of the flume.

The validation plots for wake recovery for the testing campaign behind the coarse grid are presented in Figure 7.38 for the centreline wake, and Figure 7.39 for the volumetric averaged wake. Agreement in the mid- and far-wake is good, with a tendency for the CFD to slightly under-predict the recovery in the far wake, albeit only by around 5%. The CFD also tends to over-predict the recovery at distances of $z/D \leq 6$. As with the two previous flow conditions, the near-wake may be better reproduced with a finer mesh in the near-turbine region, but the discrepancies could also be explained by the high level of turbulence, and the CFD not exactly reproducing the turbulence characteristics of the grid-generated turbulence in the flume.

7.4.4 Impact of turbulence on wake recovery

Turbulence intensity

The impact of ambient turbulence intensity on wake recovery is examined using the results in Figures 7.31 and 7.32 for flume centreline and volumetric averaged velocities respectively. In addition, four selected CFD cases have been compared which have similar turbulence conditions to each other except in respect of turbulence intensity. The CFD results are shown in Figures 7.40 for centreline
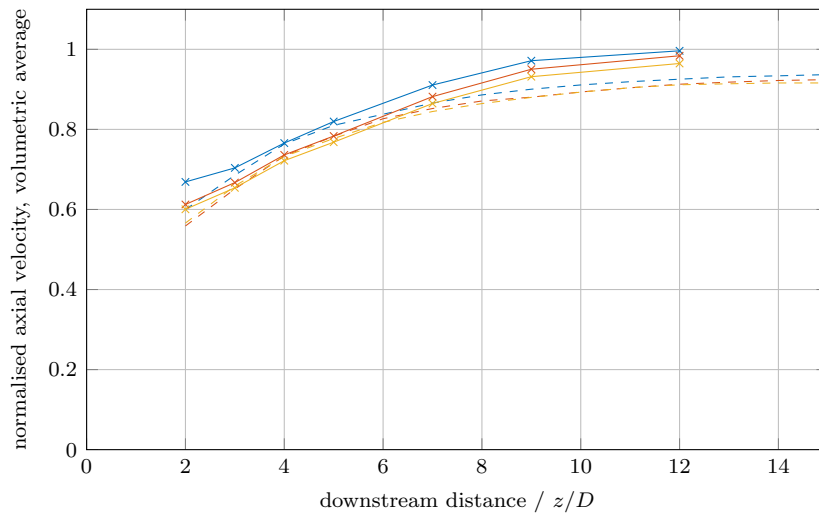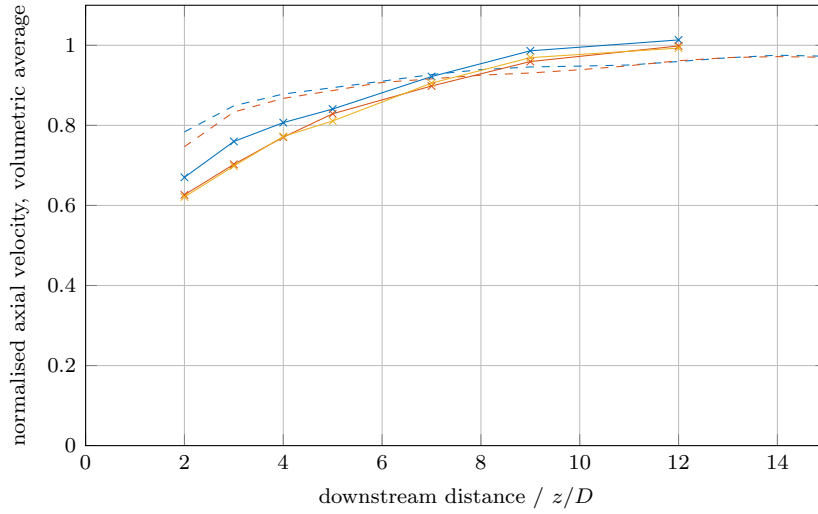
Figure 7.37: Validation using flume results with the fine grid: volumetric averaged wake recovery.
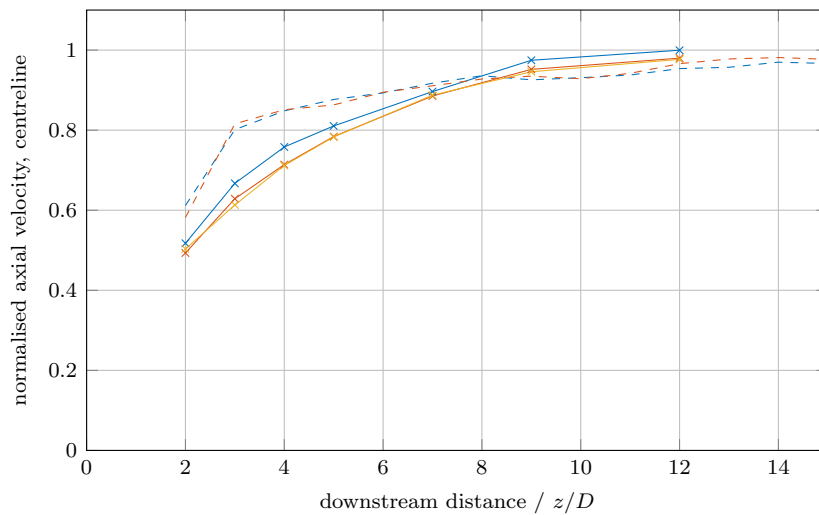
Figure 7.38: Validation using flume results with the coarse grid: centreline wake recovery.

Figure 7.39: Validation using flume results with the coarse grid: volumetric averaged wake recovery.

velocity, and Figure 7.41 for volumetric averaged wake recovery.

The flume results show a clear trend that the cases with higher turbulence intensity exhibiting more rapid wake recovery for both centreline and volumetric averaged results (Figures 7.31 and 7.32). For the volumetric averaged wake recovery curves, the wakes produced behind the fine grid and those behind the coarse grid still show only a slight difference, suggesting that there may be an upper limit beyond which an increase in turbulence intensity has little further effect on wake recovery.

The CFD results are in general agreement with the flume results, with the figures for centreline and volumetric averaged wake showing very similar behaviour (Figures 7.34–7.39). Here it can also be seen that a higher turbulence intensity promotes faster wake recovery, with the two cases of greatest turbulence intensity showing similar results from the mid-wake onwards.

These results follow trends seen in previous experimental work[53][60], with the consensus being that higher ambient turbulence promotes mixing and transfer of momentum across the wake shear layer, increasing the velocity of the wake region, and therefore promoting wake recovery.
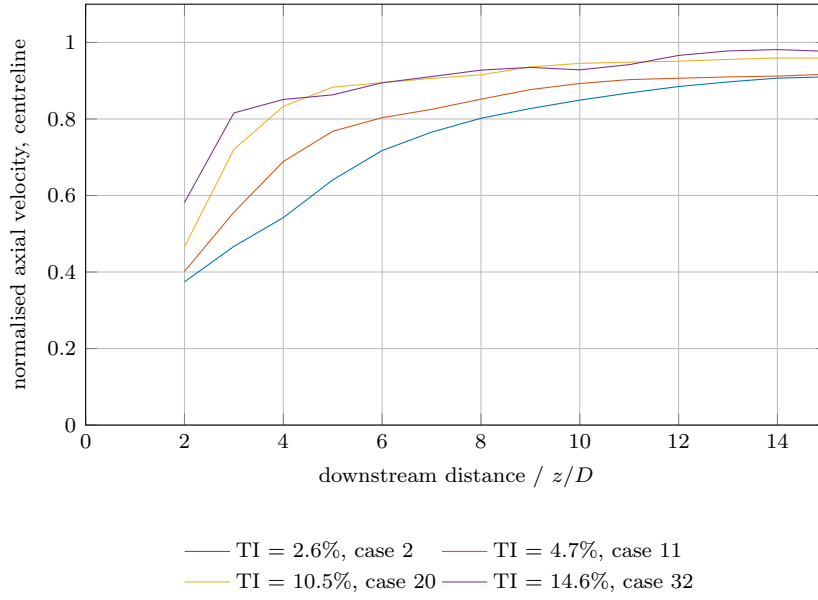
Figure 7.40: Impact of ambient turbulence intensity on centreline wake recovery, CFD cases.
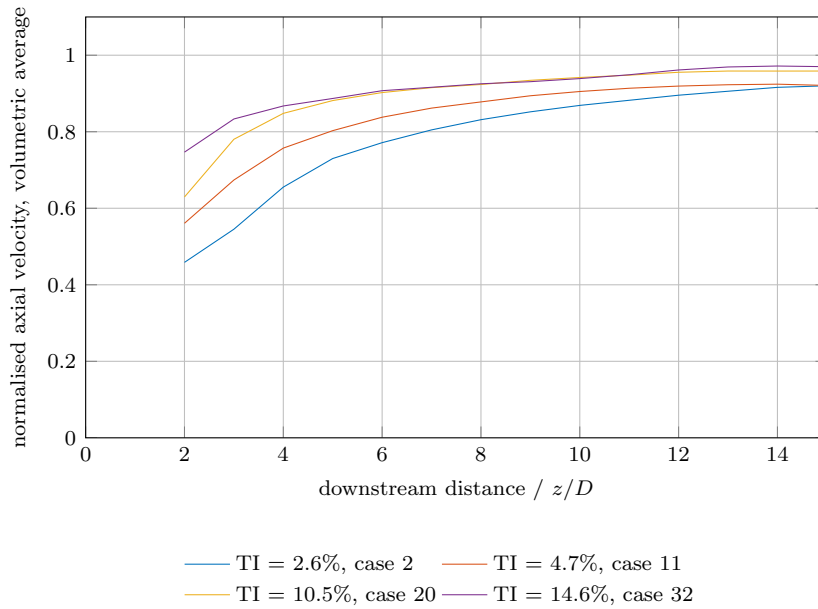
Figure 7.41: Impact of ambient turbulence intensity on volumetric averaged wake recovery, CFD cases.

Turbulence length scale

The impact of turbulence length scale on wake recovery was explored using three selected CFD runs. The results are presented in Figures 7.42 and 7.43 for the centreline and volumetric averaged wake recovery respectively.

For both centreline and volumetric averaged recovery, the medium L_t case ($L_t = 0.78$ m) initially shows a fast recovery to approximately 90% of the free stream velocity, after which very little further recovery takes place. From $z/D = 8$ the case with the largest L_t ($L_t = 1.5$ m) shows the greatest recovery, followed by the case with the shortest L_t ($L_t = 0.45$ m), followed by the medium L_t case. This suggests that L_t may have an impact in the far wake as the case presented with the largest L_t also has the lowest turbulence intensity, which would tend to reverse the order seen in the far wake.

In the near- to mid-wake ($z/D < 7$), the case with shortest L_t shows faster centreline recovery than the case with the largest L_t, however, this trend is reversed when the volumetric averaged recovery is considered. This could indicate that the short length scales increase mixing within the wake region (and therefore promote centreline wake recovery) in the near wake, with the larger length scales dominating the mixing between the wake and the free stream, which ends up dominating overall wake recovery. The effect of momentum transfer across the outer shear-layer of the wake will first be apparent in the volumetric-averaged recovery, with this trend reaching the centreline later. This could indicate that larger length scales lead to slower initial, but faster overall wake recovery. Nonetheless, the behaviour is complex, it is difficult to completely isolate the effects of L_t and turbulence intensity. In addition, this study only compares three different length scales, making non-linear effects difficult to identify.

7.4.5 Impact of tip-speed ratio on wake recovery

The impact of turbine operating condition on wake recovery can be examined using Figure 7.44 to look at the impact on the wake recovery at the centreline, and Figure 7.45 which examines the impact on the volumetric averaged wake recovery. All curves are obtained from CFD in the low-turbulence case (runs 34–40 in Table 7.1); the $\lambda = 3.65$ case is that used for validation. Comparison of the two metrics allows assertions to be made about the homogeneity of the velocity distribution in the wake region. If the trends are similar, this suggests a more homogeneous wake, where they are not, then that indicates that the velocity has a strong dependence on radial position.

The centreline velocity recovery shows a clear trend with tip-speed ratio. The higher the tip-speed ratio, the greater the initial wake recovery. Nonethe-
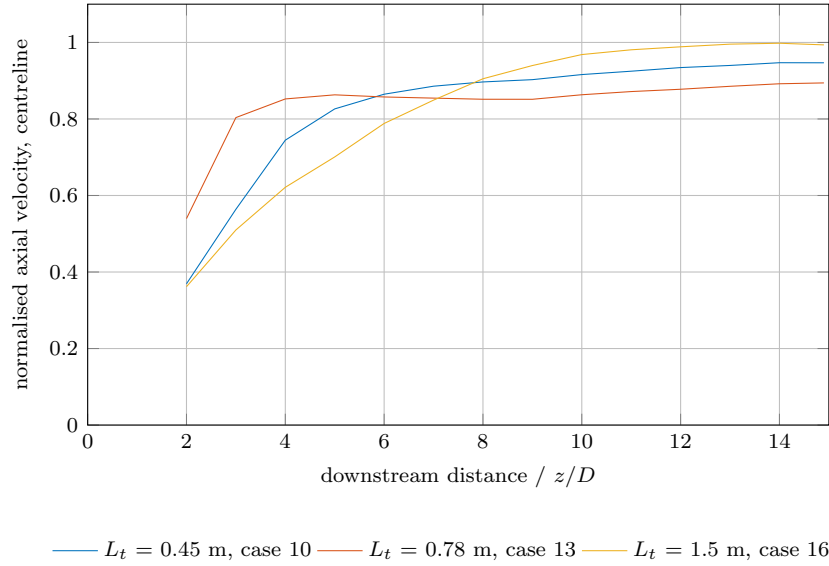
Figure 7.42: Impact of ambient turbulence length scale on centreline wake recovery, CFD cases.
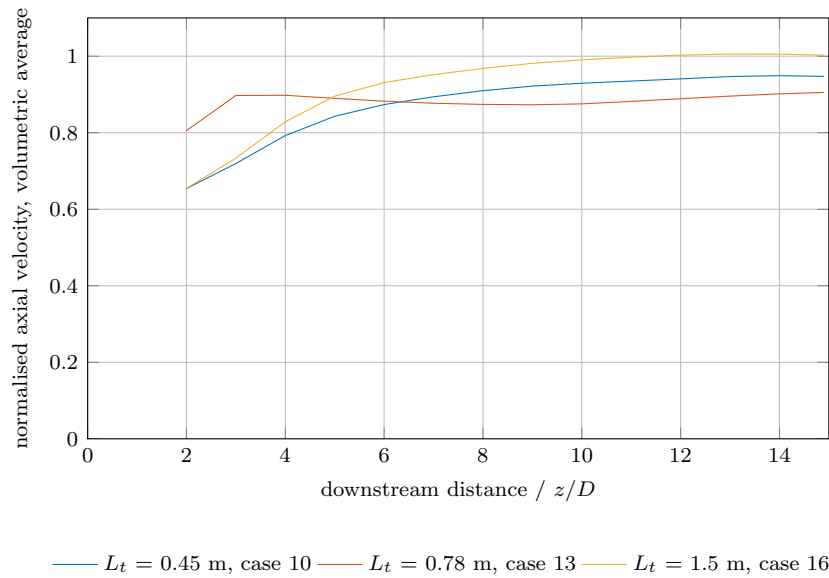
Figure 7.43: Impact of ambient turbulence length scale on volumetric averaged wake recovery, CFD cases.

167

less, beyond approximately $z/D = 10$, the tip-speed ratio seems to have little impact on the centreline wake recovery. This appears to follow the trend of the thrust curve of the turbine, with higher thrust cases showing a higher centreline recovery. This might appear counter intuitive, as a turbine with higher thrust will be presenting more resistance to the flow, causing flow to divert around the rotor swept area. However, most of the thrust is produced by the outer portion of the blades, causing flow to be diverted not only outside and around the swept area, but also inwards towards the blade roots and nacelle. This increases the velocity towards the centreline, encouraging centreline wake recovery. This effect can be seen by comparing Figures 7.24–7.30, showing the wake velocity profiles for tip-speed ratios of $\lambda = 1.5$–5.5, at downstream positions from $z/D = 2$ to $z/D = 15$. Low-thrust, low tip-speed ratios have profiles which are v-shaped, but as the tip-speed ratio and thrust increases, the shapes of the wake profiles become more like an inverted top-hat, with the highest-thrust cases exhibiting 3-dips in the nearest profiles. The peaks between these dips indicate flow being diverted inwards, towards the turbine nacelle, leading to the wake recovery curves seen in Figures 7.44 and 7.45. This trend in the shapes of wake profiles with tip-speed ratio agrees with the wake profiles measured in the flume, presented in Figure 7.33. The triple-dip profile at $z/D = 2$ is not seen in these profiles from the flume; however, given the much higher levels of turbulence and increased recovery it is to be expected that this level of detail in the profiles may not be seen. Indeed, the change in profile shape becomes less clear between the fine grid (Figures 7.33a, 7.33c and 7.33e) and coarse grid case (Figures 7.33b, 7.33d and 7.33f).

An exception to the overall trend is the $\lambda = 1.5$ case. In the very near wake, this curve appears to approximately fit the trend for tip-speed ratio, but thereafter recovers at a much greater rate than any of the other curves, such that, by $z/D = 5$, it has shown the most recovery — a trend which continues further downstream. From the torque curve presented in Figure 7.6, it can be seen that at a tip-speed ratio of $\lambda = 1.5$ the turbine is operating in the stall-region. A stalled blade can be expected to produce increased turbulence in the near-wake region than an un-stalled blade (due to flow separation over the blades themselves), contributing to more mixing in this region, whilst at the same time producing less thrust. Given this, it might be expected that the influence of the turbine nacelle might be greater for the $\lambda = 1.5$ case in the very near wake than for other tip-speed ratios, but that very quickly the effect of increased blade turbulence causes rapid mixing and consequently rapid wake recovery.

The volumetric-averaged wake recovery curves presented in Figure 7.45 show a slightly different trend. In this case, there appears to be a trend whereby the

tip-speed ratios with the highest C_P tend to show the largest deficit in the near wake. This makes sense as the high C_P cases will extract more energy from the flow, by means of reducing flow velocity. Nonetheless, this effect is only apparent in the near-wake; beyond $z/D \approx 4$, all cases except for $\lambda = 1.5$ and $\lambda = 5.5$ are virtually indistinguishable from each other, with the $\lambda = 5.5$ case merging at approximately $z/D = 8$.

As with the centreline wake recovery, the $\lambda = 1.5$ case appears to be an outlier, showing greater wake recovery than any other case. This case has the lowest power and thrust coefficients of all of the cases in the figure, meaning that the turbine neither extracts much energy from the flow, nor provides great resistance to it. This leads to flow passing through the turbine swept area without being slowed down, and hence the wake is well recovered. A comparison of Figures 7.44 and 7.45 shows that the $\lambda = 1.5$ case is highly inhomogeneous in the near wake, with a very low velocity centreline surrounded by an otherwise well recovered wake.

For array designers, the most important conclusion to be drawn from Figure 7.45 is that, with the exception of the stalled case of $\lambda = 1.5$, beyond $z/D = 8$, tip-speed ratio has little impact on the volumetric-averaged wake recovery. This means that even in the case where a turbine uses an over-speed regime to maintain rated power, this will not have an impact on longitudinal turbine spacing (assuming a spacing of at least 8 turbine diameters).
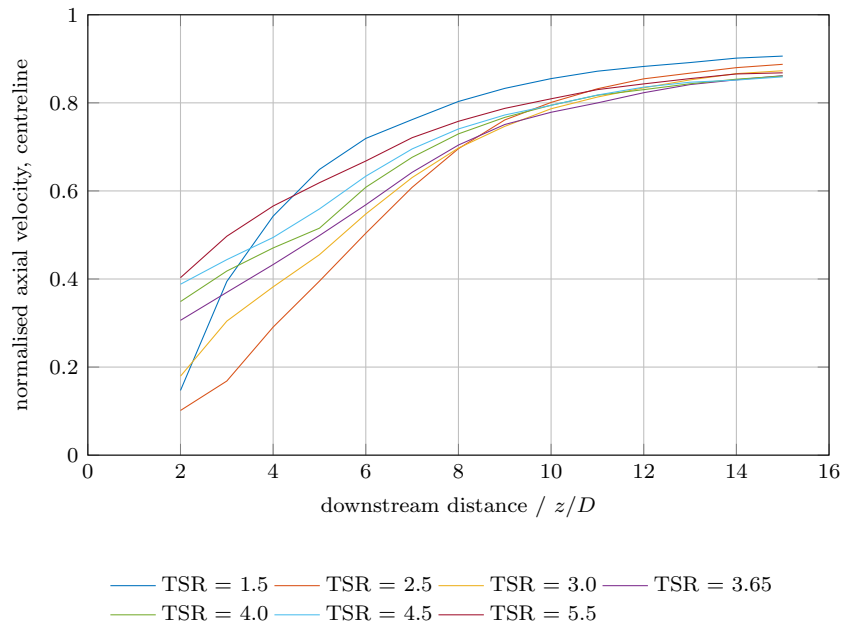
Figure 7.44: Impact of tip-speed ratio on centreline wake recovery. Low ambient turbulence condition.

169
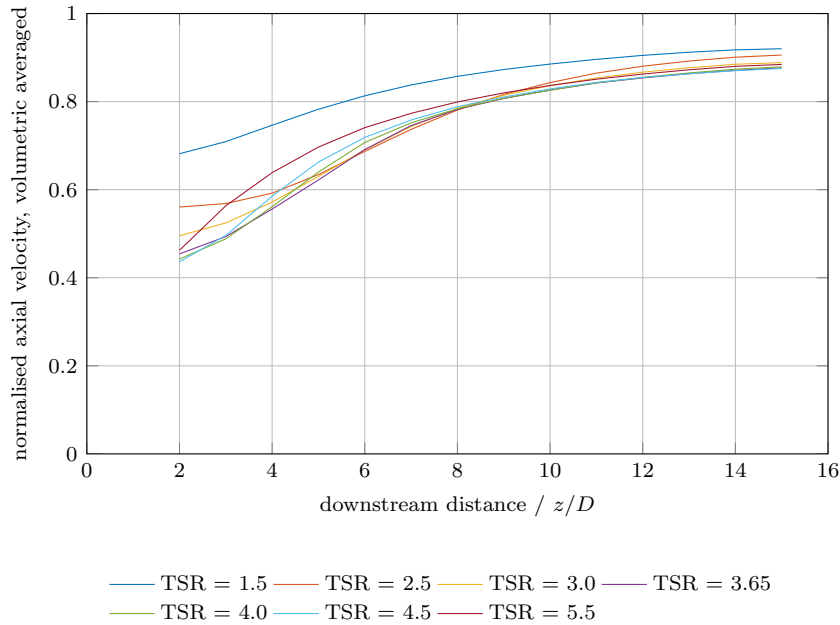
Figure 7.45: Impact of tip-speed ratio on volumetric averaged wake recovery. Low ambient turbulence condition.

7.5 Wake width

7.5.1 Flume results

Flume results for the wake width using the fixed-threshold, full-width half-minimum and maximum-shear methods are shown in Figures 7.46, 7.47 and 7.48 respectively.

Examining Figure 7.46 for the fixed-threshold method, it can be seen that, for all cases, the wake at $z/D = 2$ downstream is between 1–1.5D in width, with the width decreasing as the wake develops downstream. This is to be expected as the fixed-threshold wake method is intrinsically linked to the wake recovery. Recalling that the fixed-threshold method measures the width of the wake region which is less than 90% recovered, it is clear that, as the wake recovers, the region which is less than 90% recovered will tend to decrease. Assuming that recovery is symmetrical about the centreline, when the centreline velocity recovery reaches 90% of the free stream, the wake width using this metric will become 0.

This connection between wake recovery and fixed-threshold wake width explains the differences between the low-turbulence case (TI = 1.75%)and the cases behind the coarse and fine grids. The centreline wake recovery (Figure 7.31) shows that both grid-generated turbulence cases demonstrate 90% wake

170
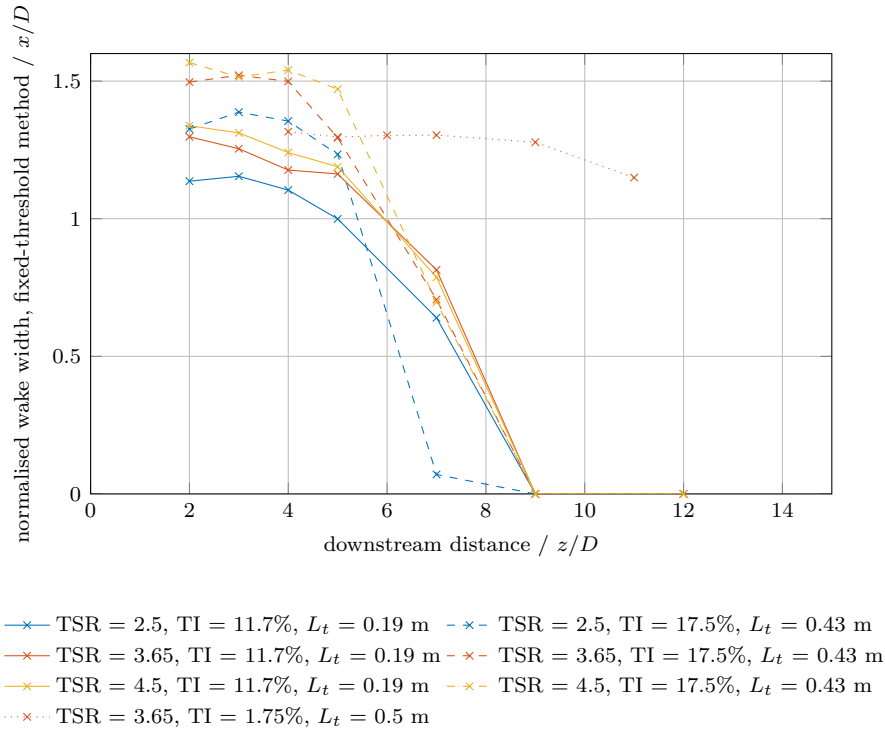
Figure 7.46: Flume results: Wake width using fixed-threshold method.

recovery in the region $7 \leq z/D \leq 9$, whereas the low-turbulence case has only achieved approximately 80% recovery by $z/D = 11$ downstream, where measurement ended. This lack of mixing and recovery in the low-turbulence case explains why the wake persists for longer, leading to a wake that retains its width for longer (Figures 7.46 7.47).

It appears that a higher ambient turbulence intensity leads to a slightly greater wake width in the near wake region, but the coarse and fine grid cases (TI = 11.7% and 17.5% respectively) show little difference from one another beyond $z/D = 6$. In addition to this, for the cases of grid-generated turbulence, there appears to be a dependence of wake width on tip-speed ratio, with greater tip-speed ratios leading to slightly wider wakes throughout their entire length. This is thought to be due to increased thrust on the turbines at the higher tip-speed ratios. A greater thrust on the turbine will tend to divert the oncoming flow outside and around the turbine swept area, causing a wider wake.

The wake width results following the full-width half-minimum method for all flume cases are presented in Figure 7.47. The shapes of the curves are slightly different to those seen in Figure 7.46 as the two metrics are affected in different ways by the shapes of the velocity profiles, however, the major

171
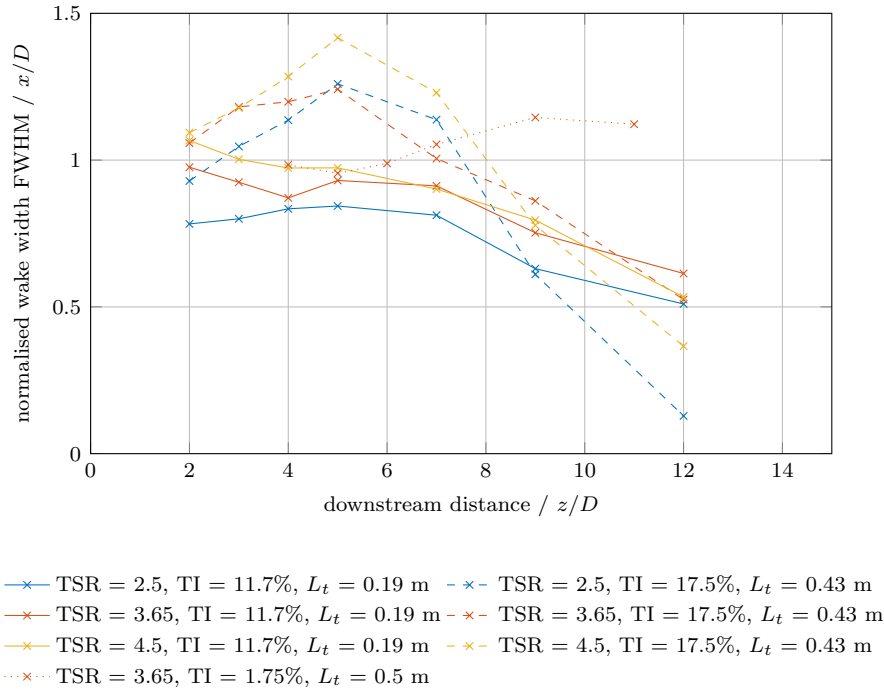
Figure 7.47: Flume results: Wake width using full-width half-minimum method.

trends from the fixed-threshold method are also apparent in the full-width half-minimum method. The same dependence of wake width on tip-speed ratio is apparent, with higher tip-speed ratios (and therefore higher thrust) leading to wider wakes. In addition to this, as before, the width of the wake in the low-turbulence case seems to persist for much further downstream than in the higher-turbulence cases. It is thought that this is due to less mixing being present, allowing the wake to maintain its shape further downstream. Again, as in the fixed-threshold case, the wake width in the high-turbulence case is initially highest of all, perhaps due to increased mixing broadening the shear layer between the wake and the free stream. As the wake develops downstream, the high-turbulence case seems to narrow at a faster rate than the other cases, again thought to be due to increased mixing.

Wake width results for the from the flume cases following the maximum-shear approach are presented in Figure 7.48. This figure does not show any clear trends; it could be suggested that the case with the highest turbulence tends to produce a wider wake, but beyond this, no clear tends are visible. This is due to convergence difficulties which are present using this method; these will be further discussed in section 7.5.3.
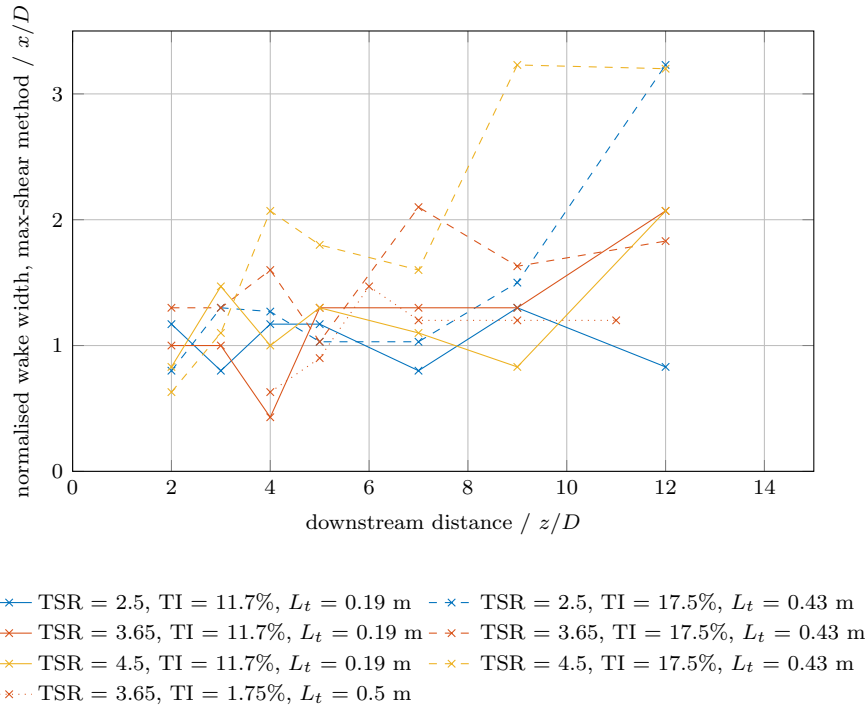
Figure 7.48: Flume results: Wake width using maximum-shear method.

7.5.2 Validation of CFD

Validation of the low-turbulence flume campaign can be seen for the fixed-threshold method, full-width half-minimum method and maximum-shear method in Figures 7.49, 7.50 and 7.51 respectively. Validation of the fixed-threshold method in Figure 7.49, shows good agreement between the CFD and the flume results, with both showing a slight narrowing of the wake as it develops downstream, and only a slight under-prediction of wake width by the CFD. A slight under-prediction of wake width by the CFD is also apparent in Figure 7.50, which compares CFD and flume results using the full-width half-minimum method. As with the fixed-threshold method, there is good agreement with the trend of wake development, this time with both methods showing a slight widening of the wake with downstream distance. Agreement between the CFD and flume results using the maximum-shear method (Figure 7.51) is less clear, although as mentioned in the discussion of Figure 7.48, and further discussed in section 7.5.3, results for the maximum-shear method suffer from convergence difficulties. Nonetheless, both CFD and flume results indicate a slight widening for the wake with increasing downstream distance, and CFD and flume results show a wake width of approximately the same order of magnitude. Agreement
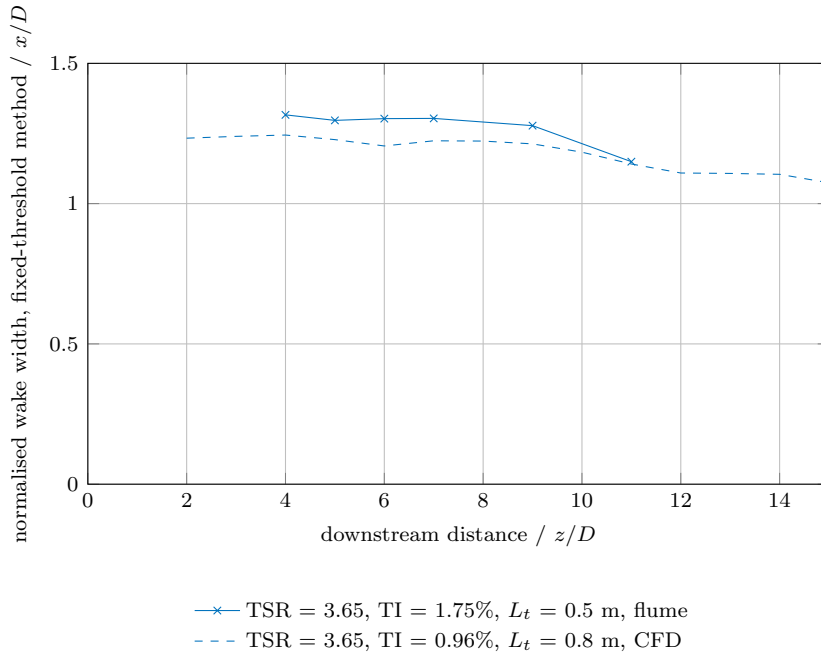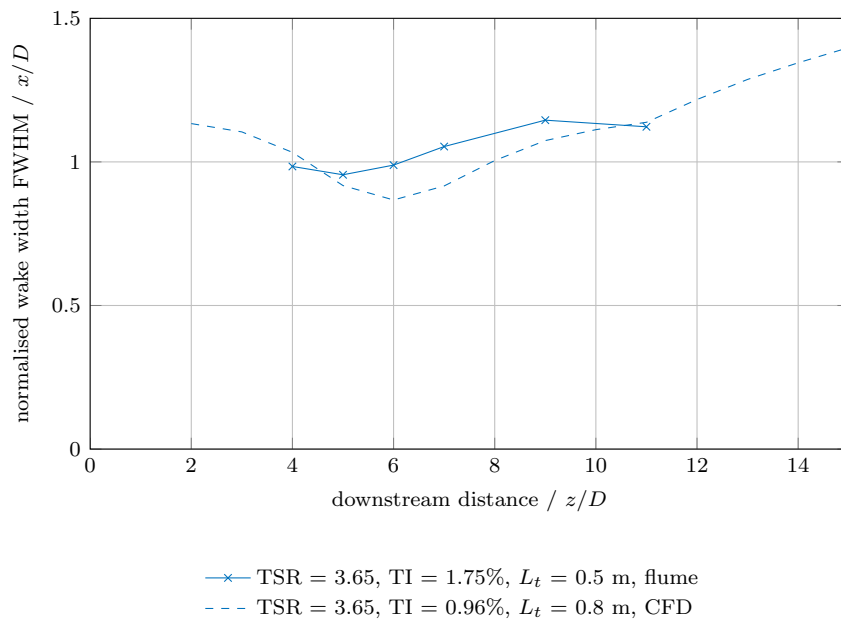
Figure 7.49: Validation of low-turbulence flume campaign: Wake width using fixed-threshold method.

is however, not as good as with the fixed-threshold and full-width half-minimum methods.

Validation of the flume campaign behind the fine grid can be seen for the fixed-threshold, full-width half-minimum and maximum-shear method in Figures 7.52, 7.53 and 7.54 respectively. Comparison of the flume results and the CFD results using the fixed-threshold method (Figure 7.52) shows that both the flume results and CFD follow the same overall trends; starting with a near-wake width of 1.1–1.5D, which stays almost constant for 3–5 diameters downstream, before narrowing. The CFD results show the same trends with tip-speed ratio as the flume results, with the $\lambda = 2.5$ case displaying a narrower wake than the other two tip-speed ratios, which produce similar, but slightly wider results. The CFD tends to under-predict the rate of wake narrowing, with changes in the CFD predicted wake occurring 2–4D further downstream than that seen in the flume.

Comparison of the flume and CFD results using the full-width half-minimum method (Figure 7.53) shows that initially there is close agreement between the flume and CFD results in the near-wake, but that from this point the results diverge, with the CFD results trending slightly wider, and the flume results trending slightly narrower. The trend with tip-speed ratio seen in the flume results ($\lambda = 2.5$ case narrower than the other two cases), is reproduced in the

Figure 7.50: Validation of low-turbulence flume campaign: Wake width using full-width half-minimum method.
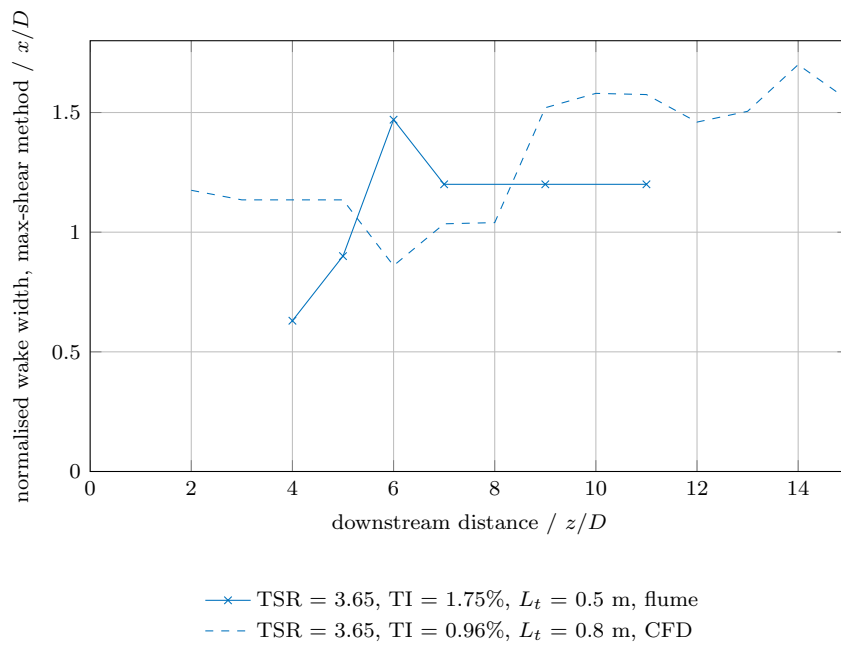
Figure 7.51: Validation of low-turbulence flume campaign: Wake width using maximum-shear method.

CFD results. Using the full-width half-minimum method, the increase in wake width with downstream distance might be expected, as the method gives an indication of the width of the region being in some way affected by the wake, and this will tend to get wider as the wake mixes with the free stream. The reason for the flume results showing a narrowing with downstream distance is not entirely clear, but if the wake profiles in Figure 7.33 are examined, then it can be seen that, outside of the wake region, the profiles indicate an increased axial velocity, and show a slight asymmetry and inhomogeneity in the flume outside of the immediate wake region. This will affect the shapes of the profiles as well as making the choice of a reference velocity for normalisation and calculation of deficit less clear, therefore affecting the width calculated using the full-width half-minimum method. For the flume results presented here, the axial velocity used for normalisation and deficit calculation is that which appears in Table 6.3, following measurement of the centreline flow conditions in flume at the point at which the turbine was placed. CFD results were normalised and wake deficits calculated using the measured values for axial velocity presented in Table 7.1.

Flume and CFD results using the maximum-shear method for the fine grid cases can be seen in Figure 7.54. Agreement is reasonable for the initial wake widths, and there is a general indication that higher-thrust cases yield a wider wake, however, the lack of convergence using this method means that there is no clear trend in the far wake.

Validation of the flume campaign behind the coarse grid can be seen for the fixed-threshold, full-width half-minimum and maximum-shear method in Figures 7.55, 7.56 and 7.57 respectively.

Wake widths calculated using the fixed-threshold method, presented in Figure 7.55, shows good agreement between the CFD and flume results. All wakes show an initial width of between 1–$1.5D$, which remains nearly constant until $z/D = 5$–7, at which point they narrow rapidly. Initial width, the point at which the wakes begin to narrow and the rate of narrowing are all well matched between the flume and CFD results. In addition, the trend of increasing wake width with tip-speed ratio seen in the flume results is reproduced in the CFD results. Agreement between CFD and flume results for the fixed-threshold method appears to be slightly better in the case of the coarse grid than for the fine grid. This is thought to be due to the increase in mixing due to the higher turbulence intensity conditions, and the inherent link between this width metric and wake recovery. The turbulence in the coarse grid cases increases the mixing and consequently the wake recovers very rapidly, with the 90% threshold being very quickly achieved. Such rapid mixing applies to both the CFD and flume cases, and means that the wake widths very quickly drop to zero following this metric. Less rapid mixing and more gradual wake recovery means that slight
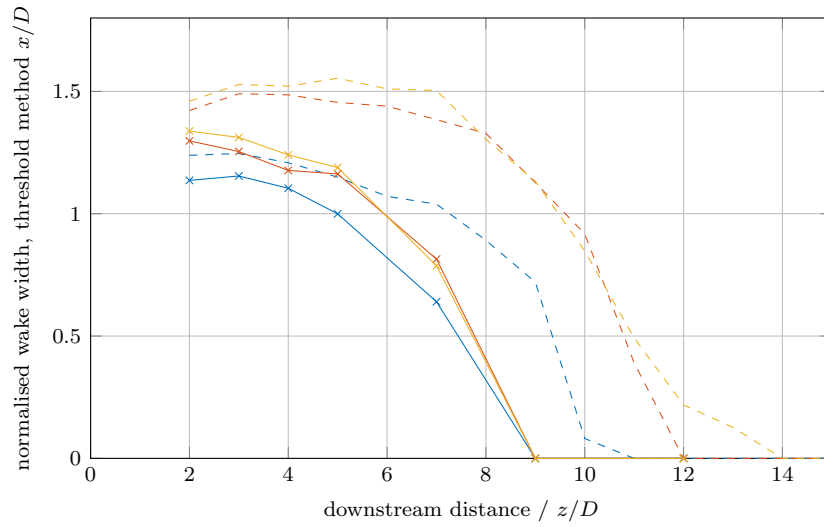
176

Figure 7.52: Validation using flume results with the fine grid: Wake width using fixed-threshold method.
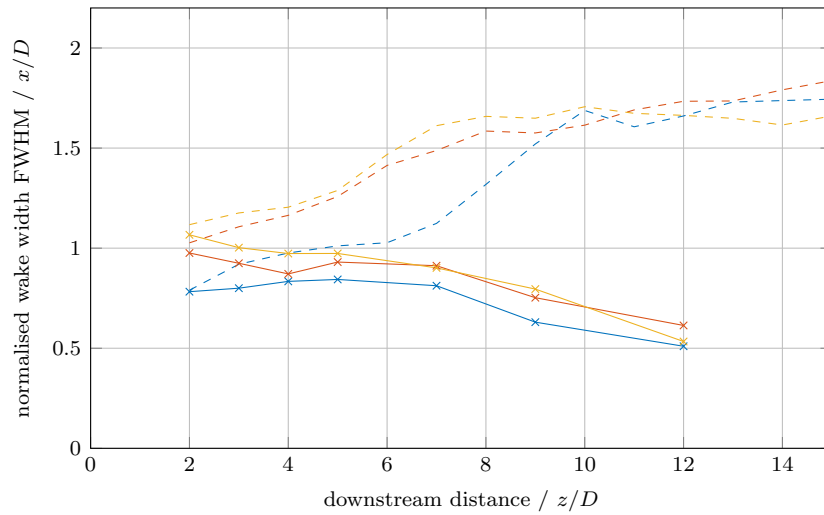
Figure 7.53: Validation using flume results with the fine grid: Wake width using full-width half-minimum method.
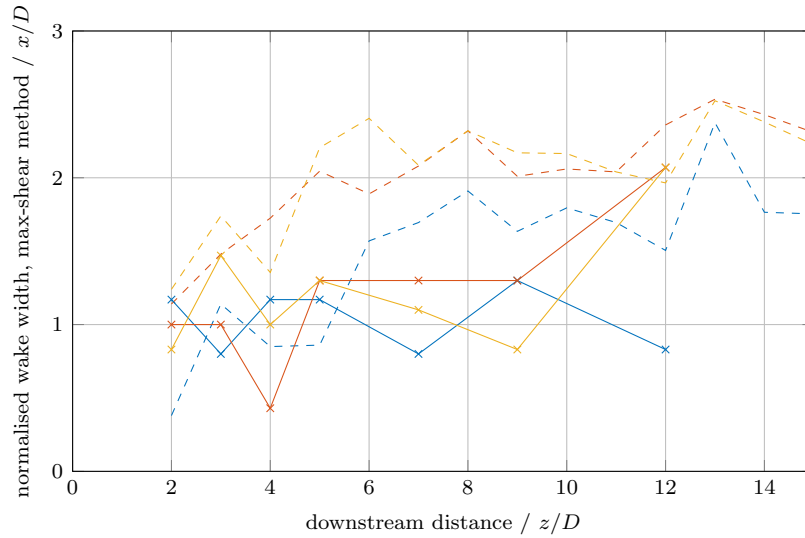
Figure 7.54: Validation using flume results with the fine grid: Wake width using maximum-shear method.

differences between the CFD and flume results become more apparent in the fine grid cases.

As with the full-width half-minimum results for the fine grid case, the flume and CFD results for the coarse grid show good agreement in the near-wake region, before diverging, with the flume results indicating a narrowing of the wake, whilst the CFD results indicate a widening of the wake (Figure 7.56). Again, examination of Figure 7.33 indicates that there is some asymmetry and inhomogeneity in the flume (due to the presence of the grid), and this will tend to distort the shape of the profiles, and affect the width calculated using the full-width half-minimum method.

Once more with the maximum-shear method (Figure 7.57), both the flume and CFD results exhibit similar widths, however, due to convergence issues, it is not possible to define any clear trends in the wakes of either flume or CFD results.

7.5.3 Evaluation of different width metrics

Three different wake width measurement metrics have been applied in this thesis: the fixed-threshold method, the full-width half-minimum method, and the
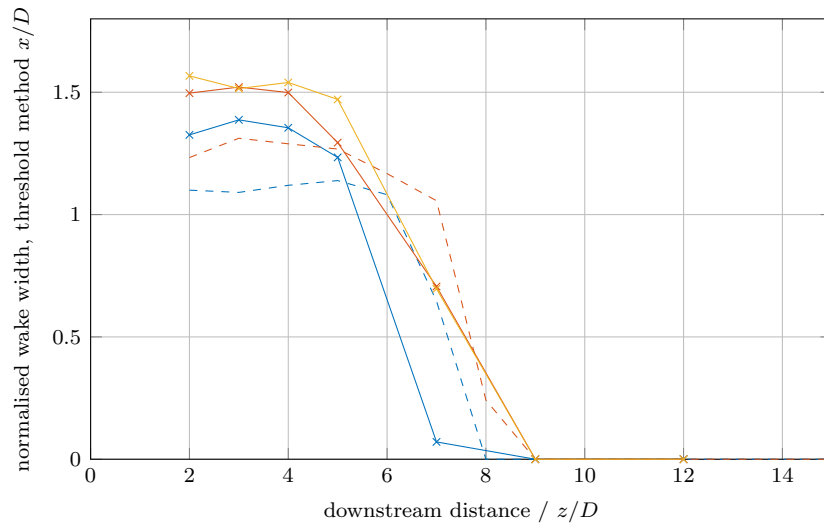
Figure 7.55: Validation using flume results with the coarse grid: Wake width using fixed-threshold method.
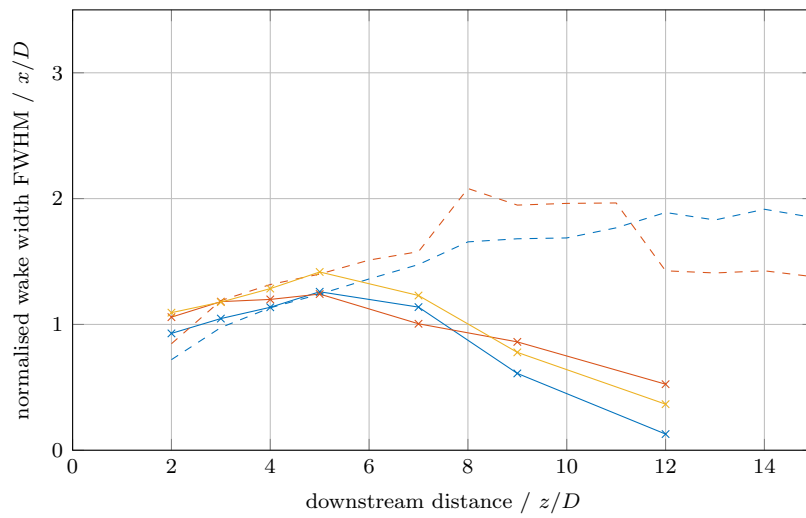
Figure 7.56: Validation using flume results with the coarse grid: Wake width using full-width half-minimum method.
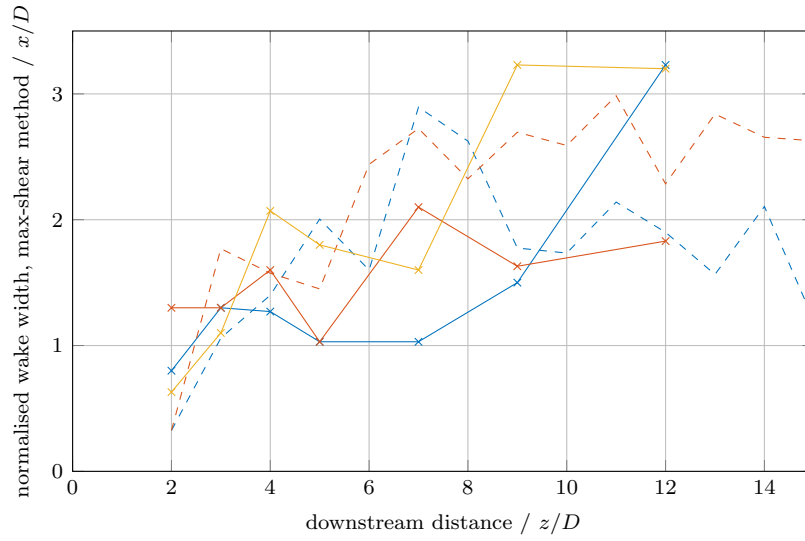
Figure 7.57: Validation using flume results with the coarse grid: Wake width using maximum-shear method.

maximum-shear method. As the wake width can be difficult to define, these three metrics were applied as they each provide a slightly different insight into the wake behaviour.

The fixed-threshold method yields the width of the region *strongly* impacted by the wake. In this work, the threshold was chosen to be 90% wake recovery, which in conditions of high ambient turbulence intensity meant that the wake width reduces to zero within the region studied (i.e. $z/D \leq 15$).

By contrast, the full-width half-minimum method applies a threshold, but calculates that threshold based on the maximum deficit at that downstream distance. Consequently, this method provides a value for wake width which is related to the total width of the region impacted by the wake (i.e. the region where the velocity has been changed due to the presence of the turbine). It may be seen as a measure of the extent to which the wake has extended out into the flow region surrounding that directly downstream of the turbine. Applying both the fixed-threshold and full-width half-minimum methods allows an assessment to be made of how the wake is developing/recovering; for example, it might be found that the full-width half-minimum method indicates a widening of the wake, whilst the fixed-threshold method indicates a narrowing of the wake. This would indicate that the width of the region affected *at all* by the wake is

increasing, but that this impact grows weaker as downstream distance increases.

The maximum-shear method does not try to define the wake width in terms of regions of greater or lesser impact, but rather uses the velocity shear to attempt to define the mid-point between the wake region and the free stream. It is useful in as much as it defines a point within the flow, but as the wake develops and width of the shear layer between the wake and free stream increases, the shapes of the wake profiles also change, and this definition of a point between the wake and free stream regions becomes less useful as a comparison metric between wake profiles of different shapes. This is, in part, because this method as applied in this thesis only accounts for the position of the point of maximum-shear, but pays no regard to the strength of the shear.

In addition, when applying these three methods it was found that they respond differently to wake profiles of different shapes. In particular, the maximum-shear method showed itself to be particularly sensitive to slight changes in the mean flow-field when the wake profiles were approximately v-shaped. Figures 7.58–7.60 show how the wake width curves converge with increasing sample time for the fixed-threshold, full-width half-minimum and maximum-shear methods respectively. The three methods have been applied to CFD case 37, the low-turbulence $\lambda = 3.65$ case. Each of the metrics has been applied to the same velocity data, so any difference in the rates of convergence are due to sensitivity inherent in the metrics themselves, rather than a lack of convergence in the velocity data. For reference, wake velocity profiles for this run can be seen in Figure 7.27.

Figures 7.58 and 7.59 for the fixed-threshold and full-width half-minimum methods both show that the wake curves are well converged. In both cases, almost all of the changes occur with the first 15–20 s of sample time. Some changes can still be observed in the far wake up to approximately 30 s, but these are small. In the near-wake, the curves are well converged with less than 10 s of time sampling.

This contrasts with Figure 7.60, showing the convergence for the wake width based on the point of maximum-shear. For the near wake ($z/D \leq 5$), the curve is converged, with less then 10 s sample time required for convergence. Beyond this point, the level of convergence rapidly deteriorates, with the curve at 50 s of sampling time still differing markedly from that with 40 s of time sampling. It is therefore difficult to have confidence that these values would not change further if time sampling were carried out for longer.

Given that these methods have been applied to identical data (the wake velocity profiles shown in Figure 7.27), these differences in convergence are due to the method as applied to those velocities, rather than the velocities themselves. The reason for this lack of convergence in the mid and far wake, despite good

convergence in the near wake can be explained by the shapes of the wake velocity profiles. As the wake develops with downstream distance, the shape of the velocity profiles changes from one with very steep sides (shaped approximately like an inverted top-hat) to profiles which are v-shaped, with an almost linear change in velocity with cross-stream position, and therefore an almost uniform velocity shear from near the centre to the very edge of the wake. This transition is a gradual one, but by approximately $z/D = 6$, the profiles have become distinctly v-shaped. For the inverted top-hat profiles, their steep-sides mean that the point of maximum-shear is located within a relatively small cross-stream extent. Any small changes in the mean flow field have little impact on the cross-stream position of the point of maximum-shear, and therefore the value of wake width in this region converges quickly. In contrast to this, for v-shaped wake profiles the almost linear change in velocity with cross-stream position means that there is a large cross-stream extent with an almost identical amount of velocity shear, the value of which is approximately the same as that of the maximum-shear. The result of this is that any small changes to the mean velocity field (and therefore the wake profiles) can cause the position of maximum-shear to move from nearly the centreline to the very edge of the wake, despite there being no significant change to the wake profile itself. This means that the wake width based on the point of maximum-shear can vary greatly, and the metric is very sensitive to slight changes in the velocity profiles.

A schematic comparing the three different metrics is presented in Figure 7.61. This comparison varies depending on the precise tip-speed ratio and inlet flow conditions; the representation here is based on the behaviour for tip-speed ratios around the point of maximum $\overline{C_P}$ for low turbulence conditions and is intended to show the general behaviour of the metrics, but is not intended to be to-scale. All three metrics initially have a similar width, slightly larger than the turbine diameter. The width measured using the fixed-threshold method tends to decrease as mixing takes place and the wake recovers. In contrast to this, the full-width half-minimum method initially shows a decrease in width as the wake velocity profile changes from an inverted top-hat shape to a v-shape, before showing a steady increase as the mixing region between the wake and the free stream spreads outwards. A similar trend occurs with the maximum-shear method, which initially exhibits a nearly constant width (due to the inverted top-hat shape of the wake velocity profiles). As the wake profiles become more v-shaped, the maximum-shear method starts to demonstrate convergence issues, and only a general trend of increasing width can be identified. This is represented in this schematic by the movement and fading of the line representing this metric. Comparing Figure 7.61 to Figure 4.1, it can be seen that the fixed-threshold method behaves in a similar way to the inner edge of the shear
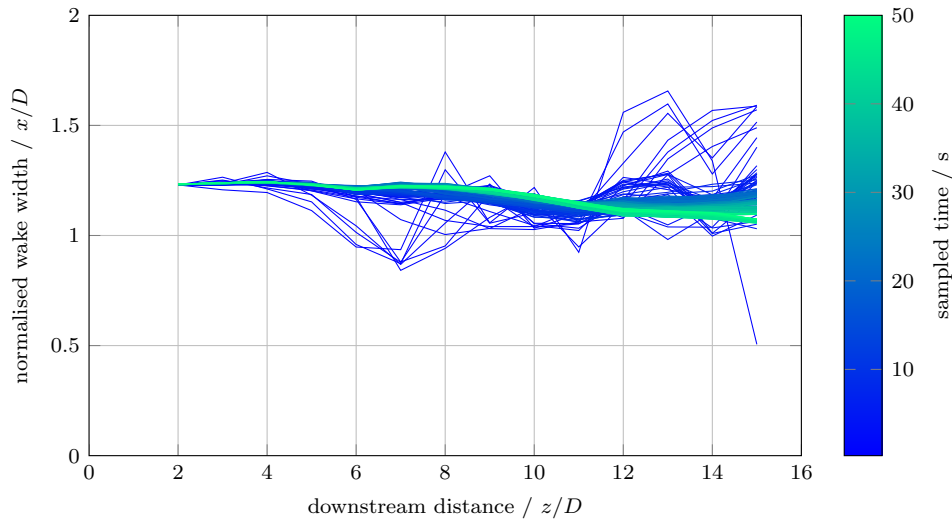
Figure 7.58: The effect of sampled time on the convergence of the curve of wake width using the fixed threshold method. The example shown here is for the low-turbulence case, $\lambda = 3.65$.

layer (between the shear layer itself and the wake core), whereas the full-width half-minimum method comes closer to representing the general expansion of the wake into the free stream region. The maximum-shear method always gives a wake 'edge' within the shear layer, but as the shear layer increases in thickness and the wake velocity profiles become v-shaped, this could be anywhere from the boundary between the shear layer and core region to the boundary between the shear layer and free stream, which leads to this metric's poor convergence. The maximum-shear method only gives reliably converged results in the near wake, where the shear layer between wake core and free stream is thin.

Given that the maximum-shear method shows convergence difficulties for v-shaped profiles which appear both in CFD flume results (Figure 7.33), and the fact that the fixed-threshold and full-width half-minimum methods provide information with more direct applicability to array designers, it is suggested that the maximum-shear method is of limited value in the discussion of wake width.

7.5.4   Impact of turbulence on wake width

Turbulence intensity

The impact of turbulence intensity on wake width is explored using the fixed-threshold, full-width half-minimum and maximum-shear methods in Figures 7.62, 7.63 and 7.64 methods respectively.
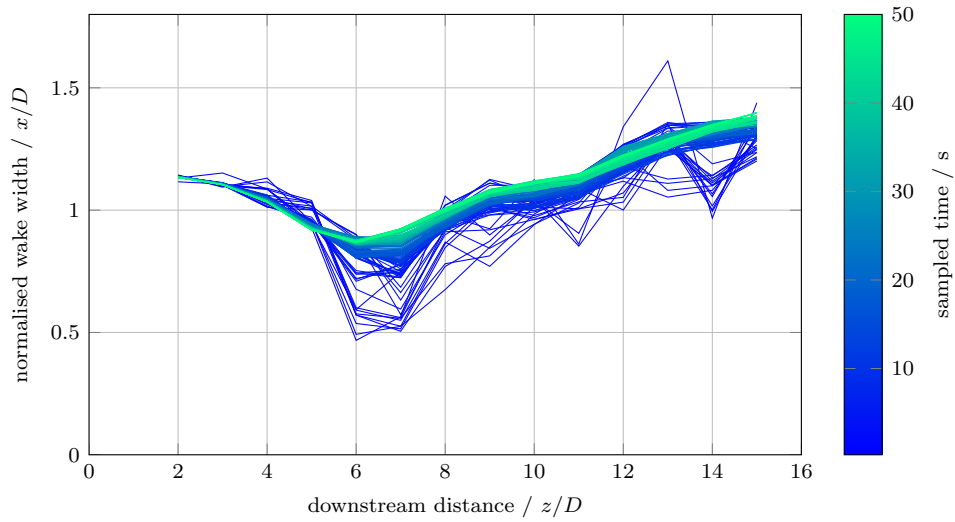
Figure 7.59: The effect of sampled time on the convergence of the curve of wake width using the full-width half-minimum method. The example shown here is for the low-turbulence case, $\lambda = 3.65$.
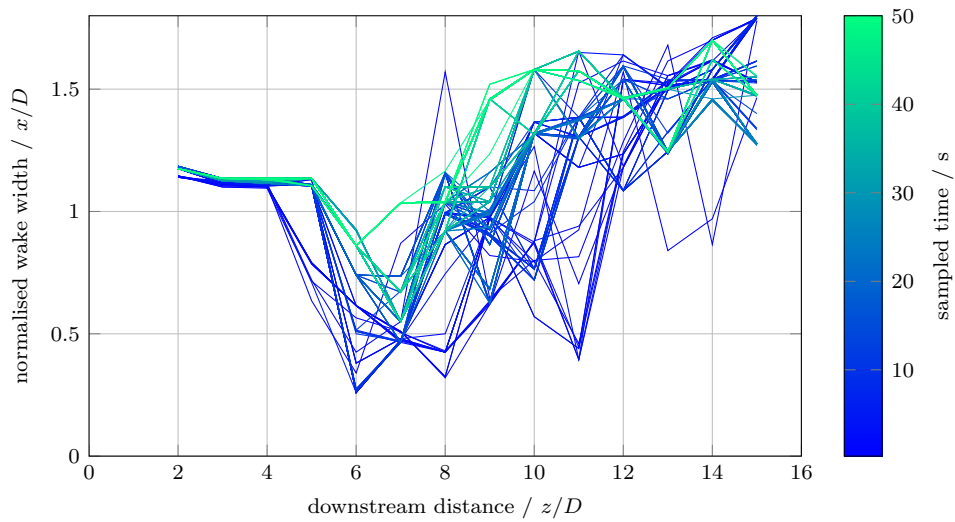
Figure 7.60: The effect of sampled time on the convergence of the curve of wake width using the maximum-shear method. The example shown here is for the low-turbulence case, $\lambda = 3.65$.
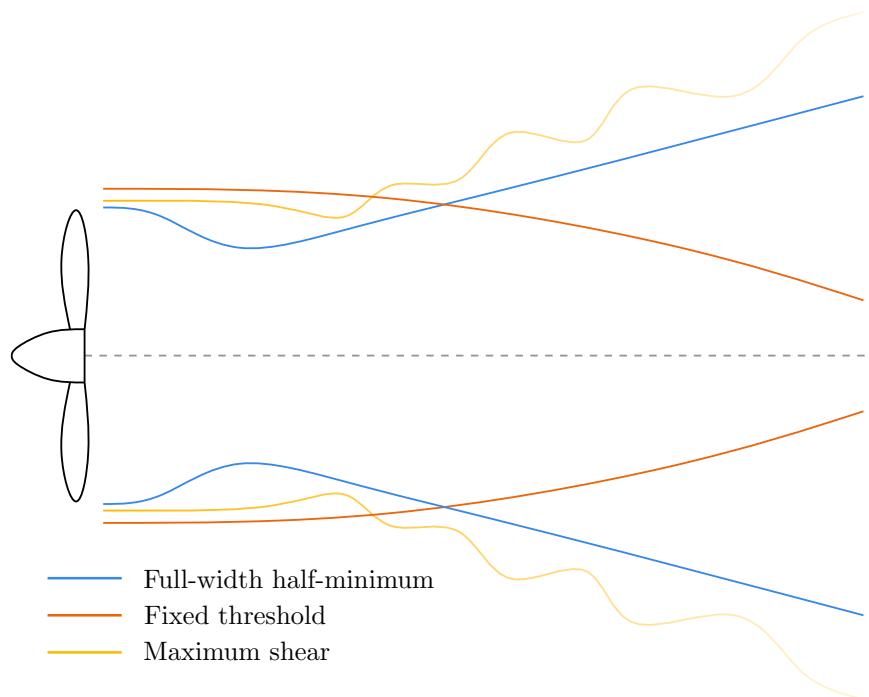
Figure 7.61: A schematic comparing the general behaviour of the three different wake measurement metrics. This comparison varies depending on the precise tip-speed ratio and inlet flow conditions; the representation here is based on the behaviour for tip-speed ratios around the point of maximum $\overline{C_P}$ for low turbulence conditions. This schematic is intended to show the general behaviour of the metrics, but is not intended to be to-scale.

The fixed-threshold metric shows that, regardless of ambient turbulence intensity, all wakes initially have very similar widths. These start to diverge from approximately $z/D = 5$ downstream, with the cases with higher turbulence intensity showing a more rapid narrowing than those with lower turbulence intensity. This is due to the increased levels of mixing encouraged by the higher turbulence intensities. The fixed-threshold method provides an indication of the width of the region strongly affected by the presence of the turbine; more mixing and faster wake recovery means that the region of the highest velocity deficit will reduce more rapidly, narrowing the wake by this metric.

The full-width half-minimum metric shows a general steady increase in wake width for all turbulence intensity cases, whilst showing that the higher turbulence intensity cases yield a wider wake. This can again be explained by the increased levels of mixing from the higher turbulence intensity ambient flow. The full-width half-minimum method gives an indication of the width of the region impacted at all by the wake; increased mixing between the wake and free stream leads to a faster transfer of momentum to the wake region from the free stream (leading to faster wake recovery), but also means that the effect of the velocity deficit in the wake region will be moved further and faster into the free stream. This leads to a greater width being affected *to some extent* by the wake in the higher turbulence intensity cases, whilst simultaneously reducing the width of the region *strongly* affected by the wake.

The maximum-shear method (Figure 7.64) also indicates a dependence of wake width on turbulence intensity, with the higher turbulence cases there is a trend to increasing wake width. This gives some information about the shape of the wake recovery profiles and suggests that they become flatter with slightly steeper sides as turbulence intensity increases. Another way to see this is that the wakes become more homogeneous with increased turbulence intensity, reflected in the increased centreline velocity recovery (Figure 7.40). As discussed in section 7.5.3, choosing to define the point of maximum-shear in the wake as the 'edge' of the wake, has less meaning than the fixed-threshold and full-width half-minimum methods, which either give the region strongly affected by the wake, or the region affected to some extent, and therefore, whilst it is interesting to see a dependence of the maximum-shear method on turbulence intensity, it does not give much further insight for array designers.

Overall, it can be said that an increase in ambient turbulence intensity has an impact on the width of the wake of a tidal stream turbine. The increase in mixing associated with the increase in turbulence intensity means that the width of the region of highest velocity deficit reduces more rapidly, whilst at the same time, the overall width of the wake increases (albeit with its impact weakened). This result will be important for array designers and suggests that, combined with

186
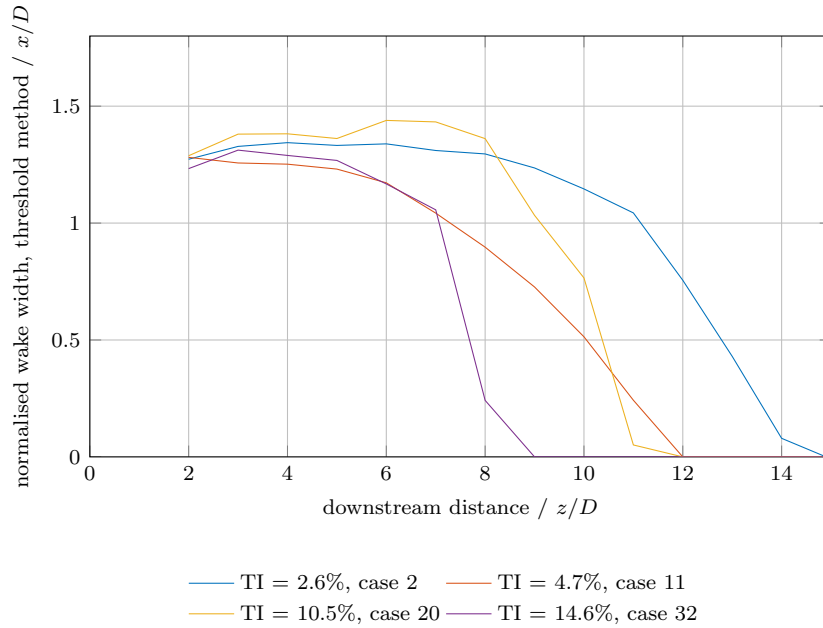
Figure 7.62: Impact of ambient turbulence intensity on wake width using fixed-threshold method, CFD cases.

the results for velocity recovery, arrays in areas of higher ambient turbulence intensity may benefit from a reduced longitudinal spacing, and increased lateral spacing. In effect, higher turbulence intensities tend to shorten and widen wakes.

Turbulence length scale

The impact of turbulence length scale on wake width is examined using the fixed-threshold, full-width half-minimum and maximum-shear methods in Figures 7.65, 7.66 and 7.67 respectively.

Figure 7.65 for the fixed threshold method shows that the width in the case with medium L_t ($L_t = 0.78$ m) remains fairly constant, whereas that with the shortest L_t ($L_t = 0.45$ m) shows the widest initial width with rapid narrowing. The case with the longest L_t ($L_t = 1.5$ m) shows a similar trend to that of the shortest L_t, albeit with narrowing which is not as rapid. The figure shows no clear overall trend of wake width with length scale using this method.

Impact of turbulence length scale using full-width half-minimum method is shown in Figure 7.66. In the mid-wake region ($3 \leq z/D \leq 11$), the shortest L_t shows the widest wake, whilst the longest L_t shows the narrowest. From $z/D \approx 11$, the longest length scale leads to the widest width. It is difficult to draw firm conclusions from this, but it could suggest that the largest turbulence length scales demonstrate less initial mixing (and therefore the narrow wake
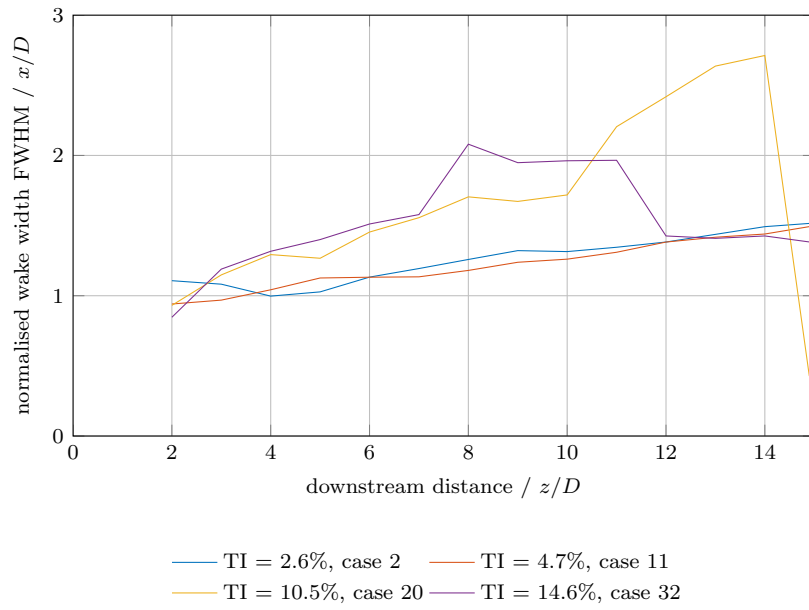
Figure 7.63: Impact of ambient turbulence intensity on wake width using full-width half-minimum method, CFD cases.
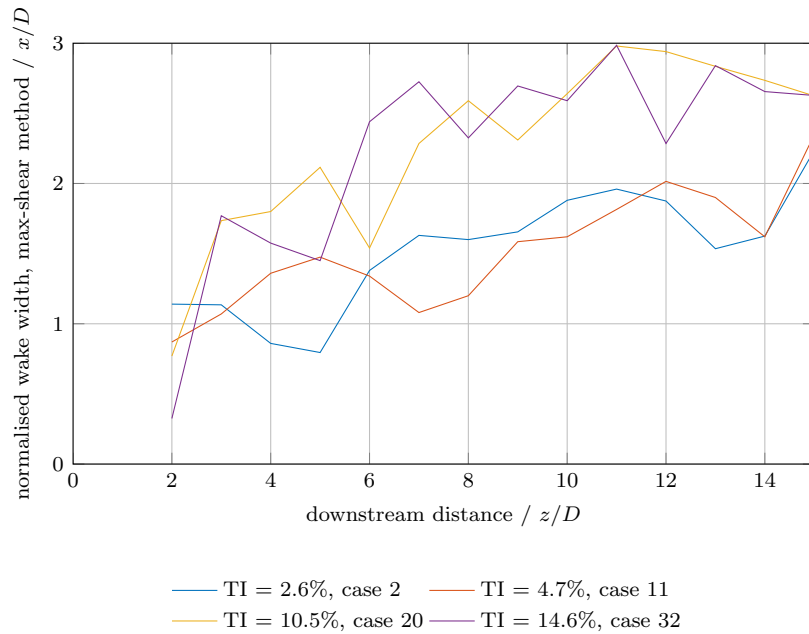
Figure 7.64: Impact of ambient turbulence intensity on wake width using maximum-shear method, CFD cases.

in the mid-wake region), but a more thorough mixing in the far wake region. Similar behaviour is also shown when the maximum-shear method is applied (Figure 7.67).

Overall, there is no clear trend of impact of L_t on wake width, regardless of which metric is used. However, only three different length scales have been compared here, and it has not been possible to completely isolate the effects of turbulence intensity and length scale. It might also be the case that turbulent length scales smaller or larger than those used here could have a different impact, and would be worthy of further investigation in order to establish any possible impact.
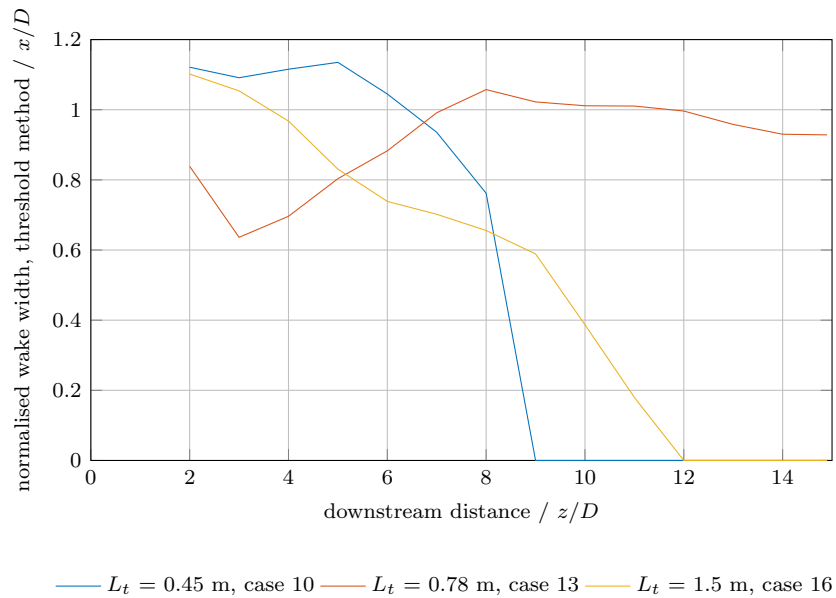
Figure 7.65: Impact of ambient turbulence length scale on wake width using the fixed-threshold method, CFD cases.

7.5.5 Impact of tip-speed ratio on wake width

The impact of tip-speed ratio on wake width can be seen in Figures 7.68, 7.69 and 7.70, for the fixed-threshold, full-width half-minimum and maximum-shear methods respectively. Regardless of which metric is used, there is a clear trend in the data that an increase in tip-speed ratio results in a wider wake. This trend is clearest when the fixed-threshold method is used. Here, all wakes maintain their initial width or widen slightly, before tending to narrow as downstream distance increases. All the wakes show the same general trends, but with the lowest thrust cases in general being the narrowest. The differences in width are most apparent for the low tip-speed ratios, whilst the higher tip-speed ratios
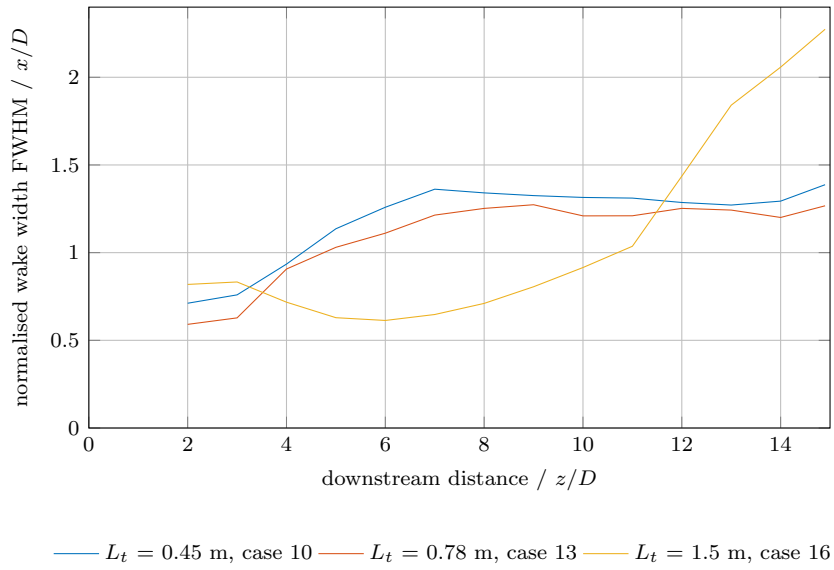
Figure 7.66: Impact of ambient turbulence length scale on wake width using the full-width half-minimum method, CFD cases.
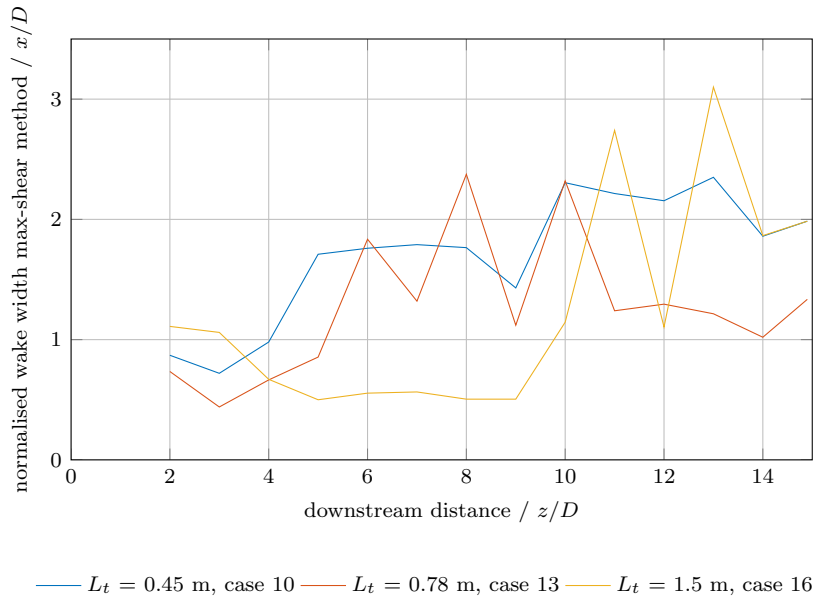
Figure 7.67: Impact of ambient turbulence length scale on wake width using maximum-shear method, CFD cases.

are more closely grouped together. This corresponds well to the thrust curve for this case, shown in Figure 7.5.

The same overall trend with tip-speed ratio can be seen in wake widths calculated using the full-width half-minimum method (Figure 7.69). As with the
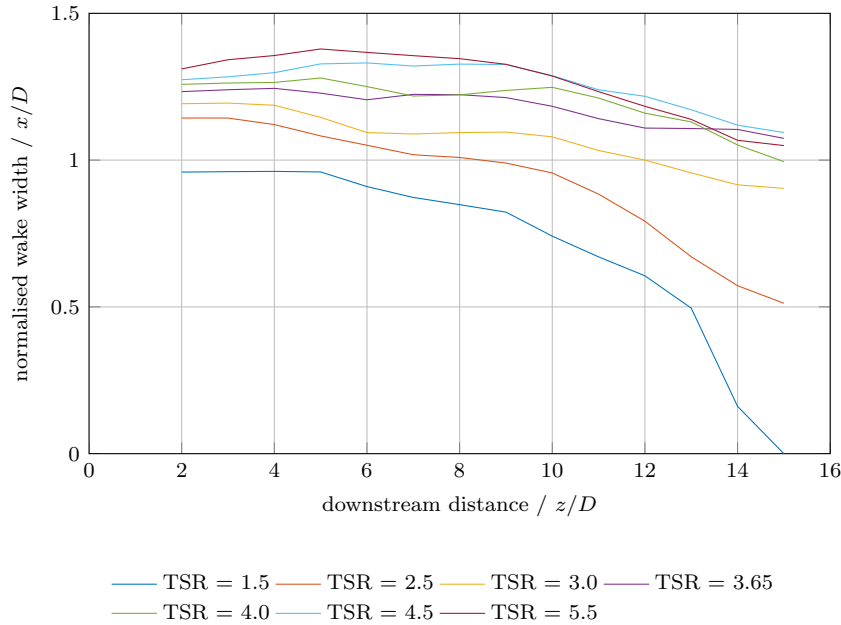
Figure 7.68: Impact of tip-speed ratio on fixed threshold wake width. Low ambient turbulence condition.

fixed-threshold method, the cases where the turbine is operating at a higher thrust demonstrate a greater wake width. However, with the full-width half-minimum method, the overall trend is that the wake width steadily increases with downstream distance. This difference, when compared to the fixed-threshold method, is due to firstly, the way that the two methods respond to wake profiles of different shapes, and secondly, as the full-width half-minimum method is a measure of the width of the region impact to some extent by the wake, this can be expected to increase as the wake spreads out downstream, even if its strength diminishes.

The cases closest to peak power, with tip-speed ratios of $\lambda = 3.0$–4.5 initially show a reduction in wake width until $z/D \approx 6$ downstream of the rotor, after which, they steadily increase in width. Tip-speed ratios of $\lambda = 3.65$ and above all show the same initial width, with the $\lambda = 3.0$ case showing a similar initial width as well. This is due to the shape of the velocity profiles, and how they change as the wake develops. All of these cases show a profile with very steep sides, similar to an inverted 'top-hat' shape, in the near wake. These steep sides are only slightly wider than the turbine, and are in the same position regardless of the velocity deficit in this region. Applying the full-width half-minimum method to an inverted top-hat shape will give an almost identical result for wake width, regardless of the maximum velocity deficit. This leads to the near-wake width of

191

each of these cases being nearly identical. In contrast, the low thrust cases with tip-speed ratios of $\lambda = 1.5$ and 2.5 do not show these inverted top-hat profiles, but show v-shaped profiles instead. As these v-shaped velocity profiles develop downstream, they reduce in depth and become proportionally wider, which is reflected in the steady increase in width measured using the full-width half-minimum method. For the cases where the initial profile is that of an inverse top-hat, as the wake develops and mixes with the free stream this inverse top-hat first becomes U-shaped, then v-shaped (leading to the apparent decrease in wake width), from which point the profiles reduce in depth and become proportionally wider, matching the trend shown with the low-thrust cases. These profiles for different tip-speed ratios can be seen in Figures 7.24–7.30. It is interesting to note that the tip-speed ratios for which the the reduction in wake width is greatest are around the point of maximum C_P. This may be coincidental, and appears to be a result in the changing shape of wake profiles, but it would make an interesting further study to investigate whether this behaviour is more universal, and applicable to other turbine designs.

Trends in wake width with tip-speed ratio are still apparent when the maximum-shear method is used (Figure 7.70), however, due to the convergence difficulties associated with this method, the differences are less clear. The convergence issues discussed in section 7.5.3 mean that there are two distinct regions: $z/D < 5$
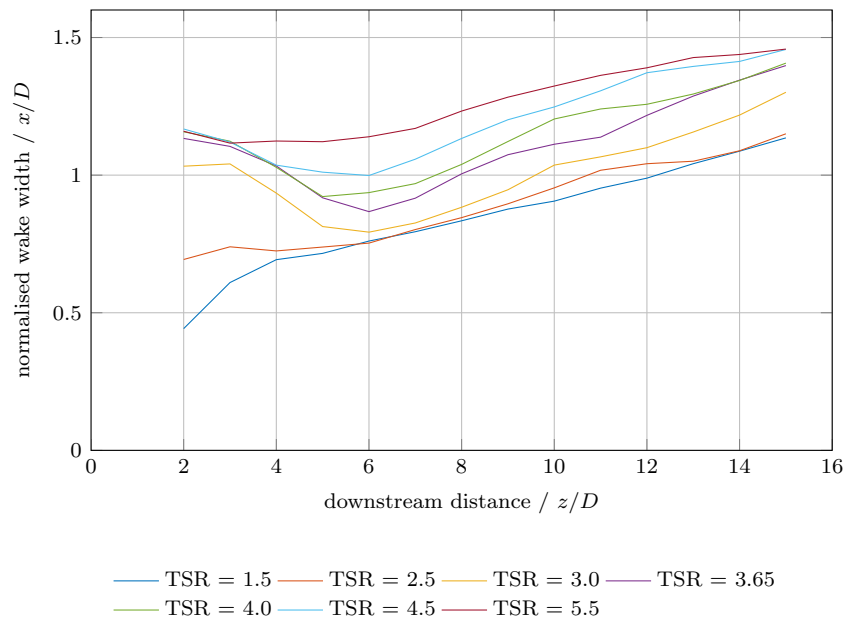
Figure 7.69: Impact of tip-speed ratio on full-width half-minimum wake width. Low ambient turbulence condition.
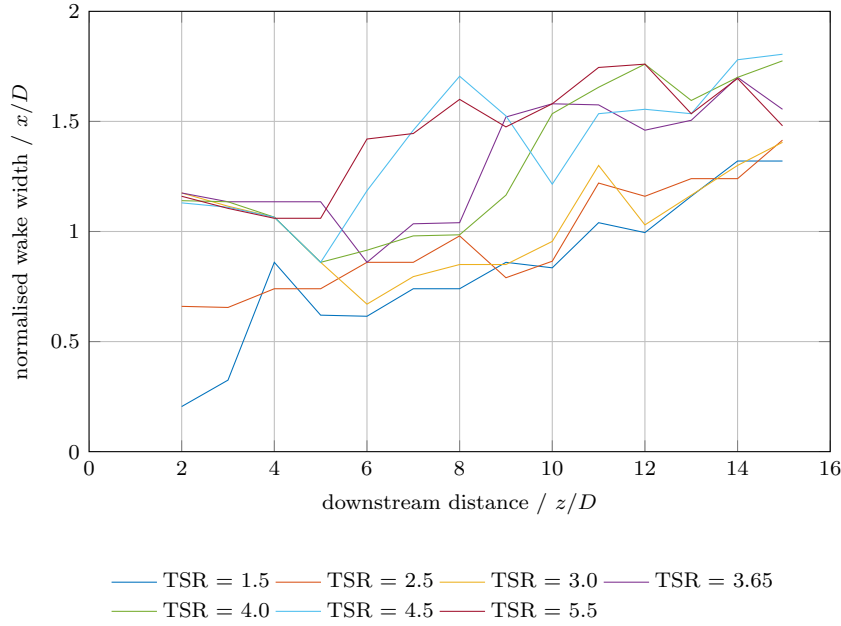
Figure 7.70: Impact of tip-speed ratio on maximum-shear wake width. Low ambient turbulence condition.

and $z/D > 5$. The reason for this difference is again the wake shape, being either an inverted top-hat, or approximately v-shaped. Tip-speed ratios of $\lambda \geq 3.0$ exhibit the inverted top-hat profile until $z/D \approx 5$, this means that the width using the maximum-shear method is well converged; there is a small cross-stream extent with the highest levels of shear. Beyond this point, the profiles become v-shaped; this means there is a large cross-stream extent with an almost identical amount of shear, which itself is approximately the maximum-shear in the wake. Any slight changes in the profiles can radically change the measured width, leading to the convergence difficulties and explaining the fluctuations visible in the region $z/D > 5$.

All three metrics demonstrate a clear impact of tip-speed ratio on wake width, with the high tip-speed ratio, high thrust cases demonstrating a wider wake. The close correlation of wake width and thrust can be most clearly seen in Figure 7.68, where not only does the sequence of the curves follow that of the thrust curve, but cases with similar levels of thrust demonstrate similar widths. An increase in width with increasing turbine thrust can be explained by the increase in resistance to the flow causing more of the flow to be divert outwards and around the swept area of the turbine, creating a wider wake.

7.6 Swirl

7.6.1 Flume results

Plots of wake swirl and maximum tangential velocity for the fine and coarse grid flume experiments are presented in Figures 7.71 and 7.72. In the low-turbulence flume experiment, velocity measurements were taken in the axial and cross-stream direction on a horizontal plane, and therefore no data were available for the tangential velocities. The figures presented here show the swirl results calculated using vertical (tangential) velocity measurements from a horizontal plane. Equation 3.19 was applied to the time-averaged axial and tangential velocities measured at downstream locations $2 \leq z/D \leq 12$ to yield the swirl number, S, at each of these locations. Measurements at $z/D < 2$ were not possible due to the length of the turbine nacelle and hose.

Figure 7.71 shows that for both the fine grid and coarse grid cases (TI = 11.7% and 17.5%, respectively), there is a clear trend of swirl with tip-speed ratio. Lower tip-speed ratios, which correspond to higher turbine torques, lead to a higher level of swirl in the wake. The greater torque exerted by the flow on the turbine induces a greater reaction torque by the turbine on the flow, inducing more rotational movement, and therefore a more swirl. An overall reduction in wake swirl is seen in the higher-turbulence case, despite the higher values of $\overline{C_\theta}$ recorded in this case (Figure 7.3), suggesting that the increased wake mixing due to the increased turbulence is reducing the level of swirl in the wake.

Figure 7.72 shows how the maximum tangential velocity present in the wake evolves with downstream distance from the turbine. In general, this figure confirms the findings of Figure 7.71, that tip-speed ratios with a higher turbine torque lead to greater rotational velocity components in the wake, and that increased turbulent mixing reduces the rotational velocity component in the wake. Nonetheless, there are some difference between the plots. Figure 7.72 shows some slight increases of maximum tangential velocity at $z/D = 9$ in the case of the fine grid, and $z/D = 7$ and 12 in the case of the coarse grid. These are thought to be due to the presence of U-shaped metal channels on the floor of the flume (used to prevent movement of the textile conveyor belt) causing a slight upward deviation of the flow. These do not appear in the swirl results, as an increase in vertical velocity on both sides of the wake will cancel itself out.

7.6.2 Validation of CFD

For the purposes of validation, plots comparing the swirl in the CFD and flume data can be seen in Figures 7.73 and 7.74 for the fine and coarse grids. Plots

194
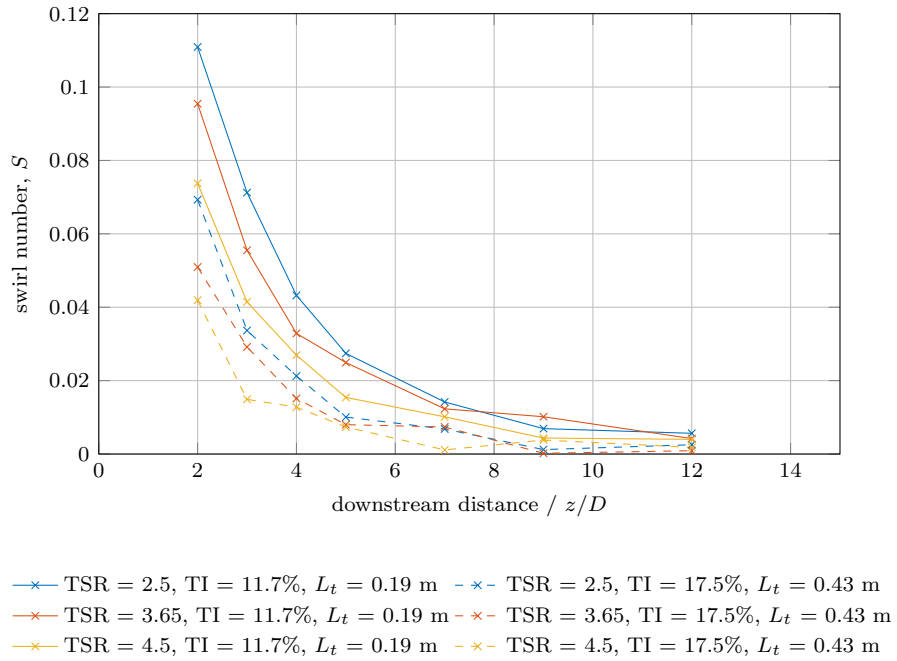
Figure 7.71: Swirl: flume results.
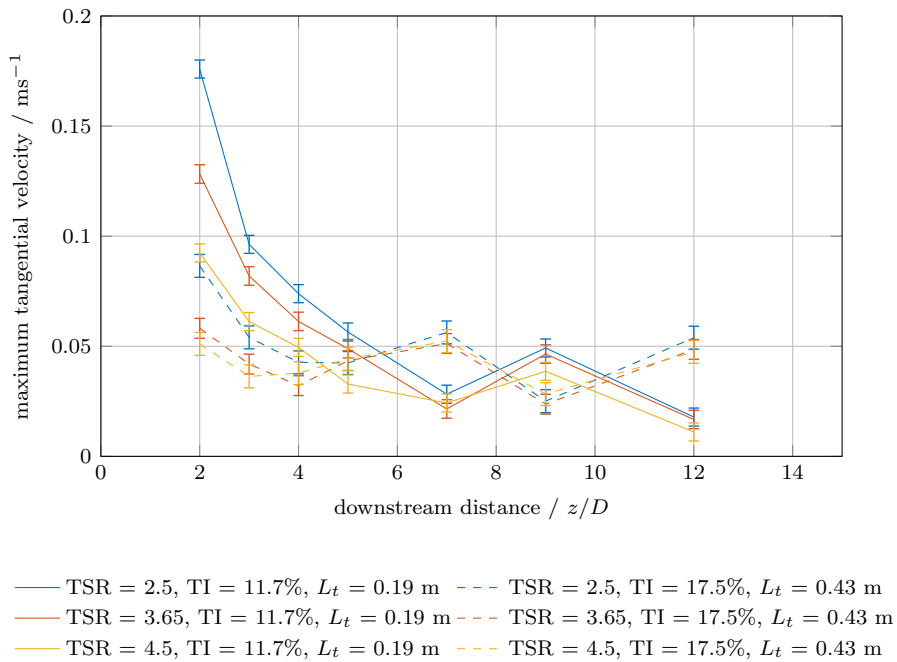
Figure 7.72: Maximum tangential velocities: flume results.

comparing the maximum tangential velocity in the CFD and flume data can be seen in Figures 7.75 and 7.76.

Figure 7.73 compares swirl for the fine grid case. In terms of the shape of the curves, there is good agreement between the CFD and the flume results, although the CFD tends to give a small over-prediction the level of swirl. In the near-wake, the CFD matches the trend in tip-speed ratio seen in the flume data, with the high torque case producing a wake with more swirl. This relationship is preserved between the $\lambda = 2.5$ and $\lambda = 3.65$ CFD cases throughout the wake, but by $z/D = 5$, the $\lambda = 4.5$ case is exhibiting slightly more swirl than the other two. It is unclear why this is the case, but it should be noted that the level of swirl has significantly weakened by this point, and therefore the differences between the wakes becomes less clear.

Swirl in the wake of the turbine in the coarse grid generated turbulence is compared to CFD data for validation in Figure 7.74. As with the fine grid case, the CFD results tend to over-predict the swirl in the wake region. For the majority of the wake, the higher-torque turbine operating condition yields more swirl in the wake. Comparison of the fine grid CFD results in Figure 7.73 and coarse grid results in Figure 7.74 shows that the CFD generally predicts lower wake swirl in the higher turbulence case, reflecting the trend seen in the flume results (Figure 7.71).
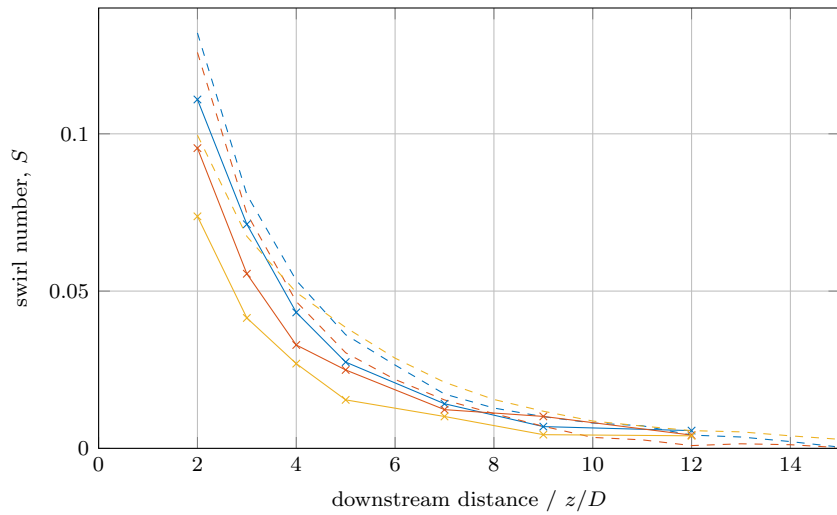
Figure 7.73: Validation using flume results with the fine grid: swirl.
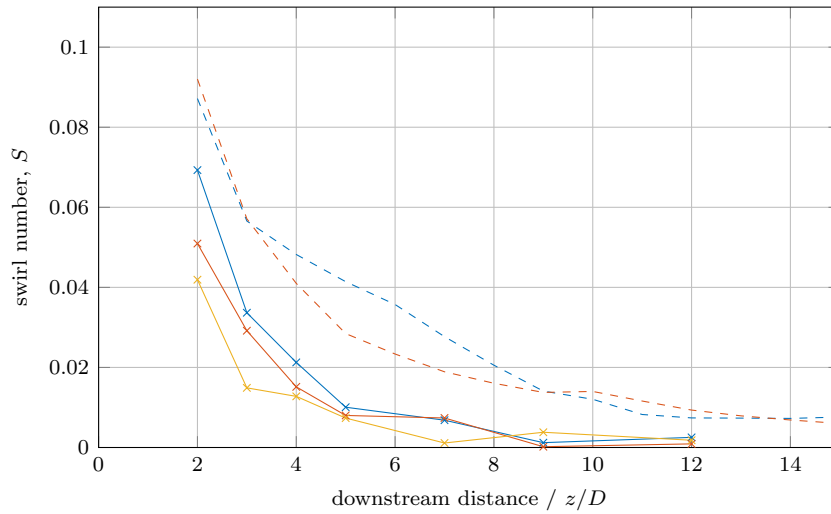
Figure 7.74: Validation using flume results with the coarse grid: swirl.

Maximum tangential velocity for the fine grid case is compared to the CFD in Figure 7.75, and for the coarse grid case in figure 7.76. The agreement in terms of trends with tip-speed ratio and downstream distance as well as numerical agreement is similar to that seen in the swirl validation plots. This is not surprising, as the tangential velocity is in part used to calculate the swirl number, S. In both the fine grid and coarse grid cases, the CFD tends to over-predict the maximum tangential velocity (consistent with over-predicting the swirl), although the increased velocities due to the U-shaped channels are not present in the CFD results, as these were not modelled. As with the swirl, the maximum tangential velocity in the turbine wake is less in the high-turbulence case, probably due to increases in mixing causing the velocity to be reduced.

7.6.3 Impact of turbulence on swirl

Turbulence intensity

The impact of turbulence intensity on wake swirl is evaluated via the flume results (Figure 7.71), as well as using four CFD cases (Figure 7.77). The flume cases show a similar trend for the three tip-speed ratios tested, but the swirl measured is lower in all cases for a higher turbulence intensity. This general trend is reproduced in Figure 7.77, with the lowest turbulence intensity case showing the greatest amount of swirl throughout the wake. The other three
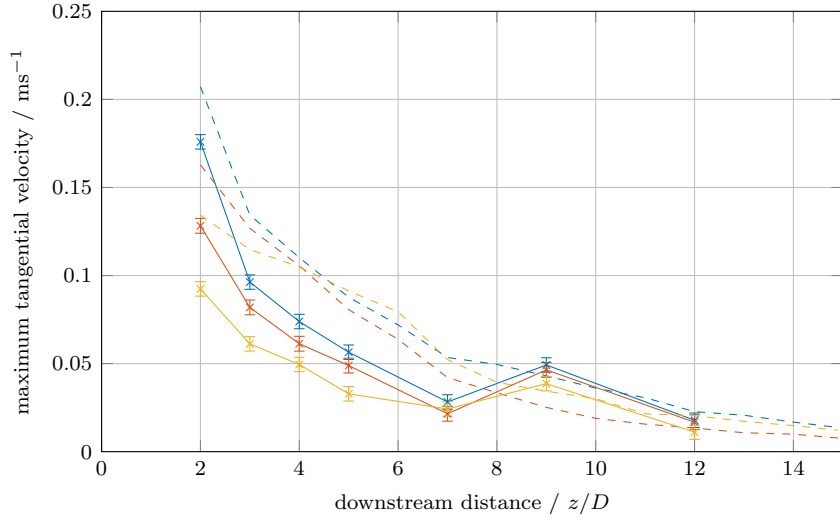
197

Figure 7.75: Validation using flume results with the fine grid: maximum tangential velocity.

cases, with turbulence intensities of 2.6–14.6%, showed similar levels of swirl initially, and decaying in a similar way without showing any clear trend between them.

The impact of ambient turbulence intensity on the recorded maximum tangential velocity in the wake is evaluated using the flume results presented in Figure 7.72, and four CFD cases presented in Figure 7.78. As with swirl, it was found that higher turbulence intensities lead to reduced maximum tangential velocities in the wake for the flume measurements. This trend is broadly reproduced in Figure 7.78; the low-turbulence curve shows significantly higher maximum tangential velocities, but there is little difference between the other three cases with turbulence intensities of 2.6–14.6%.

The dependence of both swirl and maximum tangential velocity on ambient turbulence intensity is thought to be due to an increase in turbulence leading to an increase in mixing, reducing the strength of the rotational velocity component. In addition to this, a greater turbulence intensity tends to lead to faster wake recovery; therefore, even for the same rotational velocity in the wake, at a given downstream distance the axial velocity will be higher, reducing the calculated swirl number, S. As with the impact of turbulence intensity on wake recovery, there appears to be a limit of turbulence intensity beyond which a
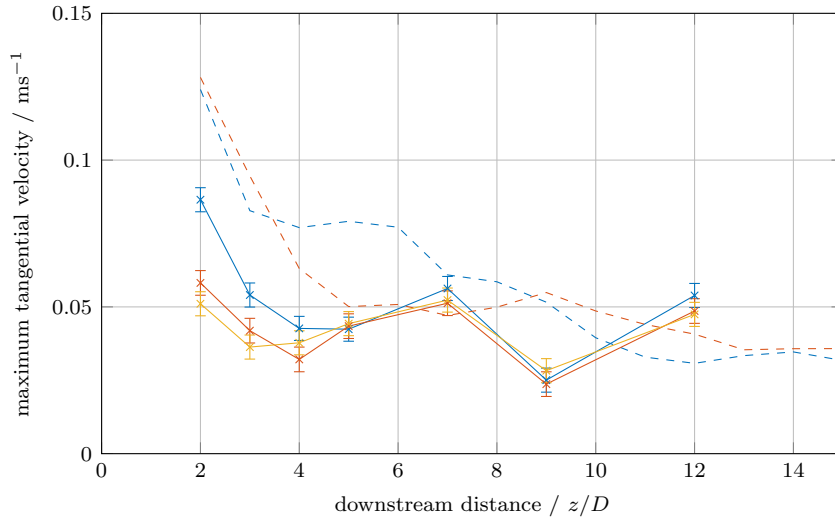
Figure 7.76: Validation using flume results with the coarse grid: maximum tangential velocity.

further increase has little impact on swirl. Turbulence intensities of 4.7% and above appear to have similar levels of swirl and maximum tangential velocity, with only the case with lowest turbulence intensity showing significantly greater rotation in the wake.

Turbulence length scale

The impact of turbulence length scale on wake swirl can be seen in Figure 7.79, which compares three CFD runs with flow conditions which are similar to each other except for turbulence length scale. In the near wake ($z/D \leq 4$), the cases with the longest ($L_t = 1.5$ m) and the shortest ($L_t = 0.45$ m) length scales show the most swirl, with the medium case ($L_t = 0.78$ m) showing the least swirl. From this point to $z/D \approx 9$, the case with the longest length scale displays the most swirl, and that with the shortest length scale displays the least swirl. A very similar trend is visible in Figure 7.80, which shows the impact of turbulence length scale on the maximum tangential velocity in the wake.

It is difficult to draw firm conclusions from this information, as only three cases are available for comparison, and it is not known if the behaviour is linear or not. It is conceivable that a particular length scale could induce the most mixing in the wake region, reducing swirl, and it is possible, for example, that the
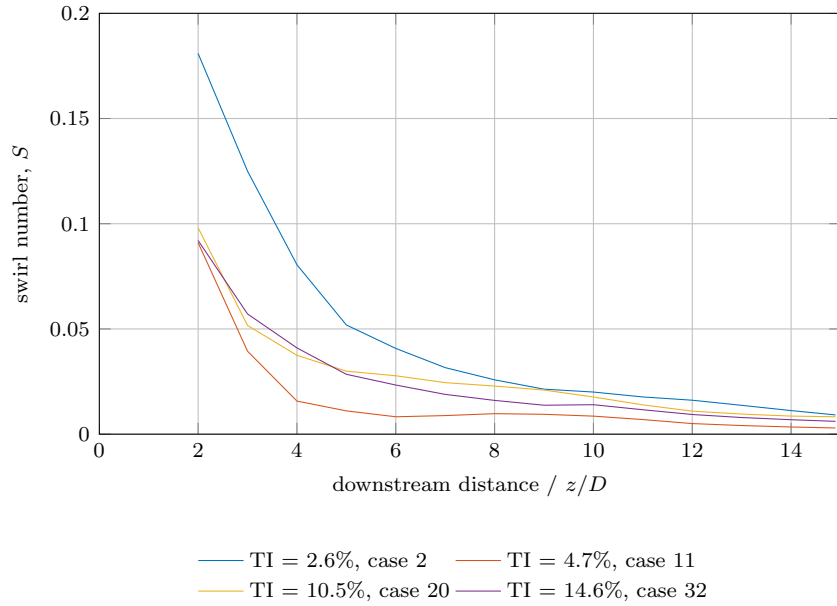
Figure 7.77: Impact of ambient turbulence intensity on wake swirl, CFD cases.
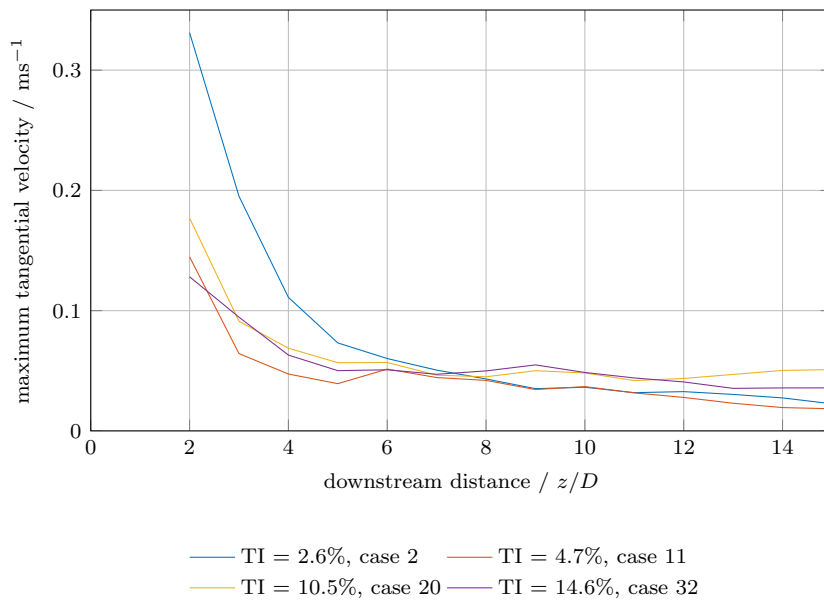
Figure 7.78: Impact of ambient turbulence intensity on maximum tangential velocity, CFD cases.
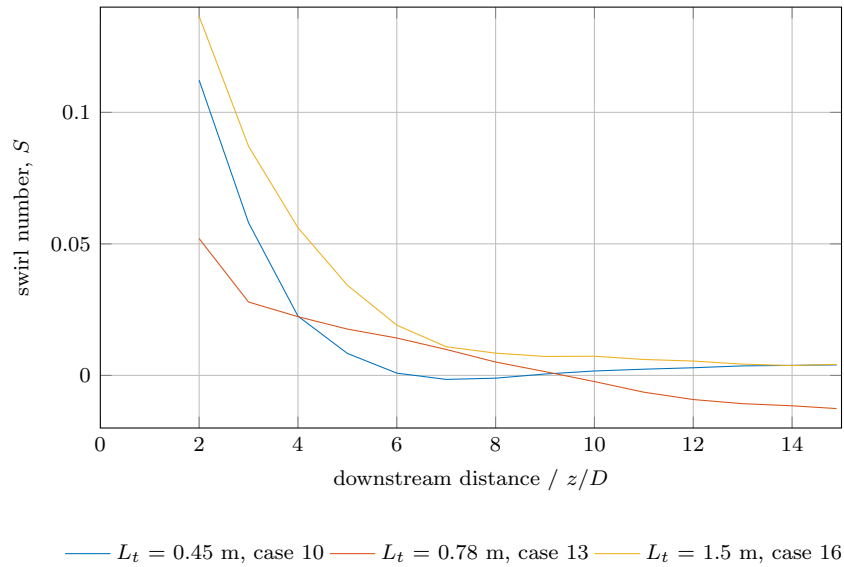
Figure 7.79: Impact of ambient turbulence length scale on wake swirl, CFD cases.

medium length scale case could be most effective at this. Large length scales may move the wake wholesale, as a surge in fluid velocity might, whereas very small length scales may be less effective at creating large-scale momentum exchange and mixing than medium length scales. However, given the information and results available, it is not possible to draw firm conclusions, other than to say that the area would be an interesting one for further research.

7.6.4 Impact of tip-speed ratio on swirl

As discussed above, the flume results presented in Figure 7.71, suggest that the swirl in the wake is dependent on the torque at which the turbine is operating, with a higher $\overline{C_\theta}$ leading to greater wake swirl. Seven tip-speed ratios were investigated for a low-turbulence case, with curves for swirl number being presented in Figure 7.81. This confirms that wake swirl generally follows the curve of $\overline{C_\theta}$ (Figure 7.6). The highest-torque tip-speed ratio, $\lambda = 2.5$, shows slightly less swirl in the very near wake ($z/D < 3.5$) than other high torque cases; the reason for this becomes clear though when Figure 7.45 is considered at the same time. This shows that the $\lambda = 2.5$ case has a slight uplift in the wake recovery in this region, and as the swirl number is calculated using the ratio of axial velocity flux to tangential velocity flux, this slightly raised axial velocity will lead to a slightly depressed swirl in this region, even if the tangential velocities in this case and its neighbours are similar. Nonetheless, beyond $z/D = 3.5$, the $\lambda = 2.5$ case shows the most swirl in the wake region, demonstrating that the
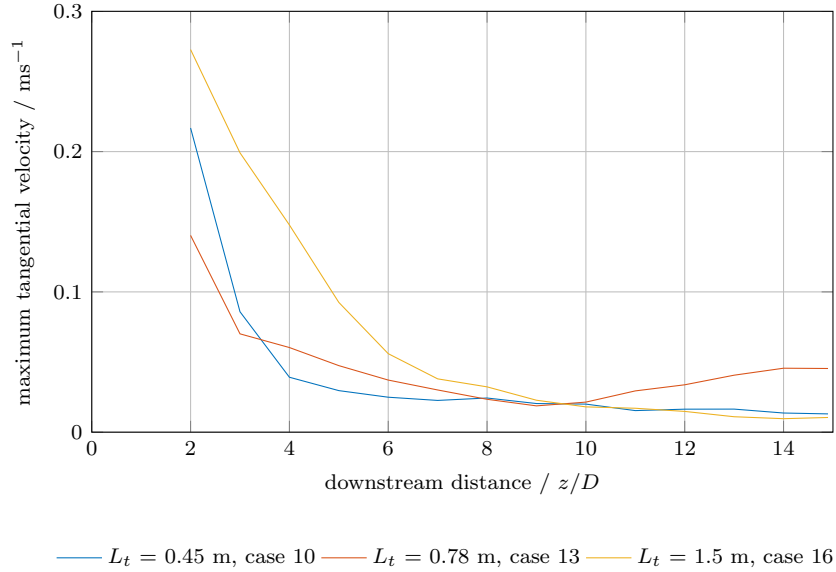
Figure 7.80: Impact of ambient turbulence length scale on maximum tangential velocity, CFD cases.

differences in wake rotation due to tip-speed ratio measured immediately behind a turbine by Morandi et al.[94] persist into the near- and mid-wake regions.

7.7 Wake turbulence characteristics

7.7.1 Flume results

Results from all flume campaigns for centreline 1D turbulence intensity and integral length scale, L_t, are presented in Figures 7.82 and 7.83 respectively.

For all cases, it can be seen that the centreline 1D turbulence intensity reduces as the distance from the turbine increases. These curves show the typical behaviour of turbulence dissipating in time, due to the action of viscous forces. Initial wake turbulence intensity appears to have some dependence on the ambient turbulence intensity, with a higher wake turbulence intensity being demonstrated in the case with higher ambient turbulence. The low-turbulence case does not fit this pattern, indicating that the level of turbulence intensity in the wake is more heavily influenced by the presence of the turbine, rather than by the ambient turbulence intensity. In the near wake for the fine-grid case (TI = 11.7%), there appears to be a dependence of wake turbulence intensity on tip-speed ratio, with higher tip-speed ratios leading to a higher near-wake turbulence intensity. Beyond $z/D = 5$ however, tip-speed ratio appears to make little difference to wake turbulence intensity, and this behaviour is not
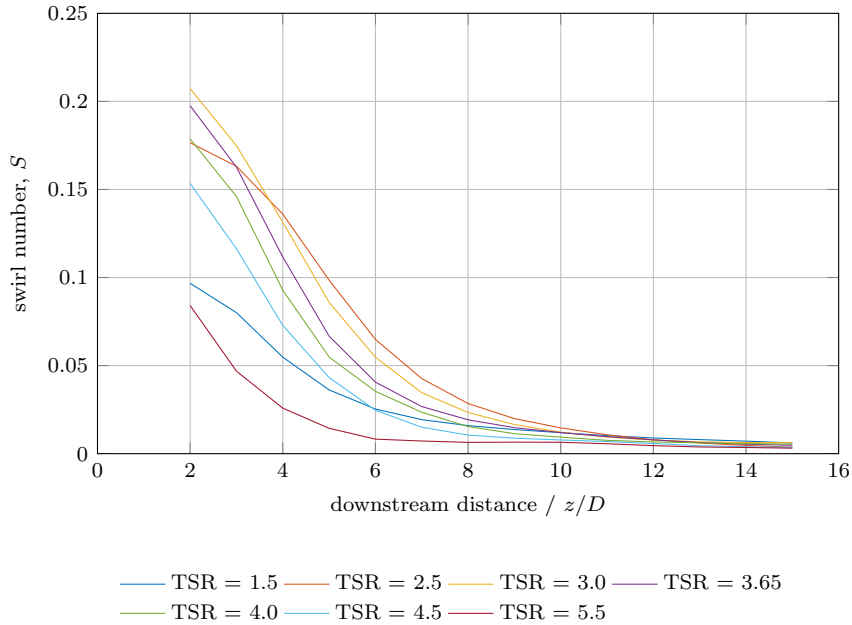
Figure 7.81: Impact of tip-speed ratio on wake swirl. Low ambient turbulence condition.

clearly apparent in the coarse-grid case (TI $= 17.5\%$). It seems that ambient turbulence intensity has little impact on the wake turbulence intensity; this result is perhaps unsurprising considering analysis here has been carried out on the wake centreline, the region which can be expected to be most affected by the turbine turbulence, and least affected by the ambient turbulence.

Flume results for centreline L_t can be seen in Figure 7.83. All cases show a steady increase in L_t as the wake develops, again typical of the behaviour of turbulence downstream of an obstruction. Through the turbulence energy cascade, energy passes from large scales to small scales, from where it is dissipated as heat by viscous forces[121]. As the smallest scales are removed by viscous action, the larger scales dominate, leading to increasing L_t as the wake develops. The flume results for the coarse grid case show a greater overall length scale than that for the fine grid, which itself demonstrates a larger length scale than the low-turbulence case. Different tip-speed ratios, whilst not producing identical results, do not show a clear trend in terms of their impact on L_t.
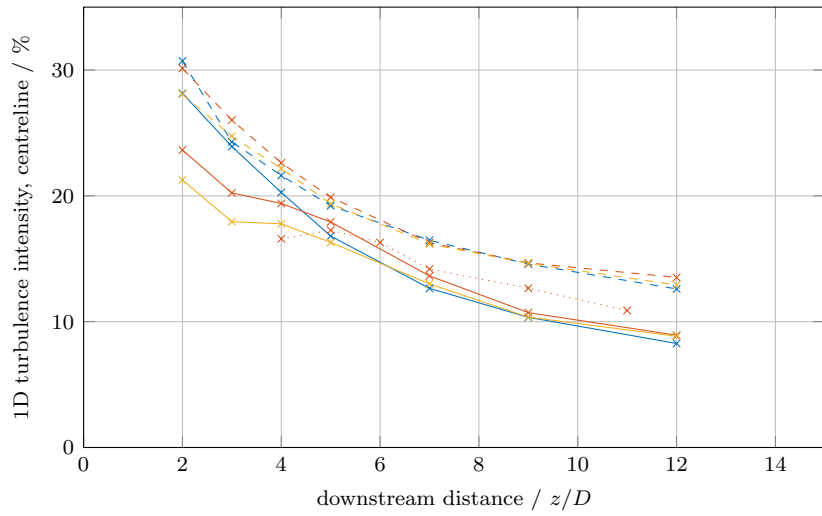
Figure 7.82: Centreline turbulence intensity: flume results.
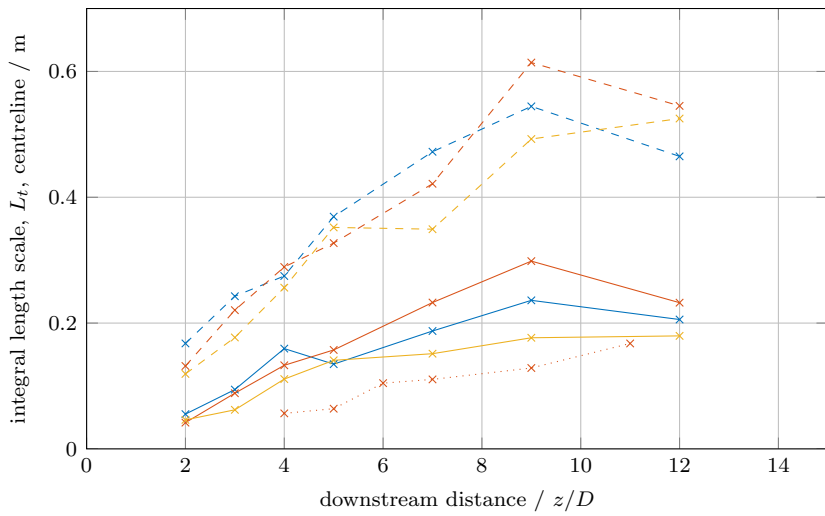
Figure 7.83: Centreline turbulence length scale, L_t: flume results.

7.7.2 Validation of CFD

Validation plots comparing flume results to CFD results for the low-turbulence (TI = 1.75%), fine grid (TI = 11.7%) and coarse grid (TI = 17.5%) flume campaign can be seen in Figures 7.84, 7.85 and 7.86 for 1D centreline turbulence intensity.

Validation using the low-turbulence flume campaign (Figure 7.84) shows that the CFD over-predicts turbulence intensity in the near wake region. However, from $z/D = 9$ to the end of the available flume data the agreement is very good, and an extrapolation of the results from the flume would show good agreement with the CFD from this point onwards, suggesting that the CFD accurately reproduces the wake by this point. Part of the reason for the over-prediction of turbulence intensity in the near wake will be down to the CFD's slight under-prediction of velocity recovery in this region (Figure 7.34), meaning that the same magnitude of fluctuations would yield a higher value of turbulence intensity. However, this is not enough to completely explain the difference. The poor agreement in the near-wake may be improved by further increasing the mesh density in the region directly surrounding the turbine.

Validation using the fine grid flume campaign (Figure 7.85) shows good agreement between flume and CFD from $z/D \approx 4$ onwards. Further upstream, it can be seen that the CFD tends to over-predict the turbulence intensity, however, the agreement is better than that in Figure 7.84. In addition, the CFD reproduces the trend seen in the near-wake of the flume results; that of a dependence of turbulence intensity on tip-speed ratio. The CFD reproduces both the trend of lower tip-speed ratios producing the highest initial turbulence intensities, but also that any difference between these cases becomes indistinguishable from $z/D \approx 4$.

Validation using the coarse grid flume campaign (Figure 7.86) shows very good agreement between the CFD and flume results throughout the region for which flume data was available. Agreement is good in terms of both the shape of the curves, as well as their magnitudes. Neither the flume data nor the CFD results demonstrate a dependence of wake turbulence intensity on tip-speed ratio.

Centreline wake L_t has been validated using data from the low-turbulence flume campaign and is presented in Figure 7.87. As with the agreement for turbulence intensity in this case (Figure 7.84), the CFD tends to over-predict L_t in the near- and mid-wake regions, but agreement is good from $z/D \approx 9$ onwards, and an extrapolation of the curve of flume data would be expected to show good agreement with the CFD data. As with turbulence intensity, it is thought that the poor agreement in the near-wake may be improved by
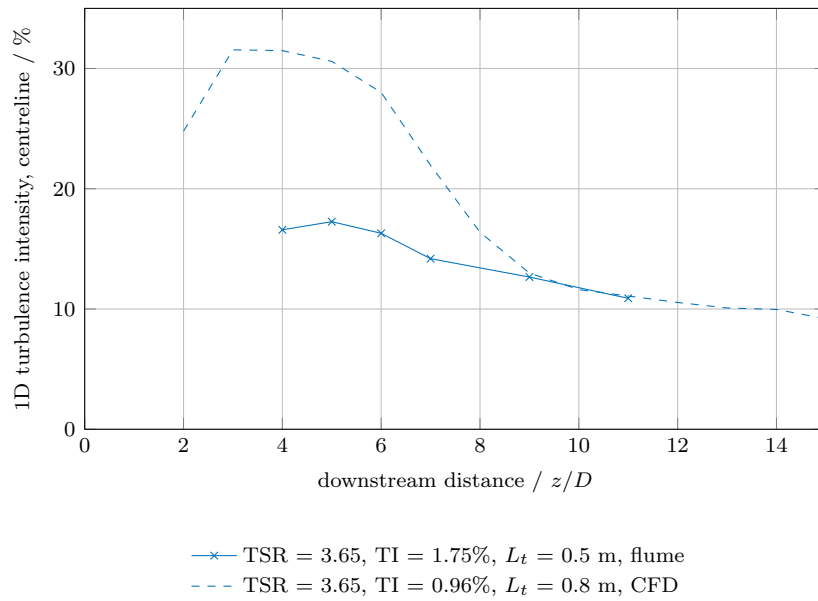
Figure 7.84: Validation of low-turbulence flume campaign: wake turbulence intensity.
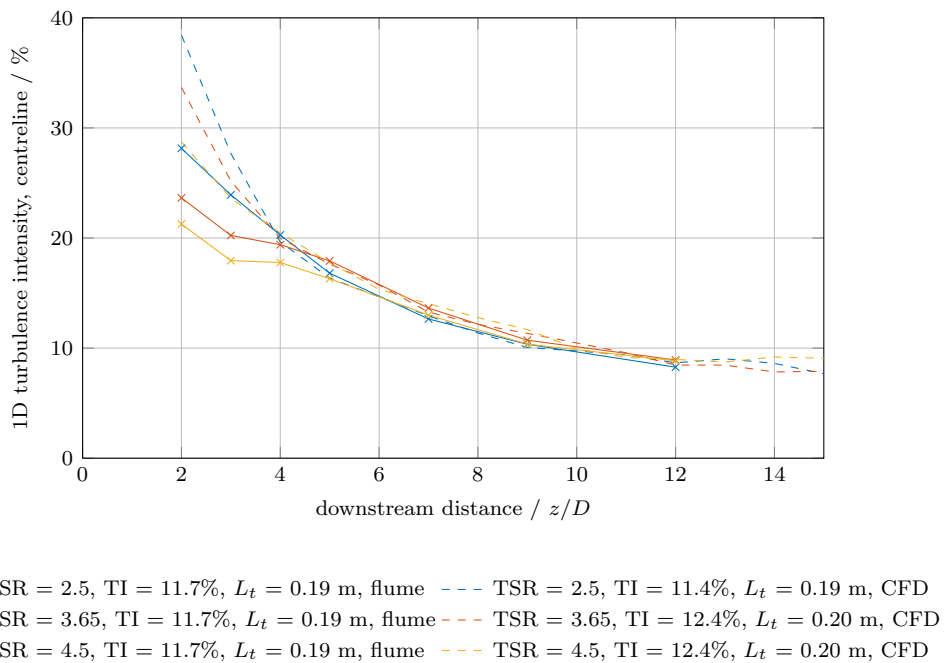
Figure 7.85: Validation using flume results with the fine grid: wake turbulence intensity.
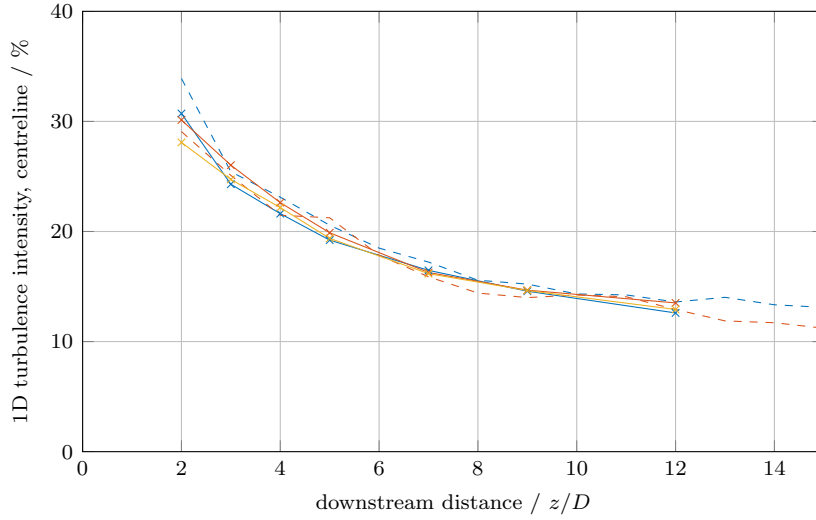
Figure 7.86: Validation using flume results with the coarse grid: wake turbulence intensity.

increasing mesh density in the region directly surrounding the turbine.

Validation of CFD results for L_t when compared to the flume results from the fine grid campaign are shown in Figure 7.88. The CFD results for the $\lambda = 2.5$ and $\lambda = 3.65$ cases reflect the trend in the flume results of a gradual rise in L_t as the wake develops, but show an under-prediction in the rate of increase. The larger changes in the $\lambda = 4.5$ case indicate a possible convergence issue; other studies have shown that a sample time of 50 s is at the lower bound of what is required to obtain reliable well converged results for a higher order statistic such as integral length scale[59].

Validation of the CFD results for the coarse grid flume cases is shown in Figure 7.89. All three tip-speed ratios modelled show similar values of L_t in the wake of approximately 0.25 m, which remains nearly constant throughout the wake, in contrast to the steady rising of L_t seen in the flume results. The agreement is good in the near-wake region, but deteriorates as the wake develops, indicating a general trend in the CFD to under-predict length scale. The value of L_t in the CFD models for the coarse grid cases is slightly higher than that for the CFD models in the fine grid cases, which reflects the trend between in the flume results.
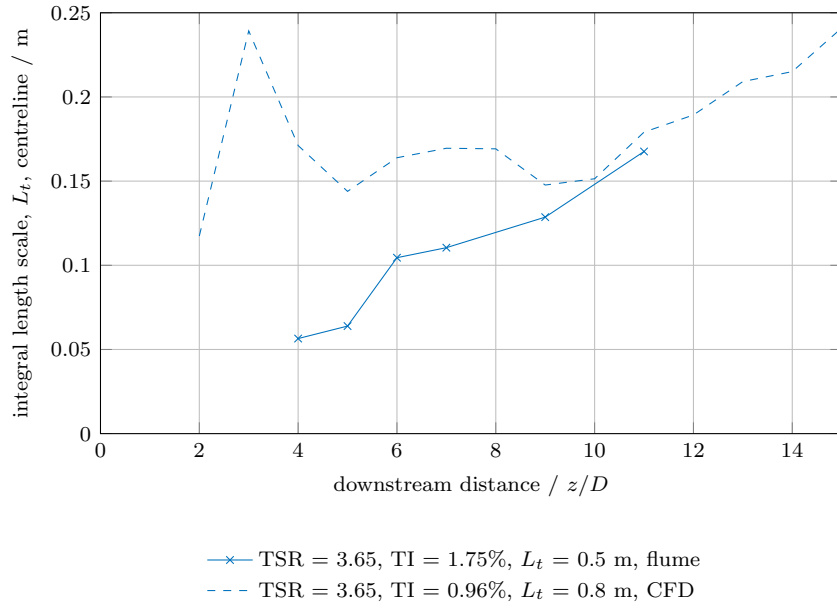
Figure 7.87: Validation of low-turbulence flume campaign: wake turbulence length scale.
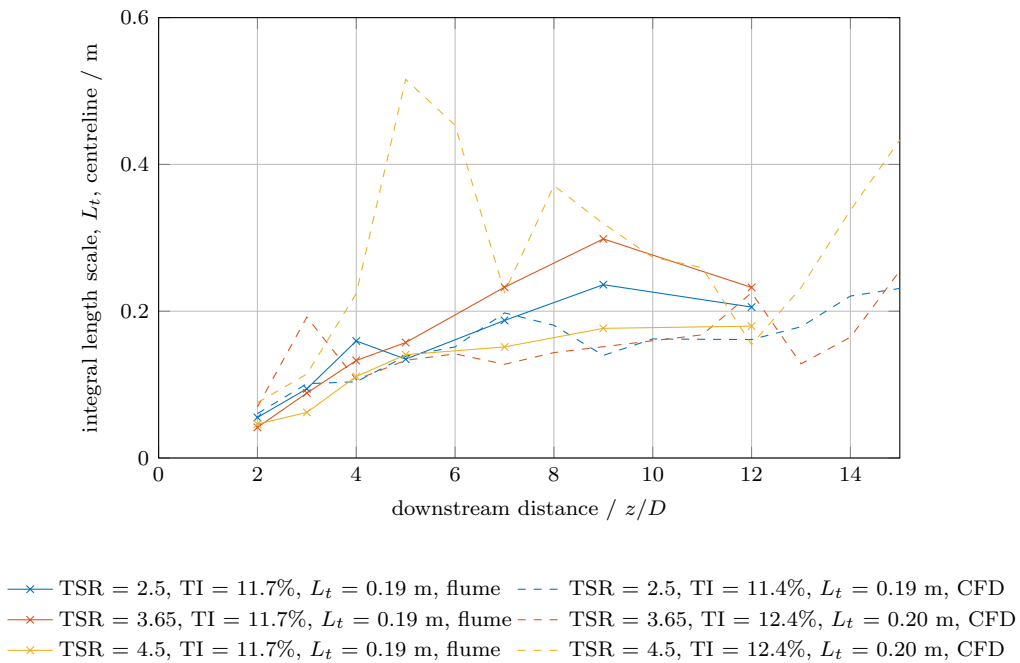
Figure 7.88: Validation using flume results with the fine grid: wake turbulence length scale.
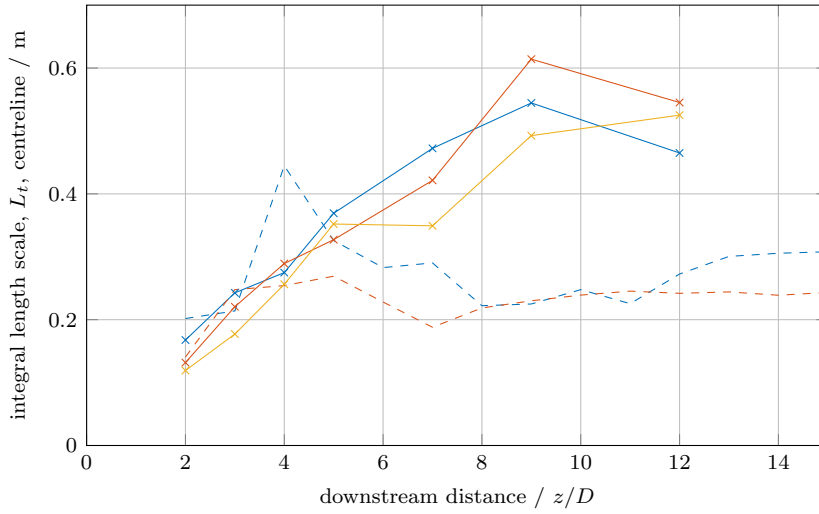
Figure 7.89: Validation using flume results with the coarse grid: wake turbulence length scale.

7.7.3 Impact of turbulence on wake turbulence characteristics

Turbulence intensity

The impact of ambient turbulence intensity on wake centreline turbulence intensity was analysed using four CFD cases, the results from which are presented in Figure 7.90. The results indicate a possible weak dependence of wake turbulence intensity on ambient turbulence intensity, with a higher ambient turbulence intensity leading to a higher wake turbulence intensity. This agrees with the mild dependence on ambient turbulence intensity shown in the flume results. The largest difference between the cases is in the near- to mid-wake region; by $z/D = 10$, there is little difference in the centreline turbulence intensities, regardless of the ambient turbulence intensity upstream.

The impact of ambient turbulence intensity on turbulence length scale can be seen through the comparison of four CFD cases presented in Figure 7.91. In general, there is little difference between the cases, with all cases showing a slight increase in length scale with increasing downstream distance. Both the trends in, and the magnitudes of L_t, are similar for all cases, indicating that ambient turbulence intensity has little dependence on wake L_t. The increase in L_t in the far-wake for case 11 is unexplained, but could again indicate a
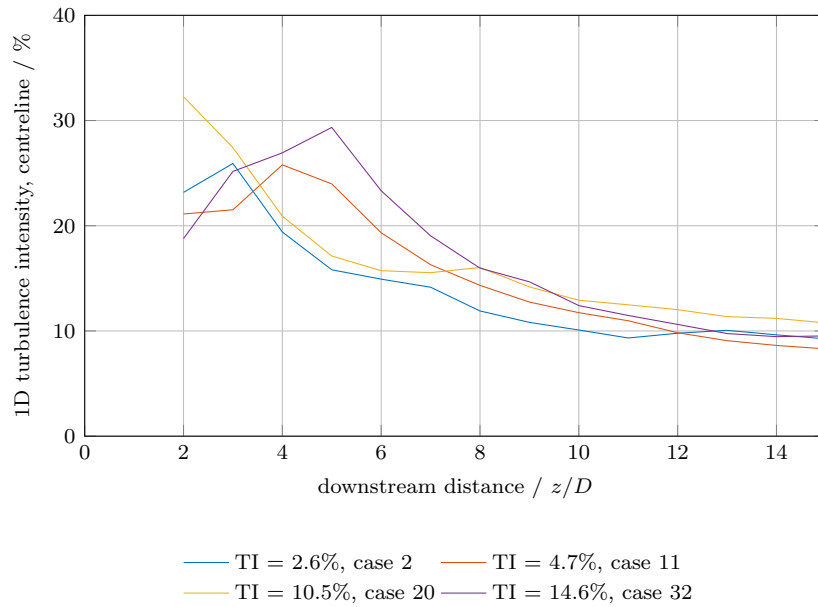
Figure 7.90: Impact of ambient turbulence intensity on centreline wake turbulence intensity, CFD cases.

convergence issue, similar to that seen in Figure 7.88.
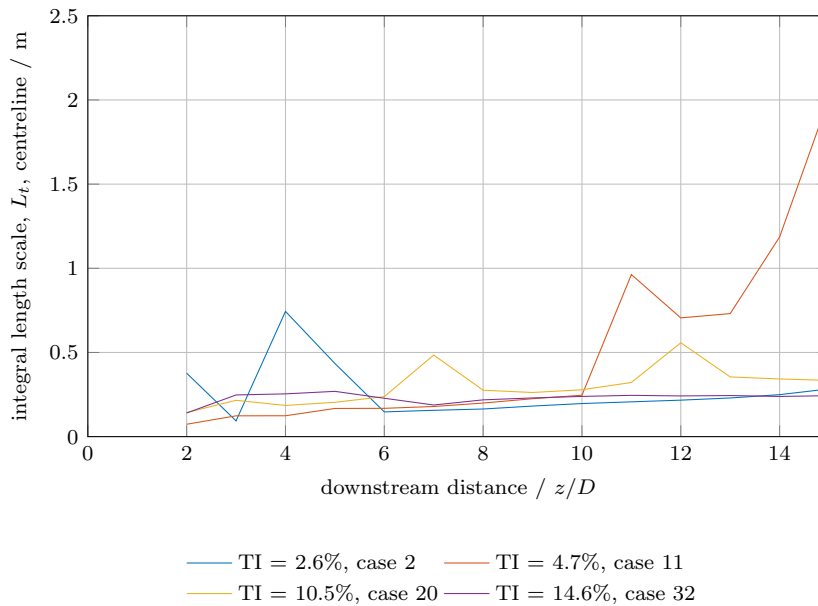
Figure 7.91: Impact of ambient turbulence intensity on centreline turbulence length scale, L_t, CFD cases.

Turbulence length scale

The impact of ambient L_t on wake centreline turbulence intensity is presented in Figure 7.92, which compares three CFD runs with identical tip-speed ratios, similar turbulence intensities, but differing turbulence length scales. No clear trend is observable, although it could be said that the cases with the shortest and longest values of ambient L_t show similar behaviours, with the medium turbulence length scale showing a significantly lower initial turbulence intensity. This could indicate a non-linear response of wake centreline turbulence intensity to L_t, for example suggesting that wake mixing might not simply increase or decrease with increasing ambient L_t, but rather that there might be a value of ambient L_t which causes most mixing, and a longer or shorter length scale leads to reduced wake mixing. However, Figure 7.92 does not provide enough information in order to be able to conclusively make this assertion.

Figure 7.93 shows the impact of ambient turbulence length scale on the wake centreline turbulence length scale. All cases show a sharp initial rise in L_t, followed by a reduction, before resuming a steady rise towards the far wake. All cases show similar results beyond approximately $z/D = 10$. Here there appears to be some dependence of wake L_t on ambient L_t. Perhaps unsurprisingly, a larger ambient L_t leads to a larger value of L_t in the near- to mid-wake, but it also seems to cause the point at which L_t peaks before reducing to move further downstream.
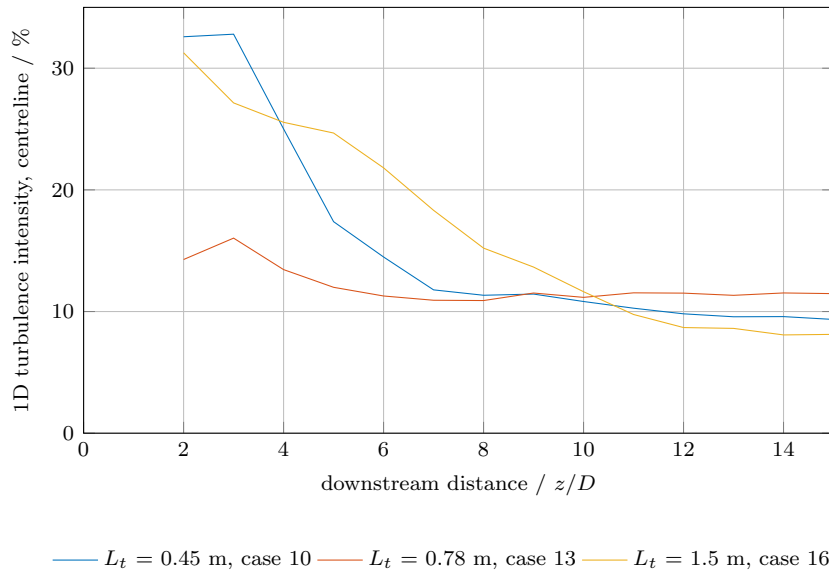
Figure 7.92: Impact of ambient turbulence length scale on centreline wake turbulence intensity, CFD cases.
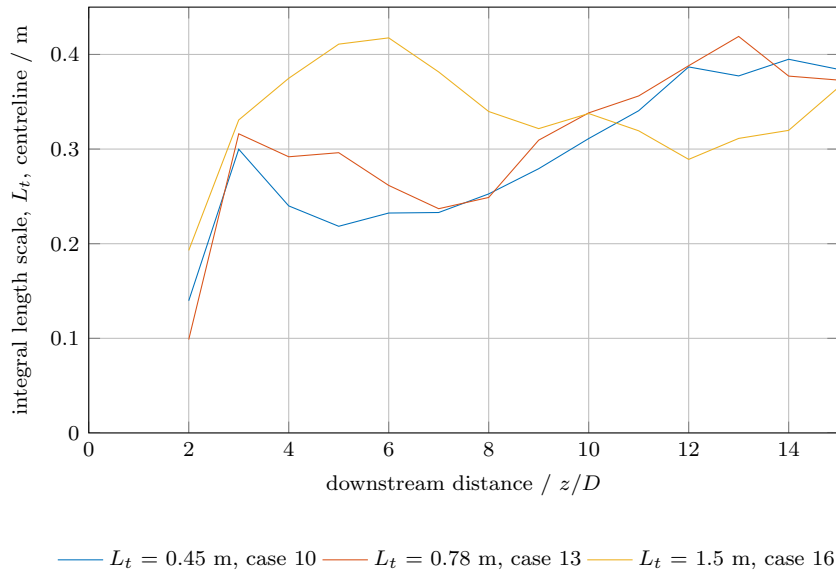
Figure 7.93: Impact of ambient turbulence length scale on centreline wake turbulence length scale, CFD cases.

7.7.4 Impact of tip-speed ratio on wake turbulence characteristics

The impact of tip-speed ratio on centreline turbulence intensity was examined via seven different CFD cases in a low-turbulence environment of approximately 1.5%. These results of these runs are presented in Figure 7.94.

This figure shows that the lowest two tip-speed ratios ($\lambda = 1.5$ and $\lambda = 2.5$) initially demonstrate a very high initial turbulence intensity, which very quickly drops. Tip-speed ratios around the point of peak C_P ($\lambda = 3.65, 4.0, 4.5$) start at approximately 25% at $z/D = 2$, rising to approximately 30% at $z/D = 5$, before reducing as the downstream distance increases further. This initial increase in turbulence intensity followed by a decrease has been observed in studies such as that by Maganga et al.[53] and Baba-Ahmadi and Dong[138], and is thought to be due to the shear layers from either side of the wake merging in the centre.

The high initial turbulence intensities for the low tip-speed ratios may be due to blade stalling changing the characteristics of the turbulence in these cases; examination of Figure 7.6 shows that these two tip-speed ratios are within or close to the stall region. The initial high turbulence intensity followed by a rapid reduction in the $\lambda = 1.5$ case may be related to the rapid centreline wake recovery in this case; a higher level of turbulence would promote more rapid mixing and wake recovery, but would also mean that fluctuations of a similar magnitude to those in other cases are smaller in proportion to the mean velocity.
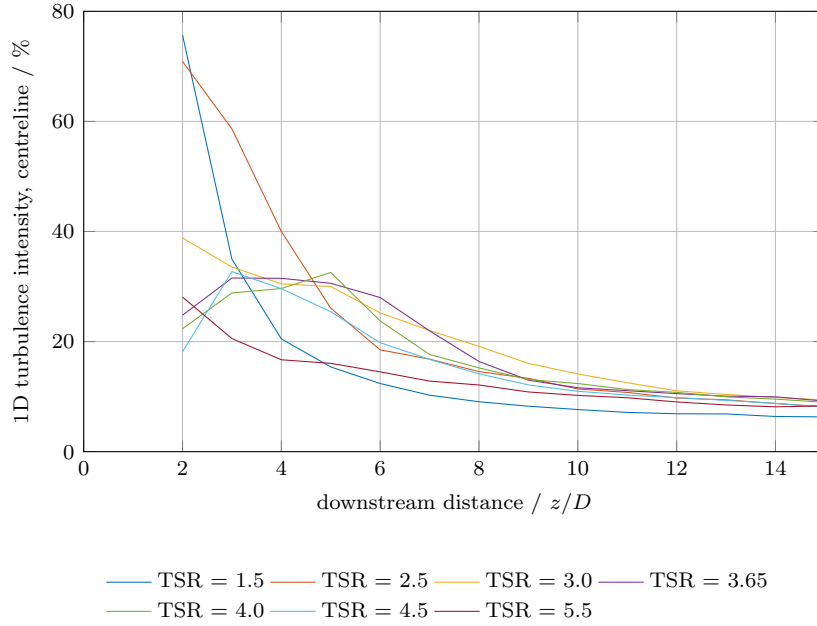
Figure 7.94: Impact of tip-speed ratio on centreline wake turbulence intensity. Low ambient turbulence condition.

For array designers concerned with the placement of turbines, the region of increased turbulence intensity in the near wake will be of some interest, however it is unlikely to be of great relevance if the turbines are to have a longitudinal spacing of more than approximately $z/D = 8$, or even possibly less in conditions of higher ambient turbulence. Perhaps of more interest would be that, from $z/D \approx 10$, tip-speed ratio (and therefore turbine operating condition) has little impact on wake turbulence intensity.

The centreline turbulence length scale, L_t for each of the seven tip-speed ratios used in the low-turbulence CFD case is presented in Figure 7.95. In general, all of the cases display a gradually increasing value of L_t as the wake develops, consistent with that seen in the flume results and due to the smaller length scales dissipating due to viscous forces, leaving larger length scales dominant. However, there is a significant difference between the cases in their initial behaviour, with some cases showing an initial increase in L_t, followed by a comparable decrease, before gradually increasing once more. This complex behaviour initially appears to be linked to C_P, as tip-speed ratios with higher values of C_P appear to show a larger initial increase than those with a lower value of C_P. However, given that this figure is showing the representative length scales of the dominant turbulent features, it might be that this behaviour is dependent on the rotational frequency of the turbine, rather than the operational condition (i.e.

where it is operating on the curves of C_P, C_T and C_θ). The ambient turbulent length scale in these cases is approximately 0.8 m, meaning that L_t downstream of the turbine is much smaller than L_t upstream of it. The presence of the turbine leads to a reduction in length scale, which may be caused by large turbulent features being broken up by their passage through the rotating turbine blades. The greater the rotational frequency, the smaller the resultant turbulent features, explaining why higher tip-speed ratios have a smaller initial length scale. The exceptions to this, $\lambda = 1.5$ and $\lambda = 2.5$, may not fit this pattern due to the blade-stall effects discussed above. A stalled blade can be expected to produce turbulence with different characteristics to that of an unstalled blade, with effects such as flow separation leading to higher wake turbulence intensities, which could explain the differences between these two cases and the others in Figure 7.95.

This more complex behaviour is only apparent in the near wake however; from $z/D \approx 10$, the length scales become similar regardless of tip-speed ratio, suggesting that it need not be considered for array layouts with a greater longitudinal distance than this.
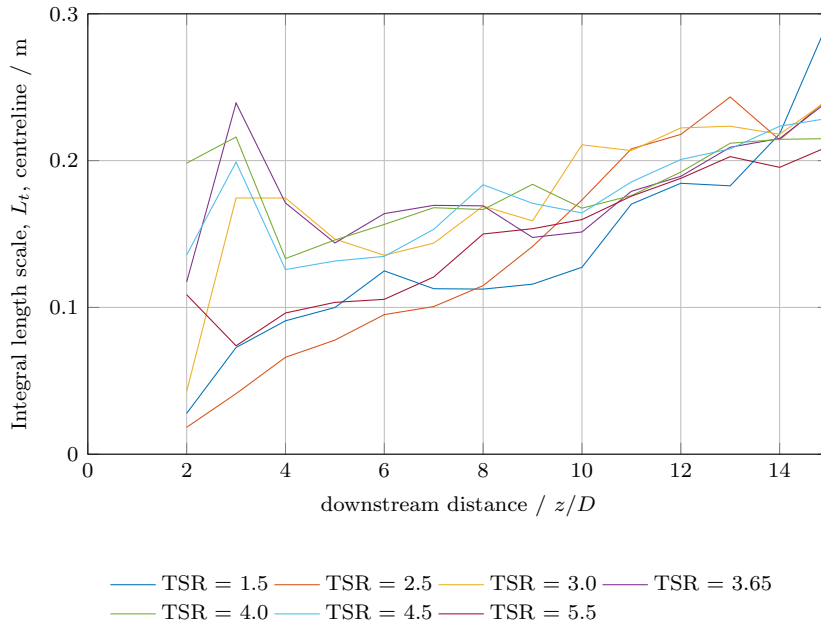
Figure 7.95: Impact of tip-speed ratio on centreline wake turbulence length scale, L_t. Low ambient turbulence condition.

7.8 Summary of results

7.8.1 Ability of DES to model tidal turbines

The results presented here show that the DES model is capable of producing results closely matched to those obtained from flume measurements. Agreement between CFD and experimental data was generally found to be very good, particularly in the medium to far wakes, and held for a wide variety of turbulence conditions. Additionally, the model also allowed direct comparison of some turbulence quantities which are not available from RANS models.

Predictions of turbine performance metrics ($\overline{C_P}$, $\overline{C_T}$ and $\overline{C_\theta}$), also generally produced good agreement, albeit with a slight tendency to over-predict the results at high values of tip-speed ratio. Nonetheless, these over-predictions were still close to the bound of the experimental uncertainty. There is some indication that complex behaviour in the near-wake region has been less well reproduced in this study; this may be improved through mesh refinement in the near-turbine region, however, this was not the main focus of this study. This is most apparent in the low-turbulence case, probably because the greater mixing in the higher turbulence cases tends to obscure this complex behaviour. For a small number of specific metrics (notably the validation of wake widths using the full-width half-minimum method for the grid-generated turbulence cases), agreement between CFD and flume result was less good, which could be due to a number of different factors. It could indicate a fundamental weakness of the turbulence model in the prediction of tidal turbine wakes, or be due to the flow asymmetries present in the flume, which were not included in the CFD model, and to which the full-width half-minimum width method is particularly sensitive. Alternatively, inaccurate matching of the full spectrum of the upstream turbulence might be the cause. This may be alleviated by modelling a grid upstream of the turbine in the CFD, or writing a User Defined Function which more accurately reproduces the upstream turbulence, rather than relying on the turbulence definitions within Fluent, which were found to be problematic when trying to achieve specific targets of inlet turbulence intensity and length scale.

7.8.2 The impact of turbulence on turbine performance

$\overline{C_P}$, $\overline{C_T}$ and $\overline{C_\theta}$ were all found to increase with increasing ambient turbulence intensity, with some suggestion that they are also subject to a slight increase at low turbulence intensities of around 4%. Turbulence length scale on the other hand, appears to have little impact on $\overline{C_P}$ $\overline{C_T}$ and $\overline{C_\theta}$.

Increases in turbulence intensity have a clear impact on the magnitude of the fluctuations in C_P, C_T and C_θ, with a higher turbulence intensity causing

215

fluctuations to have a greater magnitude. Turbulence length scale also appears to impact the size of the fluctuations, albeit mildly, with turbulence at a large length scale leading to performance fluctuations of greater magnitude. This correlation becomes more apparent as turbulence intensity increases. This is thought to be because the turbine as a whole is more likely to be subject to higher number of smaller-scale features simultaneously, which will cancel each other out to some extent. By contrast, a smaller number of larger-scale features interacting with the turbine simultaneously will be less likely to cancel each other out, increasing the fluctuations on the turbine as a whole.

7.8.3 The impact of turbulence on turbine wakes

As seen in previous studies (e.g. [53], [60], [92]), this study has found that turbulence intensity strongly impacts wake recovery, both at the centreline as well as when volumetrically averaged. In all cases studied, an increase in ambient turbulence intensity increased wake recovery, although for turbulence intensities of greater than approximately 10%, the differences in wake recovery were small, suggesting that there might be a limit beyond which increased turbulence intensities no longer lead to increased wake recovery. The impact of ambient turbulence intensity on wake recovery is thought to be due to the increase in flow mixing between the wake and free stream due to the turbulent fluctuations. This increase in mixing increases the transfer of momentum from the free stream to the wake region, aiding wake recovery.

Turbulence intensity was also found to have a profound impact on the width of the wake. For the fixed-threshold method, an increase in turbulence intensity caused the wake to decrease in width, whereas for the full-width half-minimum and maximum-shear methods, the wake width was found to increase. These results, apparently contradictory at first glance, demonstrate the insight which can be gained from analysis using multiple wake-width metrics. The combined information indicates that an increase in ambient turbulence intensity leads to a reduction in the width of the region *most strongly* impacted by the wake, whilst the width of the overall region impacted to at least some extent, increases. Again, the explanation for this lies in the increase in mixing with higher turbulence intensities. This leads to a widening of the shear layer between wake and free stream, and a more rapid equalisation of velocities between the two. In this way, the wake recovers faster and the width of the strongly impacted region narrows, whilst the area impacted *at all* by the wake increases, as lower momentum flow is mixed further into the free stream.

Rotational motion in the wake was also found to be impacted by turbulence intensity, with both wake swirl and maximum tangential velocity being found to

reduce in wakes from turbines subject to a higher ambient turbulence intensity. The reduction in maximum tangential velocity is likely to be due to increased mixing and viscous forces damping the tangential velocities; with the swirl there will also be some contribution from the fact that an increase in turbulence intensity leads to an increase in wake recovery, reducing the ratio of tangential momentum flux to axial momentum flux. As with wake recovery, there appears to be a threshold of turbulence intensity above which, further increases have little impact on the rotational behaviour in the wake. In this case, the threshold was found to be ca. 5%.

The impact of upstream turbulence intensity on wake turbulence intensity and length scale was found to be mild. Upstream turbulence intensity tended to be associated with a slight increase in wake turbulence intensity, but these differences become small beyond $z/D = 10$.

Length scale was not found to have a strong impact on any aspect of tidal turbine wakes, other than a trend of increasing wake turbulence length scale with increasing ambient turbulence length scale. No clear trends were found with increasing length scale for wake recovery, width, swirl, or wake turbulence intensity. For wake recovery and swirl, there is some indication that shorter length scales may promote mixing within the wake itself, whereas longer length scales promote mixing between the wake and the free stream, however, this study did not produce enough evidence to be able to state this conclusively. Part of the reason for this was that only three different length scales were compared, which means that establishing clear patterns of behaviour (particularly non-linear effects) is difficult. It could be that turbulence length scale has an impact on turbine wake behaviour, but that this occurs at length scale greater or less than those used in this study.

7.8.4 The impact of operating condition on wakes

The turbine operating condition was shown to have a strong impact on wakes, however, most of the differences have become small by approximately $z/D = 10$ in the low-turbulence cases. For cases with a higher turbulence intensities, the differences due to the turbine operating condition become indistinguishable more rapidly, most likely due to the increased mixing in between the wake and the free stream in these cases.

The centreline wake recovery was found to increase as turbine thrust increases. This appears to be due to the higher turbine thrust causing flow to be diverted not only outside and around the turbine rotor, but also inwards, towards the nacelle. Trends in volumetric-averaged wake recovery were found to be related to the $\overline{C_P}$ curve in the near wake, with higher energy extraction

corresponding to a greater initial velocity deficit. This can be explained as the increased energy extraction from the flow is achieved by reducing the flow velocity.

The turbine operating condition was also demonstrated to have a clear impact on wake width, with the higher thrust cases demonstrating a wider wake for all width metrics. It is thought that the increase in thrust, which leads to more flow being diverted around the turbine, leads to an increase in width.

Wake swirl was shown to be clearly correlated with turbine operating condition, with higher turbine torques being associated with greater flow rotation in the wake region. This can be explained as an increased torque on the turbine will correspond to an increased reaction torque imparted to the flow by the turbine, and confirms that the behaviour of the flow in the immediate vicinity of the blades found in earlier studies[94] persists into the mid-wake region.

The wake turbulence conditions were mildly impacted by the turbine operating condition with the largest impact being on the near-wake turbulence intensity. This was found to sharply increase when the turbine was operating at or near the stall region. It is thought that this is due to the behaviour of vortices shed from the stalled blades introducing turbulence of a different character to that seen with unstalled blades.

There was also some indication that turbulence length scale in the wake may be impacted by the rotational frequency of the turbine, as there was a mild trend of higher tip-speed ratios producing shorter length scales in the wake. This could be due to the turbulent features being broken up or created by the passage of the turbine blades. Higher blade passing frequencies at higher tip-speed ratios would tend to produce turbulence of smaller length scales. Nonetheless, these differences become small after approximately $z/D = 10$.

Chapter 8

Conclusions and Recommendations

8.1 Ability of DES to model tidal turbines

This study has shown that Detached Eddy Simulation is able to produce good to very good agreement for the wakes of a flume-scale horizontal axis tidal turbine under a variety of turbulence conditions. The scale-resolving method also allows direct comparison of turbulence characteristics to experimental measurements; something that is not available from RANS models. The closest agreement was found for predictions of wake recovery, particularly in the low-turbulence case. Trends with increasing turbulence and tip-speed ratio were also well reproduced. In addition, good agreement was found for the prediction of centreline turbulence intensity in the wake region.

Predictions for performance characteristics are less accurate, with a slight tendency to over-predict turbine performance characteristics at higher tip-speed ratios. However, these predictions were still close to the bounds of experimental uncertainty.

Where agreement between the CFD and flume experiments is less good it is unclear whether the discrepancies observed are due to the turbulence model, inaccuracies in matching the turbulence characteristics between the flume and CFD, or flow asymmetries and inhomogeneities in the flume, which are not modelled in the CFD.

8.2 The impact of turbulence on performance and wakes

8.2.1 Impact on performance

For all tip-speed ratios, an increase in $\overline{C_P}$, $\overline{C_T}$ and $\overline{C_\theta}$ is seen at higher turbulence intensities of 12-14%. There are also indications of a slight increase in these performance parameters at turbulence intensities of approximately 4%. For $\overline{C_P}$, $\overline{C_T}$ and $\overline{C_\theta}$, turbulence length scale seems to have little impact.

Regarding the fluctuations in C_P, C_T and C_θ, there is a clear correlation with an increasing turbulence intensity leading to fluctuations with a greater magnitude. There also appears to be a slight correlation with turbulence length scale, becoming clearer at higher turbulence intensities.

8.2.2 Impact on wakes

This study has examined the impact of both turbulence intensity and length scale on turbine wakes. Some clear trends were found for the impact of turbulence intensity on wakes; trends for L_t were found to be less clear.

Turbulence intensity was found to strongly impact wake recovery; both centreline recovery as well as volumetric averaged. Whilst an increase in turbulence intensity always led to increased recovery, there is some suggestion that, beyond the near wake ($z/D \leq 5$), turbulence intensities above 10% produce very similar results.

Turbulence intensity was also found to have an impact on wake width. An increase in turbulence intensity was found to cause the fixed-threshold width to narrow, and the full-width half-minimum and maximum-shear widths to widen. Taken together, this indicates that the *overall* wake width is increasing, but that the region *strongly* impacted by the wake is decreasing.

Wake swirl and maximum tangential velocity were found to reduce slightly with increasing turbulence intensity. As with wake recovery, it was found that, above a certain threshold increases in turbulence intensity had little impact. This appears to be approximately 5% turbulence intensity in the case of swirl and maximum tangential velocity.

Ambient turbulence intensity was found to have only a slight impact on centreline wake turbulence intensity with an increased wake turbulence intensity perhaps unsurprisingly being associated with higher ambient turbulence intensities. This effect was mild, with little difference being seen between cases beyond approximately $z/D = 10$. Ambient turbulent intensity was not shown to have any clear impact on turbulence length scales in the wake.

Turbulence length scale was not found to have a strong impact on turbine wakes. With the exception of a trend of increasing wake L_t with ambient L_t, it was not possible to find a clear trend for wake recovery, width, swirl or wake turbulence intensity with ambient L_t. In the case of wake recovery and swirl, it is possible that shorter ambient length scales increase mixing within the wake, whereas larger length scales promote mixing between the free stream and wake, however, such complex behaviour was difficult to identify in this study.

In addition, it was not possible to clearly isolate the effects of turbulence intensity and length scales, making the identification of trends difficult.

8.3 The impact of operating condition on wakes

Turbine operating condition was found to strongly impact the wakes of tidal turbines, although with the exception of the impact on wake width, these difference become small by approximately $z/D = 10$. In addition, an increase in ambient turbulence intensity obscures these effects, reducing the differences between operating conditions.

The centreline wake recovery increases with increasing tip-speed ratio (and therefore thrust). The volumetric averaged velocity recovery was found to follow the trend in $\overline{C_P}$ in the near wake, with the cases where the turbine is extracting most energy from the flow showing the greatest velocity deficit. Nonetheless, these differences all but disappear by $z/D = 9$.

The turbine operating condition has a clear impact on wake width. Width was found to increase (for all metrics applied) with increasing $\overline{C_T}$, and this effect was found to persist through the complete length of wake modelled.

Wake swirl was also found to be impacted by the turbine operating condition, with higher $\overline{C_\theta}$ cases producing the most swirl. An increase in torque on the turbine requires an increase in the reaction torque on the flow, which manifests itself as greater swirl. However, for realistic turbulence conditions, it is unlikely that this will have a great impact on the wake, as swirl was found to decrease rapidly with increasing turbulence intensity.

Wake turbulence intensity was found to be slightly impacted by turbine operating condition, with the only really significant differences being seen as increased turbulence in cases operating around or within the stall region. Tip-speed ratios around peak C_P showed a slight rise in turbulence intensity in the near wake, but from $z/D = 10$ onwards, all cases show similar levels of turbulence. Turbulence length scales in the wake appear to be related to the rotational frequency of the turbine, with higher rotational frequencies producing

shorter length scales. Tip-speed ratios around or within the stall region showed different turbulence behaviour, and from $z/D = 10$ onwards, all cases were found to be similar.

8.4 Wake width metrics

Three different metrics were used to examine the wake width, and applied to both the flume and CFD results. Defining the wake width by the point of maximum shear was found to show convergence problems for the v-shaped wake profiles found in both CFD and flume results. The fixed-threshold and full-width half-minimum methods were found to be less sensitive to wake shape, but they also provide more specific information about the wake; the width of the region strongly impacted by the wake, and a measure of the width of the region impacted at all by the wake. Combining the information obtained from these two metrics allows a deeper understanding to be gained of the behaviour of the wake (for example, the impact the turbulence intensity has on wake width). Because of this, and the convergence issue associated with the maximum-shear wake width, it is recommended that future studies examining wake width use the fixed-threshold and full-width half-minimum methods.

8.5 Implications for tidal turbine arrays

Given the impact that turbulence intensity has been shown to have on the length and width of a turbine wake, it is clear that ambient turbulence intensity must be taken into account when considering the placement of turbines within an array. In addition, tidal turbines which are not in the first row of an array are likely to experience a higher turbulence intensity due to the wakes of upstream turbines. Turbulence characteristics within a wake have been shown to be well reproduced using the DES turbulence model. Being able to accurately predict and quantify these wakes will allow array designers to optimise array layouts with respect to array power output, turbine structural loading, or a combination of multiple variables. In addition, the sensitivity of wakes to free stream turbulence implies that a comprehensive survey of any proposed array location must be made in order that the position of individual turbines may be optimised.

The relationship between turbulence intensity and wake recovery and wake

width suggests that, for an array site with higher ambient turbulence intensity, longitudinal spacing may be reduced (due to increased wake recovery), while lateral spacing may need to be increased (due to the widening of the overall area affected by the wakes). Further work is required to determine whether the benefits of the narrowing of the region most heavily impacted by the wake outweighs potential increased loading by being in a region somewhat impacted by the wake. Array designers can be reassured that, as long as longitudinal spacings are greater than $z/D = 10$, the impact of tip-speed ratio on wake recovery can be expected to be minimal. On the other hand, arrays of turbines which are designed to maintain rated power through overspeed (and therefore an increase in thrust) will require a greater lateral spacing as both the overall width of the region affected by the wake, as well as the width of the region most heavily impacted, increase with greater C_T.

8.6   Recommendations for further work

The DES turbulence model shows promise when applied to tidal turbines and their wakes.

This study used the specification of inlet turbulence and perturbations within Fluent, and compared this to grid-induced turbulence within a flume. Further work should be carried out concentrating on trying to more closely match the true turbulence conditions found in the flume, and eventually, the sea. This may involve writing a UDF to synthesise specific turbulence spectra, the modelling of grids upstream of the turbines or using auxiliary simulations to produce well developed upstream turbulence conditions which are then applied to the inlet boundary of a flume working section containing a turbine. Any of these methods would give the user more control over the exact length scales and intensity at the inlet, which was found to be difficult to control using the tools within Fluent.

It was not possible within this study to ascertain a relationship between turbulence length scales and turbine wakes. However, a lack of evidence of an impact is not the same as evidence of a lack of impact. Further work should be conducted to establish with more certainty whether or not length scales have an impact on turbine wakes; a thorough study would involve increasing the range of length scales explored (ideally from the length of the blade chord to the width of the flume), as well as the number of length scales used, in order to allow determination of any non-linear effects. In addition, and despite the associated increase in computational time, a study specifically focusing on length scales should sample for a longer period of time to ensure convergence of this higher

order statistic.

The question of turbulence length scales naturally leads on to the question of scaling. It has been shown that turbine performance characteristics can be non-dimensionalised as long as a minimum Reynolds number has been achieved. This thesis has used velocities normalised against the free stream velocity, and distances normalised with turbine diameter. Carrying out similar studies on turbines of different sizes would help to establish what (if any) scale-relationship exists for turbine wakes, and whether such non-dimensionalisation with turbine diameter and free stream velocity is valid. Clearly the ultimate test of the model is to apply it to full scale turbines and arrays, and see if the predictions made by the CFD are found with real turbines, in real flows.

Both the experimental and modelling work in this study has been carried out at relatively modest Reynold numbers of approximately 500 000 based on turbine diameter and free stream velocity. Based on the same criteria, full-sized turbines can be expected to have Reynolds numbers approximately two orders of magnitude greater. It is unclear whether the conclusions reached here would still be applicable at such Reynolds numbers, where it would be expected that inertial forces would play a more dominant role with respect to the viscous forces, potentially allowing wakes to sustain themselves for longer. Such knowledge is important if wake modelling is to play a role in turbine and array design, and as such, further work in this area would be of great value.

Turbulence and its potential impact on turbines is an area which merits much further study. This thesis examined 1D turbulence intensity and length scales, but it might be that these two parameters are insufficient for a full understanding of the impact of turbulence on turbines. Applying realistic turbulence spectra and analysis in three dimensions would help provide answers to this question, as well as providing more information about the mechanisms responsible for recovery within the wake. Such a set of detailed flow measurements in a flume over the complete wake volume would require a large investment of time.

Appendix A

User Defined Functions

This UDF was used to produce turbine performance data at every timestep, returning C_P, turbine torque about the origin for all three Cartesian axes as well as turbine thrust, and blade bending moments for blade 1. At the end of each timestep, this information is written to a text file called `turbine_data.txt`, and a selection is printed to the screen.

```c
/*******************************************************/
/* UDF adapted by Darrell A. Egarr from one written    */
/*  by David Hargreaves, Fluent Inc., October 2003     */
/* UDF annotated by Darrell A. Egarr,                  */
/*  Cardiff Uni. Jan. 2004                             */
/*  Further modified by Tim Ebdon                      */
/*  Cardiff Uni. Jul. 2016                             */
/*******************************************************/

/*************************************************************************/
/*                                                                       */
/* July 2016 adaptations includes the addition of the following fuctionality: */
/*                                                                       */
/*    - UDF adapted to execute at the end of every timestep (when hooked onto */
/*    a transient simulation) or every iteration (when hooked onto a steady */
/*    state simulation                                                   */
/*    - Moments are calculated for all three cartesian axes, about the origin */
/*    - Bending moments are calculated for blade1 and are returned in x,y,z. */
/*      These need to be converted (e.g. using MS Excel) to give twist, flap */
/*    and sweep moments on blade                                         */
/*    - Calculation of torques has been changed to follow cross-product sign */
/*    convention                                                         */
/*    - Critial turbine performance data is written to an external text file */
/*    - The UDF has been configured for use for both serial and parallel */
/*    processing. This requires no additional user input                */
/*                                                                       */
/*************************************************************************/

/*******************************************************/
/* UDF originally written for use with FLUENT 6.1.18/6.1.22 */
/*******************************************************/

/*******************************************************/
/* UDF to report the power, torque, angular velocity   */
/*  and forces in x, y and z for turbine               */
/*  and torques in x, y and z for blade1               */
/*******************************************************/

#include "udf.h" /* FLUENT header file with FLUENT macros */
#include "stdio.h" /*I/O headerfile required for filewriting output*/
#include "prf.h" /* header file containing global summation macros */

/***********************************************************************************/
/*                                                                       */
/* The following need to be defined for each model                       */
/* A file called "turbine_data.txt" needs to be created and placed in same place as this  */
/* UDF, as well as the case and data files This should be a single line of text as follows: */
/* timestep \t flow time \t Omega \t x-moment \t y-moment \t z-moment \t thrust \t        */
/* blade1 x-torque \t blade1 y-torque \t blade1 z-torque                 */
/* where \t is a tab.                                                    */
/*                                                                       */

#define T1_WALLS 4    /* Number of walls forming the blades for turbine 1 */

static int T1wall_ids[T1_WALLS] = { 18, 19, 20, 21 }; /* Wall IDs for turbine blades
from fluent utility */

static int T1b1wall_id = 18;    /* wall ID for turbine blade 1 */
```

```
   #define U_fs 3.086        /* Free strem velocity */
61 #define T1_Diameter 10       /* Diameter of turbine 1 */

   #define T1_Domain 15       /* Domin ID for turbine 1 from fluent utility */ /*MRF domain*/
   static real T1_Omega = 2.25;  /* Angular velocity of turbine 1 cell zone */

66 /*****************************************************************************************/

   #define pi 3.141592654  /* pi() */

   static real T1_centre_x;  /* x coordinate of turbine 1 centre */
71 static real T1_centre_y;  /* y coordinate of turbine 1 centre */
   static real T1_centre_z;  /* z coordinate of turbine 1 centre */

   static real fluid_rho;    /* Fluid density */

76 static real total_T1_torque_x;  /* totals for final calculations and printing to screen */
   static real total_T1_torque_y;
   static real total_T1_torque_z;

   static real total_T1_b1_torque_x; /* totals for final calculations (blade) and printing to screen */
81 static real total_T1_b1_torque_y;
   static real total_T1_b1_torque_z;


   static real total_T1_force_x; /* totals for final calculations and printing to screen */
86 static real total_T1_force_y;
   static real total_T1_force_z;

   static  real T1_torque_x;   /* variables for use on each compute node */
   static  real T1_torque_y;
91 static  real T1_torque_z;

   static  real T1_b1_torque_x;    /* variables for use on each compute node (for blade) */
   static  real T1_b1_torque_y;
   static  real T1_b1_torque_z;
96
   static  real T1_Force_x;    /* variables for storage of forces in components */
   static  real T1_Force_y;
   static  real T1_Force_z;

101 static real T1_Power; /* Turbine 1 power */
   static real fl_time;  /* flow time */
   static int time_s; /* time step*/

   static real T1_Max_Power; /* Power available to the turbine */
105
   static real efficiency;   /* Efficiency of turbine */

   FILE * fPointer;  /*File pointer for output writing*/

111 DEFINE_EXECUTE_AT_END(power_blade_load)
   {
   #if !RP_HOST  /* run thread calculation loops on compute nodes and serial */
   Domain *domain = Get_Domain(1);

116 Thread *T1ct = Lookup_Thread(domain,T1_Domain); /* Looks up the thread pointer
   to zone T1_Domain */

   Thread *T1ft; /* Pointer to face thread data type on turbine 1 */

121 Thread *T1b1ft; /* Pointer to face thread data type on blade 1 */

   face_t f; /* Face data type */

   int i;
126
   /* Declaration of variables */
   /* Turbine static pressure force */
   real T1_tp_force[ND_ND];  /* Stores T1_tp_force in a matrix i.e. x, y and z components */

131 real T1_b1_tp_force[ND_ND];  /* static pressure force on blade 1 */

   /* Declaration of variables */
   /* Turbines shear stress force */
   real T1_ts_force[ND_ND];  /* Stores T1_ts_force in a matrix i.e. x, y and z components */
136
   real T1_b1_ts_force[ND_ND];  /* shear force on blade 1 */


   /* Declaration of variables */
141 /* Force on turbines (sum of static and shear) */
   real T1_Force[ND_ND];   /* Stores T1_Force in a matrix i.e. x, y and z components */

   real T1_b1_Force[ND_ND];  /* Total force on blade 1 */

146
   real f_A[ND_ND];  /* Stores f_A (face area) in a matrix
   i.e. x, y and z components */

   real f_cen[ND_ND];  /* Stores f_cen (face centroid) in a matrix
151 i.e. x, y and z components */

   T1_torque_x = 0.0;  /* Initializes/Resets the torque to zero */
   T1_torque_y = 0.0;  /* Initializes/Resets the torque to zero */
   T1_torque_z = 0.0;  /* Initializes/Resets the torque to zero */
156
   T1_b1_torque_x = 0.0; /* Initializes/Resets the blade torque to zero */
```

```
         T1_b1_torque_y = 0.0; /* Initializes/Resets the blade torque to zero */
         T1_b1_torque_z = 0.0; /* Initializes/Resets the blade torque to zero */

161    T1_Force_x = 0.0;    /* initializes force components */
         T1_Force_y = 0.0;
         T1_Force_z = 0.0;

         NV_S(T1_Force,=,0); /* Initializes/Resets the force vector to zero */
166

         T1_centre_x = THREAD_VAR(T1ct).fluid.origin[0];
         T1_centre_y = THREAD_VAR(T1ct).fluid.origin[1];
         T1_centre_z = THREAD_VAR(T1ct).fluid.origin[2];
171
         fluid_rho = MATERIAL_PROP(THREAD_MATERIAL(T1ct),PROP_rho);

         /* Turbine */

176    for (i=0;i<T1_WALLS;i++)
         {

         T1ft=Lookup_Thread(domain,T1wall_ids[i]);
         /* Lookup the face threads for the wall ids on turbine 1 */
181

         begin_f_loop(f,T1ft)  /* Loop over all face threads of the wall ids */
         {

186    F_AREA(f_A,f,T1ft);
         /* Macro for face area containing pointers
         to face area, face and face thread */

         F_CENTROID(f_cen,f,T1ft);
191    /* Macro for face centroid containing pointers
         to face centroid, face and face thread */

         /* Store shear force on turbine 1*/
         N3V_V(T1_ts_force,=,F_STORAGE_R_N3V(f,T1ft,SV_WALL_SHEAR));
196
         /* Store static pressure force on turbine 1*/
         T1_tp_force[0] = f_A[0]*F_P(f,T1ft);  /* defines the tp_force in x-component */
         T1_tp_force[1] = f_A[1]*F_P(f,T1ft);  /* defines the tp_force in y-component */
         T1_tp_force[2] = f_A[2]*F_P(f,T1ft);  /* defines the tp_force in z-component */
201    /* F_P(f,ft) is the face static pressure */

         /* For turbine axis in the x and y-component */

         T1_Force[0] += T1_tp_force[0] - T1_ts_force[0]; /*Summation of forces in x direction*/
206
         T1_Force[1] += T1_tp_force[1] - T1_ts_force[1]; /*Summation of forces in y direction*/


         /* N.B. Shear force subtracted due to sign convention
211    i.e. subtract a negative equals a plus */

         /* Calculation of moments on turbine: */
         /* z moment */
         T1_torque_z += (T1_tp_force[1]-T1_ts_force[1])*(f_cen[0]-T1_centre_x)
216    - (T1_tp_force[0]-T1_ts_force[0])*(f_cen[1]-T1_centre_y);

         /* y moment */
         T1_torque_y += (T1_tp_force[0]-T1_ts_force[0])*(f_cen[2]-T1_centre_z)
         - (T1_tp_force[2]-T1_ts_force[2])*(f_cen[0]-T1_centre_x);
221
         /* x moment */
         T1_torque_x += (T1_tp_force[2]-T1_ts_force[2])*(f_cen[1]-T1_centre_y)
         - (T1_tp_force[1]-T1_ts_force[1])*(f_cen[2]-T1_centre_z);

226    /* Force acting on blades in direction of flow */
         T1_Force[2] += T1_tp_force[2]-T1_ts_force[2];

         }

231    end_f_loop(f,T1ft);

         T1_Force_x = T1_Force[0];    /* write forces from array components to individual variables */
         T1_Force_y = T1_Force[1];
         T1_Force_z = T1_Force[2];
236
         }

         /***************/

241    /* Blade bending moments */

         T1b1ft=Lookup_Thread(domain,T1b1wall_id);
         /* Lookup the face threads for the wall ids on turbine 1 */

246
         begin_f_loop(f,T1b1ft)  /* Loop over all face threads of the wall ids */
         {

         F_AREA(f_A,f,T1b1ft);
251    /* Macro for face area containing pointers
         to face area, face and face thread */

         F_CENTROID(f_cen,f,T1b1ft);
         /* Macro for face centroid containing pointers
256    to face centroid, face and face thread */
```

```
/* Store shear force on turbine 1*/
N3V_V(T1_b1_ts_force,=,F_STORAGE_R_N3V(f,T1b1ft,SV_WALL_SHEAR));

/* Store static pressure force on turbine 1*/
T1_b1_tp_force[0] = f_A[0]*F_P(f,T1b1ft); /* defines the tp_force in x-component */
T1_b1_tp_force[1] = f_A[1]*F_P(f,T1b1ft); /* defines the tp_force in y-component */
T1_b1_tp_force[2] = f_A[2]*F_P(f,T1b1ft); /* defines the tp_force in z-component */
/* F_P(f,ft) is the face static pressure */

/* N.B. Shear force subtracted due to sign convention
i.e. subtract a negative equals a plus */

/* Calculation of moments on blade: */
/* z moment */
T1_b1_torque_z += (T1_b1_tp_force[1]-T1_b1_ts_force[1])*(f_cen[0]-T1_centre_x)
- (T1_b1_tp_force[0]-T1_b1_ts_force[0])*(f_cen[1]-T1_centre_y);

/* y moment */
T1_b1_torque_y += (T1_b1_tp_force[0]-T1_b1_ts_force[0])*(f_cen[2]-T1_centre_z)
- (T1_b1_tp_force[2]-T1_b1_ts_force[2])*(f_cen[0]-T1_centre_x);

/* x moment */
T1_b1_torque_x += (T1_b1_tp_force[2]-T1_b1_ts_force[2])*(f_cen[1]-T1_centre_y)
- (T1_b1_tp_force[1]-T1_b1_ts_force[1])*(f_cen[2]-T1_centre_z);

}

end_f_loop(f,T1b1ft);

/**************/

T1_Force_x = T1_Force[0];    /* write forces from array components to individual variables */
T1_Force_y = T1_Force[1];
T1_Force_z = T1_Force[2];

#endif /* end thread loop on compute nodes and serial */

#if PARALLEL  /* for parallel calculations, gather calculations from individual compute nodes and sum */

PRF_GSYNC();  /* ensure all compute nodes have carried out their calculations */

total_T1_torque_x = PRF_GRSUM1(T1_torque_x);  /* totals for final calculations and printing to screen */
total_T1_torque_y = PRF_GRSUM1(T1_torque_y);
total_T1_torque_z = PRF_GRSUM1(T1_torque_z);

total_T1_b1_torque_x = PRF_GRSUM1(T1_b1_torque_x);  /* totals for final calculations and printing to screen
        */
total_T1_b1_torque_y = PRF_GRSUM1(T1_b1_torque_y);
total_T1_b1_torque_z = PRF_GRSUM1(T1_b1_torque_z);

total_T1_force_x = PRF_GRSUM1(T1_Force_x);    /* totals for final calculations and printing to screen */
total_T1_force_y = PRF_GRSUM1(T1_Force_y);
total_T1_force_z = PRF_GRSUM1(T1_Force_z);

PRF_GSYNC();  /* synchronise the nodes once more */

/* Pass data from compute node 0 to host */
node_to_host_real_7(total_T1_torque_x, total_T1_torque_y, total_T1_torque_z, total_T1_force_x,
        total_T1_force_y, total_T1_force_z, fluid_rho);
node_to_host_real_3(total_T1_b1_torque_x, total_T1_b1_torque_y, total_T1_b1_torque_z);

#endif   /* PARALLEL */

#if !PARALLEL /* rename variables in serial calculation */
total_T1_torque_x = T1_torque_x;
total_T1_torque_y = T1_torque_y;
total_T1_torque_z = T1_torque_z;

total_T1_force_x = T1_Force[0];
total_T1_force_y = T1_Force[1];
total_T1_force_z = T1_Force[2];

total_T1_b1_torque_x = T1_b1_torque_x;  /* totals for final calculations and printing to screen */
total_T1_b1_torque_y = T1_b1_torque_y;
total_T1_b1_torque_z = T1_b1_torque_z;

#endif /* !PARALLEL */

#if !RP_NODE  /* use host or serial node to calculate results, print to screen and write file */

T1_Max_Power = 0.5*fluid_rho*( (T1_Diameter/2.0)*(T1_Diameter/2.0) )*pi*(U_fs*U_fs*U_fs);

T1_Power = fabs(total_T1_torque_z)*fabs(T1_Omega);

efficiency = 100.0*T1_Power/T1_Max_Power;

/*Extract time step and flow time*/
fl_time = CURRENT_TIME;   /*get flow time*/
time_s = N_TIME;       /*get timestep*/

/*Write to file "turbine_data.txt", which is stored with UDF and case/data files. See preamble for required
        format*/
fPointer = fopen("turbine_data.txt", "a");  /*Open file to append*/
fprintf(fPointer,"%d\t%12.4e\t%12.4e\t%12.4e\t%12.4e\t%12.4e\t%12.4e\t%12.4e\t%12.4e\n", time_s,
        fl_time,
T1_Omega, total_T1_torque_x, total_T1_torque_y, total_T1_torque_z, total_T1_force_z, total_T1_b1_torque_x,
total_T1_b1_torque_y, total_T1_b1_torque_z);
fclose(fPointer);
```

228

```
    /* Message used to try to get it to write just once to the screen */
    Message("\n ********************************************************");
    Message("\n * WARNING: Did you set the correct zone IDs in the UDF? *");
356 Message("\n ********************************************************\n");

    Message("\n ********************************************************");
    Message("\n * Turbine Report:                                      *");
    Message("\n *                                                      *");
361 Message("\n * Timestep:              %d                            *", time_s);
    Message("\n * Flow time:            %12.4e s                       *", fl_time);
    Message("\n * Turbine Torque:      %12.4e Nm                       *", total_T1_torque_z);
    Message("\n * Turbine Omega:       %12.4e rad/s                    *", T1_Omega);
    Message("\n * Turbine Power:       %12.4e W                        *", T1_Power);
366 Message("\n * Power Available:     %12.4e W                        *", T1_Max_Power);
    Message("\n * Turbine Efficiency:  %g Percent                      *",efficiency);
    Message("\n *                                                      *");
    Message("\n * Turbine total forces:                                *");
    Message("\n *   Force in x-comp.: %12.4e N                         *", total_T1_force_x);
371 Message("\n *   Force in y-comp.: %12.4e N                         *", total_T1_force_y);
    Message("\n *   Force in z-comp.: %12.4e N                         *", total_T1_force_z);
    Message("\n *   Moment around x-axis: %12.4e Nm                    *", total_T1_torque_x);
    Message("\n *   Moment around y-axis: %12.4e Nm                    *", total_T1_torque_y);
    Message("\n * Blade forces:                                        *");
376 Message("\n *   Blade x-moment: %12.4e Nm                          *", total_T1_b1_torque_x);
    Message("\n *   Blade y-moment: %12.4e Nm                          *", total_T1_b1_torque_y);
    Message("\n *   Blade z-moment: %12.4e Nm                          *", total_T1_b1_torque_z);
    Message("\n *                                                      *");
    Message("\n ********************************************************\n");
381
    /* 'Message' prints the requested data to the Fluent window
    %12.4e:  12:  the field width i.e. space for 12 characters
    .4  reserves 4 charracters after the decimal place
    e    defines scientific notation; useful for copying
386 the data into other programs e.g. Microsoft Excel */

    #endif /* !RP_NODE */
    }
```

References

[1] T. C. McErlean, C. Earwood, D. Moore, and E. Murphy, "The Sequence of Early Christian Period Horizontal Tide Mills at Nendrum Monastry: An Interim Statement," *Historical Archaeology*, vol. 41(3), pp. 63–75, 2007.

[2] F. O'Rourke, F. Boyle, and A. Reynolds, "Tidal energy update 2009," *Applied Energy*, vol. 87, pp. 398–409, 2010.

[3] IPCC, "Climate Change 2014: Synthesis Report. Contribution of Working Groups I, II and III to the Fifth Assessment Report of the Intergovernmental Panel on Climate Change."

[4] Wind Europe, "Wind in power 2017." `https://windeurope.org/wp-content/uploads/files/about-wind/statistics/WindEurope-Annual-Statistics-2017.pdf`, 2018. [Online; accessed 19-Nov-2018].

[5] Sustainable Development Commision, "Turning the tide," 2007. `http://www.sd-commission.org.uk/publications.php?id=607`.

[6] R. Kirby and C. Retière, "Comparing environmental effects of Rance and Severn barrages," *Proceedings of the ICE - Maritime Engineering*, vol. 162, pp. 11–26, 2009.

[7] J. Hardisty, "Power intermittency, redundancy and tidal phasing around the United Kingdom," *The Geographical Journal*, vol. 174, pp. 76–84, 2008.

[8] A. Mason-Jones, *Performance assessment of a Horizontal Axis Tidal Turbine in a high velocity shear environment*. PhD thesis, School of Engineering, Cardiff University, 2010.

[9] Y. Zhang, J. Zhang, Y. Zheng, C. Yang, W. Zang, and E. Fernandez-Rodriguez, "Experimental Analysis and Evaluation of the Numerical Prediction of Wake Characteristics of Tidal Stream Turbine," *Energies*, vol. 10:2057, 2017.

[10] T. A. Adcock, S. Draper, and T. Nishino, "Tidal power generation – a review of hydrodynamic modelling," *Proceedings of the Institution of Mechanical Engineers, Part A: Journal of Power and Energy*, vol. 229, no. 7, pp. 755–771, 2015.

[11] G. D. Egbert and R. D. Ray, "Semi-diurnal and diurnal tidal dissipation from topex/poseidon altimetry," *Geophysical Research Letters*, vol. 30, 9 2003.

[12] A. S. Bahaj, "Generating electricity from the oceans," *Renewable and Sustainable Energy Reviews*, vol. 15, no. 7, pp. 3399 – 3416, 2011.

[13] A. Bahaj and L. Myers, "Fundamentals applicable to the utilisation of marine current turbines for energy production," *Renewable Energy*, vol. 28, pp. 2205–2211, 2003.

[14] P. Evans, A. Mason-Jones, C. Wilson, C. Wooldridge, T. O'Doherty, and D. O'Doherty, "Constraints on extractable power from energetic tidal straits," *Renewable Energy*, vol. 81, pp. 707–722, 2015.

[15] A. Mason-Jones, D. O'Doherty, C. Morris, T. O'Doherty, C. Byrne, P. Prickett, R. Grosvenor, I. Owen, S. Tedds, and R. Poole, "Non-dimensional scaling of tidal stream turbines," *Energy*, vol. 44, pp. 820–829, 2012.

[16] W. Batten, A. Bahaj, A. Molland, and J. Chaplin, "Hydrodynamics of marine current turbines," *Renewable Energy*, vol. 31, pp. 249–256, 2006.

[17] D. Kerr, "Marine energy," *Phil Trans R Soc A*, vol. 365, pp. 971–992, 2007.

[18] S. Waters and G. Aggidis, "Tidal range technologies and state of the art in review," *Renewable and Sustainable Energy Reviews*, vol. 59, pp. 514–529, 2016.

[19] A. Vaughan and S. Morris, the Guardian Online, "Government rejects plan for £1.3bn tidal lagoon in Swansea." `https://www.theguardian.com/business/2018/jun/25/government-rejects-plan-for-tidal-lagoon-in-swansea`, 2018. [Online; accessed 19-Sep-2018].

[20] A. Kermode, *Mechanics of flight*. Longman Group UK, 1987.

[21] Simtec Atlantis Energy, "AR1500 Brochure." `https://simecatlantis.com/wp/wp-content/uploads/2016/08/AR1500-Brochure-Final-1.pdf`, 2016. [Online; accessed 20-July-2018].

[22] Orkney Marine Renewables, "Tidal world record set." `http://www.orkneymarinerenewables.com/news/26-sep-2017-tidal-world-record-set`, 2017. [Online; accessed 20-July-2018].

[23] theswitch.com, "References for wave and tidal." `https://theswitch.com/wave-and-tidal/references-for-wave/`, 2017. [Online; accessed 17-February-2017].

[24] Siemens PLC, "Siemens uk - world-leading tidal energy system achieves 5GWh milestone." `http://www.siemens.co.uk/en/news_press/index/news_archive/seagen-achieves-5gw-tidal-power-generation-milestone.htm`, 2012. [Online; accessed 18-July-2018].

[25] B. Bornemann, "SCHOTTEL HYDRO, a new strategy." `https://www.energiesdelamer.eu/publications/51-hydrolienne/3542-schottel-hydro-a-new-strategy`, 2017. [Online; accessed 18-July-2018].

[26] V. Groizeleau, "Hydroliennes au Canada : OpenHydro et emera créent une société commune." `https://www.meretmarine.com/fr/content/h ydroliennes-au-canada-openhydro-et-emera-creent-une-societ e-commune`, 2014. [Online; accessed 18-July-2018].

[27] C. Douglas, G. Harrison, and J. Chick, "Life cycle assessment of the Seagen marine current turbine," *Proc. IMechE Part M: J. Engineering for the Marine Environment*, vol. 222, pp. 1–12, 2008.

[28] BBC News, "Strangford tidal energy turbine to be removed." `https://www.bbc.com/news/uk-northern-ireland-35416282`, 2016. [Online; accessed 19-July-2018].

[29] C. Frost, *Flow Direction Effects On Tidal Stream Turbines*. PhD thesis, School of Engineering, Cardiff University, 2016.

[30] Schottel Hydro GmbH, "Schottel Hydro cost effective power from currents." `https://www.schottel.de/fileadmin/data/pdf/SCHOTTEL_H YDRO/SCHOTTEL_HYDRO_Instream_Energy.pdf`, 2014. [Online; accessed 19-July-2018].

[31] P. Jeffcoate, R. Starzmann, B. Elsaesser, S. Scholl, and S. Bischoff, "Field measurements of a full scale tidal turbine," *International Journal of Marine Energy*, vol. 12, pp. 3–20, 2015.

[32] OpenHydro, "Open centre turbine." `http://www.openhydro.com/Tech nology/Open-Centre-Turbine`, 2016. [Online; accessed 19-July-2018].

[33] The Irish Times, "Ocean energy europe 'disappointed' at openHydro liquidation." `https://www.irishtimes.com/business/energy-and-res ources/ocean-energy-europe-disappointed-at-openhydro-liquida tion-1.3577586`, 2018. [Online; accessed 21-Nov-2018].

[34] S. Eriksson, H. Bernhoff, and M. Leijon, "Evaluation of different turbine concepts for wind power," *Renewable and Sustainable Energy Reviews*, vol. 12, pp. 1419–1434, 2008.

[35] M. Khan, G. Bhuyan, M. Iqbal, and J. Quaicoe, "Hydrokinetic energy conversion systems and assessment of horizontal and vertical axis turbines for river and tidal applications: A technology status review," *Applied Energy*, vol. 86, pp. 1823–1835, 2009.

[36] EEL Energy, "The EEL Tidal Energy Converter." `http://www.eel-en ergy.fr/en/eel-tidal-energy-convertor/`, 2015. [Online; accessed 24-July-2018].

[37] Minesto UK Ltd., "Our Technology." `https://minesto.com/our-tech nology`, 2018. [Online; accessed 24-July-2018].

[38] M. Reder, E. Gonzalez, and J. Melero, "Wind Turbine Failures - Tackling current Problems in Failure Data Analysis," *J. Phys.: Conf. Ser.*, vol. 753, p. 072027, 2016.

[39] T. Burton, N. Jenkins, D. Sharpe, and E. Bossanyi, *Wind Energy Handbook*. Wiley, 2nd ed., 2011.

[40] J. Schluntz and R. Willden, "The effect of blockage on tidal turbine rotor design and performance," *Renewable Energy*, vol. 81, pp. 432–441, 2015.

[41] I. Masters, A. Williams, T. N. Croft, M. Togneri, M. Edmunds, E. Zangiabadi, I. Farley, and H. Karunarathna, "A Comparison of Numerical Modelling Techniques for Tidal Stream Turbine Analysis," *Energies*, vol. 8, pp. 7833–7853, 2015.

[42] S. R. Turnock, A. B. Phillips, J. Banks, and R. Nicholls-Lee, "Modelling tidal current turbine wakes using a coupled RANS-BEMT approach as a tool for analysing power capture of arrays of turbines," *Ocean Engineering*, vol. 38, pp. 1300–1307, 2011.

[43] L. Myers and A. Bahaj, "Power output performance characteristics of a horizontal axis marine current turbine," *Renewable Energy*, vol. 31, pp. 197–208, 2006.

[44] K. Porter, S. Ordonez-Sanchez, T. Nevalainen, S. Fu, and C. Johnstone, "Comparative Study of Numerical Modelling Techniques to Estimate Tidal Turbine Blade Loads," in *Proc. of 3rd Asian Wave & Tidal Energy Conference (AWTEC 2016)*, 24th–28th Oct. 2016.

[45] P. J. Moriarty and A. C. Hansen, "AeroDyn Theory Manual," tech. Rep. NREL/EL-500-36881, National Renewable Energy Laboratory, 2005.

[46] H. Versteeg and W. Malalasekera, *An Introduction to Computational Fluid Dynamics, The Finite Volume Method*. Pearson Education Limited, 2007.

[47] A. F. Molland, A. S. Bahaj, J. R. Chaplin, and W. M. J. Batten, "Measurements and predictions of forces, pressures and cavitation on 2-D sections suitable for marine current turbines," *Proceedings of the Institution of Mechanical Engineers, Part M: Journal of Engineering for the Maritime Environment*, vol. 218, no. 2, pp. 127–138, 2004.

[48] W. Batten, A. Bahaj, A. Molland, and J. Chaplin, "The prediction of the hydrodynamic performance of marine current turbines," *Renewable Energy*, vol. 33, pp. 1085–1096, 2008.

[49] A. Bahaj, A. Molland, J. Chaplin, and W. Batten, "Power and thrust measurements of marine current turbines under various hydrodynamic flow conditions in a cavitation tunnel and a towing tank," *Renewable Energy*, vol. 32, no. 3, pp. 407–426, 2007.

[50] R. Malki, A. Williams, T. Croft, M. Togneri, and I. Masters, "A coupled blade element momentum – Computational fluid dynamics model for evaluating tidal stream turbine performance," *Applied Mathematical Modelling*, vol. 37, pp. 3006–3020, 2013.

[51] M. E. Harrison, W. M. J. Batten, and A. S. Bahaj, "A blade element actuator disc approach applied to tidal stream turbines," in *OCEANS 2010 MTS/IEEE SEATTLE*, pp. 1–8, Sept 2010.

[52] C. H. Frost, P. S. Evans, M. J. Harrold, A. Mason-Jones, T. O'Doherty, and D. M. O'Doherty, "The impact of axial flow misalignment on a tidal turbine," *Renewable Energy*, vol. 113, pp. 1333–1344, 2017.

[53] F. Maganga, G. Germain, J. King, G. Pinon, and E. Rivoalen, "Experimental characterisation of flow effects on marine current turbine behaviour and on its wake properties," *IET Renewable Power Generation*, vol. 4, pp. 498–509, November 2010.

[54] C. Morris, D. O'Doherty, A. Mason-Jones, and T. O'Doherty, "Evaluation of the swirl characteristics of a tidal stream turbine wake," *International Journal of Marine Energy*, vol. 14, pp. 198–214, 2016.

[55] L. Luznik, K. A. Flack, E. E. Lust, and K. Taylor, "The effect of surface waves on the performance characteristics of a model tidal turbine," *Renewable Energy*, vol. 58, pp. 108–114, 2013.

[56] T. de Jesus Henriques, S. Tedds, A. Botsari, G. Najafian, T. Hedges, C. Sutcliffe, I. Owen, and R. Poole, "The effects of wave-current interaction on the performance of a model horizontal axis turbine," *International Journal of Marine Energy*, vol. 8, pp. 17–35, 2014.

[57] S. Tatum, C. Frost, M. Allmark, D. O'Doherty, A. Mason-Jones, P. Prickett, R. Grosvenor, C. Byrne, and T. O'Doherty, "Wave-current interaction effects on tidal stream turbine performance and loading characteristics," *International Journal of Marine Energy*, vol. 14, pp. 161–179, 2016.

[58] T. Blackmore, W. M. J. Batten, G. U. Müller, and A. S. Bahaj, "Influence of turbulence on the drag of solid discs and turbine simulators in a water current," *Exp Fluids*, vol. 55, p. 1637, 2014.

[59] T. Blackmore, L. E. Myers, and A. S. Bahaj, "Effects of turbulence on tidal turbines: Implications to performance, blade loads, and condition monitoring," *International Journal of Marine Energy*, vol. 14, pp. 1–26, 2016.

[60] P. Mycek, B. Gaurier, G. Germain, G. Pinon, and E. Rivoalen, "Experimental study of the turbulence intensity effects on marine current turbines behaviour. part I: One single turbine," *Renewable Energy*, vol. 66, pp. 729–746, 2014.

[61] P. Ouro, M. Harrold, T. Stoesser, and P. Bromley, "Hydrodynamic loadings on a horizontal axis tidal turbine prototype," *Journal of Fluids and Structures*, vol. 71, pp. 78–95, 2017.

[62] U. Ahmed, D. Apsley, I. Afgan, T. Stallard, and P. Stansby, "Fluctuating loads on a tidal turbine due to velocity shear and turbulence: Comparison of CFD with field data," *Renewable Energy*, vol. 112, pp. 235–246, 2017.

[63] I. Afgan, J. McNaughton, S. Rolfo, D. Apsley, T. Stallard, and P. Stansby, "Turbulent flow and loading on a tidal stream turbine by LES and RANS," *International Journal of Heat and Fluid Flow*, vol. 43, pp. 96–108, 2013.

[64] Bavarian ministry for Economy, Development and Energy, "Energie-Atlas Bayern." `https://www.energieatlas.bayern.de/thema_wind/potenzial.html`, 2018. [Online; accessed 21-Nov-2018].

[65] P. Lissaman, "Energy effectiveness of arbitrary arrays of wind turbines," *J. Energy*, vol. 3, no. 6, pp. 323–328, 1979.

[66] N. Jensen, "A note on wind generator interaction," tech. rep., Risø National Laboratory, Denmark, 1983.

[67] S. Frandsen, R. Barthelmie, S. Pryor, O. Rathmann, S. Larsen, J. Højstrup, and M. Thøgersen, "Analytical modelling of wind speed deficit in large offshore wind farms," *Wind Energy*, vol. 9, no. 1-2, pp. 39–53, 2006.

[68] M. Bastankhah and F. Porté-Agel, "A new analytical model for wind-turbine wakes," *Renewable Energy*, vol. 70, pp. 116 – 123, 2014. Special issue on aerodynamics of offshore wind energy systems and wakes.

[69] W.-H. Lam and L. Chen, "Equations used to predict the velocity distribution within a wake from a horizontal-axis tidal-current turbine," *Ocean Engineering*, vol. 79, pp. 35–42, 2014.

[70] W.-H. Lam, L. Chen, and R. Hashim, "Analytical wake model of tidal current turbine," *Energy*, vol. 79, pp. 512 – 521, 2015.

[71] G. Pinon, P. Mycek, G. Germain, and E. Rivoalen, "Numerical simulation of the wake of marine current turbines with a particle method," *Renewable Energy*, vol. 46, pp. 111 – 126, 2012.

[72] R. Gómez-Elvira, A. Crespo, E. Migoya, F. Manuel, and J. Hernández, "Anisotropy of turbulence in wind turbine wakes," *Journal of Wind Engineering and Industrial Aerodynamics*, vol. 93, pp. 797–814, 2005.

[73] A. Makridis and J. Chick, "Validation of a CFD model of wind turbine wakes with terrain effects," *J. Wind Eng. Ind. Aerodyn.*, vol. 123, pp. 12–29, 2013.

[74] Y.-T. Wu and F. Porté-Agel, "Atmospheric Turbulence Effects on Wind-Turbine Wakes: An LES study," *Energies*, vol. 5, no. 12, pp. 5340–5362, 2012.

[75] D. Sturge, D. Sobotta, R. Howell, A. While, and J. Lou, "A hybrid actuator disc – Full rotor CFD methodology for modelling the effects of wind turbine wake interactions on performance," *Renewable Energy*, vol. 80, pp. 525–537, 2015.

[76] A. E. Kasmi and C. Masson, "An extended $k - \varepsilon$ model for turbulent flow through horizontal-axis wind turbines," *Journal of Wind Engineering and Industrial Aerodynamics*, vol. 96, pp. 103–122, 2008.

[77] A. M. AbdelSalam and V. Ramalingam, "Wake prediction of horizontal-axis wind turbine using full-rotor modeling," *J. Wind Eng. Ind. Aerodyn.*, vol. 124, pp. 7–19, 2014.

[78] J. Liu, H. Lin, and S. R. Purimitla, "Wake field studies of tidal current turbines with different numerical methods," *Ocean Engineering*, vol. 117, pp. 383–397, 2016.

[79] J. Whale, C. Anderson, R. Bareiss, and S. Wagner, "An experimental and numerical study of the vortex structure in the wake of a wind turbine," *Journal of Wind Engineering and Industrial Aerodynamics*, vol. 84, pp. 1–21, 2000.

[80] L. Vermeer, J. Sørensen, and A. Crespo, "Wind turbine wake aerodynamics," *Progress in Aerospace Sciences*, vol. 39, pp. 467–510, 2003.

[81] Y.-T. Wu and F. Porté-Agel, "Large-Eddy Simulation of Wind-Turbine Wakes: Evaluation of Turbine Parametrisations," *Boundary-Layer Meteorology*, vol. 138, no. 3, pp. 345–366, 2011.

[82] T. Blackmore, W. Batten, and A. Bahaj, "Influence of turbulence on the wake of a marine current turbine simulator," *Proc. R. Soc. A*, vol. 470, p. 20140331, 2014.

[83] H. Sarlak, C. Meneveau, and J. Sørensen, "Role of subgrid-scale modeling in large eddy simulation of wind turbine wake interactions," *Renewable Energy*, vol. 77, pp. 386–399, 2015.

[84] J. Mo, A. Choudhry, M. Arjomandi, and Y. Lee, "Large eddy simulation of the wind turbine wake characteristics in the numerical wind tunnel model," *J. Wind Eng. Ind. Aerodyn.*, vol. 112, pp. 11–24, 2013.

[85] S. Wußow, L. Sitzki, and T. Hahm, "3D-simulation of the turbulent wake behind a wind turbine," *Journal of Physics: Conference Series*, vol. 75, no. 1, p. 012033, 2007.

[86] M. E. Harrison, W. M. J. Batten, L. E. Myers, and A. S. Bahaj, "Comparison between CFD simulations and experiments for predicting the far wake of horizontal axis tidal turbines," *IET Renewable Power Generation*, vol. 4, pp. 613–627, November 2010.

[87] G. Bai, J. Li, P. Fan, and G. Li, "Numerical investigations of the effects of different arrays on power extractions of horizontal axis current turbines," *Renewable Energy*, vol. 53, pp. 180–186, 2013.

[88] G. Bai, G. Li, Y. Ye, and T. Gao, "Numerical analysis of the hydrodynamic performance and wake field of a horizontal axis tidal current turbine using an actuator surface model," *Ocean Engineering*, vol. 94, pp. 1–9, 2015.

[89] T. Nishino and R. H. Willden, "Effects of 3-D channel blockage and turbulent wake mixing on the limit of power extraction by tidal turbines," *International Journal of Heat and Fluid Flow*, vol. 37, pp. 123–135, 2012.

[90] A. Good, *Near Wake Hydrodynamics of a Horizontal Axis Tidal Turbine*. PhD thesis, School of Planning, Architecture and Civil Engineering, Queen's University, Belfast, 2013.

[91] M. Churchfield, Y. Li, and P. Moriarty, "A large-eddy simulation study of wake propagation and power production in an array of tidal-current turbines," *Phil. Trans. R Soc. A*, vol. 371, p. 20120421, 2013.

[92] M. H. Ahmadi, "Influence of upstream turbulence on the wake characteristics of a tidal stream turbine," *Renewable Energy*, vol. 132, pp. 989–997, 2019.

[93] A. Bahaj and L. Myers, "Shaping array design of marine current energy converters through scaled experimental analysis," *Energy*, vol. 59, pp. 83–94, 2013.

[94] B. Morandi, F. D. Felice, M. Costanzo, G. Romano, D. Dhomé, and J. Allo, "Experimental investigation of the near wake of a horizontal axis tidal current turbine," *International Journal of Marine Energy*, vol. 14, pp. 229–247, 2016.

[95] T. Stallard, T. Feng, and P. Stansby, "Experimental study of the mean wake of a tidal stream rotor in a shallow turbulent flow," *Journal of Fluids and Structures*, vol. 54, pp. 235–246, 2015.

[96] S. Tedds, I. Owen, and R. Poole, "Near-wake characteristics of a model horizontal axis tidal stream turbine," *Renewable Energy*, vol. 63, pp. 222–235, 2014.

[97] Y. Chen, B. Lin, J. Lin, and S. Wang, "Experimental study of wake structure behind a horizontal axis tidal stream turbine," *Applied Energy*, vol. 196, pp. 82–96, 2017.

[98] L. Myers and A. Bahaj, "Wake studies of a 1/30th scale horizontal axis marine current turbine," *Ocean Engineering*, vol. 34, pp. 758–762, 2007.

[99] N. Kolekar and A. Banerjee, "Performance characterization and placement of a marine hydrokinetic turbine in a tidal channel under boundary proximity and blockage effects," *Applied Energy*, vol. 148, pp. 121–133, 2015.

[100] R. Malki, I. Masters, A. J. Williams, and T. N. Croft, "Planning tidal stream turbine array layouts using a coupled blade element momentum-computational fluid dynamics model," *Renewable Energy*, vol. 63, pp. 46–54, 2014.

[101] D. O'Doherty, A. Mason-Jones, C. Morris, T. O'Doherty, C. Byrne, P. Prickett, and R. Grosvenor, "Interaction of marine turbines in close proximity," in *Proc. of 9th European Wave and Tidal Energy Conference (EWTEC), Southampton, UK*, 2011.

[102] W. Hunter, T. Nishino, and R. H. Willden, "Investigation of tidal turbine array tuning using 3D Reynolds-Averaged Navier-Stokes Simulations," *International Journal of Marine Energy*, vol. 10, pp. 39–51, 2015.

[103] T. Stallard, R. Collings, T. Feng, and J. Whelan, "Interactions between tidal turbine wakes: experimental study of a group of three-bladed rotors," *Philosophical Transactions of the Royal Society of London A: Mathematical, Physical and Engineering Sciences*, vol. 371, no. 1985, 2013.

[104] M. Nuernberg and L. Tao, "Experimental study of wake characteristics in tidal turbine arrays," *Renewable Energy*, vol. 127, pp. 168–181, 2018.

237

[105] P. Jeffcoate, T. Whittaker, C. Boake, and B. Elsaesser, "Field tests of multiple 1/10 scale tidal turbines in steady flows," *Renewable Energy*, vol. 87, pp. 240–252, 2016.

[106] P. Mycek, B. Gaurier, G. Germain, G. Pinon, and E. Rivoalen, "Experimental study of the turbulence intensity effects on marine current turbines behaviour. part II: Two interacting turbines," *Renewable Energy*, vol. 68, pp. 876–892, 2014.

[107] C. Morris, *Influence of Solidity on the Performance, Swirl Characteristics, Wake Recovery and Blade Deflection of a Horizontal Axis Tidal Turbine.* PhD thesis, School of Engineering, Cardiff University, 2014.

[108] T. Divett, R. Vennell, and C. Stevens, "Optimization of multiple turbine arrays in a channel with tidally reversing flow by numerical modelling with adaptive mesh," *Phil Trans R Soc A*, vol. 371, p. 20120251, 2013.

[109] S. Funke, P. Farrell, and M. Piggott, "Tidal turbine array optimisation using the adjoint approach," *Renewable Energy*, vol. 63, pp. 658–673, 2014.

[110] R. Vennell, S. W. Funke, S. Draper, C. Stevens, and T. Divett, "Designing large arrays of tidal turbines: A synthesis and review," *Renewable and Sustainable Energy Reviews*, vol. 41, pp. 454–472, 2015.

[111] T. Divett, R. Vennell, and C. Stevens, "Channel-scale optimisation and tuning of large tidal turbine arrays using LES with adaptive mesh," *Renewable Energy*, vol. 86, pp. 1394–1405, 2016.

[112] E. González-Gorbeña, R. Y. Qassim, and P. C. C. Rosman, "Multidimensional optimisation of Tidal Energy Converters array layouts considering geometric, economic and environmental constraints," *Renewable Energy*, vol. 116, pp. 647–658, 2018.

[113] S. P. Neill, E. J. Litt, S. J. Couch, and A. G. Davies, "The impact of tidal stream turbines on large-scale sediment dynamics," *Renewable Energy*, vol. 34, pp. 2803–2812, 2009a.

[114] T. Roc, D. Greaves, K. M. Thyng, and D. C. Conley, "Tidal turbine representation in an ocean circulation model: Towards realistic applications," *Ocean Engineering*, vol. 78, pp. 95–111, 2014.

[115] D. Fallon, M. Hartnett, A. Olbert, and S. Nash, "The effects of array configuration on the hydro-environmental impacts of tidal turbines," *Renewable Energy*, vol. 64, pp. 10–25, 2014.

[116] S. Nash, N. O'Brien, A. Olbert, and M.Hartnett, "Modelling the far field hydro-environmental impacts of tidal farms — A focus on tidal regime, inter-tidal zones and flushing," *Computers and Geosciences*, vol. 71, pp. 20–27, 2014.

[117] I. Fairley, I. Masters, and H. Karunarathna, "The cumulative impact of tidal stream turbine arrays on sediment transport in the Pentland Firth," *Renewable Energy*, vol. 80, pp. 755–769, 2015.

[118] J. Thiébot, P. B. du Bois, and S. Guillou, "Numerical modeling of the effect of tidal stream turbines on the hydrodynamics and the sediment transport – Application to the Alderney Race (Raz Blanchard), France," *Renewable Energy*, vol. 75, pp. 356–365, 2015.

[119] T. Roc, D. C. Conley, and D. Greaves, "Methodology for tidal turbine representation in ocean circulation model," *Renewable Energy*, vol. 51, pp. 448–464, 2013.

[120] L. Myers and A. Bahaj, "Experimental analysis of the flow field around horizontal axis tidal turbines by use of scale mesh disk rotor simulators," *Ocean Engineering*, vol. 37, pp. 218–227, 2009.

[121] H. Tennekes and J. Lumley, *A First Course in Turbulence*. The MIT Press, 1972.

[122] ANSYS, *ANSYS Fluent Theory Guide*, November 2013. Release 15.0.

[123] P. Mycek, B. Gaurier, G. Germain, G. Pinon, and E. Rivoalen, "Numerical and experimental study of the interaction between two marine current turbines," *International Journal of Marine Energy*, vol. 1, pp. 70–83, 2013.

[124] F. R. Menter, M. Kuntz, and R. Langtry, "Ten Years of Industrial Experience with the SST Turbulence Model," in *Turbulence, Heat and Mass Transfer 4* (K. Hanjalić, Y. Nagano, and M. Tummers, eds.), Begell House, Inc., 2003.

[125] ANSYS, *ANSYS Fluent User's Guide*, November 2013. Release 15.0.

[126] O. Lucca-Negro and T. O'Doherty, "Vortex breakdown: a review," *Progress in Energy and Combustion Science*, vol. 27, pp. 431–481, 2001.

[127] D. G. Lilley, "Prediction of inert turbulent swirl flows," *AIAA Journal*, vol. 11, no. 7, pp. 955–960, 1973.

[128] J. Beér and N. Chigier, *Combustion aerodynamics*. Applied Science Publishers Ltd., 1972.

[129] O. Lucca-Negro, *Modelling of swirling flow instabilities*. PhD thesis, School of Engineering, University of Wales, Cardiff, 1999.

[130] S. Farokhi, R. Taghavi, and E. Rice, "Effect of initial swirl distribution on the evolution of a turbulent jet," *AIAA Journal*, vol. 27, no. 6, pp. 700–706, 1989.

[131] P. R. Bevington and D. K. Robinson, *Data reduction and error analysis for the physical sciences*. McGraw-Hill, 2003.

[132] National Institute of Standards and Technology, "e-Handbook of Statistical Methods." `http://www.itl.nist.gov/div898/handbook/`, 2013. [Online; last accessed 23-August-2018].

[133] B. Everitt and A. Skrondal, *The Cambridge Dictionary of Statistics*. Cambridge University Press, 2010.

[134] M. Allmark, *Condition Monitoring and Fault Diagnosis of Tidal Stream Turbines Subjected to Rotor Imbalance Faults.* PhD thesis, School of Engineering, Cardiff University, 2016.

[135] D. Diezel, D. Messig, F. Piscaglia, A. Montorfano, G. Olenik, O. T. Stein, A. Kronenburg, A. Onorati, and C. Hasse, "Evaluation of scale resolving turbulence generation methods for Large Eddy Simulation of turbulent flows," *Computers & Fluids*, vol. 93, pp. 116–128, 2014.

[136] T. Blackmore, W. Batten, and A. Bahaj, "Inlet grid-generated turbulence for large-eddy simulations," *International Journal of Computational Fluid Dynamics*, vol. 27, no. 6–7, pp. 307–315, 2013.

[137] ANSYS, *ANSYS Fluent UDF Manual*, November 2013. Release 15.0.

[138] M. H. Baba-Ahmadi and P. Dong, "Numerical simulations of wake characteristics of a horizontal axis tidal stream turbine using actuator line model," *Renewable Energy*, vol. 113, pp. 669–678, 2017.